

**Mechanics and execution of homologous  
recombination: a single-molecule view**

**Ondrej Belan**

Imperial College London

and

The Francis Crick Institute

PhD Supervisor: Dr Simon J Boulton

A thesis submitted for the degree of

Doctor of Philosophy

Imperial College London

September 2021

## **Declaration of Originality**

I, Ondrej Belan, confirm that the work presented in this thesis is my own. Where information has been derived from other sources, I confirm that this has been indicated in the thesis.

## **Copyright Declaration**

The copyright of this thesis rests with the author. Unless otherwise indicated, its contents are licensed under a Creative Commons Attribution-Non Commercial 4.0 International Licence (CC BY-NC). Under this licence, you may copy and redistribute the material in any medium or format. You may also create and distribute modified versions of the work. This is on the condition that: you credit the author and do not use it, or any derivative works, for a commercial purpose. When reusing or sharing this work, ensure you make the licence terms clear to others by naming the licence and linking to the licence text. Where a work has been adapted, you should indicate that the work has been changed and describe those changes. Please seek permission from the copyright holder for uses of this work that are not included in this licence or permitted under UK Copyright Law.

## Abstract

Homologous recombination (HR) is an essential mechanism for the repair of toxic DNA double-strand breaks (DSBs), which, when not repaired accurately, can give rise to cancer and hereditary disorders. During HR, RAD51 forms helical nucleoprotein filaments on RPA-coated ssDNA with the help of mediator proteins (BRCA2 and RAD51 paralogs) and catalyses strand invasion into homologous duplex DNA. How this is achieved is not completely understood. To dissect the process on molecular level, I first reconstituted nematode RAD-51 presynaptic filament assembly in the presence of mediator proteins at the single-molecule level and demonstrated that BRC-2 promotes RAD-51 nucleation, while RAD-51 paralogs transiently bind 5' RAD-51 filament ends to stimulate RAD-51 growth in a 3' to 5' direction. In the second part of the thesis, I investigated the consequences of a permanently 'switching on' RAD-51 by engineering a variant of human RAD51, I287T, that forms presynaptic complexes efficiently without the recombination mediators present and analysed its impact on cellular DNA metabolism. I showed that RAD51 I287T is toxic in cells as it interferes with genome duplication by promiscuously loading at replication forks. Lastly, I demonstrated that nematode RAD-51 is surprisingly tolerant to mismatches during DNA strand exchange catalysis. The mismatch tolerance can be abolished by engineering specific mutations into the DNA binding loop of RAD-51, which causes meiotic HR stalling in the absence of regulatory motor proteins. Together, this work has uncovered unappreciated mechanisms that promote and maintain optimal RAD51 filament assembly and how deviations to optimal assembly rates can lead to disease - a phenomenon referred to as the 'Goldilocks principle' of RAD51 assembly.

## Acknowledgement

First, I would like to thank my supervisor, Dr. Simon J Boulton, for giving the opportunity to do PhD in his lab, for all his guidance and professional advice. Similarly, I would like to thank Prof. David S Rueda, my secondary supervisor, for giving me the opportunity to work in this lab on this collaborative PhD project, and for his guidance during my first professional encounter with the single-molecule world. I would like to thank also to the remaining members of my thesis committee: Dr. Thomas Surrey and Dr. Jesper Svejstrup for their help and constructive feedback.

Next, I would like to thank all the members of the Boulton lab with a few specific mentions: Roopesh – a friend and spectacular biochemists, Valerie – for all the work on RAD51 IT mice, Roberto – for cell culture training and being a great friend, Tim Lippert – for our science discussions and friendship, Panos – for teaching me the DNA fiber technology. I also thank all the members of Rueda lab, specifically: Artur – for his friendship and data analysis, Matt Newton – for his friendship and showing me the ropes in the wet lab, Mohamed – for all the discussions and teaching me how SM FRET works, Adam – for help with photobleaching analysis. Many thanks to George, Paul PD, Paul G and other members who made a very pleasant work environment to be in. I would also like to acknowledge the collaborators: Consuelo and Fadri from MRC; Justin and Eric Greene from Columbia University, Luke and Eric from West lab for unlabelled RPA, Crick STPs– fermentation, peptide chemistry, structural biology, transgenics, and media preparation teams.

I would also like to thank to my friends here in London, who put a lot of joy into my time spent doing PhD: Terka, Marie, Erik, Damini, Miguel, Zuzana and Nikita.

Last, but not least, I would like to thank my closest family, my mum, Adriana, and my two sisters, Anka and Borka, for their endless support in everything I am doing. I thank my dad, Jan, who raised me in a way, that rooted important life values in me. I could not be here without the help from my family. Finally, I would like to thank Aleks, who has been there recently in the some of the most difficult, but also most joyful moments in my life. You will always have a special place in my heart <3.

# Table of Contents

<b>Abstract.....</b>	<b>4</b>
<b>Acknowledgement.....</b>	<b>5</b>
<b>Table of Contents .....</b>	<b>6</b>
<b>Table of figures.....</b>	<b>8</b>
<b>List of tables... ..</b>	<b>10</b>
<b>Abbreviations.....</b>	<b>11</b>
<b>Chapter 1. Introduction.....</b>	<b>14</b>
1.1 <i>DNA double-strand breaks and their repair .....</i>	14
1.2 <i>DSB repair via homologous recombination.....</i>	19
1.3 <i>Single-molecule investigation of DNA repair.....</i>	32
1.4 <i>Thesis Objectives.....</i>	48
<b>Chapter 2. Materials &amp; Methods.....</b>	<b>50</b>
2.1 <i>Materials and reagents .....</i>	50
2.2 <i>Protein biochemistry and single-molecule biophysics.....</i>	57
2.3 <i>Nematode genetics .....</i>	66
2.4 <i>Mammalian cell biology and genetics .....</i>	70
<b>Chapter 3. Results 1: Single-molecule analysis reveals cooperative stimulation of RAD-51 filament nucleation and growth by mediator proteins</b>	<b>75</b>
3.1 <i>Single-molecule imaging system establishment .....</i>	75
3.2 <i>RAD51 nucleation and growth regulation .....</i>	80
3.3 <i>RAD-51 filament growth polarity .....</i>	84
3.4 <i>RFS-1/RIP-1 chaperones RAD-51 filaments .....</i>	87
3.5 <i>ATPase controls RFS-1/RIP-1 dynamics.....</i>	93
3.6 <i>Nematode phenotype of RFS-1 Walker A mutants.....</i>	97
<b>Chapter 4. Results 2: Exploring the genetic consequences of recombination mediator bypass.....</b>	<b>99</b>
4.1 <i>Engineering a self-loading human RAD51 variant.....</i>	99

4.2	<i>RAD51 I287T causes replication stress in vivo.....</i>	103
4.3	<i>RAD51 I287T accumulation at replicating chromatin.....</i>	107
4.4	<i>RAD51 I287T and sensitivity to fork-blocking lesions.....</i>	109
4.5	<i>RAD51 I287T and fork slowing after DNA damage.....</i>	113
<b>Chapter 5. Results 3: The influence of mismatch tolerance during meiotic</b>		
<b>DNA pairing..... 116</b>		
5.1	<i>C. elegans RAD-51 tolerates mismatches.....</i>	116
5.2	<i>Engineering mismatch-intolerant RAD-51 mutant.....</i>	120
5.3	<i>Mismatch (in)tolerance of CeRAD-51-TM in vivo.....</i>	123
5.4	<i>Genetic interactions of CeRAD-51-TM.....</i>	125
<b>Chapter 6. Discussion ..... 128</b>		
6.1	<i>Mechanism of Rad51 presynaptic filament assembly.....</i>	128
6.2	<i>DNA metabolism and optimal Rad51 filament assembly.....</i>	136
6.3	<i>Role of mismatch tolerance during meiotic recombination.....</i>	142
<b>Chapter 7. Conclusion..... 147</b>		
7.1	<i>Thesis conclusion.....</i>	147
7.2	<i>Future perspectives.....</i>	149
<b>Reference List..... 150</b>		

## Table of figures

Figure 1.1: An overview of metazoan DSB repair..	17
Figure 1.2: An overview of metazoan HR and its branches..	20
Figure 1.3: RAD51 presynaptic filament assembly.	23
Figure 1.4: DNA strand exchange steps.	27
Figure 1.5: Recombination at stalled RFs and DNA ICLs.	30
Figure 1.6: Principles of optical trapping.	36
Figure 1.7: DNA force-distance (FD) plot..	37
Figure 1.8: Single-molecule imaging of bacterial DNA end resection.	40
Figure 1.9: Physical properties of recombinase-ssDNA filaments..	41
Figure 1.10: Single-molecule studies of RecA filament assembly.....	42
Figure 1.11: Single-molecule studies of RAD51 filament disassembly.	44
Figure 1.12: Bacterial homology search.	46
Figure 1.13: Eukaryotic RAD51 homology search and strand exchange models. .	47
Figure 2.1: Biochemical assays to interrogate RAD51.....	61
Figure 2.2: DNA substrate preparation for SM experiments.	62
Figure 2.3: Nematode crossover assays.....	69
Figure 2.4: A schematic of nascent DNA strand labelling for SMARD.....	71
Figure 3.1: Recombinant proteins.	76
Figure 3.2: Fluorescent labelling of proteins..	77
Figure 3.3: Single-molecule imaging setup.	79
Figure 3.4: Single-molecule imaging of RAD-51 filament assembly in the presence of mediator proteins.....	81
Figure 3.5: BRC-2 and RFS-1/RIP-1 synergize to promote RAD-51 filament assembly.	83
Figure 3.6: A method to generate gapped $\lambda$ DNA substrates.	85
Figure 3.7: RFS-1/RIP-1 promotes filament growth in 3' to 5' direction.	86
Figure 3.8: 'Dipping' protocol to determine RAD-51 nucleation rates..	88
Figure 3.9: RFS-1/RIP-1 'chaperones' DNA-bound RAD-51 clusters by preventing RAD-51 dissociation.....	90
Figure 3.10: Single-step photobleaching analysis.....	92



Figure 3.11: Transient engagement of RFS-1/RIP-1 with 5' filament ends mediated by ATP hydrolysis.....	94
Figure 3.12: RFS-1/RIP-1 K56A fails to disengage from RAD-51 clusters. ....	95
Figure 3.13: RFS-1/RIP-1 K56A hinders RAD-51 filament assembly and growth..	96
Figure 3.14: RFS-1 Walker A mutants cause DNA damage sensitivity and abnormal RAD-51 focus formation <i>in vivo</i> .....	98
Figure 4.1: Biochemical characterization of RAD51 I287T.....	101
Figure 4.2: Replication stress in RAD51 IT/IT MEFs.....	105
Figure 4.3: RAD51 I287T accumulates on replicating chromatin. ....	108
Figure 4.4: Genotoxin sensitivity of RAD51 IT/IT MEFs.....	110
Figure 4.5: RAD51 IT/IT MEFs displays HDR efficiency similar to that of RAD51 +/- MEFs. ....	112
Figure 4.6: Further analysis of DNA damage sensitivity in RAD51 IT/IT MEFs. ..	114
Figure 5.1: Nematode RAD-51 tolerates mismatches during DNA strand exchange. ....	118
Figure 5.2: Characterization of RAD-51 triple mutant. ....	120
Figure 5.3: RAD-51 triple mutant fails to tolerate mismatches during strand exchange.....	122
Figure 5.4: RAD-51 triple mutant is intolerant to heterology <i>in vivo</i> . ....	124
Figure 5.5: RAD-51 triple mutant causes toxicity in the absence of RTEL-1 or HELQ-1 <i>in vivo</i> . ....	126
Figure 6.1: Model of metazoan RAD-51 presynaptic filament assembly.....	128
Figure 6.2: Proposed models for recombinase presynaptic filament assembly in nematode and mammalian cells.....	133
Figure 6.3: The Goldilocks principle of optimal RAD51 assembly rates.....	137
Figure 6.4: Mechanisms of genome instability in RAD51 IT/IT MEFs.....	138
Figure 6.5: Model depicting mismatch processing during meiotic recombination.	143

## List of tables

Table 1: Materials used in this study .....	54
Table 2: Oligonucleotides used in this study .....	56
Table 3: Recombinase activity decreases with organism complexity.....	99

## Abbreviations

53BP1	p53 binding protein 1
ADP	adenoside diphosphate
AFM	atomic force microscopy
APH	aphidicolin
ATM	Ataxia Telangiectasia mutated
ATP	adenoside triphosphate
ATP- $\gamma$ -S	adenosine-5-o-(3-thio-triphosphate)
ATR	ATM-related
BIR	break-induced replication
BLM	Bloom syndrome helicase
bp	base pair
BTR	BLM-TOP3-RMI1-RMI2
CDDP	dis-diammineplatinum (II) dichloride
<i>C. elegans</i>	<i>Caenorhabditis elegans</i>
CI	confidence interval
CO	crossover
CPT	camptothecin
crRNA	crispr RNA
CRISPR	clustered regularly interspaced short palindromic repeats
<i>D. melongaster</i>	<i>Drosophila melongaster</i>
dHJ	double Holliday junction
D-loop	displacement loop
DMC1	DNA meiotic recombinase 1
DNA	deoxyribonucleic acid
DNA-PKcs	DNA-dependent protein kinase catalytic subunit
DSB	DNA double-strand break
dsDNA	double-stranded DNA
DTT	dithiothreitol
EDTA	ethylenediaminetetraacetic acid
eGFP	enhanced green fluorescent protein
EM	electron microscopy

EXO1	exonuclease 1
eWLC	extensible worm-like chain
FA	Fanconi anemia
FBS	fetal bovine serum
FD	force-distance
FJL	freely jointed chain
FRET	Forster resonance energy transfer
gDNA	gapped DNA
GFP	green fluorescent protein
<i>H. sapiens</i>	<i>Homo sapiens</i>
HJ	Holliday junction
HN2	bis(2-chloroethyl)methylamine
HR	homologous recombination
HU	hydroxyurea
ICL	inter-strand crosslink
IR	ionising radiation
kb	kilobases
kDa	kilo Daltons
knts	kilo nucleotides
<i>M. musculus</i>	<i>Mus musculus</i>
MBP	maltose binding protein
MDC1	mediator of DNA damage checkpoint protein 1
MEF	mouse embryonic fibroblast
MMEJ	microhomology-mediated end joining
M-phase	mitotic phase
NA	numerical aperture
NCO	non-crossover
NER	nucleotide excision repair
NHEJ	non-homologous end joining
NLS	nuclear localisation signal
NP-40	nonidet P40
nts	nucleotides
OB	oligosaccharide binding
PAGE	polyacrylamide gel electrophoresis

PALM	photo activated localization microscopy
PARP1	poly-ADP ribose polymerase 1
PCR	polymerase chain reaction
RF	replication fork
RPA	replication protein A
RNA	ribonucleic acid
RNAi	RNA interference
RNF8	RING finger 8
RNF168	RING finger 168
<i>S. cerevisiae</i>	<i>Saccharomyces cerevisiae</i>
S-DNA	stretched DNA
SDS	sodium dodecyl sulfate
SIM	structured illumination microscopy
SD	standard deviation
SDSA	synthesis-dependent strand annealing
SEM	standard error of the mean
siRNA	small interfering RNA
SM	single-molecule
SMARD	single-molecule replication analysis of replication dynamics
SMX	SLX1-SLX4-MUS81-EME1-XPB-ERCC1
SSA	single-strand annealing
SSB	single-strand binding protein
STORM	stochastic optical reconstruction microscopy
ssDNA	single-stranded DNA
TIRF	total internal reflection fluorescence
TLS	translesion synthesis
Tris	Tris (hydroxymethyl) aminomethane
trRNA	transfer RNA
<i>U. maydis</i>	<i>Ustilago maydis</i>
UV	ultraviolet
WCE	whole cell extract
WLC	worm-like chain
WT	wild-type
<i>X. laevis</i>	<i>Xenopus laevis</i>

## Chapter 1. Introduction

### 1.1 DNA double-strand breaks and their repair

DNA double-strand breaks (DSBs) are among the most toxic lesions that our genome can encounter. DSBs arise spontaneously as a result of fork breakage during DNA replication, after exposure to ionising radiation or can be programmed to promote meiosis or V(D)J recombination during lymphocyte development (Chapman et al., 2012). Either way, an inability to accurately repair DSBs results in accelerated ageing, cell death and/or cancer development in metazoans. To counter these deleterious lesions, our cells have evolved multiple pathways to repair DSBs. These pathways share common steps during the repair reaction. In general, DSB repair involves three steps (Figure 1.1):

- I) DSB sensing by sensor proteins.
- II) Signal transduction and DSB repair pathway choice.
- III) Mechanistic DSB repair performed by multiple effector pathways.

#### 1.1.1 DSB sensing and DSB repair pathway choice

Cells possess specialized proteins that sense, recognize and bind to DSB ends with high affinity. In eukaryotic cells, two major DSB sensors are: KU70/80 dimer and MRN (MRE11-RAD50-NBS1) complex, that bind broken DNA ends (Myler et al., 2017; Symington, 2016). While KU70/80 plays an important role in repair of DSBs via non-homologous end joining (NHEJ), the MRN complex is involved in DSB sensing and also the subsequence resection step necessary for HR and micro-homology mediated end joining (MMEJ). MRN also acts as a 'molecular velcro' to physically tether broken DNA ends together (Williams et al., 2008).

As part of its sensing function, the MRN complex recruits the effector kinase ATM, which upon its recruitment triggers a DSB signalling cascade through the phosphorylation of multiple proteins. ATM phosphorylates a histone variant  $\gamma$ H2AX (Burma et al., 2001), which rapidly accumulates at the site of DSB (Rogakou et al., 1998). The spreading and amplified  $\gamma$ H2AX signal can be detected by immunofluorescence staining as so called 'foci' in the cell nucleus, which is a reliable

marker of DNA damage. ATM-phosphorylated  $\gamma$ H2AX is then recognized by mediator of DNA damage checkpoint protein 1 (MDC1) (Stewart et al., 2003; Stucki et al., 2005). MDC1 is also phosphorylated by ATM, which leads to the recruitment of an E3 ubiquitin ligase RING finger 8 (RNF8). RNF8 ubiquitylates an unknown protein that is bound by another E3 ubiquitin ligase, RNF168. RNF8, RNF168 and possibly other E3 ubiquitin ligases then ubiquitinate multiple targets among which is H2A (Doil et al., 2009; Huen et al., 2007; Mailand et al., 2007; Mattioli et al., 2012; Stewart et al., 2009). Depending on the cell cycle position, H2A ubiquitination at lysine 15 (H2AK15ub) then recruits either p53 binding protein 1 (53BP1) or Breast cancer type 1 susceptibility protein (BRCA1) in complex with BRCA1 Associated RING Domain 1 (BARD1) protein (Doil et al., 2009; Kim et al., 2007; Sobhian et al., 2007; Stewart et al., 2009; Wang et al., 2007). 53BP1 promotes NHEJ in G1 and limits DNA end resection, while BRCA1-BARD1 promotes DNA end resection in S/G2 required for HR and MMEJ. The antagonism between these two factors is most clearly demonstrated in BRCA1-deficient cells, wherein loss of 53BP1 is sufficient to rescue the DNA end resection defect (Bunting et al., 2010). How the decision between BRCA1 and 53BP1 recruitment made is currently poorly understood, however chromatin likely plays a major role. It has been suggested that 'old' parental histones marked by H4K20methyl serve to facilitate 53BP1 recruitment in G1 phase of the cell cycle (Nakamura et al., 2019), while newly deposited histones bearing no methylation at H4K20 (H4K20me0) are bound by the ankyrin domain of BARD1 (and its partner BRCA1) in S/G2 phase (Figure 1.1).

The choice between DSB repair pathways mediated by 53BP1 (pro-NHEJ) and BRCA1-BARD1 (pro-HR/MMEJ) ultimately impinges on DSB resection. DNA ends must be adequately processed for each different repair pathways to take place. In the case of 53BP1-mediated DSB repair, extensive DNA end resection is suppressed by 53BP1-binding shieldin complex, which is recruited to 53BP1 via RIF1 (Chapman et al., 2013; Dev et al., 2018; Di Virgilio et al., 2013; Ghezraoui et al., 2018; Gupta et al., 2018; Mirman et al., 2018; Noordermeer et al., 2018; Xu et al., 2015; Zimmermann et al., 2013). The Shieldin complex consists of 4 proteins: SHL1, SHL2, SHL3 and REV7. The single-stranded (ss)DNA binding domain of SHL2 containing 3 tandem oligosaccharide binding (OB) folds then tightly binds any short ssDNA tails generated at the break site and prevents further nucleolytic processing of DNA ends.

If longer ssDNA tracks are present at the break site, shieldin can also recruit the CST-Pol $\alpha$  complex to re-synthesize the opposing strand (Mirman et al., 2018). Whether this so-called fill-in reaction and direct resection inhibition by SHL2 are mutually exclusive phenomena, or if one of them is the predominant one is not well understood. In the case of BRCA1/BARD1-mediated DSB repair, unshielded DNA ends are nucleolytically processed to yield 3' ssDNA overhangs bound by replication protein A (RPA). RPA binding to ssDNA also stimulates the endonuclease activity of short-range resection nuclease MRE11 (Cannavo et al., 2019) and long-range DNA digestion by the DNA2 helicase-nuclease (Ceppi et al., 2020). Whether BRCA1 plays a direct role in promoting DNA end resection or simply competes with 53BP1 is not known (Figure 1.1).



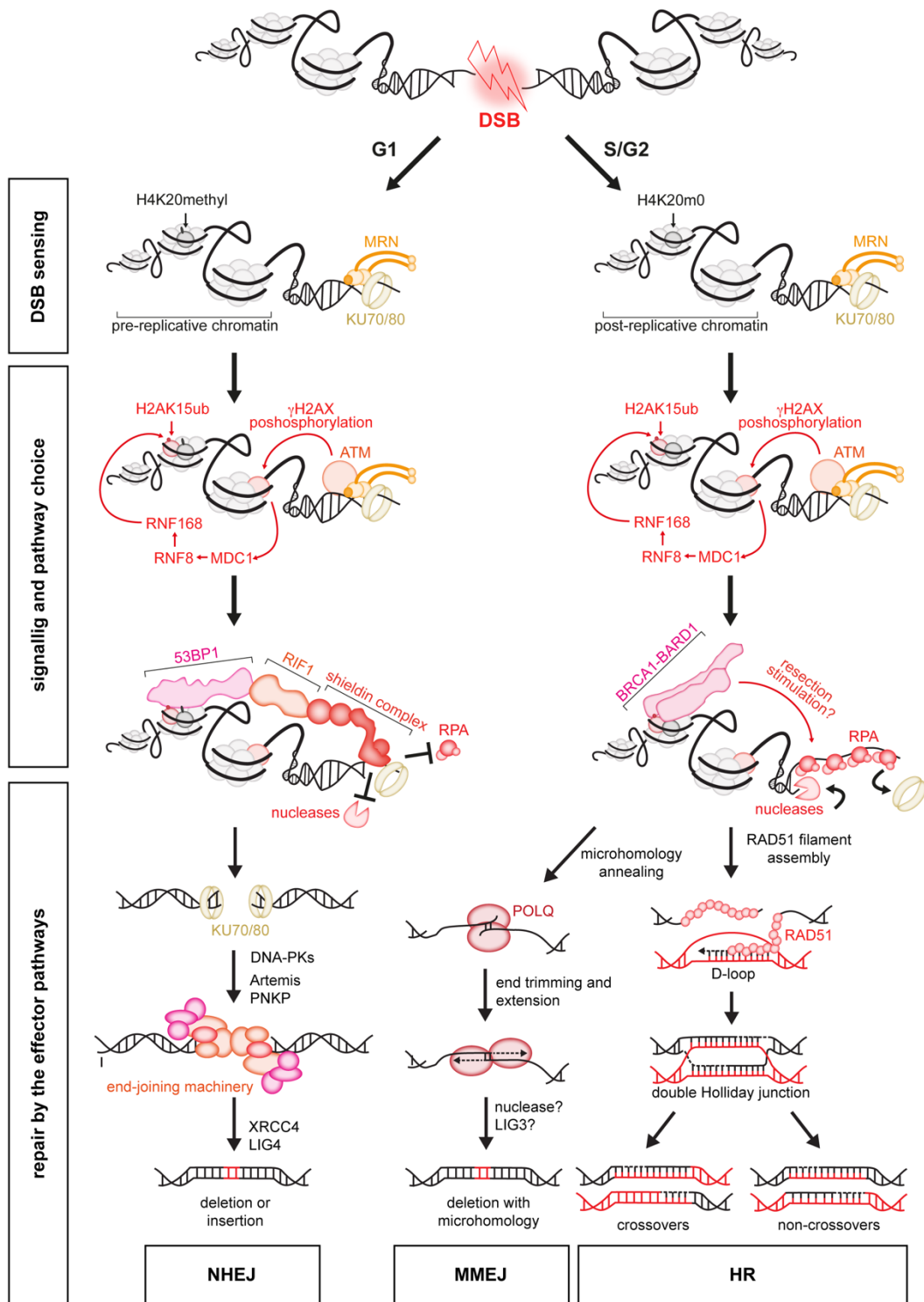


**Figure 1.1: An overview of metazoan DSB repair.** Examples of endogenous and exogenous sources of DSBs are indicated on top. Following DSB induction, DSB is sensed, and downstream cycle stage-regulated signalling cell takes place to decide which effector pathway will ultimately repair the DSB.

### 1.1.2 DSB repair effector pathways: NHEJ and MMEJ

The three major pathways that deal with DSBs are non-homologous end joining (NHEJ), homologous recombination (HR) and microhomology-mediated end joining (MMEJ). The choice between these pathways is dictated by the cell cycle stage, chromatin environment and DNA sequence context.

**Non-homologous end joining (NHEJ)** is a simple pathway for DSB repair of predominantly transcriptionally inactive genes in G1 phase of the cell cycle. NHEJ is error-prone by nature and generates mutations, typically small deletions and insertions (Chapman et al., 2012). During NHEJ, KU70/80-bound DNA ends recruit DNA-dependent protein kinase (DNA-PK) (Gottlieb and Jackson, 1993). DNA-PKs then phosphorylate multiple targets. dsDNA ends are processed by the Artemis nuclease and polynucleotide kinase-phosphatase PNKP among other proteins (Lieber et al., 2003). Processed DNA ends are then re-joined by the action of the XRCC4-LIG4 complex (Frank et al., 1998; Grawunder et al., 1997).

**Microhomology-mediated end joining (MMEJ)** is a highly mutagenic DSB repair pathway operating in eukaryotic cells in all phases of the cell cycle, when higher levels of DNA end resection and RPA loading are present. MMEJ generates small deletions containing 2-6 nt of microhomology at the break site. Initial work identified ligase 3 (LIG3) and poly-ADP ribose polymerase 1 (PARP1) as potential factors participating in MMEJ. More recently, POLQ was identified as a major MMEJ factor in mammalian cells (Sfeir and Symington, 2015). This is evident by POLQ-mediated joining of synthetic substrates containing microhomology *in vivo* and *in vitro* and synthetic lethality between POLQ and HR and/or 53BP1 loss (Ceccaldi et al., 2015; Feng et al., 2019; Kent et al., 2015; Mateos-Gomez et al., 2015). Diverse enzymatic activities of POLQ also play a part in MMEJ. POLQ helicase domain displaces RPA to allow for strand annealing of micro-homologies (Mateos-Gomez et al., 2017), POLQ polymerase domain potentially clips the resulting DNA flaps and extends 3' ends of annealed ssDNA strands (Zahn et al., 2021).

## 1.2 DSB repair via homologous recombination

**Homologous recombination** (HR) is a complex largely error-free pathway for the repair of mitotic and meiotic DSBs. HR operates in S/G2 phase of the cell cycle and consists of several steps including:

- I) Resection of broken DNA ends, which are coated by RPA.
- II) RPA displacement and formation of presynaptic recombinase-ssDNA filament.
- III) Homology search within sister chromatid of homologous chromosome and formation of a displacement loop (D-loop) intermediate, which is then extended by DNA polymerases.
- IV) Extended D-loop processing by multiple redundant pathways to restore the broken genetic information and formation of crossover and/or non-crossover products.

Multiple proteins are involved in HR and create many parallel branches that can complete the repair reaction once the strand invasion step has occurred (Figure 1.2).

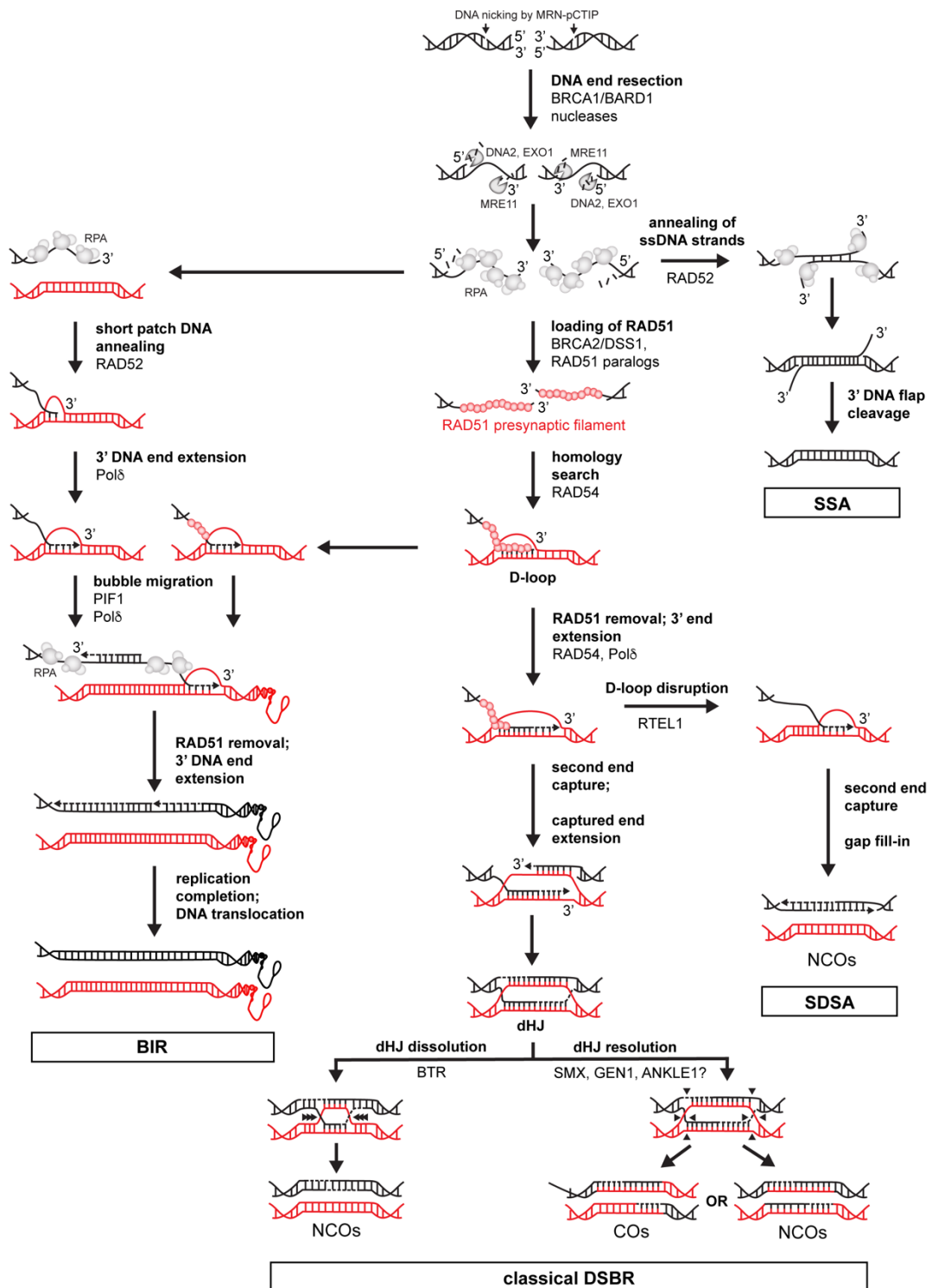


**Figure 1.2: An overview of metazoan HR and its branches.** Key HR sub-pathways are marked: SSA – single-strand annealing, MMEJ – microhomology-mediated end-joining, SDSA – synthesis-dependent strand annealing. Key HR intermediates: D-loop – displacement loop and dHJ – double Holliday junction. Recombination products, NCOs – non-crossovers and COs – crossovers. See main text for more details.

### 1.2.1 DNA end resection

DSB repair via HR can either occur directly following exposure to certain DNA damaging agents or may arise as intermediates of various DNA repair processes such as DNA inter-strand crosslink (ICL) repair. Depending on the nature of the damaging agent, DSBs can be either single-(replication block) or double-ended DSBs (i.e. ionizing radiation). During canonical double-ended DSB repair, DNA breaks are sensed and processed by the MRN complex, consisting of MRE11 nuclease, RAD50 ATPase and the NBS1 adaptor protein (Paull and Gellert, 1998; Symington, 2016). This complex is critical for DNA end resection, which entails the endonucleolytic cleavage of a DNA strand by MRE11. MRE11 endonuclease activity is stimulated by phosphorylated CTIP (Anand et al., 2016). CTIP phosphorylation occurs in S/G2 phase of the cell cycle upon DNA damage (Sartori et al., 2007), which helps to restrict HR from taking over in G1, where NHEJ is actively repairing DSBs. KU70/80 and RPA presence at the DNA ends also stimulates MRE11 to help further overcome DSB repair via NHEJ (Reginato et al., 2017). MRE11 then also performs initial short-range exonucleolytic digestion of DSBs in a 5' to 3' direction. The short 3' ssDNA overhang generated by short-range resection is further extended by DNA2, EXO1, BLM and WRN proteins that constitute the long range resection machinery to yield long (1-3 knt) ssDNA overhangs covered by RPA (Mimitou and Symington, 2008; Nimonkar et al., 2011). Single-strand annealing (SSA) catalysed by RAD52 (Mortensen et al., 1996) can also operate on resected DSBs, taking advantage of short homologies flanking the DSB site, which are annealed together to promote repair.

### 1.2.2 RAD51 presynaptic filament formation

The most well-studied process in mitotic recombination is the formation of the helical RAD51-ssDNA nucleoprotein filament following DNA end resection (Figure 1.3). This step is aided by multiple factors either directly by helping RAD51 to displace RPA bound to resected DNA or by stabilizing the nascent filaments. Once the presynaptic filament is established, RAD51 engages with the template duplex to search for homologous sequences. So called recombination mediator proteins, BRCA2 and RAD51 paralogs facilitate RPA displacement and assembly of RAD51

nucleoprotein filaments on ssDNA. Mutations in these proteins confer breast and ovarian cancer predisposition in humans, as well as Fanconi anemia (FA) – a complex congenital disease associated with bone marrow failure and cancer predisposition (Howlett et al., 2002; King et al., 2003; Meindl et al., 2010). The process of RAD51 filament formation is complex with multiple proteins involved. Next, I will describe in more detail several critical components involved in eukaryotic presynaptic filament assembly.

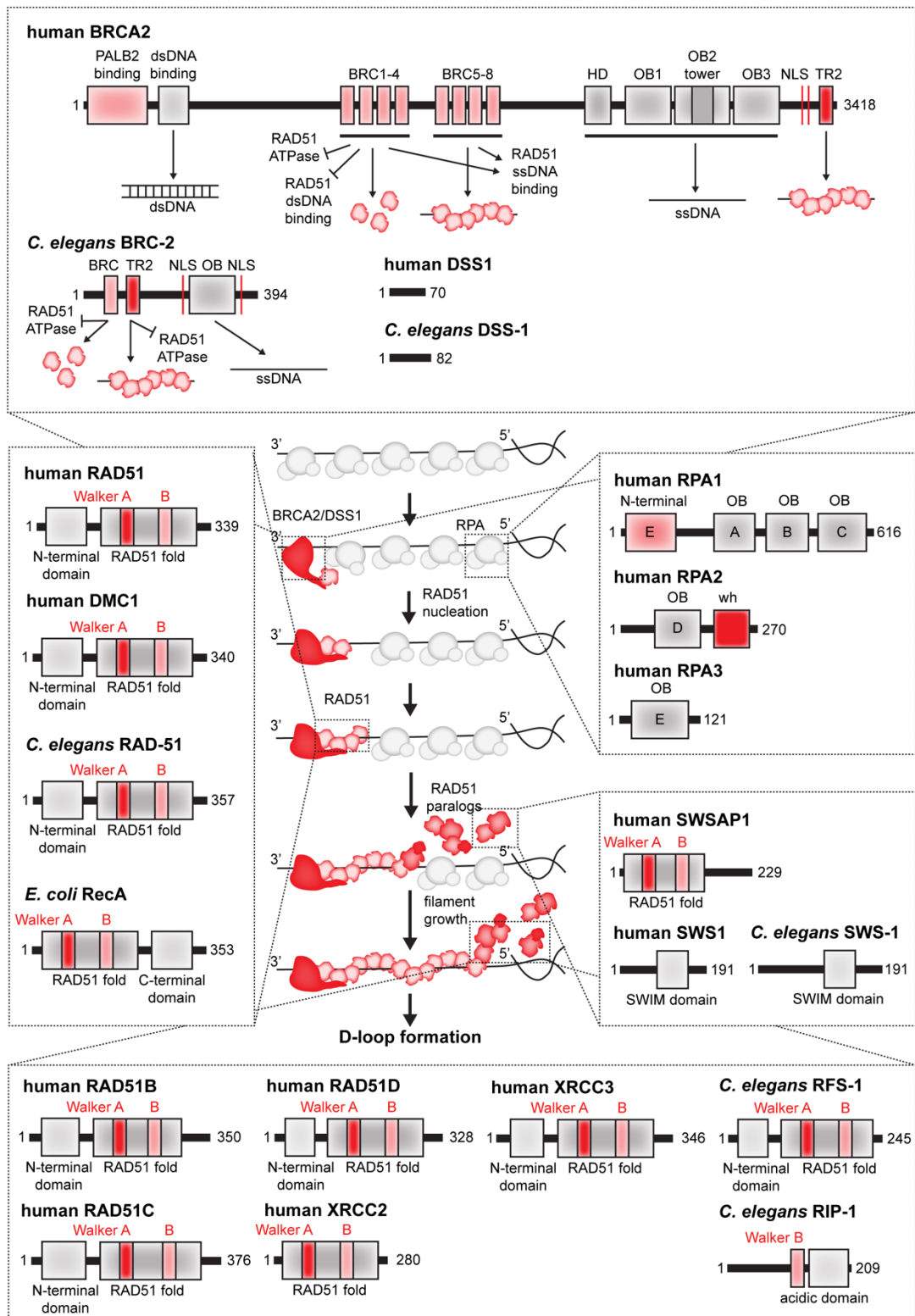


**Figure 1.3: RAD51 presynaptic filament assembly.** Human and nematode orthologs are shown. Given the complete RPA complex has not been identified in *C. elegans*, only human complex is shown. OB (A-E) – oligosaccharide binding domain. Wh - winged-helix domain. NLS – nuclear localization signal. Size of each polypeptide is indicated in aa.

**BRCA2/DSS1.** In human cells, PALB2 links BRCA1 to the recombination mediator protein, BRCA2 (Zhang et al., 2009). At present, a PALB2 ortholog has not been identified in other organisms, such as *C. elegans*. In human cells, DSS1 interacts with BRCA2 and directly facilitates RPA displacement via a DNA mimicry-like mechanism (Zhao et al., 2015). Although co-expression of nematode DSS-1 with the nematode BRCA2 homolog (BRC-2) improves overall BRC-2 solubility (Petalcorin et al., 2006), evidence for stable complex formation between DSS-1 and BRC-2 is lacking. Furthermore, DSS-1 addition does not have any effect on BRC-2's mediator activity in bulk assays suggesting that DSS-1 does not perform a key role in HR in *C. elegans* (Petalcorin et al., 2006). Human BRCA2 is a large, 3418 amino acid-long protein harbouring multiple domains important for its function. These include 8 BRC repeats interacting with RAD51, an extreme C-terminal RAD51-interaction region called TR2 domain, a C-terminal DNA-binding domain composed of three OB folds and a protruding tower domain and multiple other domains serving as protein-protein interaction hubs. BRCA2 homologs in other species vary in size and domain composition. For instance, nematode BRC-2 contains a single BRC repeat, a TR2 domain and a DNA-binding domain composed of a single OB fold (Martin et al., 2005). Importantly, a human "mini-BRCA2" constructed as a fusion of one or two BRC-repeats, a C-terminal DBD and TR2 region is sufficient to largely complement loss of full-length BRCA2 in mammalian cells (Siaud et al., 2011) as well as in strand exchange assays *in vitro* (Zhao et al., 2015). Thus, nematode BRC-2 represents a minimal functional RAD-51 ssDNA loading factor, analogous to mammalian mini-BRCA2. Due to the large size of human BRCA2, initial mechanistic studies were performed using full-length purified *C. elegans* and *Ustilago maydis* homologs (Petalcorin et al., 2006; Yang et al., 2005). Nematode BRC-2 interacts with nematode RAD-51 through its N-terminal BRC-TR2 domains and binds to ssDNA, but not dsDNA. This allows for specific RAD-51 targeting to RPA-covered resected ssDNA. Furthermore, BRC-2 was shown to inhibit RAD-51 ATPase activity (Martin et al., 2005). Since ATP-bound RAD-51 is more stable on ssDNA than ADP-bound form (Carreira et al., 2009), this mechanistically explained how BRC-2 stabilizes a RAD-51 nucleus on ssDNA. The BRC-repeat and TR2 domain of BRC-2 display two different modes of interaction with RAD-51. The BRC repeat binds RAD-51 in a 1:1 stoichiometry and when injected into the worm germline is sufficient to strip RAD-51



from ssDNA, causing loss of RAD-51 foci. Conversely, the TR2 domain binds specifically to RAD51-ssDNA filaments and when injected into the worm germline, stabilizes and increases the number of RAD-51 foci (Petalcorin et al., 2007). A similar mechanism was proposed later for human BRCA2. Specifically, human BRCA2 BRC repeats 1-4 were shown to bind RAD51 in solution with 1:1 stoichiometry, inhibit ATPase activity of RAD51, promote RAD51 binding to short ssDNA oligonucleotides and disrupt RAD51-dsDNA filaments (Carreira et al., 2009). BRC repeats 5-8 on the other hand, do not inhibit ATPase activity of RAD51, bind specifically to RAD51-ssDNA filaments and stabilize them, but fail to prevent RAD51-dsDNA filament formation (Carreira and Kowalczykowski, 2011). The TR2 domain of human BRCA2 was shown to bind RAD51-ssDNA filaments and stabilize them (Davies and Pellegrini, 2007; Esashi et al., 2007). Taken together, these observations indicate that BRC and TR2 act as a RAD51 loading unit, with the BRC repeat recruiting RAD51 monomers and acting to transport a portion of the RAD51 pool to damage sites and then uses TR2 as a stabilizing region to load a RAD51 nucleus on ssDNA.

**RAD51 and RPA.** Once loaded on ssDNA, RAD51 displaces trimeric ssDNA-bound RPA complex. RPA complex binds ssDNA with nanomolar affinity and plays a universal role as an ssDNA-binding factor in eukaryotic replication and DNA repair (Arunkumar et al., 2003). While in other eukaryotes RPA consists of three subunits, the third small subunit of RPA has not yet been identified in nematodes. In yeast and humans, during meiosis, a meiotic specific recombinase, DMC1 (Bishop et al., 1992), assembles on ssDNA together with RAD51. No meiotic RAD-51 paralog is found in *C. elegans*.

**RAD51 paralogs and Shu complex.** RAD51 paralogs are proteins similar in sequence, size and domain organization to RAD51. RAD51 paralogs are highly unstable when expressed on their own but form stable heteromeric complexes. In humans, there are 5 canonical RAD51 paralogs: RAD51B, RAD51C, RAD51D, XRCC2 and XRCC3. They form two distinct complexes: RAD51C-XRCC3 (X3) and RAD51B-RAD51C-RAD51D-XRCC2 (BCDX2) (Masson et al., 2001). Similarly, in nematodes, two RAD-51 paralogs, RFS-1 and RIP-1 form a heterodimeric RFS-1/RIP-1 complex (Taylor et al., 2015). *In vitro*, the RFS-1/RIP-1 complex binds the 5' end of RAD-51 filaments (Taylor et al., 2016), stabilizes them and promotes DNA

strand exchange. *In vivo*, RAD51 paralogs were shown to be important for RAD51 focus formation following exposure to DNA damage and repair of DSBs induced by DNA crosslinking agents and IR (Ward et al., 2007). RAD51 paralogs are recruited to DNA damage downstream of RAD51 as RAD51 depletion leads to loss of RAD51 paralogs from chromatin in *Xenopus* egg extract (Raschle et al., 2015). How RAD51 paralogs promote RAD51 accumulation on chromatin after DNA damage is not fully understood.

Recent work has shown that *C. elegans* Shu protein, SWS-1, contains a conserved SWIM domain, which interacts with RIP-1 through its Walker B motif (McClendon et al., 2016). The precise role of SWS-1 or its human homolog (SWS1, which forms a complex with SWSAP1) is currently unknown. One possibility is that it may function in targeting RAD51 paralogs to replication forks or post-replicative gaps as proposed for yeast Shu complex and yeast RAD51 paralogs, Rad55-Rad57 (Godin et al., 2013). In humans, Shu complex-deficient cells display meiotic defects, partial loss of RAD51 and DMC1 foci, subtle sensitivity to DNA damaging agents and subtle reduction in HR efficiency (Abreu et al., 2018; Prakash et al., 2021). Finally, RAD-51 paralogs were proposed to possess post-synaptic functions stemming from synthetic lethality with nematode HELQ-1 in meiosis (Ward et al., 2010). In agreement, human BCDX2 complex was shown to directly interact with HELQ in human cells (Adelman et al., 2013).

### 1.2.3 Homology search and DNA strand invasion

Following RAD51 presynaptic filament formation, a homology search takes place to locate corresponding DNA sequence within the sister chromatid DNA strand followed by strand invasion. RAD51 is uniquely shaped by evolution to efficiently catalyse this reaction. First, RAD51 filaments contain two DNA binding sites, one that accommodates both ssDNA and dsDNA with high affinity, and another that binds preferentially dsDNA, once the first site is occupied with ssDNA strand (Chen et al., 2008; Muller et al., 1990). Within this unique configuration, a strand-exchange reaction can take place. ATP plays an important role in the homology search process, but rather as a switch, than as the energy for a motor. The ATP-bound form of RAD51 is very stably bound to both ssDNA and dsDNA and in turn is highly active

in strand invasion assays *in vitro* (Chi et al., 2006). However, RAD51 needs to be turned over to allow for downstream processing of D-loops and replication forks. It is hypothesized that ATP hydrolysis allows for RAD51 dissociation from heteroduplex DNA once strand invasion has taken place. Indeed, ADP-bound RAD51 binds DNA with lower affinity and is less stable (Qi et al., 2015; Spirek et al., 2018). The molecular mechanism of the entire strand exchange process is poorly understood, but can be divided into several general steps (Figure 1.4):

- I) Initial dsDNA capture by a presynaptic filament formed on ssDNA
- II) Formation of a transient triplex DNA structure – so called paranemic joint
- III) Heteroduplex formation within short tracts of homology
- IV) D-loop formation
- V) Heteroduplex extension by polar branch migration
- VI) Recombinase release via ATP hydrolysis from the heteroduplex product

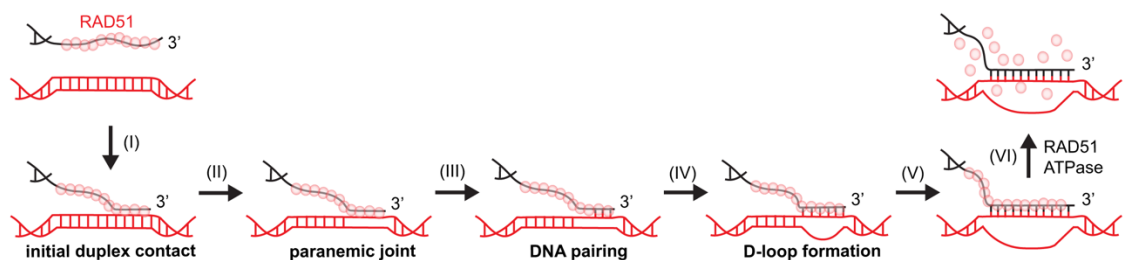


**Figure 1.4: DNA strand exchange steps.** RAD51-ssDNA presynaptic filament searches for homology, once homology is located, initial duplex capture occurs, followed by local triplex DNA formation. Initial pairing and heteroduplex formation then take place. Once longer tract of DNA strand has been exchanged, D-loop structure is formed and extended by branch migration. Finally, RAD51 is released from dsDNA via ATP hydrolysis.

This process is partially catalysed by RAD51 itself and partially aided by multiple eukaryotic recombination proteins. Among the most known is RAD54, a SWI2-SNF2 family dsDNA translocase and heteroduplex pump (Wright and Heyer, 2014). *In vitro*, RAD54 and its ATPase activity are critical for optimal formation of displacement loop (D-loop) invasion product by RAD51 (Petukhova et al., 1998; Solinger et al., 2001). It is proposed that RAD54 performs many functions to stimulate D-loop formation including enhancing homology search, aiding heteroduplex formation by RAD51

presynaptic filaments and clearing off RAD51 from heteroduplex DNA once the D-loop has formed to allow for D-loop extension (Wright and Heyer, 2014). In human cells, reports have proposed that BRCA1-BARD1 binds RAD51 filaments to stimulate homologous dsDNA capture *in vitro* (Zhao et al., 2017). More recent work also suggested that the BRCA1/BARD1 is important for stabilization of RAD51 at perturbed replication forks (RFs) to prevent fork degradation after HU-treatment (Daza-Martin et al., 2019). In *C. elegans*, a direct interaction between BRC-1/BRD-1 and RAD-51 has not been observed. Yet, in meiosis, *brc-1* deletion delays RAD-51, but not RPA focus formation indicating that it may perform a similar function in RAD-51 stabilization/loading as its human counterpart (Janisiw et al., 2018; Li et al., 2018). During meiosis, DMC1 catalyses DNA strand exchange, while RAD51 serves as an accessory factor, binding ssDNA, but not performing strand exchange reaction (Cloud et al., 2012). Why have these two recombinases evolved is not yet understood. Interestingly, unlike in yeast and mammalian cells, no meiotic RAD-51 paralog is found in *C. elegans*.

#### 1.2.4 Downstream processing of D-loops

D-loops must be extended by DNA polymerases for HR to proceed. Analysis of synthetic D-loop extension activity in fractionated cell extracts identified 2 DNA polymerases capable of extending D-loops: Pol $\delta$  and Pol $\eta$  (McIlwraith et al., 2005). During D-loop extension, multiple helicases can engage with D-loop structures and funnel recombination to different sub-pathways. During synthesis-dependent strand annealing (SDSA), a helicase engages with the D-loop to migrate and eventually disrupt it, so that extension product can be annealed with daughter strands yielding non-crossover products. In metazoans, genetic screens have identified RTEL1 as a *bona-fide* SDSA factor (Barber et al., 2008). Nematode RTEL-1 loss was shown to be synthetically lethal with loss of HIM-6 (nematode BLM homologue) and MUS-81, recombinant RTEL1 efficiently disrupts D-loops *in vitro* and RTEL-1 deletion leads to increased formation of crossovers in nematode meiosis (Youds et al., 2010). Collectively, this suggests that RTEL1 acts in an anti-crossover pathway by disrupting extended D-loops. Another factor, HELQ, plays a role downstream of RAD51 filament formation in *C. elegans* and human cells. RTEL1 and

HELQ operate in parallel pathways as evident from their synthetic lethal genetic interaction (Ward et al., 2010). The role of HELQ is not well understood. HELQ disruption in mammalian cells reduces HR efficiency in DR-GFP reporter assay (Adelman et al., 2013). Biochemical work suggests that nematode HELQ-1 can prevent binding of RAD-51 to dsDNA, but not ssDNA (Ward et al., 2010). One possibility is that HELQ-1 could disrupt RAD-51 bound to heteroduplex dsDNA after strand invasion. However, the exact role of HELQ in HR remains to be determined. Another branch of HR, break-induced replication (BIR), involves extensive DNA synthesis extension along the length of the entire chromosome arm coupled to D-loop migration by PIF1 helicase. BIR occurs when homology downstream of invasion site is not available and can be both RAD51-dependent or independent. BIR has been best described in yeast, where it was shown that it is highly mutagenic due to long stretches of ssDNA left behind the migrating D-loop and an unusual mode of DNA synthesis, where two DNA strands are synthesized in a conservative manner, with Pol $\delta$  synthesizing both strands (Saini et al., 2013; Wilson et al., 2013).

The displaced strand formed during D-loop extension can also be captured by the second strand to form a double-Holliday junction (dHJ), which must be resolved for proper chromosome segregation. This is achieved by multiple redundant pathways that process dHJs to complete repair. BLM-TOP3A-RMI1-RMI2 (BTR), possesses HJ dissolution activity (Karow et al., 2000), which yields exclusively non-crossover (NCO) products, which is evident by a synthetic lethality between HIM-6 and RTEL-1 in nematodes (Barber et al., 2008). The second pathway to process dHJ is termed resolution, which can be catalysed by multiple nucleases (also known as resolvases). Two predominant pathways for dHJ resolution are catalysed by SMX complex (SLX4-SLX1-MUS81-EME1-XPF-ERCC1) and GEN1 dimer (Ip et al., 2008; Wyatt et al., 2017). Recently, a possible third pathway of late HR intermediate resolution by the LEM-3 was identified in *C. elegans* (Hong et al., 2018). It remains to be established whether LEM-3 or its human homolog ANKLE1 can resolve dHJ.

### **1.2.5 Recombination and DNA inter-strand crosslink repair**

In addition to conventional DSBs repair, HR can function as a response to replication collision with DNA damage (trapped TOP1, UV-C adducts) or a DNA inter-strand

crosslink (ICL) (induced by cisplatin or nitrogen mustards). Cellular response to these agents also involves recruitment of HR factors but with multiple distinct features. In *E. coli*, the majority of spontaneous recombination events occur at ssDNA gaps behind the replisome (Xia et al., 2016). Similarly, BRCA2-deficient human cells accumulate ssDNA gaps behind the replisome, especially upon inhibition of PARP1 (Cong et al., 2021). Similarly, in nematodes, RAD-51 is recruited to perturbed forks. This is aided by recombination mediator proteins similarly to conventional DSB repair. In *C. elegans*, unlike BRC-2, the RFS-1/RIP-1/SWS-1 complex is largely dispensable for RAD-51 focus formation at IR-induced DSBs, but critical for RAD-51 focus formation after exposure to CPT, UV-C, CDDP and nitrogen mustards. Accordingly, RAD-51 paralog deficient nematode strains are only slightly sensitive to IR but display strong sensitivity to CPT and cisplatin (Ward et al., 2007). This indicates that RAD-51 paralogs are preferentially required to repair damaged replication forks (RFs) (Figure 1.5A).

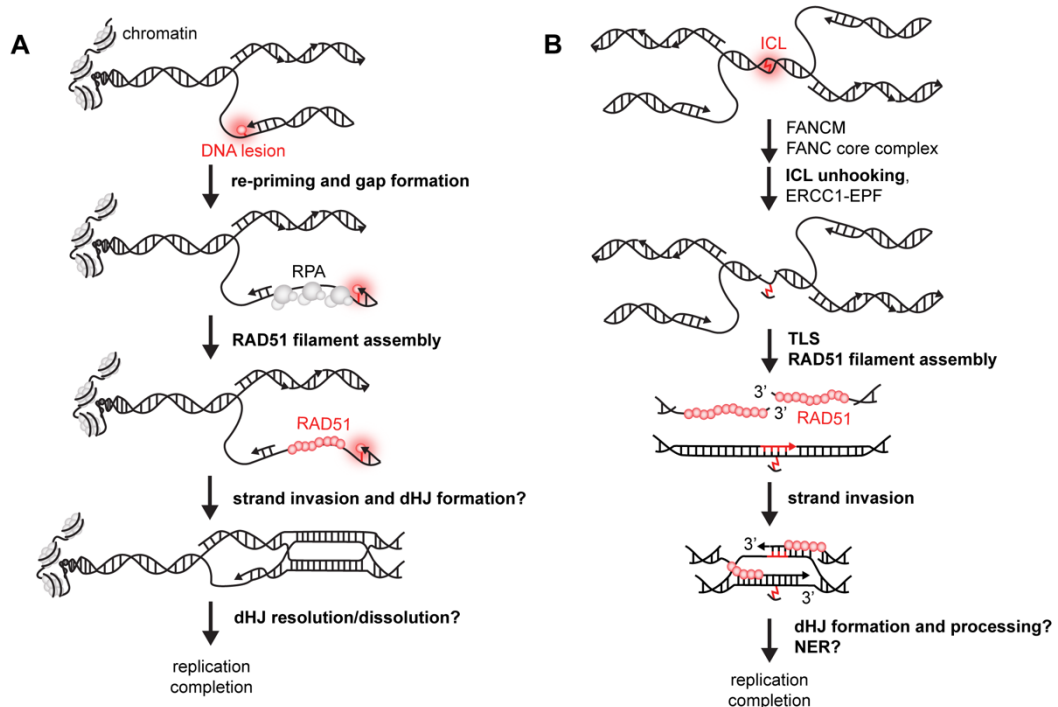


**Figure 1.5: Recombination at stalled RFs and DNA ICLs. (A)** During stochastic RF stalling, replisome can skip past the lesion leaving RPA-coated ssDNA behind the replisome. This serves as a substrate for RAD51 filament assembly, which then performs strand exchange with sister chromatid to seal the gap. **(B)** DNA ICLs are recognized by FA proteins leading to double incision (unhooking) around ICL site. When converging RFs meet the unhooked ICL, DSB is formed. Translesion DNA synthesis (TLS) incorporates nucleotides opposite the lesion, while RAD51

assembles on resected ssDNA strands. Subsequently, strand invasion takes place for HR to repair the break. Resulting crosslink adduct is repaired probably by NER.

DNA ICLs are a complex lesion requiring HR-mediated repair. Due to the fact that the lesion cross-links both DNA strands, nucleotide excision alone in G1 would not yield productive repair. Work in *Xenopus laevis* egg extracts using synthetic substrates containing ICL described in detail the ICL repair upon RF convergence (Semlow and Walter, 2021; Zhang et al., 2015). In metazoans, ICL repair involves the so called Fanconi anemia complementation (FANC) group of proteins. Fanconi anemia pathway is named after Guido Fanconi, a Swiss paediatrician, who, in 1927, documented specific birth defects and bone marrow failure in three siblings (Fanconi, 1927). These symptoms, including increased spontaneous chromosomal aberration in patient-derived cells and predisposition to certain types of cancer – such as acute myeloid leukaemia, were classified as a heterogenous clinical syndrome known as Fanconi anemia (FA). FA was shown to be associated with mutations in specific FANC group proteins. There are 4 FANC groups divided according to their role in FA pathway of ICL repair (Figure 1.5B):

- I) FANC group 1: FANCM helicase
- II) FANC group 2: FA core complex (FANCA-G, FANCL and FANCT)
- III) FANC group 3: FANCI-FANCD2 complex
- IV) FANC group 4: HR proteins and translesion DNA polymerases

During ICL repair, lesion recognition is likely triggered by convergence and/or stalling of RFs. This leads to recruitment of FANCM. Upon RF recognition by FANCM, a large multi-subunit E3 ubiquitin ligase FA core complex is recruited, which monoubiquitylates FANCI-FANCD2. Monoubiquitylated FANCI-FANCD2 binds in the physical proximity of the ICL and recruits the SLX4 nuclease scaffold protein together with ERCC1-XPF nuclease that ‘unhooks’ the DNA ICL by making a cut upstream and downstream of an ICL lesion (Semlow and Walter, 2021). Following ICL unhooking, a DSB is generated. Translesion polymerase REV1-Pol $\zeta$  fills the gap opposite to unhooked ICL (Semlow and Walter, 2021). The resulting monoadduct can be repaired later via NER. RAD51 then catalyses DNA strand invasion for HR to complete the repair and restore an active RF.

### 1.3 Single-molecule investigation of DNA repair

Over the past four decades, pioneering work has revealed the cellular pathways responsible for repair of various DNA lesions. Classical ensemble protein biochemistry methods have yielded invaluable insights into how different enzymatic activities help to resolve the potentially detrimental consequences of persistent DNA damage. However, given the complexity of these pathways including genetic redundancy, complex protein-protein interaction networks and components shared by multiple repair pathways (e.g. SLX4 and RAD51), our detailed understanding of how cells maintain genome stability has been limited. A great example is presynaptic filament formation - a critical process for HR to take place. Ensemble methods such as negative stain electron microscopy have informed us that the bacterial recombinase, RecA, rapidly forms long nucleoprotein filaments on both ssDNA and dsDNA plasmids (Di Capua et al., 1982; Williams and Spengler, 1986). However, how this process occurs remained poorly understood due to one critical obstacle – it's heterogeneity. RecA forms heterogenous species in solution, anything from a monomer to large species containing more than 10 RecA monomers (Kelley and Knight, 1997). There is no clear sequence preference for RecA binding to DNA, excluding formation of secondary structures (Bar-Ziv and Libchaber, 2001). In addition, long RecA filaments are likely formed a growth process, which involves addition of a RecA species to filament ends. What species addition is preferred – a RecA monomer, or a dimer? Does RecA filament growth occur from both ends? Or is there a directionality preference, similarly to actin filaments? And finally, how does ATP hydrolysis occur within the context of the filament? Interstitially or at the ends? Is there ATPase coordination between neighbouring RecA monomers? How do these filaments fall apart when no longer needed? All these questions are very difficult to address using standard bulk biochemistry methods. However, recent developments of single-molecule techniques has allowed us to address the heterogeneity problem and study these biochemical processes at an unprecedented detail.



### 1.3.1 The single-molecule approach

Classic ensemble biochemistry methods report on a value of a particular parameter of the system. This value is a mean of individual values of thousands of molecules in the system. Single-molecule techniques allow inspection of the distribution of values around the mean. Bulk averaging can obscure important activities, if they occur in only a fraction of the overall population of molecules, or for a short time period. Furthermore, by tracking individual molecules, previously unappreciated intermediates and reaction steps can be identified. A wide variety of single-molecule techniques has been established to address these issues. In very broad terms, these methods can be categorized as fluorescence of force-based techniques for *in vitro* analysis of biochemical systems, or *in vivo* analysis of cellular processes.

***In vitro* fluorescence-based approaches** are based on tracking of individual fluorescently labelled molecules such as motor proteins on microtubules or DNA-binding proteins on a single molecule of DNA. Reduction of background fluorescent signal can be achieved for instance by monitoring only a fraction of molecules present near the slide surface using total internal reflection microscopy (TIRF) (Axelrod et al., 1983), or a fraction of molecules present in the same plane using confocal fluorescence microscopy (Heller et al., 2013).

***In vivo* fluorescence-based approaches.** Individual fluorescently labelled low-abundance molecules can be tracked *in vivo* using the same methods described above. An example of this is single-molecule tracking of individual Halo-tagged telomerase molecules (Schmidt et al., 2016). Cells can be also pulse-labelled with specific probes and subsequently processed in a way that allows imaging on sparsely coated microscope slides. An example of this is single-molecule replication analysis of replication dynamics (SMARD) (Pasero et al., 2002). However, most protein complexes are more abundant in the cell, than in single-molecule *in vitro* systems, which complicates the analysis, as individual molecules are more difficult to resolve by conventional fluorescence microscopy methods (Hell et al., 2015). In recent years, development of super-resolution techniques has partially bypassed this issue. Techniques such as STORM and PALM which activate only a small fraction of fluorophores at a time, allows for localization of individual fluorophores by

gaussian fitting. This helps to overcome the diffraction limit and achieve super-resolution (30-50 nm) imaging of different sub-cellular structures. Similarly, structured illumination microscopy (3D-SIM) achieves super resolution by illuminating the sample with a known specially structured pattern of light. It relies on the Moiré effect – which is created when two grids are overlaid at a small angle. This allows a much higher image resolution of the observed sample, especially along the z-axis of the specimen. For instance, 3D-SIM has been successfully used to visualize recombination intermediates in the nematode germline despite its relative thickness (Woglar and Villeneuve, 2018).

***In vitro* force-based approaches** include magnetic, optical tweezers and atomic-force microscopy, among others. Using these approaches, force can be applied and measured on individual molecules tethered to microspheres (Neuman and Nagy, 2008). Microspheres can then be manipulated with either magnetic fields or optical traps. Both approaches have their benefits and their downsides. Optical tweezers are more readily amenable to simultaneous fluorescence imaging and force detection, while magnetic tweezers have the advantage of multiplex data acquisition and twisting the trapped molecules by rotation of the magnet. Atomic force microscopy, AFM relies on force measurements using a cantilever tip to interact with the surface of the sample. In addition to force data, it can provide limited structural information (high-resolution AFM) or real-time imaging of both label-free biological molecules in the solution (high-speed AFM).

***In vivo* force-based approaches** are still in relative infancy due to difficulty with measuring forces inside a living cell and/or organism without disrupting its integrity. Most studies measure forces along the cell surface by AFM. Similar approaches were also taken to measure cuticular stiffness of immobilized nematodes during the ageing process (Essmann et al., 2020). Several pilot studies have demonstrated optical trapping of particles inside transparent organisms such as zebrafish (Johansen et al., 2016) and *C. elegans* (LUMICKS, 2019).

### 1.3.2 Optical trapping and mechanical properties of DNA

Optical trapping is a phenomenon first observed more than 50 years ago (Ashkin, 1970; Ashkin et al., 1986). The principle of optical trapping is momentum transfer of photons to a dielectric particle resulting in its trapping in close proximity to the focus of a laser. Resulting force exerted on the trapped particle has two components: the scattering force and the gradient force (Neuman and Block, 2004). The scattering force component can be sought as a result of incident light impinged on the particle from one direction and being scattered. The change of momentum of these photons results in an opposing force exerted on the particle (Newton's third law), effectively pushing it in the same direction as the laser propagation. The second force component – the gradient force, results from refraction of light passing through the particle, if the particle has higher refractive index than its surrounding environment. Change of momentum of refracted photons results in a force in the opposite direction – towards the laser focus (Figure 1.6A). Near the laser beam focus, a high intensity gradient is present. Dielectric particles then experience the gradient force in the direction of the intensity gradient, due to dipole fluctuation. To achieve high gradient force that can exceed the scattering force and effectively trap the particle in all three dimensions, objectives with high numerical aperture (NA) are typically employed, which results in steeper intensity gradients. The trapped particles at the end are slightly displaced from the focal point of the laser in the 'down-beam' direction as a result of the balance between the two force components.

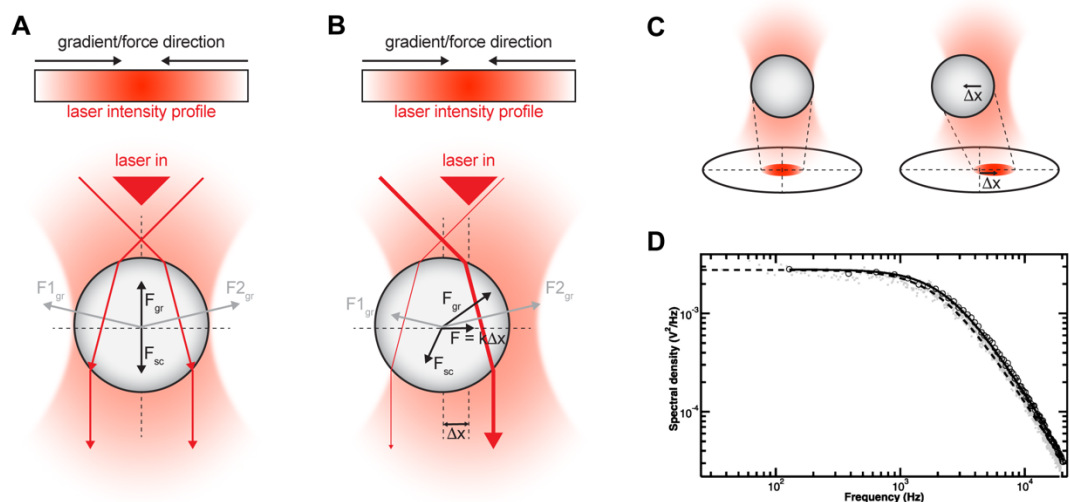


**Figure 1.6: Principles of optical trapping.** **(A)** Scattering ( $F_{sc}$ ) and gradient ( $F_{gr}$ ) forces acting on a bead in centre of an optical trap without any external force. Two representative rays of light with intensities indicated by line thickness are shown (red arrows). Gray lines (F1 and F2) represent corresponding gradient forces. **(B)** Scattering and gradient forces ( $F_{sc}$  and  $F_{gr}$ ) acting on a particle deflected from the centre of an optical trap over a distance  $\Delta x$  by an applied external force. Two representative rays of light with intensities indicated by line thickness are shown (red arrows). Gray lines (F1 and F2) represent corresponding gradient forces. **(C)** Deflection of the laser path caused by bead displacement is detected on a quadrant photodiode, QPD. **(D)** Force calibration using Lorentzian fit (black line) of the power spectra to calculate rolloff frequency  $f_0$ . (Neuman and Block, 2004)

Typically, a spherical particle – a bead, is trapped for the purpose of the experiment. The bead displacement from the trap by a specific distance,  $x$ , requires the force,  $F$ , which follows Hook's law with the trap acting as a spring (Figure 1.6B):

$$\mathbf{F} = -\alpha \times \mathbf{x} \quad (1)$$

where  $\alpha$  is the trap stiffness.

Particle displacement,  $x$ , is detected by using a quadrant photodiode, which measures deflection of the trapping laser (Figure 1.6C). Position of the bead centre relative to the trap centre in two dimensions is used to calibrate the stiffness of the trap and subsequently calculate the forces exerted on the bead. For trap stiffness calibration, Brownian motion of a particle, of a known size, is measured when no external forces are applied (Neuman and Block, 2004). The higher the stiffness of the trap, the more high frequency motion will dominate. A one-sided power spectrum is measured. It corresponds to the thermal motion of the particle at different frequencies (Figure 1.6D). The power spectrum of a trapped bead can be fitted with a Lorentzian fit:

$$S_{xx}(f) = \frac{k_B T}{\pi^2 \beta (f_0^2 + f^2)} \quad (2)$$

where  $S_{xx}(f)$  is in units of displacement (nm or V)<sup>2</sup>/Hz

$k_B$  is the Boltzmann's constant

$T$  is the absolute temperature

$\beta$  is hydrodynamic drag coefficient of the object  $\beta=6\pi\eta a$  for Stokes drag coefficient on a sphere of radius  $a$  in a medium with viscosity  $\eta$ .

$f_0$  is the rolloff frequency

Once  $f_0$  is determined from the fit, trap stiffness ( $\alpha$ ) can be calculated as follows:

$$\alpha = 12\pi^2 \times f_0 \times \eta \times r \quad (3)$$

where  $\eta$  is the viscosity of the medium and  $r$  is the radius of the bead.

Once the force calibration has been performed, molecules can be tethered between the beads and forces exerted on them can be accurately measured. Although it is possible to trap a variety of biological molecules, for the purpose of this thesis, I will focus on trapping of DNA and its biophysical properties.

The first experiments that examined the elastic properties of trapped DNA molecules were performed at the end of the last century (Bustamante et al., 1994; Marko and Siggia, 1995; Perkins et al., 1994a; Perkins et al., 1994b; Smith et al., 1996; Smith et al., 1992; Wang et al., 1997). Using optically trapped beads, DNA was tethered to either one or two of them and subsequently stretched, allowing the force exerted on the DNA to be measured and the corresponding DNA extension. Stretching a single dsDNA molecule between the two beads gives a well-described force-distance (FD) curve (Figure 1.7A).

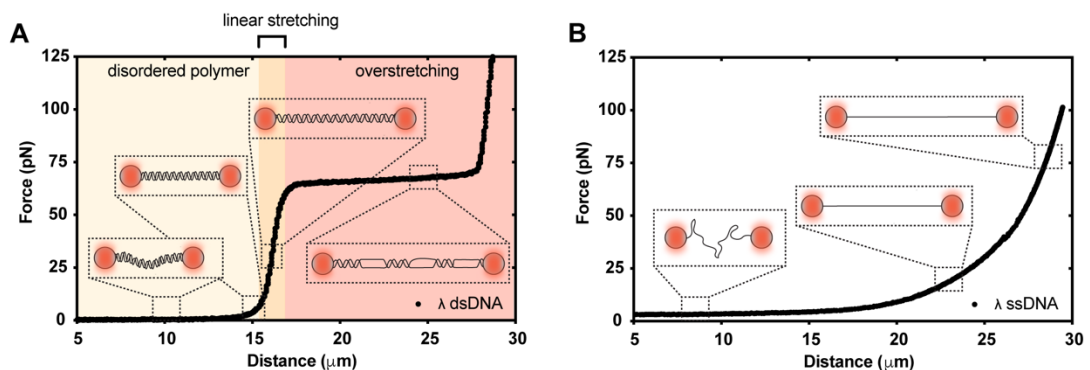


**Figure 1.7: DNA force-distance (FD) plot. (A)** FD curve obtained from stretching a single molecule of  $\lambda$  dsDNA from 0 to 125 pN. Once the distance in between the beads reaches  $L_c$ ,

dsDNA begins to stretch linearly with distance. At high forces (>65 pN) the DNA begins to melt. **(B)** FD curve obtained from stretching a single molecule of  $\lambda$  ssDNA from 0 to 100 pN. At low forces (<15 pN) pairing between complementary regions and secondary structure formation is possible.

When the distance between the beads is lower than the DNA contour length,  $L_c$ , the molecule is randomly disordered. As the distance between the beads increases, the DNA is straightened out. When the distance exceeds the contour length, the molecule enters an enthalpic phase, where the DNA is stretched. Small change in distance result in a large increase in force. This state is referred to as S-DNA (stretched DNA) - an elongated base-paired DNA conformation under high tension. Finally, at very high forces, DNA enters the overstretching phase, where the base pairing between the two DNA strands slowly breaks down as the dsDNA begins to melt. At low force regimes, < 5 pN, the behaviour of the DNA can be described using the Worm-like Chain Model, WLC, where DNA is described as a polymer with relatively high stiffness over short distances but being relatively flexible over long distances. An important parameter describing local stiffness of DNA in this model is persistence length,  $L_p$ , which indicates the distance scale over which the DNA molecule remains straight. Within the low force regime, the length of the DNA,  $L_{DNA}$ , is described as a function of force,  $F$ , according to WLC model as follows:

$$L_{DNA} = L_c \left( 1 - \frac{1}{2} \sqrt{\frac{k_B T}{F \times L_p}} \right) \quad (4)$$

where  $k_B$  is the Boltzmann's constant and  $T$  is absolute temperature in Kelvin.

This equation, however, fails to describe FD curve for DNA stretching at forces above 5 pN. At higher forces, the elastic response resulting from extension cannot be neglected. This is solved by including the enthalpic term, which describes polymer stretching due to external forces. The extension of material,  $\Delta L$ , due to application of external force,  $F$ , is described by the stretching modulus,  $S$ . For DNA:

$$\Delta L = L_c \times \frac{F}{S} \quad (5)$$

Upon incorporation of the stretching modulus into the WLC formula, the extensible WLC, eWLC, is given as follows (Odijk, 1995; Wang et al., 1997):

$$L_{\text{DNA}} = L_c \left( 1 - \frac{1}{2} \sqrt{\frac{k_B T}{F \times L_p}} + \frac{F}{S} \right) \quad (6)$$

where  $L_c$  is the contour length of dsDNA (0.34 nm/bp)

$L_p$  is the persistence length of dsDNA (50 nm in 150 mM NaCl at pH = 7)

$S$  is the stretching modulus of dsDNA (1400 pN in 150 mM NaCl at pH = 7)

$k_B$  is Boltzmann's constant

$T$  is absolute temperature in Kelvin

eWLC can fit FD curves close to the overstretching transition. Twisting of the DNA double helix can also be taken into account (Gross et al., 2011) to fit the FD curve even closer to the overstretching transition (>35 pN), however this analysis is beyond the scope of this work.

Beyond the overstretching regime, dsDNA is fully melted and becomes ssDNA. ssDNA is far more flexible and requires a different model to describe its FD curve (Figure 1.7B). This model is referred to as freely jointed chain, FJC. Each of the neighbouring bases are able to move freely relative to each other. At low forces (<15 pN), potential base pairing within a relaxed ssDNA molecules prevents the use of the FJC model. However, at forces >15 pN, the FJC, with addition of a stretching modulus to account for backbone length change with increasing force, can be used as follows (Wang et al., 1997):

$$L_{\text{DNA}} = L_c \left( \cot \left( \frac{2 \times F \times L_p}{k_B T} \right) - \left( \frac{k_B T}{2 \times F \times L_p} \right) \right) \times \left( 1 + \frac{F}{S} \right) \quad (7)$$

where  $L_c$  is the contour length of ssDNA (0.42 nm/bp)

$L_p$  is the persistence length of ssDNA (10 nm in 150 mM NaCl at pH = 7)

$S$  is the stretching modulus of ssDNA (800 pN in 150 mM NaCl at pH = 7)

$k_B$  is the Boltzmann's constant

$T$  is absolute temperature in Kelvin

### 1.3.3 Single molecule enzymology of HR

Single-molecule methods have been instrumental to provide invaluable insights into how accurate DSB repair is achieved. Here, I provide an overview of with specific examples of how single-molecule techniques helped to shine light on individual steps of HR.

**DNA end resection.** After demonstrating that a single DNA molecule can be manipulated using optically trapped beads (Bustamante et al., 1994; Marko and Siggia, 1995; Smith et al., 1996; Wang et al., 1997) and also directly imaged by fluorescence microscopy (Perkins et al., 1994a; Perkins et al., 1994b), a next step was direct visualization of DNA processing by an enzyme. This was achieved by monitoring nucleolytic degradation of individual, singly tethered, 48.5 kb-long,  $\lambda$ -phage DNA ( $\lambda$  DNA) molecules by the *E. coli* end-resection machinery, RecBCD (Bianco et al., 2001), in a two-channel microfluidics device, under constant buffer flow (Figure 1.8A). For the first time, translocation rates and processivity of single enzyme molecules were directly measured (Figure 1.8B).

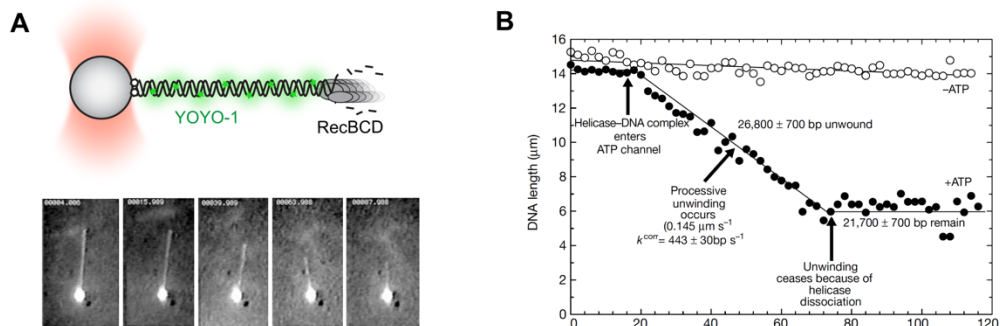


**Figure 1.8: Single-molecule imaging of bacterial DNA end resection.** (A) A schematic of an experiment, where singly tethered YOYO-1-stained  $\lambda$  DNA was digested by single molecule of RecBCD complex. Corresponding frames of the experiment are shown. (B) Quantification of RecBCD processivity and unwinding rate from experiment in (A). (Bianco et al., 2001).

**Recombinase-ssDNA filament formation** is a critical step in HR downstream of DNA end resection. Within the structure of RecA/RAD51-DNA filaments, both ssDNA and dsDNA are extended approximately 1.5-fold over the contour length of B-form



dsDNA (Chen et al., 2008; Conway et al., 2004; Short et al., 2016; Xu et al., 2017), with one RecA/RAD51 monomer contacting 3 nt of DNA (Figure 1.9A). Furthermore, RecA/RAD51-ssDNA filaments are significantly stiffer than ssDNA (Hegner et al., 1999), resulting in a very characteristic change in FD plot (Figure 1.9B). This property of RecA was used to monitor RecA filamentation in real-time at a single-molecule level by measuring decreasing force exerted on ssDNA stretched between two optical traps.

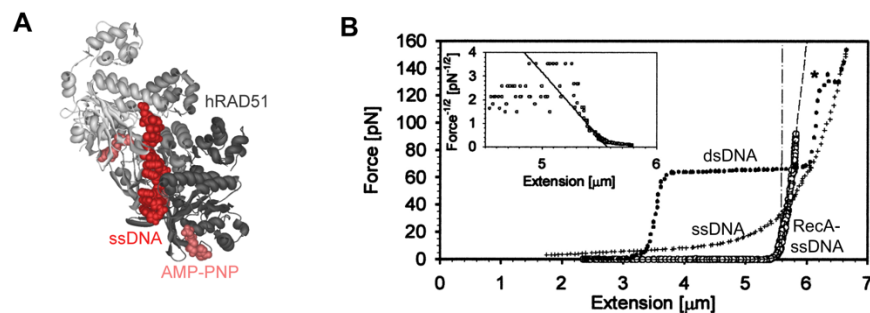


**Figure 1.9: Physical properties of recombinase-ssDNA filaments. (A)** CryoEM structure of human RAD51-ssDNA filament segment. Adapted from (Xu et al., 2017) **(B)** FD plots of single 10.4 kb dsDNA, 10.4 knt ssDNA and 10.4 knt RecA-coated ssDNA (in ATP- $\gamma$ -S) molecules. (Hegner et al., 1999).

To directly visualize the process, initial work (Galletto et al., 2006) took advantage of fluorescently labelled RecA filament formation on single-tethered double-stranded  $\lambda$  DNA stretched by laminar flow (Figure 1.10A). This work showed that RecA filaments form rapidly by a two-step mechanism: rate-limiting nucleation (Figure 1.10B), followed by rapid, bi-directional filament growth (Figure 1.10C). Given the kinetic fit of apparent nucleation rates, it was suggested that a minimum of 4-5 monomers are required to form a stable RecA nucleus on dsDNA. Furthermore, preventing ATP hydrolysis by using slowly hydrolysable ATP analog, ATP- $\gamma$ -S, dramatically increases apparent nucleation rates, consistent with ATP-bound nucleofilaments being more stable species. The main drawback of this system is the lack of a proper substrate – SSB (RPA homolog in bacterial)-coated ssDNA. To circumvent this, long SSB-bound surface-tethered ssDNA substrates were used to measure RecA assembly (Figure 1.10D) (Bell et al., 2012). Kinetic fits of apparent nucleation rates revealed that in contrast to dsDNA, the minimal nucleation species on ssDNA is a RecA dimer. In

addition, bi-directional growth with a 2-fold kinetic preference for the 5' → 3' direction along an ssDNA backbone can be also observed (Figure 1.10D, E, F).

Tethering of long ssDNA between optical traps is significantly more difficult. Among methods to generate these substrates is *in vitro* site-specific integration of partially single-stranded plasmid into linear phage DNA. Using this relatively laborious method, long ssDNA gaps flanked by biotinylated dsDNA handles can be generated and used to monitor RecA filament assembly (Figure 1.10G). Imaging using these substrates has shown that addition of bacterial recombination mediator complex, RecFOR, increases both nucleation and growth of RecA filaments. For human RAD51 protein, similar experiments were performed on both dsDNA (Hilario et al., 2009) and bare ssDNA (Candelli et al., 2014). Surprisingly, even though RAD51 nucleation was readily detectable, with dimer constituting the minimal nucleus on ssDNA, filament growth events were rare and very slow (Candelli et al., 2014; Hilario et al., 2009). This raises the possibility, that perhaps in contrast to the bacterial system, a strong growth-mediator is required in eukaryotes.

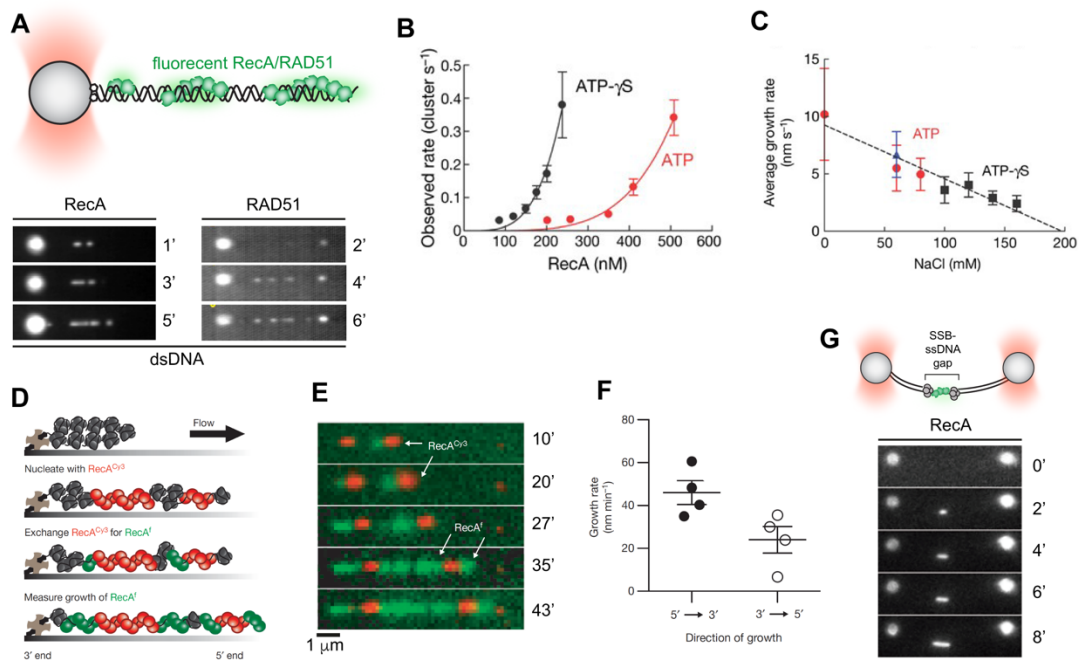


**Figure 1.10: Single-molecule studies of RecA filament assembly.** (A) Experimental setup. Images showing RecA or RAD51 assembly on  $\lambda$  dsDNA tethered to an optically trapped bead. RecA filaments grow rapidly, while RAD51 do not. (B) Nucleation rate of RecA cluster formation as a function of RecA concentration in different conditions. Lines represent power fit. (C) Growth rate of RecA filaments at different conditions. (D) Experimental setup to measure RecA filament growth rate in 5' and 3' direction along the ssDNA backbone. (E) TIRF images of a single  $\lambda$  ssDNA

molecule with FAM-labelled RecA nuclei growing bidirectionally by addition of Cy3-labelled RecA monomers. **(F)** Quantification of **(E)**. **(G)** Growth of fluorescently labelled RecA filaments on SSB-coated ssDNA gap with long dsDNA substrate. Figures adapted from (Bell et al., 2012; Galletto et al., 2006; Hilario et al., 2009).

Filament disassembly was also investigated (van Mameren et al., 2009) using fluorescently labelled human RAD51 and doubly tethered  $\lambda$  DNA between optically trapped beads (**Figure 1.11A**). It was revealed that RAD51-dsDNA filament disassembly occurs in bursts, where multiple RAD51 monomers dissociate at once. These bursts are coupled to release of tension stored on the filament and interspersed by long pauses where no dissociation of RAD51 is observed (**Figure 1.11B**). In accordance with previous work on RecA, where filament shrinkage exclusively occurs from the ends (Joo et al., 2006), a unified model was proposed, where an ATP-bound terminal RAD51 monomer in the filament acts as a filament cap, preventing dissociation from the ends even though ADP-RAD51 monomers are stochastically accumulating within the filament in the proximity of filament end. Once ATP hydrolysis occurs within the terminal monomer, all adjoined ADP-bound monomers dissociate in a single disassembly burst (**Figure 1.11C**). Later, similar behaviour was confirmed also for RAD51-ssDNA filaments (Candelli, 2013). How this process is influenced by additional mediator factors is currently unknown. Based on the proposed filament end-recognition model of nematode Rad51 paralogs, it seems tempting to speculate that *in vivo*, filaments could be stabilized by end-capping factors, similarly to tropomodulin capping and stabilizing pointed ends of actin filaments (Ono, 2010).

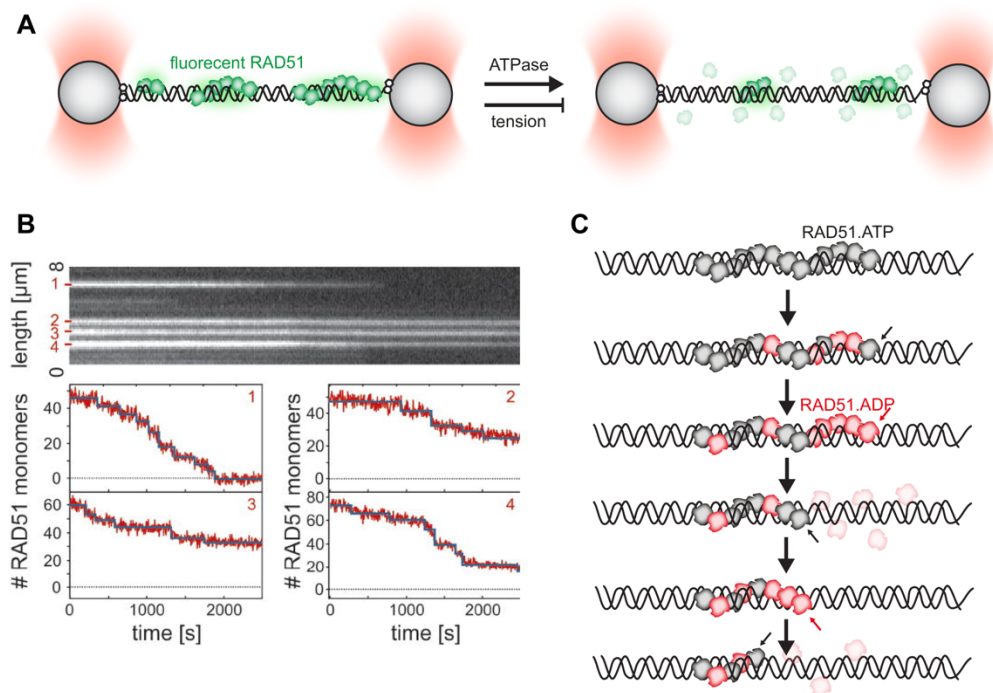


**Figure 1.11: Single-molecule studies of RAD51 filament disassembly.** (A) Experimental setup. RAD51 are assembled on double-tethered  $\lambda$  dsDNA in the presence of ATP and then disassembly is visualized in protein-free channel. Inhibiting RAD51 ATP hydrolysis or DNA stretching slows down RAD51 filament disassembly. (B) Kymograph showing real-time disassembly of dsDNA bound RAD51 clusters. Number of RAD51 monomers (estimated from fluorescent intensity and previous photobleaching analysis) as a function of time is shown. (C) Burst-pause RAD51 filament shrinkage model with terminal ATP-bound monomer acting as a filament ‘cap’. Figure adapted from (van Mameren et al., 2009).

**Homology search and DNA strand exchange** are among the most difficult processes to study by conventional ensemble biochemistry techniques. The problem of a protein finding a target DNA sequence seems rather simple at first glance. However, considering a short time window where a target needs to be found and excess of heterologous DNA that needs to be sampled makes it incredibly difficult – a good analogy being finding a needle in a haystack. Target search is a universal problem in biology, not unique to recombinase filaments, but also shared with such proteins as transcription factors, restriction enzymes and Cas9. The process is generally driven by diffusion – either 1D diffusion along a given lattice, 2D diffusion in a plane and/or 3D diffusion in space. Several diffusion-based mechanisms were proposed to facilitate DNA target search along heterologous DNA (Berg and von

Hippel, 1985; Berg et al., 1981; von Hippel and Berg, 1989) more than 30 years ago (Figure 1.12A):

- I) Sliding along the DNA lattice, where the protein randomly steps towards or away from its initial binding site.
- II) Hopping, where protein undergoes dissociation and re-binding cycles. Given DNA behaves like a rod-like structure on a short distance-scale, protein re-binding probability on adjoined DNA site (10-20 bp away) is high.
- III) Jumping while similar to hopping, takes advantage of DNA folding within 3D space, where a 'hop' over short physical distance, might mean a large 'jump' between sites far apart on linear DNA strand.
- IV) Intersegmental transfer occurs when proteins contain multiple DNA binding sites. One site can independently engage and/or release DNA, while the other remains bound. This leads to sampling of different DNA segments in physical proximity.

For RecA, single-molecule experiments using long (>1 knt) ssDNA donors and long (48.5 kb) dsDNA acceptors and optical trapping (Forget and Kowalczykowski, 2012) demonstrated that the predominant search mechanism occurs via intersegmental transfer (Figure 1.12B). Later, TIRF-based experiments using short (<40 bp/nt) substrates demonstrated that filament sliding over very short distances (<6 nt) also occurs (Ragunathan et al., 2012). Recently, it has been demonstrated that in contrast to a passive diffusion search model for RecA, in higher eukaryotes, active translocation of RAD51 filaments by RAD54 motor is critical for homology search along a linear dsDNA backbone (Crickard et al., 2020). RAD54 can translocate bidirectionally alongside the dsDNA backbone and physically bring RAD51-ssDNA to the sites of homology where DNA invasion aided by RPA-binding to the displaced strand takes place (Figure 1.13A, B).

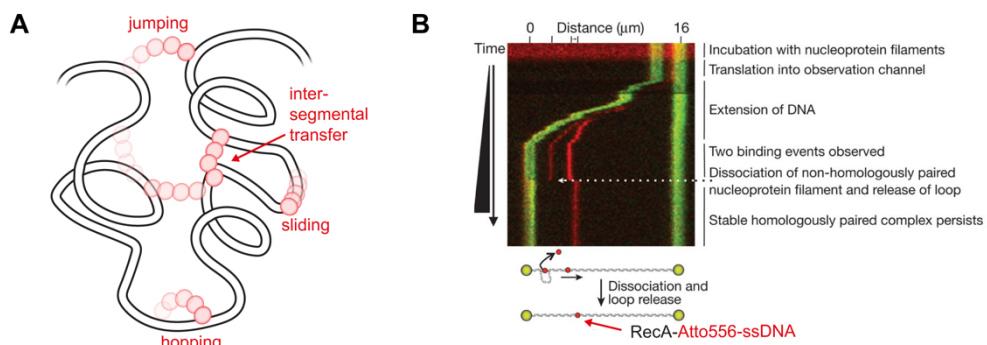


**Figure 1.12: Bacterial homology search. (A)** Target search models for DNA-binding proteins. **(B)** Transient loop formation mediated on  $\lambda$  dsDNA by RecA filaments assembled of long fluorescently labelled ssDNA, confirming inter-segmental transfer homology search mechanism for RecA filaments. Adapted from (Forget and Kowalczykowski, 2012).

During homology search by either 1D sliding, intersegmental transfer or RAD54-assisted translocation, the donor duplex is probed by the filament for the presence of homology. In line with structural information, work using ssDNA curtains and short microhomology-containing dsDNA substrates (Figure 1.13C, D) has shown that homology probing occurs in 3-nucleotide steps (1 RAD51 monomer at a time, Figure 1.13E), with a minimum of 8-9 nucleotides of homology required to achieve initial stable capture and  $\geq 15$  nt or homology required to achieve very stable product capture (Qi et al., 2015), presumably through D-loop formation. In line with these observations is a recent report of the first cryoEM structure of 15 nt-long RecA-D-loop intermediate (Yang et al., 2020). DNA extension within the filament greatly facilitates the probing process. Interestingly, the presence of even a single mismatch in the middle triplet of 9 nt minimal homology region destabilizes dsDNA capture intermediate when RAD51, or RecA is present, but not DMC1 – a meiosis-specific recombinase (Figure 1.13F) (Lee et al., 2015). Whether this intrinsic ability of DMC1 to overcome the presence of DNA mismatches *in vitro* is important also *in vivo* is not understood.

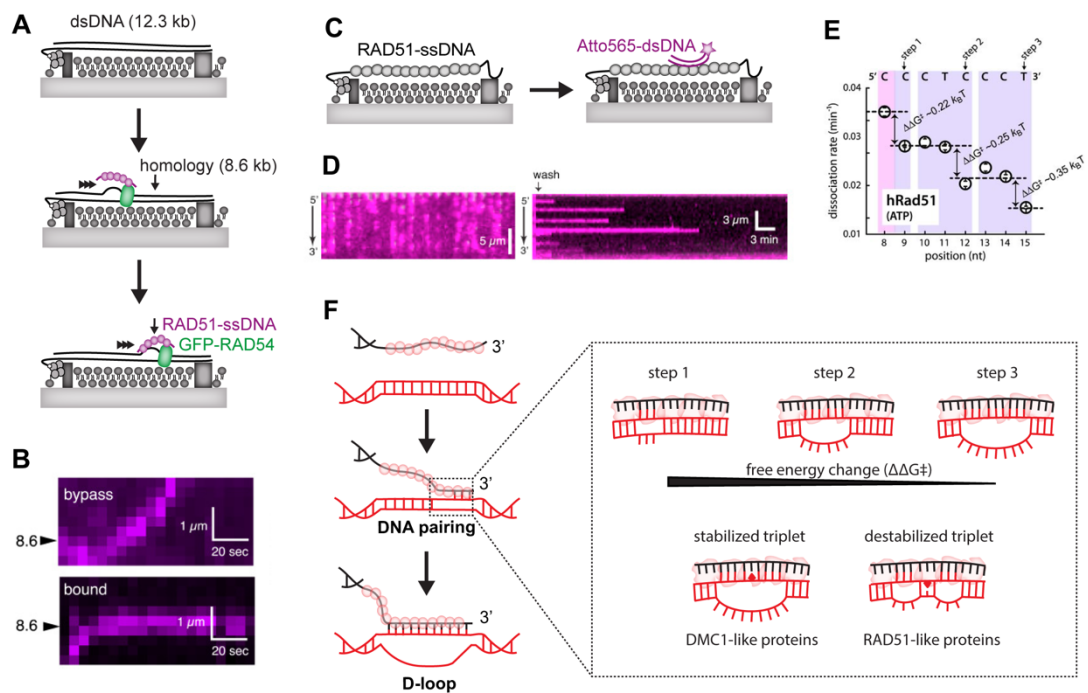


**Figure 1.13: Eukaryotic RAD51 homology search and strand exchange models.** (A) Experimental setup. dsDNA curtains immobilized on functionalized surface are incubated with RAD51 filaments assembled on fluorescent ssDNA and GFP-RAD54 to visualize the reaction using TIRF. (B) Images showing target recognition or bypass by translocating RAD51-ssDNA-RAD54 complex. Adapted from (C) Experimental setup to visualize DNA strand exchange using ssDNA curtains. (D) Left - images of fluorescent dsDNA captured by RAD51 filaments. Right - kymograph showing dissociation of fluorescently labelled dsDNA captured by RAD51 filaments. (E) Dissociation rate of captured dsDNA molecules as a function homology length. (F) Triplet-stepping model for homologous DNA pairing by recombinase proteins. More triplets paired, more stable the capture (lower calculated free energy). Unlike RAD51, DMC1 can 'overstep' a mismatch (shown as triangle) in the middle triplet during DNA pairing to achieve stable capture. Figure adapted from (Crickard et al., 2020; Lee et al., 2015; Qi et al., 2015).

## 1.4 Thesis Objectives

Homologous recombination is a critical pathway for largely error-free DSB repair and cancer suppression. A significant amount of work over the past decade has broadened our understanding of bacterial and eukaryotic recombinase filament assembly and homology search at the single-molecule level. However, our knowledge of how these processes are regulated by eukaryote-specific mediator factors is limited. Indeed, poor assembly parameters (such as filament growth) of eukaryotic recombinase compared to bacterial RecA suggest the need for additional factors to properly assemble RAD51 filaments *in vivo*. Similarly, given the poor strand exchange activity of RAD51, compared to RecA, a similar scenario likely applies to the homology search. Key questions that remain to be addressed:

- I) Which steps of eukaryotic RAD51 filament assembly/homology search do recombination mediators (BRCA2 and RAD51 paralogs) regulate? And how?
- II) Additionally, why is there a need for so many mediators (namely RAD51 paralogs) in eukaryotes, compared to bacteria, where RecA can perform many of its functions efficiently on its own?

Finally, in eukaryotes, two main recombinases have evolved – RAD51 and meiosis-specific DMC1. From single-molecule work, it seems that the main difference between the two is the ability to discriminate and tolerate DNA mismatches during homology search.

- III) Why has a meiosis-specific mismatch-tolerant recombinase evolved? And what is the role of potentially deleterious mismatch tolerance *in vivo*?

In my thesis, I will present my work addressing these open questions, with the aim of improving our understanding of HR as a genome stability maintenance mechanism critical to prevent disease development such as cancer. To this end, I have employed a combination of approaches, which include protein biochemistry, single-molecule



biophysics and genetics. As a primary model system for my work, I chose the nematode *C. elegans*. The nematode is an attractive model to study HR due to several key aspects:

- I) The small size and short life cycle of nematodes.
- II) The spatial organisation of the germline, with mitotic cells located at the distal tip followed by progressive stages of meiosis I, which facilitates the simultaneous evaluation of HR factors in mitosis and different meiotic stages in the same sample.
- III) Reverse genetic manipulation by RNAi or CRIPSR-Cas9 are particularly robust and can be readily delivered by feeding or injecting into the germline (Cho et al., 2013; Friedland et al., 2013).
- IV) The deletion of many HR genes, lethal in mammalian cells, is tolerated in the nematode (Barber et al., 2008).
- V) Compared to mammalian systems, many nematode HR proteins are readily amenable to biochemical and biophysical characterization due to their smaller size, better solubility and optimal activity at room temperature. A great example is nematode BRC-2, which is only 394 aa-long and can be expressed and purified from *E. coli*, while human BRCA2 is 3418 aa-long protein and only obtainable in very low quantity from human or insect cell expression systems (Martin et al., 2005).

The overall workflow of the thesis involves expression and purification of nematode core recombination machinery factors, fluorescent labelling of the proteins, so that they retain their activity, visualization of RAD51 presynaptic filament formation and homology search at a single-molecule level using a commercially available C-TRAP setup (optical tweezes, confocal fluorescence microscopy and microfluidics) or DNA curtains (in collaboration with Dr. Eric Greene lab at Columbia University) and engineering/characterization of specific mutants both *in vitro* and *in vivo* to validate the proposed mechanism of recombination machinery action.

## Chapter 2. Materials & Methods

### 2.1 Materials and reagents

REAGENT	COMPANY/REFERENCE	CATALOGUE N./ IDENTIFIER
<b>Antibodies</b>		
rabbit polyclonal anti-RAD-51	Dr. Anton Gartner	N/A
rat monoclonal anti-BrdU	Abcam	Cat# ab6326
mouse monoclonal anti-BrdU	Becton Dickinson	Cat# 347580
rabbit anti-RAD51 (Ab-1)	Merck	Cat# PC130
goat anti-Rat IgG (H+L), Alexa Fluor 594 conjugated	Thermo Fisher	Cat# A-11007
rabbit anti-Mouse IgG (H+L), Alexa Fluor488 conjugated	Thermo Fisher	Cat# A-11059
anti-PARP1	Cell Signalling Technology	Cat# 9542
anti-H3	Abcam	Cat# ab10799
anti-RPA70	Abcam	Cat# ab12320
goat anti-mouse immunoglobulins/HRP	Agilent-Dako	Cat# P0447
swine anti-rabbit immunoglobulins/HRP	Agilent-Dako	Cat# P0399
anti- $\alpha$ -Tubulin	Sigma Aldrich	Cat# T6199
anti-phospho- $\gamma$ H2AX	Millipore	Cat# 05-636
<b>Bacterial and Virus Strains</b>		
<i>E. coli</i> BL21(DE3)	NEB	Cat# C25271
<i>E. coli</i> DH5alpha	NEB	Cat# C2987H
<i>E. coli</i> (OP50)	Dr. Enrique-Martinez Perez	N/A
<i>E. coli</i> Rosetta(DE3)pLysS	Merck	Cat# 70956-3
<i>E. coli</i> BLR(DE3)pLysS	Novagen	Cat# 69956
<b>Chemicals, Peptides, and Recombinant Proteins</b>		
albumin from bovine serum	Sigma-Aldrich	Cat# A7030
HiTrap SP FF 1 mL column	Merck	Cat# GE17-5054-01
mono Q 5/50 GL column	Merck	Cat# GE17-5166-01
anti-FLAG M2 resin	Merck	Cat# A2220
3xFLAG peptide	Crick Peptide Chemistry STP	N/A
Ni-NTA agarose resin	Qiagen	Cat# 30210
amylose resin	NEB	Cat# E8021S
streptavidin coated polystyrene particles 0.5% w/v	Spherotech	Cat# SVP-40-5
lambda DNA	Thermo Fisher	Cat# SD0011
3,4-dihydroxybenzoic acid	Merck	Cat# 99-50-3
protocatechuate 3,4-dioxygenase	Merck	Cat# P8279-25UN

## Chapter 2 Materials and Methods

creatine kinase (CK)	Roche	Cat# 10127566001
creatine phosphate	Roche	Cat# 10621714001
5(6)-FAM, SE	Invitrogen	Cat# C1311
CoA Alexa 555 conjugate	Crick Peptide Chemistry STP	N/A
CoA Alexa 647 conjugate	Crick Peptide Chemistry STP	N/A
Cy3 Mono NHS Ester	Merck	Cat# GEPA13101
Cy3 Mono NHS Ester	Merck	Cat# GEPA13101
Ce his <sub>6</sub> -MBP-BRC-2	Belan et al, 2021	N/A
Ce RAD-51	Belan et al, 2021	N/A
Ce RFS-1/RIP-1-3xFLAG	Belan et al, 2021	N/A
Ce RFS-1 K56A/RIP-1-3xFLAG	Belan et al, 2021	N/A
Ce RFS-1 K56R/RIP-1-3xFLAG	Belan et al, 2021	N/A
Ce RFS-1/RIP-1-3xFLAG-YBBR	Belan et al, 2021	N/A
Ce RFS-1 K56A/RIP-1-3xFLAG-YBBR	Belan et al, 2021	N/A
Hs RAD51	Belan et al, 2021	N/A
Hs RAD51 I287T	Belan et al, 2021	N/A
his <sub>6</sub> -SUMO protease	Dr. Peter Cherepanov	N/A
hRPA	Dr. M. R. G. Taylor	N/A
hRPA-eGFP	Dr. Mauro Modesti	N/A
hRPA-mCherry	Dr. Eric C. Greene	N/A
Sfp - phosphopantetheinyl transferase	Belan et al, 2021	N/A
S. p. Cas9 nuclease V3	IDT	Cat# 1081059
S. p. Cas9 D10A nickase	IDT	Cat# 1081062
indole-3 acetic acid	Alfa Aesar	Cat# A10556
cis-diammineplatinum (II) dichloride	Sigma-Aldrich	Cat# P4394-250M
hydroxyurea	Sigma-Aldrich	Cat# H8627-5G
bis(2-chloroethyl)methylamine	Sigma-Aldrich	Cat# 122564-5G
(S)-(+)-Camptothecin	Sigma-Aldrich	Cat# C9911-250MG
hydroxyapatite 'fast flow'	Sigma-Aldrich	Cat# 391947
Q sepharose fast flow	Cytiva	Cat# 17051004
CldU	Sigma-Aldrich	Cat# C6891
IdU	Sigma-Aldrich	Cat# I7125
EdU	Thermo Fisher	Cat# A10044
thymidine	Sigma-Aldrich	Cat# T9250
biotin-azide	Thermo Fisher	Cat# B10184
PhosSTOP phosphatase inhibitor cocktail	Roche	Cat# PHOSS-RO
EDTA-free Complete protease inhibitor cocktail	Roche	Cat# COEDTAF-RO
streptavidin sepharose high performance	GE Healthcare	Cat# 17-5113-01
Lipofectamine 2000	Thermo Fisher	Cat# 11668019
ProLong Gold antifade with DAPI	Thermo Fisher	Cat# P36931
olaparib	Selleck Chemicals	Cat# S1060
etoposide	Sigma-Aldrich	Cat# BP885

aphidicolin	Sigma-Aldrich	Cat# A0781-1MG
methyl methanesulfonate (MMS)	Sigma-Aldrich	Cat# 129925-5G
pyridostatin hydrochloride	Merck	Cat# SML2690-5MG
Clarity western ECL	Bio-Rad	Cat# 1705061
Clarity Max western ECL	Bio-Rad	Cat# 1705062
Critical Commercial Assays		
QIAquick PCR Purification Kit	Qiagen	Cat# 28104
QuikChange Lightning site-directed mutagenesis kit	Agilent	Cat# 210519
subcellular protein fractionation kit	Thermo Fisher	Cat# 78840
Nano-Glo dual-luciferase reporter assay system	Promega	Cat# N1630
CellTiter-Glo luminescent cell viability assay	Promega	Cat# G7572
Experimental Models: Organisms/Strains		
<i>C. elegans rfs-1(fq127 [K56R]) III/hT2 (I;III)</i>	Belan et al, 2021	ATG563
<i>C. elegans rfs-1(fq130 [K56A]) III/hT2 (I;III)</i>	Belan et al, 2021	ATG567
<i>C. elegans brc-2(fq140[HA::AID::brc-2]) III; ieSi38 [Psun-1::TIR1::mRuby::sun-1 3' UTR, cb-unc-119(+)] IV</i>	Belan et al, 2021	ATG600
<i>C. elegans brc-2 (fq140 [HA::AID::brc-2]) rfs-1 (fq130 [K56A]) III; ; ieSi38 [Psun-1::TIR1::mRuby::sun-1 3' UTR, cb-unc-119(+)] IV</i>	Belan et al, 2021	ATG608
<i>C. elegans rad-51(knu529[N246S,E256A,K260H])COP1580 IV</i>	Steinfeld et al, 2019	DW778
<i>C. elegans rtel-1(tm1866) I</i>	Steinfeld et al, 2019	N/A
<i>C. elegans rcq-5(fx424) III</i>	Steinfeld et al, 2019	N/A
<i>C. elegans helq-1(tm2134) III</i>	Steinfeld et al, 2019	N/A
<i>C. elegans mln1[mls14 rol-1(e91)]/dpy-25(e817) II</i>	Steinfeld et al, 2019	N/A
<i>C. elegans rcq-5(fx424)III/rad-51(knu529[N246S,E256A,K260H])COP1580 IV</i>	Steinfeld et al, 2019	N/A
<i>C. elegans rtel-1(tm1866) I/rad-51(knu529[N246S,E256A,K260H])COP1580 IV</i>	Steinfeld et al, 2019	N/A
<i>C. elegans helq-1(tm2134) III/rad-51(knu529[N246S,E256A,K260H])COP1580 IV</i>	Steinfeld et al, 2019	N/A
<i>C. elegans mln1[mls14 rol-1(e91)]/dpy-25(e817) II/rad-51(knu529[N246S,E256A,K260H])COP1580 IV</i>	Steinfeld et al, 2019	N/A
<i>C. elegans dpy-17(e164) unc-36(e251) III</i>	Steinfeld et al, 2019	KR180
<i>C. elegans dpy-17(e164) unc-36(e251) III/rad-51(knu529[N246S,E256A,K260H])COP1580 IV</i>	Steinfeld et al, 2019	N/A

<i>C. elegans</i> N2 (Bristol)	Belan et al, 2021	CB
<i>C. elegans rfs-1(ok1372) III</i>	Belan et al, 2021	RB1279
<i>S. cerevisiae yJF1 (W303-1a pep4::KanMx4 bar1::Hph-NT1 ade2-1 ura3-1 his3-11 trp1-1 leu2-3)</i> parental strain for protein expression	Belan et al, 2021	N/A
Recombinant DNA		
Champion pET-SUMO-RAD-51	Belan et al, 2021	N/A
pBluescript SK(-)	Dr. Lumir Krejci	N/A
Pem1-NanoLuc-HDR substrate	Artios Pharma	N/A
pET-29-Sfp	Dr. Meindert Lamers	N/A
pET-MBP-1a-BRC-2	Belan et al, 2021	N/A
pJF2.1(pRS303)-RFS-1/RIP-1-3xFLAG	Belan et al, 2021	N/A
pJF2.1(pRS303)-RFS-1 K56A/RIP-1-3xFLAG	Belan et al, 2021	N/A
pJF2.1(pRS303)-RFS-1/RIP-1-3xFLAG-YBBR	Belan et al, 2021	N/A
pJF2.1(pRS303)-RFS-1 K56A/RIP-1-3xFLAG-YBBR	Belan et al, 2021	N/A
phRPA-eGFP	Dr. Mauro Modesti	N/A
pET11c-Rad51	Dr. Lumir Krejci	N/A
Software and Algorithms		
GraphPad Prism 7	Graphpad	<a href="https://www.graphpad.com/scientific-software/prism/">https://www.graphpad.com/scientific-software/prism/</a>
IgorPro 8.0	WaveMetrics	<a href="https://www.wavemetrics.com/products/igorpro">https://www.wavemetrics.com/products/igorpro</a>
SoftWoRx 3.0	Applied Precision	N/A
Fiji	Open source	<a href="https://imagej.net/Fiji">https://imagej.net/Fiji</a>
Matlab R2018b (9.5.0)	MathWorks	<a href="https://uk.mathworks.com">https://uk.mathworks.com</a>
Lumicks Pylake	Python package from Lumicks	<a href="https://lumicks-pylake.readthedocs.io/en/latest/index.html#">https://lumicks-pylake.readthedocs.io/en/latest/index.html#</a>
CellProfiler	Open source	<a href="https://cellprofiler.org">https://cellprofiler.org</a>
Other		
C-trap optical trapping and confocal microscopy setup	Lumicks	N/A
ÄKTA pure protein purification system	Cytiva	N/A
Optima LE-80K Ultracentrifuge	Beckman Coulter	N/A
Branson sonifier 450	Branson	N/A

Econo-Pac chromatography columns	Bio-Rad	Cat# 7321010
SnakeSkin dialysis tubing, 10 KDa MWCO	Thermo Fisher	Cat# 88243
Amicon Ultra-4 centrifugal filter unit	Merck	Cat# UFC803024

**Table 1: Materials used in this study**

OLIGONUCLEOTIDE	SOURCE
Cy5-90mer 5'-Cy5- AAATCAATCTAAAGTATATATGAGTAAACTTGGTCTG ACAGTTACCAATGCTTAATCAGTGAGGCACCTATCT CAGCGATCTGTCTATTT-3'	Sigma Aldrich
FAM-90mer 5'-FAM- AAATCAATCTAAAGTATATATGAGTAAACTTGGTCTG ACAGTTACCAATGCTTAATCAGTGAGGCACCTATCT CAGCGATCTGTCTATTT-3'	Sigma Aldrich
FAM-allT90mer 5'-FAM- TTTTCTTTCTTTTGTGTTTTTGTGTTTTCTTGGTCTGT CTGTTTCCTTTGCTTTTTCTGTGTGGCTCCTTTCTCT GCGTTCTGTCTTTTT-3'	Sigma Aldrich
Cy5-49mer 5'-Cy5- AGCTACCATGCCTGCACGAATTAAGCAATTCGTAAT CATGGTCATAGCT-3'	Sigma Aldrich
FAM-49mer 5'-FAM- AGCTACCATGCCTGCACGAATTAAGCAATTCGTAAT CATGGTCATAGCT-3'	Sigma Aldrich
49mer complementary strand 5'- AGCTATGACCATGATTACGAATTGCTTAATTCGTGC AGGCATGGTAGCT-3'	Sigma Aldrich
60mer 5'- ACGCTGCCGAATTCTACCAGTGCCTTGCTAGGACAT CTTTGCCACCTGCAGGTTACCCC-3'	Sigma Aldrich
150mer 5'- TCTTATTTATGTCTCTTTTATTTCAATTCCTATATTTAT TCCTATTATGTTTTATTCATTTACTTATTCTTTATGTT CATTTTTTATATCCTTTACTTTATTTTCTCTGTTTATTC ATTTACTTATTTTGTATTATCCTTATCTTATTTA -3'	Sigma Aldrich
FAM-40mer 5'-FAM- TAATACAAAATAAGTAAATGAATAAACAGAGAAAATA AAG-3'	Sigma Aldrich

Complimentary 40mer 5'- CTTTATTTTCTCTGTTTATTCATTTACTTATTTTGTATT A -3'	Sigma Aldrich
crRNA <i>rfs-1</i> K56 5'-TTTAGGAGTTGGTAAAACAC-3'	IDT
crRNA <i>HA::AID::brc-2</i> 5'-TTTTTAGATGAGTCACCCAT -3'	IDT
crRNA <i>dpy-10</i> 5'-GCTACCATAGGCACCACGAG-3'	IDT
ssDNA repair template <i>rfs-1K56A</i> 5'- TTCATCCAGGAAAATGCTACGAAATTGATGGCGATC TGGGTGTAGGAGCTACGCAAGTATGAATTCATATAT TTTATTTAGAGAATTTTCC-3'	IDT
ssDNA repair template <i>rfs-1K56R</i> 5'- TTCATCCAGGAAAATGCTACGAAATTGATGGCGATC TGGGTGTAGGACGAACGCAAGTATGAATTCATATAT TTTATTTAGAGAATTTTCC-3'	IDT
ssDNA repair template <i>HA::AID::brc-2</i> oligo 1 5'- CAGACTTTACCAGAATATTGTGACATCGACCGATGT ACCCATACGATGTTCCAGATTACGCTATGCCTAAAG ATCCAGCCAAACCTCCGGCCAAGGCACAAGTTGTG GGATGGCCACCGGTGAGATCATACCGGAA-3'	IDT
ssDNA repair template <i>HA::AID::brc-2</i> oligo 2 5'- GTTGTGGGATGGCCACCGGTGAGATCATACCGGAA GAACGTGATGGTTTCCTGCCAAAATCAAGCGGTG GCCCCGAGGCGGCGGCGTTCGTGAAGGGTGACTC ATCTAAAAAAGTGTAGTCAAGATTTA-3'	IDT
ssDNA repair template <i>dpy-10</i> 5'- CACTTGAACCTCAATACGGCAAGATGAGAATGACTG GAAACCGTACCGCATGCGGTGCCTATGG TAGCGGAGCTTCACATGGCTTCAGACCAACAGCCT AT-3'	IDT
RAD-51 wt PCR validation primer 5'- TCTAGCGGACGTCAGATGAAG-3'	Sigma Aldrich
RAD-51 TM PCR validation primer 5'- TCGCAGCCAGACAAATGCAT-3'	Sigma Aldrich
RAD-51 wt/TM common PCR validation primer 5'- ACGCGATTCTCTCCTTTTCCTT-3'	Sigma Aldrich
ssDNA lambda precursor oligo 1 5'- GGGCGGCGACCTGGACAA-3'	IDT

ssDNA lambda precursor oligo 2 5'- AGGTCGCCGCCCTTTTTTTT(BT)TT(BT)TT(BT)-3'	IDT
ssDNA lambda precursor oligo 2 5'- T(BT)TT(BT)TT(BT)TTTTTTTAGAGTACTGTACCTAGC ATCAATCTTGTCC-3'	IDT
lambda DNA hairpin oligo 1 5'- AGGTCGCCGCCCGGAGTTGAACG(BT) (BT)T(BT) T(BT)ACGTTCAACTCC-3'	IDT
lambda DNA hairpin oligo 2 5'- GGGCGGCGACCTCAA GTTGGACAA(BT)T(BT)T(BT)(BT)TGTCCTTGG-3'	IDT
tracr RNA (trRNA) 5'-GGACAGCAUAGCAAGU UAAAAUAAGGCUAGUCCGUUAUCAACUUGAAA AAGUGGCACCGAGUCGGUGCUUUUU-3'	IDT
crRNA λ2 5'-GUGAUAAGUGGAAUGCCA UGUUUUAGGAGCUAUGCUGUUUUUG-3'	IDT
crRNA λ4 5'-CAGATATAGCCTGGTGGTTCG UUUUAGGAGCUAUGCUGUUUUUG-3'	IDT
crRNA λ5 5'-GGCAAUGCCGAUGGCGAUA GGUUUUAGGAGCUAUGCUGUUUUUG-3'	IDT
crRNA λ4.2 5'- GCCAUUCUGCUUAUCAGGAA GUUUUAGGAGCUAUGCUGUUUUUG -3'	IDT
crRNA λ4.1 5'- GGCCAUGUAAGCUGACUUU AGUUUUAGGAGCUAUGCUGUUUUUG-3'	IDT
crRNA λ4.02 5'- AUUGCCAGGCUUAAAUGAG UGUUUUAGGAGCUAUGCUGUUUUUG-3'	IDT

**Table 2: Oligonucleotides used in this study**



## 2.2 Protein biochemistry and single-molecule biophysics

### 2.2.1 Protein expression and purification

**RAD-51, RFS-1/RIP-1 complex and human RPA complex** were expressed and purified as described previously (Taylor et al., 2015; Taylor and Yeeles, 2018). Human RPA-eGFP expression plasmid was a kind gift from Mauro Modesti (CRCM, Marseille).

To bypass solubility problems, codon-optimized BRC-2 ORF was cloned into pET MBP-1a. **His<sub>6</sub>-MBP-BRC-2** (referred to as BRC-2 in the thesis) was expressed in BL21(DE3) *E. coli* strain at 17 °C overnight using 0.1 mM IPTG for the induction of protein expression. Cells were lysed in Lysis Buffer (25 mM Tris-HCl pH 7.5, 500 mM KCl, 10% glycerol, 1 mM DTT, 0.01% NP40 substitute, cOmplete EDTA-free protease inhibitor tablets (1/50 ml), cat no. 11873580001, Roche). After sonication and centrifugation at 20 000 rpm for 1h, clarified lysate was applied to Ni-NTA (nitrilotriacetic acid, Qiagen) resin for 1.5h, washed with Lysis buffer and Lysis buffer containing 20 mM imidazole. Proteins were eluted using Elution buffer 500 (25 mM Tris-HCl pH 7.5, 300 mM KCl, 10% glycerol, 0.5 mM EDTA, 1 mM DTT, 0.01% NP40 substitute, 200 mM imidazole). Sample was then directly applied to amylose resin and allowed to be bound for 1h, amylose beads were washed with Wash buffer 300 (25 mM Tris-HCl pH 7.5, 300 mM KCl, 10% glycerol, 0.5 mM EDTA, 1 mM DTT, 0.01% NP40 substitute). Protein was eluted using Elution buffer 300 (25 mM Tris-HCl pH 7.5, 300 mM KCl, 10% glycerol, 0.5 mM EDTA, 1 mM DTT, 0.01% NP40 substitute, 30 mM maltose) and diluted two times with Elution buffer lacking KCl and maltose). Sample was then loaded onto pre-equilibrated HiTrap SP column, column was washed with 10 column volumes of Buffer A (25 mM Tris-HCl pH 7.5, 150 mM KCl, 10% glycerol, 0.5 mM EDTA, 1 mM DTT, 0.01% NP40 substitute) and eluted using linear salt gradient (0-80%) of Buffer B (25 mM Tris-HCl pH 7.5, 1000 mM KCl, 10% glycerol, 0.5 mM EDTA, 1 mM DTT, 0.01% NP40 substitute). Fractions containing BRC-2 were pooled, concentrated, frozen and subsequently checked for purity using SDS-PAGE. Ability of his<sub>6</sub>-MBP-BRC-2 to stimulate RAD-51 in DNA strand exchange in sub-stoichiometric amounts was confirmed using previously established protocol (Thorslund et al., 2010) prior to single-molecule analysis. All

protein concentrations were determined by Coomassie Blue staining using BSA standards for quantification.

**Human RAD51** and its I287T (engineered by site-directed mutagenesis) variant was purified as described previously with minor modifications. Briefly, expression plasmid pET11c-Rad51 was transformed *E. coli* BLR(DE3)pLysS cells (Novagen). The culture was grown to OD<sub>600</sub> ~0.7 in 2×TY media supplemented with ampicillin (100 mg/l) and chloramphenicol (33 mg/l). RAD51 expression was induced by 1 mM IPTG at 37 °C for 3–4 h, and cells were harvested by centrifugation. Cells were then resuspended in cell breakage (CBB) buffer (50 mM Tris–HCl pH 7.5, 10% sucrose, 0.5 mM EDTA, 1 M KCl, 1 mM DTT and 0.01% NP-40, cocktail of protease inhibitors, and PMSF), sonicated and centrifuged at 100000 g for 60 min. Clarified supernatant was mixed with ammonium sulphate (0.242 g/ml). After multiple rounds of centrifugation at 9000 x g, the pellet was resuspended in K buffer (20 mM K<sub>2</sub>HPO<sub>4</sub> pH 7.5, 10% glycerol, 0.5 mM EDTA, 1 mM DTT and 0.01% NP-40) and loaded onto a 20 ml Q Sepharose FastFlow column (Cytiva) pre-equilibrated in K buffer supplemented with 175 mM KCl. The column was washed with 10 CV K buffer supplemented with 175 mM KCl and proteins were eluted with a gradient of 200 - 600 mM KCl in K buffer. Fractions containing RAD51 were pooled and loaded onto a 5 ml hydroxyapatite (Sigma Aldrich) column equilibrated with T buffer (25 mM Tris–HCl pH 7.5, 10% glycerol, 0.5 mM EDTA, 1 mM DTT and 0.01% NP-40) supplemented with 100 mM KCl. RAD51 was eluted by 60 – 500 mM KH<sub>2</sub>PO<sub>4</sub> gradient in T buffer. Pooled peak fractions were pooled and dialyzed for 2 h against T buffer lacking glycerol. Sample was loaded on 1 ml MonoQ column (GE Healthcare) equilibrated with T buffer with 100 mM KCl lacking glycerol. Protein was eluted with 200–450 mM KCl gradient in T buffer lacking glycerol. Peak fractions were pooled and concentrated using Vivaspin centrifugal concentrator (30 000 MWCO PES). Glycerol was added to a final concentration of 10%, protein was aliquoted and flash-frozen for storage at – 80 °C.

## 2.2.2 Fluorescent labelling of proteins

**RAD-51** was labelled using amine-reactive FAM, Cy5 and Cy3 NHS-esters as described previously for RecA with modifications (Amitani et al., 2010). Briefly, protein storage buffer was exchanged using Zeba Column (0.5 mL resin, 3 KDa MWCO) for labelling buffer (50 mM  $K_2HPO_4/KH_2PO_4$  (pH 7.0), 200 mM KCl, 0.1 mM DTT, and 25% glycerol). Dyes were diluted in dry DMSO to 50 mM. Dyes and protein were mixed to final concentration of 50  $\mu$ M protein and 500  $\mu$ M FAM-SE or 150  $\mu$ M Cy3/Cy5-NHS. Incubation on rotary shaker at 4 °C followed for 2 h 45 min (FAM-SE) or 2h (Cy5, Cy3-NHS). Reaction was terminated by the addition of Tris-HCl (pH 7.5) to a final concentration of 50 mM. Proteins were then buffer exchanged at least twice into storage buffer (50 mM Tris-HCl, pH 7.5, 300 mM KCl, 1 mM DTT, 0.01% NP40 substitute, 0.1 mM EDTA, 10% glycerol). Protein concentration was estimated by Coomassie staining and dye concentration was measured spectrophotometrically. Presence of minimum free dye concentration was assessed using SDS-PAGE on labelled proteins. Protein to dye concentration ratio was consistently 0.8-1.0.

**For RFS-1/RIP-1 labelling** I genetically fused ybbr tag (DSLEFIASKLA) on the C-terminus of RIP-1 downstream of 3xFLAG tag, separated by GGGSGGG linker. Proteins were expressed and purified using a previously established protocol (Yin et al., 2006). The labelling followed a protocol described elsewhere (Lim et al., 2017). Plasmid for Sfp expression was a kind gift from Dr. Meindert Lamers (LUMC). Sfp transferase was expressed and purified as described previously (Yin et al., 2006). The purified protein complexes (5  $\mu$ M) were then labelled with CoA-Cy3 (30  $\mu$ M) using recombinant Sfp phosphopantetheinyl transferase (1  $\mu$ M) in final buffer condition of 50 mM HEPES pH 7.5, 300 mM KCl, 10 mM  $MgCl_2$ , 1 mM DTT. After overnight incubation at 4 °C, the labelled protein complex was purified away from Sfp and free dye using Zeba column gel filtration system (0.5 mL resin, 50.000 MWCO). Proteins were stored in 20 mM Tris-acetate (pH 8.0), 100 mM potassium acetate, 10% glycerol, 1 mM EDTA, 0.5 mM DTT and subjected to SDS-PAGE and the fluorescent gel was scanned with a Typhoon9500 Scanner.

### 2.2.3 Ensemble protein biochemistry assays

**Electrophoretic mobility shift assay (EMSA).** For human RAD51 protein DNA binding experiments, proteins were diluted from concentrated stocks into T Buffer (25 mM Tris-HCl (pH 7.5), 10% glycerol, 0.5 mM EDTA (pH 8.0), 100 mM KCl, 1 mM DTT) which was also used in no protein controls. Proteins were mixed with a master mix (containing 30 nM (nucleotides) 5'-FAM-labelled 49mer oligonucleotide (AGCTACCATGCCTGCACGAATTAAGCAATTCGTAATCATGGTC ATAGCT) or dsDNA 49mer made by annealing with unlabelled complementary ssDNA strand, 25 mM Tris-HCl (pH 7.5), 50 mM KCl, 1 mM DTT, 2 mM MgCl<sub>2</sub> and 2 mM ATP, and incubated for 10 min at 37 °C. Reactions were resolved on 1% agarose gels in 1X TAE (70 V, 60 min). Gels were imaged by Typhoon9500 and quantified using Fiji. For fluorescence experiments using RAD-51<sup>f</sup> and/or labelled RFS-1/RIP-1 complex, proteins were incubated with 20 nM 49mer oligonucleotide AGCTACCATGCCTGCACGAATTAAGCAATTCGTAATCATGGTC ATAGCT in 35 mM Tris-HCl (pH 7.5), 50 mM KCl, 1 mM DTT, 2 mM MgCl<sub>2</sub>, 2 mM ATP and incubated for 10 min at 25°C followed by resolution on 0.8% agarose gel in 1X TAE (70 V, 60 min). Gels were dried and imaged using Typhoon9500 and appropriate filter settings. Percentage of DNA binding was assessed using Fiji.

**Oligonucleotide-based DNA strand exchange assay.** To test the stimulatory activity of labelled RFS-1/RIP-1 on RAD51-mediated DNA strand exchange ([Figure 2.1A](#)), 40mer dsDNA was prepared by annealing 5'-fluorescein-labelled 40mer oligonucleotide (TAATACAAAATAAGTAAATGAATAAACAGAGAAAATAAAG) to the complementary unlabelled 40mer oligonucleotide (CTTTATTTTCTCTGTTTATTTCAT TTAATTATTTTGTATTA) in 50 mM Tris-HCl (pH 7.5), 100 mM NaCl, 10 mM MgCl<sub>2</sub>, and stored at stock concentration 200 nM (moles). Proteins were diluted from concentrated stocks into T Buffer (25 mM Tris-HCl (pH 7.5), 10% glycerol, 0.5 mM EDTA (pH 8.0), 50 mM KCl), which was also used in no protein controls. Proteins were mixed with 5.6 nM (moles) 150mer oligonucleotide (TCTTATTTATGTCTCTTTTATTTTCATTTCCCTATATTTATTCCTATTATGTTTTATC ATTTACTTATTCTTTATGTTTCATTTTTATATCCTTTACTTTATTTTCTCTGTTTAT TCATTTACTTATTTTGTATTATCCTTATCTTATTTA), 50 mM Tris-HCl (pH 7.5), 1 mM DTT, 100 µg/ml of BSA, 2 mM ATP, 4 mM CaCl<sub>2</sub> in 12.5 µl reaction volume at

25 °C for 10 min. 0.5 µl dsDNA stock and 0.5 µl 0.1 M spermidine were then added incubated for 1.5 h. The samples were deproteinized with 0.1% SDS and 12.5 µg proteinase K at 37 °C and resolved in 10% polyacrylamide gels in 1X TBE (80 V, 1 h 15 min). Gels were imaged on a Typhoon9500 and quantified using Fiji.

**D-loop formation assay.** To test that RAD51 retains activity after fluorescent labelling, D-loop formation assay was employed (Figure 2.1B). RAD-51 and RAD-51<sup>f</sup> were diluted from concentrated stocks into T Buffer (25 mM Tris-HCl (pH 7.5), 10% glycerol, 0.5 mM EDTA (pH 8.0), 100 mM KCl, 1 mM DTT), which were also used in no protein controls. Proteins were mixed with 30 nM Cy5-labelled 90mer ssDNA (AAATCAATCTAAAGTATATATGAGTAACTTGGTCTGACAGTTACCAATGCTTATCAGTGAGGCACCTATCTCAGCGATCTGTCTATTT) in 35 mM Tris-HCl (pH 7.5), 50 mM KCl, 1 mM DTT, 2 mM MgCl<sub>2</sub> and 2 mM ATP and incubated for 10 min at 25 °C followed by addition of 0.54 µg pBS(-) dsDNA plasmid for further 15 min incubation at 25 °C. Reactions were terminated by SDS-PK treatment for 10 min at 37 °C. Resolution using 1xTAE, 0.8% agarose gel electrophoresis at 90 V for 35 min followed. Gels were scanned using Typhoon9500 with appropriate filter settings. For reactions containing human RAD51, 2 mM CaCl<sub>2</sub> was used instead of 2 mM MgCl<sub>2</sub>.

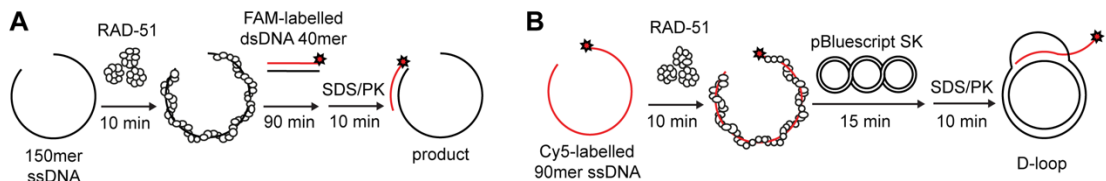


**Figure 2.1: Biochemical assays to interrogate RAD51: (A)** A schematic of oligonucleotide-based DNA strand exchange. **(B)** A schematic of D-loop formation assay.

**ATPase assay.** 0.75 µM RAD51 and/or its variants were incubated in A-buffer (50 mM Tris, pH 7.5, 50 mM KCl, 2 mM MgCl<sub>2</sub>) in the presence or absence of 120 nM (dT)63 homopolymer oligonucleotide. Mixtures were pre-incubated on ice for 15 minutes. Reactions were started by the addition of ATP up to 100 µM in the final volume followed by incubation at 37°C. Each time point, 50 µl of reaction was withdrawn and mixed with 12.5 µl of Goldmix/Accelerator (1:100) (Innova Biosciences PiColorLock Gold Colorimetric Assay kit) followed by 5 min incubation at 25°C. Then, 5 µl of Stabilizer was added for further 30 min. Standard curve was

constructed according to manufacturer's instructions. Fluorescence signal was measured using Infinity F500 microplate reader (Tecan Group Ltd.) in 96-well plates (25°C).

## 2.2.4 Single molecule analysis

**DNA substrate preparation.** Biotinylated ssDNA precursor (Figure 2.2A) was prepared as described previously (Candelli et al., 2014). To generate gapped  $\lambda$  DNA, (Figure 2.2B) biotinylated hairpin oligonucleotides (Table S1) were annealed to  $\lambda$  dsDNA ends and ligated (King et al., 2019). *S. p.* Cas9 D10A nickase (IDT) bound to previously described (Sternberg et al., 2014) guide RNAs (G) were subsequently used to generate targeted DNA nicks. The reaction was then stored at 4 °C and directly diluted in PBS on the day of the experiment. Details on preparation of gapped  $\lambda$  DNA can be found in the published protocol (Belan et al., 2021b).

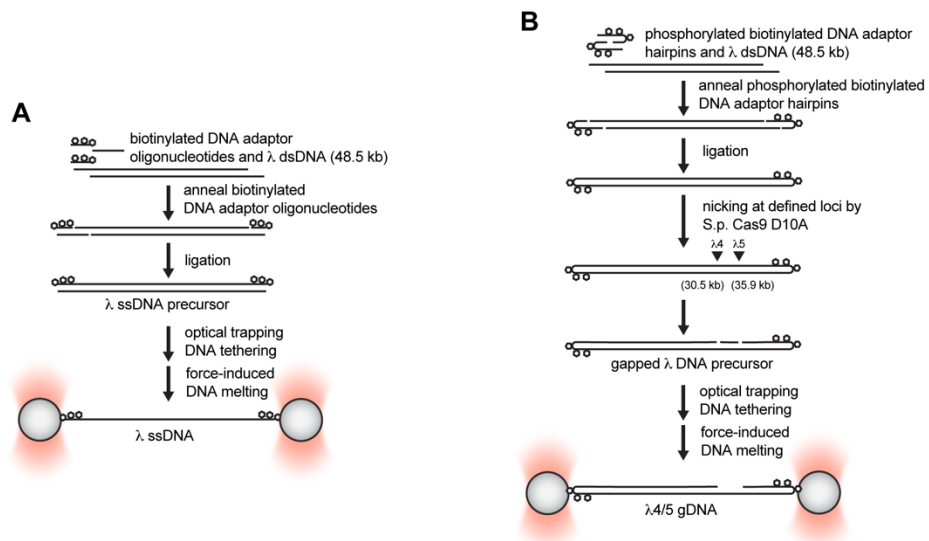


**Figure 2.2: DNA substrate preparation for SM experiments. (A)** A schematic of  $\lambda$  ssDNA generation. **(B)** A schematic of  $\lambda$  gDNA generation (I gDNA 45 used as an example).

## DNA micromanipulation, optical trapping and fluorescence imaging.

Experiments were performed using commercially available C-trap (LUMICKS) setup. Protein channels of the microfluidics chip were first passivated with BSA (0.1% w/v in PBS) and Pluronic F128 (0.5% w/v in PBS), minimum 500  $\mu$ l of both flowed through prior to use. 4.5  $\mu$ m SPHERO Streptavidin Coated polystyrene beads at

0.005% w/v were flown into the laminar flow cell, captured by trapping laser (0.14 pN/nm trap stiffness) and force calibration was performed as described in [Section 1.3.2](#). DNA was captured between the polystyrene beads using the laminar flow cell, stretched and held at forces of 100 pN and higher until the strands were fully melted. The presence of ssDNA was verified by comparison to built-in freely joined chain model ([Section 1.3.2](#)). For all the imaging conditions, ssDNA was held at forces between 10 and 20 pN, which corresponds roughly to 1.5-fold extension of B-form lambda dsDNA. Proteins were flown into incubation channels and bound to ssDNA by a previously described (Candelli et al., 2014) dipping protocol. Importantly, under low-coverage regime (concentrations of 10-100 nM), a constant flow was kept during the incubations to minimize concentration variations due to surface adhesion of labelled proteins. Beads and DNA were kept in PBS during the experiment, while DNA was melted in 0.5xNTM buffer (25 mM Tris-HCl pH 7.5, 50 mM NaCl, 0.5 mM MgCl<sub>2</sub>) supplemented with 1mM ATP, oxygen scavenging system (2.5 mM 3,4-dihydroxybenzoic acid, 250 nM protocatechuate dioxygenase) and 0.2 mg/ml BSA. Proteins were flowed into the system in 1xNTM buffer (50 mM Tris-HCl pH 7.5, 100 mM NaCl, 1 mM MgCl<sub>2</sub>) supplemented with 1 mM ATP, oxygen scavenging system (2.5 mM 3,4-dihydroxybenzoic acid, 250 nM protocatechuate dioxygenase) and 0.2 mg/ml BSA. When high protein concentrations were used ( $\geq 500$  nM), ATP-regeneration system consisting of 20 mM phospho-creatine and 20  $\mu$ g/mL creatine kinase was also added into the reaction.

For 'dipping assays' performed with different cofactors, controls using AMP-PNP-Mg<sup>2+</sup> and ADP-aluminium fluoride-Mg<sup>2+</sup> were performed in addition to ATP- $\gamma$ -S. However, no RFS-1/RIP-1(A647) binding to RAD-51<sup>f</sup> clusters was observed under these conditions. For confocal imaging, three excitation wavelengths were used, 488 nm for eGFP and 6-FAM, 532 nm for Cy3 and 638 nm for Cy5, with emission detected in three channels with blue filter 512/25 nm, green filter 585/75 nm and red filter 640 LP. Imaging conditions for 'dipping assay': 15% laser power, 0.1ms/pixel dwell-time, 100 nm pixel size. Imaging conditions for 'RPA-eGFP displacement assay': 2% blue laser power, 5% red laser power, 0.1ms/pixel dwell-time, 100 nm pixel size, 1.5 s inter-frame wait time.

**Single-step photobleaching and image analysis.** 15% blue laser power was used to bleach RAD-51<sup>f</sup> clusters in minimal imaging area to obtain sufficiently high bleaching time resolution. Scans were sectioned and stacked in Fiji using a custom-written script. Maximum likelihood estimation was used to determine each of the photobleaching steps within a maximum intensity/frame  $n$ . trace as previously described (Autour et al., 2018). The step sizes were subsequently binned, and the histogram was fit to a double Gaussian equation in GraphPad Prism. 7.0.

For nucleation rate analysis, number of observed bound RAD51 clusters ( $N_{clusters}$ ) per 10 knt of ssDNA was scored after a fixed incubation time ( $\Delta t$ ) in RAD-51 containing channel, to calculate apparent nucleation rate  $k_{obs}$ :

$$k_{obs} = \frac{N_{clusters}}{\Delta t} \quad (8)$$

Subsequently, apparent nucleation rate was plotted as a function of RAD-51 concentration and fitted with power fit (Galletto et al., 2006) as follows:

$$k_{obs} = J[\text{RAD51}]^n \quad (9)$$

where  $J$  is a rate constant,  $[\text{RAD51}]$  is concentration of nematode RAD-51 and  $n$  is number of RAD51 monomers in a critical nucleus.

For cluster growth analysis, individual clusters were analysed for intensity increase in-between frames normalized to single-step intensity values. A cluster was considered as growing if the number of RAD-51<sup>f</sup> promoters in the cluster increased by at least a single RAD-51<sup>f</sup> protomer during the time the cluster dwelled on ssDNA. The growth frequency of RAD-51<sup>f</sup> clusters was reported for each individual ssDNA molecule. For real-time RPA-eGFP displacement analysis, real-time force and fluorescence data were exported from BlueLake HDF5 files and analysed using custom-written scripts in Pylake Python package (available at [github.com/singlemoleculergroup](https://github.com/singlemoleculergroup)). Force was downsampled to 3 Hz for plotting. For RPA-eGFP free patch edge binding analysis, custom position-analysis script was built by Dr. Artur Kaczmarczyk, Imperial College London (available at



github.com/singlemoleculergroup) to extract the position of individual RPA-eGFP peaks and depressions, A647 intensity peaks were then aligned, and their maxima position extracted to monitor proximity to the RPA-eGFP signal depression edges.

eWLC model for  $\lambda$  dsDNA was used as a reference for force-extension curve comparison. Custom-written eWLC fitting script (based on a custom-written scrips by Dr. Artur Kaczmarczyk, Imperial College London, available at github.com/singlemoleculergroup) was used to calculate contour length and subsequently gapped length of gapped DNA substrates. Growth rates in real-time experiments as well as dwell-times and binding frequencies were estimated in Fiji. Nucleation frequencies were plotted as a function of RAD-51<sup>f</sup> concentration and fitted with power-law in GraphPad Prism 7. Dwell-times of RAD-51 clusters were binned into appropriate dwell-time categories and fitted with exponential decay to obtain  $\tau$  values. Mann-Whitney test was used to assess statistical significance of the data where appropriate.

## 2.3 Nematode genetics

### 2.3.1 Strain maintenance and genome editing using CRISPR-Cas9

**Strain maintenance.** Strains were maintained using standard techniques on OP50 seeded NG agar plates supplemented with nystatin as described (Brenner, 1974). *Rad-51(knu529)* strain was generated by Kundra transgenics (*rad-51(knu529[N246S,E256A,K260H])COP1580, DW778*). There were no apparent phenotypical variations in between three independently generated CRISPR clones.

**Genome editing** by CRISPR-Cas9 was performed using preassembled Cas9-sgRNA complexes (trRNA, crRNA, Cas9) and single-stranded DNA oligos (used as repair templates) as described before (Paix et al., 2016). *dpy-10* was used as a co-injection marker to select progeny carrying Cas9-induced edits. The following sequences were used to generate crRNAs (IDT): *rfs-1* K56 mutants: TTTAGGAGTTGGTAAAACAC; *HA::AID::brc-2*: TTTTAGATGAGTCACCCAT; *dpy-10*: GCTACCATAGGCACCACGAG. The repair templates used (Table S1) were ordered as single-stranded DNA oligos at 4 nmol (IDT).

**Injection mix for CRISPR-Cas9 editing.** crRNAs and trRNA were reconstituted with nuclease-free duplex buffer to 200  $\mu$ M and mixed in equal volumes to generate crRNA:trRNA duplex at 100  $\mu$ M. Cas9/crRNA/trRNA complexes were generated by adding 2  $\mu$ l of crRNA:trRNA duplex (100  $\mu$ M) of the target gene, 0.2  $\mu$ l of *dpy-10* crRNA:trRNA duplex (100  $\mu$ M), and 2.95  $\mu$ l of Cas9 nuclease V3 (at 61  $\mu$ M, #1081059, IDT) and incubating the mix at room temperature for 5 minutes. The final injection mix was prepared by adding 0.6  $\mu$ l of each ssDNA repair template from a 100  $\mu$ M stock and 0.5  $\mu$ l of *dpy-10* repair template (10  $\mu$ M stock) to 5.15  $\mu$ l of the Cas9/crRNA/trRNA complex, the mix was completed with H<sub>2</sub>O to obtain a final volume of 10  $\mu$ l. The injection mix was directly injected into the gonads of young adult worms. Following injection, worms were placed onto individual NG agar plates seeded with *E. coli* (OP50) and incubated at 25 °C for three days. Roller and dumpy worms, caused by Cas9-dependent editing of the *dpy-10* gene, were picked individually to plates and allowed to produce progeny that was screened by PCR for the presence of the desired edit.

### 2.3.2 Treatment of *C. elegans* with genotoxic agents

**RFS-1 mutants.** Exposure of worms to indicated doses of Cis-Diammineplatinum (II) dichloride (#P4394-250MG, Sigma, CDDP), Hydroxyurea (#H8627-5G, Sigma, HU), bis(2-chloroethyl)methylamine (122564-5G Sigma, HN2), and (S)-(+)-Camptothecin (#C9911-250MG, Sigma, CPT), was performed by placing worms on NG agar plates containing the desired amount of each genotoxic agent. Randomly picked young adult animals were placed on MYOB plates containing 200  $\mu$ M CDDP, 500 nM CPT, 60  $\mu$ M HN2 cisplatin or control plates. 3-5 worms were plated on each plate. Worms were moved every 24 hours to new drug-containing plates. Embryonic survival of progeny was then determined by determining the number of hatched eggs (calculated from initial number of laid eggs and dead eggs) on the 0-24, 24-48 and 48-72 hour plates. For HU treatment, worms were plated on plates containing indicated concentration of HU, for indicated period of time. Animals were transferred to HU-free plates and allowed to recover for 3 h. Worms were then allowed to lay eggs for 4 h. Dead eggs were counted 24 h after removing the parent animals.

**RAD51 TM variant.** For UVC treatment, randomly picked young adult animals were exposed to the indicated dose of UVC light on OP50 seeded MYOB plates. After irradiation plates were incubated for 24 h 23°C. Animals (3–6 per dose and genotype) were then allowed to lay eggs on OP50 seeded MYOB plates for 4 hours. Dead eggs were counted 24 h after removing the parent animals; living animals were counted 24 h later. For ionising radiation (IR) treatment, randomly picked young adult animals were exposed to the indicated dose of ionizing radiation on OP50 seeded MYOB plates in a Cs-137 irradiator. After irradiation plates were incubated for 24 h at 23 °C. Animals (typically 3–6 per dose and genotype) were then allowed to lay eggs on OP50 seeded MYOB plates for 4 hours. Dead eggs were counted 24 h after removing the parent animals; living animals were counted 24 h later. For hydroxyurea (HU) treatment, randomly picked L4s (3–15 per dose per genotype) were plated on OP50 seeded MYOB containing indicated concentration of HU. After 21 h at 20 °C in the dark, animals were transferred to HU-free plates and allowed to recover for 3 h. Worms were then allowed to lay eggs for 4 h at 23 °C. Dead eggs were counted 24

h after removing the parent animals; living animals were counted 24 h later. For TMP-UVA treatment, randomly picked young adult animals (3–15 per dose per genotype) were immersed into M9 medium with 10  $\mu\text{g/ml}$  thioxalen (TMP, Sigma) for 1h shielded from light. Worms were then washed with M9 containing 0.01% TritonX-100. Animals were exposed to indicated doses of UVA, then transferred to fresh plates and allowed to recover for 22 h 20 °C. Worms were then allowed to lay eggs for 4 h 20 °C. Dead eggs were counted 24 h after removing the parent animals; living animals were counted 24 h later.

### 2.3.3 Immunostaining and image acquisition

Randomly picked gravid adult hermaphrodites were treated with cisplatin (CDDP, 180  $\mu\text{M}$ ) for 19 h and camptothecin (CPT, 500 nM) for 18 h in liquid culture. Ionizing irradiation and UV-C (254 nm) treatment were performed on seeded plates. UV-C treatment of worms was performed on seeded plates using BLX-254 instrument. After treatment, animals were transferred to fresh seeded plates and allowed to recover (CDDP, 18 h; CTP, 7h; UV-C, 2h). Worms were washed twice in PBS, transferred to poly-L-lysine coated slides and germlines dissected. Germ lines from young adults hermaphrodites were dissected in egg buffer (118 mM NaCl, 48 mM  $\text{KCl}_2$ , 2 mM  $\text{CaCl}_2$ , 2 mM  $\text{MgCl}_2$ , 5 mM HEPES at pH 7.4) and fixed in 1% paraformaldehyde containing 0.1% Tween for 5 min. Slides were frozen in liquid nitrogen, then immersed for 1 min in methanol at  $-20^\circ\text{C}$  and transferred to PBST (1 $\times$  PBS, 0.1% Tween). After washing the slides three times in PBST for 5 minutes, they were blocked in PBST 0.5% BSA for 30 minutes before incubating then overnight at room temperature with PBST containing anti-RAD-51 antibodies (a kind gift from A. Gartner) diluted 1:500 were incubated overnight at room temperature. Following three washes of 10 minutes each in PBST, slides were incubated with secondary antibodies (Alexa 488  $\alpha$ -rabbit, 1:500) for two hours in the dark. Following three washes of 10 minutes each in PBST, slides were counterstained with DAPI, washed in PBST for 1 hour and mounted using Vectashield. All images were acquired as stacks of optical sections with an interval of 0.2  $\mu\text{m}$  using a Delta Vision deconvolution system equipped with an Olympus 1X70 microscope using 100x lens. Images were subjected to deconvolution using SoftWoRx 3.0 (Applied Precision).

### 2.3.4 Nematode crossover assays

**Recombination at homologous genetic interval.** *Rad-51(knu529)* was crossed into KR180 (*dpy-17(e164) unc-36(e251) III.*; Anne Rose laboratory) background. Genetic recombination was assessed by scoring recombinant progeny of individually picked heterozygous worms (Figure 2.3A) for *dpy-17(e164) unc-36(e251)*.

**Heterologous recombination (het-rec) assay and RNAi.** Scoring of heterologous recombination was performed as previously described (Leon-Ortiz et al., 2018). Briefly, to score recombination between divergent sequences using visible markers (Figure 2.3B). *rad-51(knu529[N246S,E256A,K260H])COP1580* was crossed with previously described *mln1[mls14 rol-1(e91)]/dpy-25(e817) II* strain harbouring *mln-1* inversion on chromosome II. These two strains were then plated on NGM plates supplemented with 1 mM IPTG and 50 µg/mL ampicillin seeded with bacteria from Ahringer RNAi library (Kamath and Ahringer, 2003) expressing siRNA against *rtel-1* or *brc-1* previously kept at 25 °C overnight to induce siRNA expression. Worms were transferred between fresh RNAi plates until egg laying ceased. Het-rec progeny was two and a half days following egg laying and the sterility of het-rec progeny was verified by plating individual recombinant worms after the experiment.

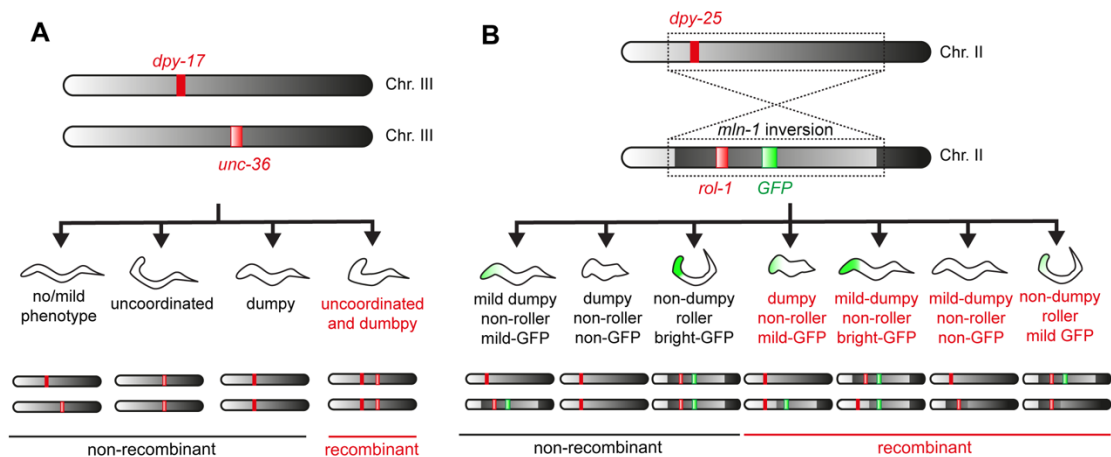


**Figure 2.3: Nematode crossover assays.** (A) A schematic of recombination assessment using visible markers at homologous genetic interval. (B) A schematic of het-rec assessment using a combination of visible markers at heterologous chromosomal region (*mln-1* inversion).

## 2.4 Mammalian cell biology and genetics

### 2.4.1 Mouse embryonic fibroblast isolation and tissue culture

Sources of cell lines used in the study are listed in the reagent and resource table. Primary RAD51 +/+, RAD51 IT/IT mouse embryonic fibroblasts were isolated and immortalized using Large T-SV40 by Dr. Valerie Borel. Immortalized MEFs were subsequently cultured at 37 °C, 5% CO<sub>2</sub>, 20% O<sub>2</sub> in Dulbecco's modified Eagle's medium (DMEM) (Invitrogen) supplemented with 10% fetal bovine serum (FBS; Sigma) and 1% penicillin-streptomycin (Invitrogen). The sex of the cells was not determined for this study. Once subconfluent, a standard 3T3 protocol was followed to determine accumulation of population doubling level (PDL): every 3 days cells were trypsinized and counted using Auto 2000 (Nexcelom Bioscience) cell counter, and then replated at a fixed density (8x10<sup>5</sup> cells per 100-mm dish) PDL was calculated using the formula:

$$\Delta PDL = \frac{\log\left(\frac{n_h}{n_i}\right)}{\log 2} \quad (10)$$

where  $n_i$  is the initial number of cells and  $n_h$  is the cell number at each passage.

### 2.4.2 Drug treatment and cell survival analysis

Individual drugs are listed in [Table 1](#). RAD51 +/+ and RAD51 IT/IT MEFs were seeded at the density of 1050 cells per well in a 96 well plates, cells were treated with indicated dose of drug for 24 h following plating and grown for 5 more days. CellTiter-Glo assay (Promega) was performed as described in manufacturer's instruction. Luminescence was measured using CLARIOstar Plus plate reader (BMG Labtech). Luminescence signal in treated wells was normalized to untreated wells for each genotype. Data were fitted with sigmoid fit in GraphPad Prism 7.0.

### 2.4.3 Single-molecule analysis of replication dynamics (SMARD)

Cells were seeded at places at appropriate confluency 24 hours before the experiment or 24 hours before drug treatment. In case of drug treatment, cells were treated for 24 hours the day before the experiment with indicated dose of olaparib or cisplatin. On the day of the experiment, cells were pulse labeled with 25  $\mu$ M CldU and 250  $\mu$ M IdU for indicated time period (Figure 2.4).

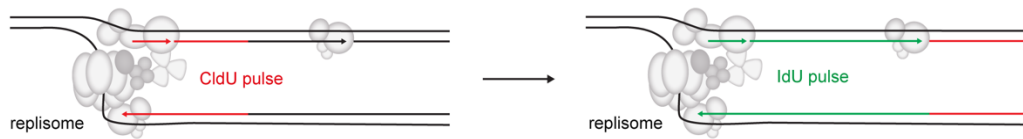


**Figure 2.4: A schematic of nascent DNA strand labelling for SMARD.**

Cells were trypsinized, washed with cold PBS and resuspended at  $5 \times 10^5$  cells/ml in cold PBS. DNA spreads were prepared by spotting 2  $\mu$ l of cells on a glass slide, followed by lysis with 7  $\mu$ l of spreading buffer (200 mM Tris-HCl pH 7.4, 50 mM EDTA, 0.5% SDS). Slides were tilted (15° horizontal), allowing DNA to run slowly down the slide and spread well, air-dried and then fixed in methanol/acetic acid (3:1) for 10 min at 25 °C. Slides were then washed multiple 3 times for 5 min with H<sub>2</sub>O. DNA was denatured by 2.5 M HCl for 75 min at 25 °C, followed by washing with PBS and blocking solution (1% BSA, 0.1% Tween20 in PBS). Slides were blocked for 1 h at 25 °C in blocking solution and subsequently incubated with rat anti-bromodeoxyuridine (detects CldU, abcam, ab6326, 1:1.200 dilution in blocking solution) and mouse anti-bromodeoxyuridine (detects IdU, B44, Becton Dickinson, 1:500 dilution in blocking solution) for 1 h, rinsed 3 times with PBS and washed 3 times (2, 2 and 10 min) with blocking solution and incubated with anti-rat IgG AlexaFluor 555 and anti-mouse IgG AlexaFluor 488 (both at 1:500 dilution in blocking solution, Molecular Probes) for 1.5 h. Slides were then rinsed 2 times with PBS, washed 3 times (2, 2 and 10 min) with blocking solution and rinsed again 2 times with PBS. Slides were mounted with ProLong<sup>TM</sup> Gold Antifade (Invitrogen). Images were acquired using a Zeiss AxioImager M1, equipped with a Hamamatsu digital camera and the Volocity software (Perkin Elmer). Fiber length was analyzed using Fiji. For fork speed analysis, during each independent experiment, a minimum of 200-300 fibers were measured per condition. Fork asymmetry was measured as a

percentage of the length ratio of the shortest to the longest fiber of first label origin fibers. Replication fork speed ( $r_f$ ) was calculated as follows:

$$r_f = \frac{\Delta l \times c_f}{\Delta t} \quad (11)$$

where  $\Delta l$  is length of the DNA fibre in mm and  $c_f$  is a conversion factor of 2.59 kb per  $\mu\text{m}$  (Jackson and Pombo, 1998).

#### 2.4.4 Indirect immunofluorescence

RAD51  $+/+$  and RAD51 IT/IT MEFs were washed in PBS and treated with pre-extraction buffer (10 mM HEPES pH 7, 50 mM NaCl, 300 mM sucrose, 3 mM  $\text{MgCl}_2$ , 5 mM EDTA, and 0.5% Triton X-100) for 7 min on ice, washed with PBS and then fixed with 4% paraformaldehyde in PBS for 15 min at 25 °C. Coverslips with cells were washed 3 times for 5 min with PBS at 25 °C and stored at 4 °C. Coverslips with fixed cells were then permeabilized with detergent solution (0.1% Triton X-100, 0.02% SDS in PBS), washed with PBS, incubated with 2% BSA in PBS for 10 min and blocked with blocking solution (10% normal goat serum (Sigma Aldrich, cat. n. G9023-10mL), 2% BSA in PBS). Primary antibodies were added in blocking solution and incubated with the coverslips for 1 h at 25 °C. Coverslips were then washed three times for 4 min each with 2% BSA in PBS. Fluorescent secondary antibodies were added and samples were incubated for 45 min at 25 °C. Coverslips were washed three times for 4 min each with 2% BSA in PBS, dipped in water, allowed to dry and mounted onto microscope slides with ProLong™ Gold Antifade with DAPI (Invitrogen). Images were acquired using a Zeiss AxioImager M1, equipped with a Hamamatsu digital camera and the Volocity software (Perkin Elmer). Images were processed in Fiji and foci were counted automatically using customized pipeline based on 'speckle' template in CellProfiler.

#### 2.4.5 Sub-cellular fractionation and western blotting

Cells were treated with indicated concentration of drug for 24 hours. Followed by harvest and processing using subcellular protein fractionation kit (Thermo Fisher, cat.



n. 78840) according to manufacturer's instructions. Each fraction was mixed with equivalent volume of 2x Laemmli buffer, incubated for 5-10 min at 99 °C and loaded onto 4–12% NUPAGE Bis-Tris gels for SDS-PAGE analysis. Gels were run at 150 V for 90 min, alongside a SeeBlue Plus2 pre-stained protein ladder (Thermo Fisher). Proteins were transferred to 0.2 µm nitrocellulose membranes in transfer buffer (25 mM Tris-HCl pH 7.5, 190 mM glycine, 20% methanol) at 0.4 A for 60 min at 4 °C. Membranes were incubated with blocking solution (3% BSA, 0.1 % Tween20 in PBS) for 1 hour with agitation at 25 °C. Primary antibodies (in blocking solution) were incubated with the membrane overnight at 4 °C with mild agitation. Membranes were washed 3 times for 10 minutes with 0.1 % Tween20 in PBS and subsequently incubated with HRP-conjugated secondary antibodies in blocking solution for 1 h at 4 °C. Membranes were washed further 3 times for 10 min each wash with 0.1 % Tween20 in PBS. Proteins were detected using ChemiDoc imaging system (Bio-Rad).

#### **2.4.6 Isolation of proteins on nascent DNA (iPOND)**

iPOND was performed according to standard protocols (Sirbu et al., 2011). RAD51 +/- and RAD51 IT/IT MEFs were pulse labelled with 10 mM EdU (5-ethynyl-20-deoxyuridine, Invitrogen) for 10 min. After washing in normal media, cells were released or not for 30 min in media containing 10 mM thymidine (Sigma Aldrich). Cells were then washed in PBS and fixed in 1% formaldehyde (Sigma Aldrich) for 20 min at 25 °C. Glycine was added to a final concentration of 125 mM for 10 min at 25 °C to quench the crosslinking. Fixed cells were scraped and washed 3 times in PBS. At this point, washed pellets can be frozen and stored at – 80 °C. Pellets were then thawed in 0.25% TritonX-100 in PBS and for 30 min at 25 °C. Following washing in 0.5% BSA in PBS and PBS, pellet was resuspended in Click solution (10 mM biotin-azide (Invitrogen), 10 mM sodium ascorbate (Sigma Aldrich) and 2 mM CuSO<sub>4</sub> (Sigma Aldrich)) and incubated for 1 h at 25 °C in the dark. Controls were resuspended in the same buffer containing DMSO instead of biotin-azide. Pellets were washed in 0.5% BSA in PBS and PBS, and subsequently lysed in RIPA buffer (100 mM Tris-HCl pH 7.5, 150 mM NaCl, 1% NP-40, 0.1% SDS, 0.5% sodium deoxycholate) containing protease and phosphatase inhibitors (ROCHE). Lysed pellets were then sonicated using a BIORUPTOR sonifier (20-25 cycles at 30 s-on/30

s-off). Lysates were clarified by centrifugation (13200 rpm, 15 min at 4 °C) and incubated with streptavidin Sepharose beads (GE Healthcare) for 16 hours at 4 °C. Beads were washed in RIPA and 1M NaCl. Subsequently, beads were resuspended in 2x Laemmli buffer, incubated for 25 min at 99 °C and loaded onto 4–12% NUPAGE Bis-Tris gels for SDS-PAGE analysis, followed by western blotting.

#### **2.4.7 DNA transfection and plasmid-based HDR efficiency assay**

RAD51  $+/+$  and RAD51 IT/IT MEFs were transfected with 1.6  $\mu$ g of CMV-FireFly plasmid and 5  $\mu$ g of I-SceI digested Pem1 HR reporter substrate (courtesy of Artios Pharma) per 96 well plate (45 000 cells in 80  $\mu$ l/well) using Lipofectamine 2000 (Thermo Fisher) reagent as per manufacturer's instructions. Following 16 h incubation, 80  $\mu$ l of ONE-Glo EX (Promega, cat. n. N1630) substrate per well was added. Plates were incubated for 3 min at 25 °C on microplate shaker at 300 rpm. FireFly luminescence signal (at 580 nm) was measured using CLARIOstar Plus plate reader (BMG Labtech). After the reading, 80  $\mu$ l of NanoDLR Stop & Glo (Promega, cat. n. N1630) reagent was added per well. Plate was shaken for 3 min at 25 °C on microplate shaker at 300rpm, then incubated for further 7 min at 25 °C in the dark. NanoLuciferase luminescent signal (at 470 nm) was measured using CLARIOstar Plus plate reader (BMG Labtech). Relative HDR efficiency for RAD51 IT/IT cells was calculated from ratio of NanoLuciferase to FireFly luminescence signal normalised to RAD51  $+/+$  control.

## Chapter 3. Results 1: Single-molecule analysis reveals cooperative stimulation of RAD-51 filament nucleation and growth by mediator proteins

### 3.1 Single-molecule imaging system establishment

Given the lower affinity of Rad51 for ssDNA, when compared to RPA, mediator proteins that promote RAD51 assembly on RPA-coated ssDNA strand are critical for efficient HR and maintenance of genome stability. In higher eukaryotes, BRCA2 and Rad51 paralogs are amongst the most important mediator proteins. While current evidence implicate BRCA2 and Rad51 paralogs in positively regulating Rad51 function, an understanding of their dynamics during Rad51 filamentation was unclear. Single-molecule studies of the *E. coli* RecA have revealed that nucleoprotein filaments form rapidly by a two-step mechanism: rate-limiting nucleation followed by rapid bi-directional filament growth with two-fold kinetic preference for the 5'→3' direction along a ssDNA backbone (Bell et al., 2012; Galletto et al., 2006). In contrast, human Rad51 filaments formed in the presence of RPA *in vitro* are rare and grow very slowly (Candelli et al., 2014; Hilario et al., 2009).

To examine how recombination mediator proteins impact on the nucleation and/or growth of Rad51 filaments, I have reconstituted a model of a minimal core recombination machinery using purified nematode recombinase, RAD-51 (Figure 3.1A), BRC-2 (Figure 3.1B) and RAD-51 paralog complex, RFS-1/RIP-1 (Figure 3.1C). Given RAD-51 assembles into filaments in the presence of its physiological competitor, RPA, I also purified human RPA complex, where RPA70 is C-terminally tagged with eGFP (Figure 3.1D). Since the small subunit of *C. elegans* RPA remains unknown (Kim et al., 2005), precluding the purification of a nematode RPA heterotrimeric complex, all eGFP-RPA displacement assays were performed with human eGFP-RPA purified as described previously (Belan et al., 2021b; Modesti, 2018). The substitution is justified given the lack of interaction between RPA and BRCA2 or RAD51 in solution (Jensen et al., 2010) and the established notion that RPA serves only as a competitor of RAD51 and can be replaced by bacterial SSB in bulk mediator assays (Jensen et al., 2010). Both BRCA2 (Jensen et al., 2010) and

human RAD51 paralog complex (Sigurdsson et al., 2001) are also capable of stimulating strand exchange activity of RAD51 even in the absence of RPA under sub-saturating conditions. It should be noted that fusion of RPA to eGFP was shown to be functional for DNA repair previously both *in vivo* (Lisby et al., 2004) and *in vitro* (Ma et al., 2017).

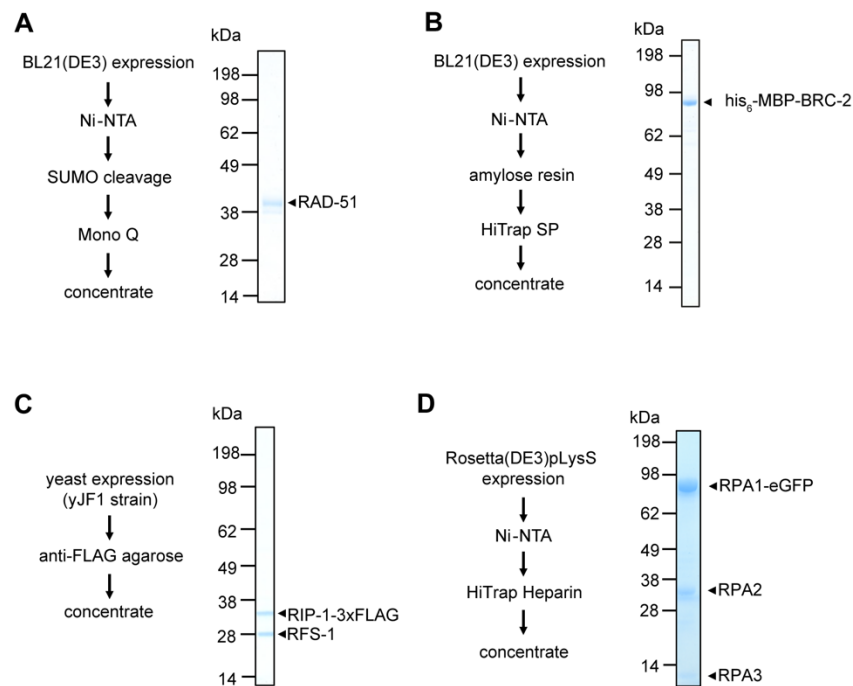


**Figure 3.1: Recombinant proteins. (A)** Purification scheme for nematode RAD-51. Coomassie blue staining of protein (1  $\mu$ g) after SDS-PAGE. **(B)** Purification scheme for nematode BRC-2. Coomassie blue staining of protein (1  $\mu$ g) after SDS-PAGE. **(C)** Purification scheme for nematode RFS-1/RIP-1. Coomassie blue staining of protein (2  $\mu$ g) after SDS-PAGE. **(D)** Purification scheme for human RPA-eGFP. Coomassie blue staining of protein (4  $\mu$ g) after SDS-PAGE.

Following protein purification, multiple strategies were devised to fluorescently label individual components of the system. RAD-51 (Figure 3.2A) was stoichiometrically labelled with fluorescein (6-FAM) (Amitani et al., 2010) using amine-reactive esters of dye (referred to as RAD-51<sup>f</sup>). RAD-51<sup>f</sup> retained wild type levels of DNA binding (Figure 3.2B) and D-loop formation activity (Figure 3.2C). To fluorescently label RFS-1/RIP-1, I fused the C-terminus of RIP-1 to a ybbr tag (Yin et al., 2006) and labelled the corresponding complex (Figure 3.2D) with Alexa 647 dye (referred to as RFS-1/RIP-1(A647)). I verified that RFS-1/RIP-1(A647) retains its ability to stimulate strand exchange (Figure 3.2E).

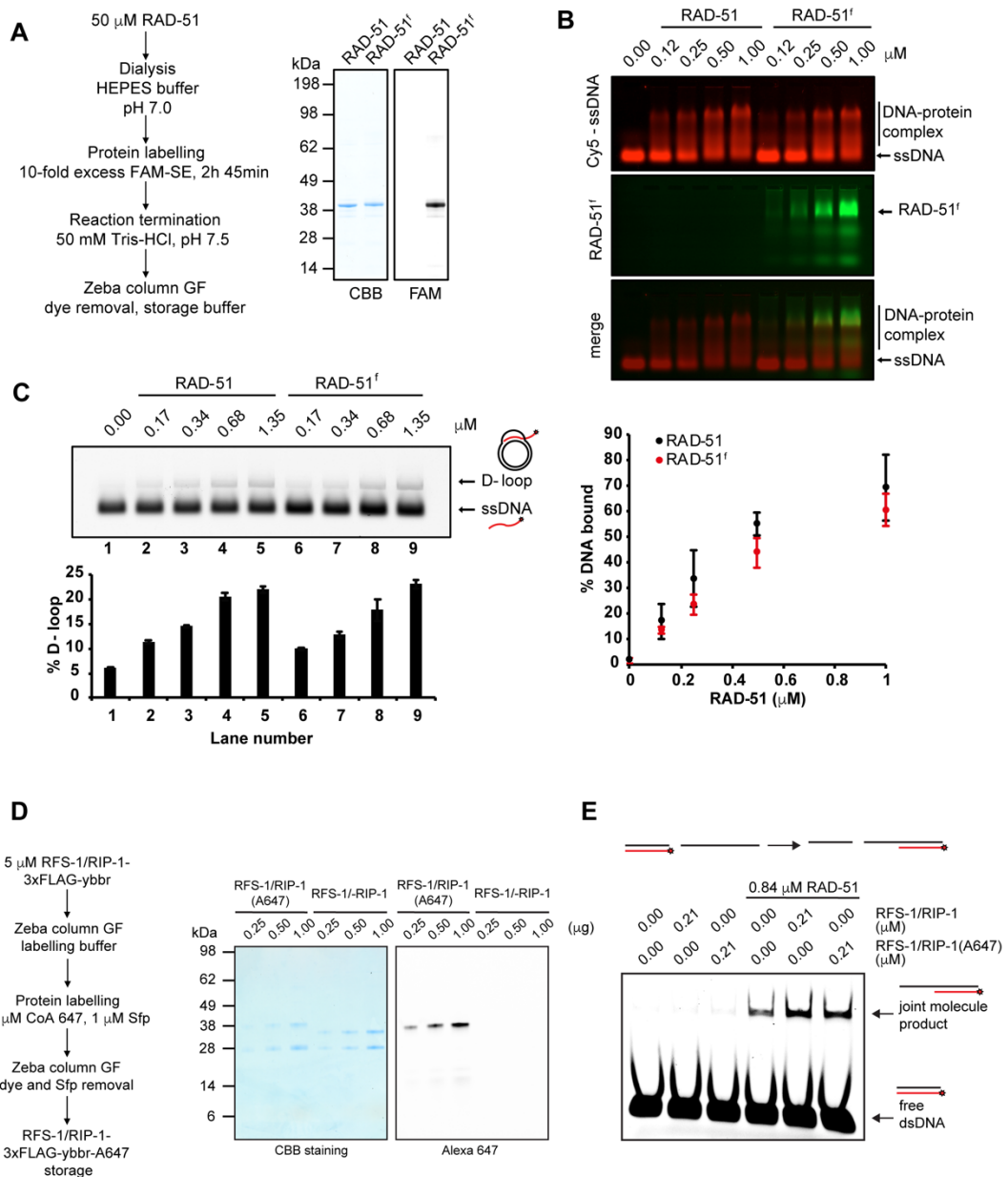


**Figure 3.2: Fluorescent labelling of proteins. (A)** Chemical labelling of RAD-51. RAD-51 was labelled in pH 7.0 using succinyl esters of 6-FAM (FAM-SE). Proteins were labelled typically with 80-100% labelling efficiency. **(B)** EMSA comparing ssDNA binding of RAD-51 and RAD-51<sup>f</sup>. N = 3 replicates. Error bars represent SD. **(C)** D-loop formation assay comparing DNA-pairing activities of RAD-51 and RAD-51<sup>f</sup>. N = 3 replicates. Error bars represent SD. **(D)** Scheme and protocol for fluorescent labelling of ybbr-tagged RFS-1/RIP-1 complex (left). Coomassie Brilliant Blue staining and A647 fluorescence of SDS-PAGE resolved RFS-1/RIP-1-3xFLAG or RFS-1/RIP-1-3xFLAG-ybbr-CoA-Alexa647 proteins (right). Proteins were labelled typically with 70-80% labelling efficiency. **(E)** Strand exchange assay comparing stimulatory activities of unlabelled or labelled RAD-51 paralogs on RAD-51-mediated DNA pairing.

To visualize RAD-51 filament assembly at a single-molecule level, I employed the fluorescently labelled proteins, biotinylated  $\lambda$  ssDNA precursor and a combination of optical tweezers, confocal fluorescence microscopy and microfluidics (Figure 3.3A), - the C-trap set-up (Gutierrez-Escribano et al., 2019; Newton et al., 2019). To generate a physiologically relevant HR substrate, 48.5 kb doubly-biotinylated  $\lambda$  ssDNA precursor substrate was trapped between two streptavidin-coated microspheres (microfluidic channels I and II), force-melted *in situ* to produce ssDNA and coated with RPA-eGFP (channel III). The presence of an ssDNA substrate was validated by comparing its FD curve to FJC model (Equation 7) of 48.5 knt ssDNA. Interestingly, the FD curve of RPA-eGFP coated ssDNA was almost identical to that of a bare ssDNA (Figure 3.3B). This contrasts with both bacterial SSB, which strongly compacts ssDNA (Bell et al., 2012), and crystal structure of *Ustilago maydis* RPA, where ssDNA is bent into a U-shape configuration (Fan and Pavletich, 2012). However, our FD data are more in line with recent cryoEM structure of *S. cerevisiae* RPA (validated by bulk FRET assays), where ssDNA adopts an extended configuration (Yates et al., 2018). To keep DNA in the imaging plane, beads were kept 23  $\mu$ m apart during the experiment, which results in  $\sim$ 15 pN force exerted on RPA-eGFP-coated  $\lambda$  ssDNA. To start the experiment, the traps were moved to channel IV to initiate RAD-51 assembly. Loss of eGFP fluorescence was used as a proxy for monitoring of RAD-51 filament assembly. A simultaneous decrease in the force exerted on ssDNA that accompanies stiff recombinase filament formation was observed (Hegner et al., 1999) (Figure 3.3C), further confirming the filamentation process.

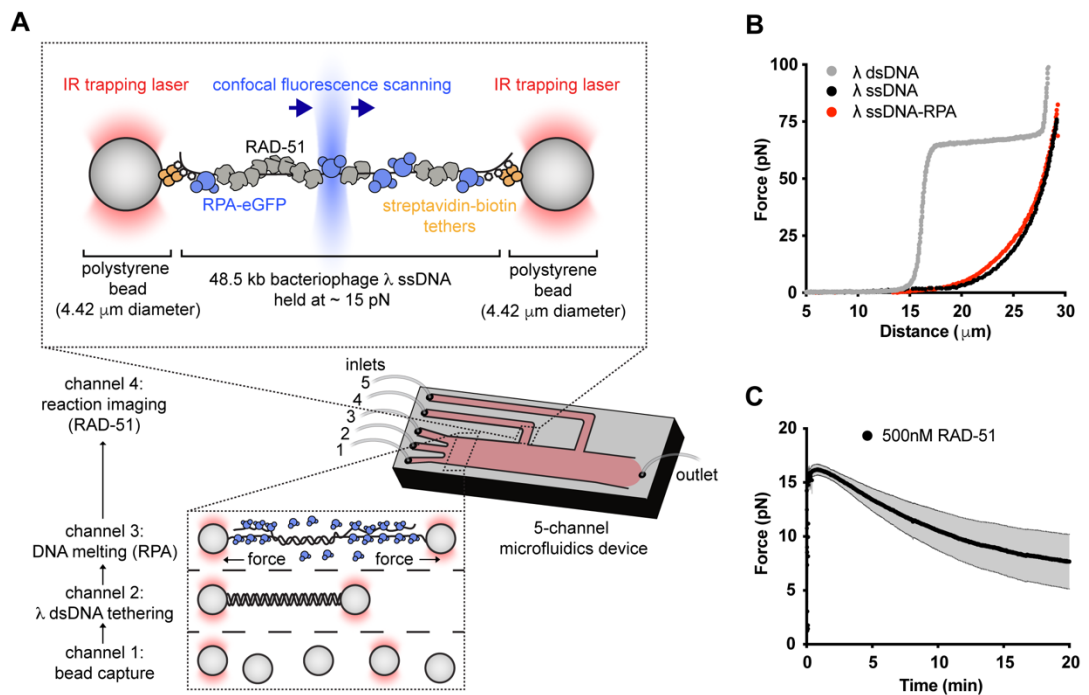


**Figure 3.3: Single-molecule imaging setup.** (A) Schematic of the experimental C-trap set-up. (B) Force-extension curves of 48.5 kb  $\lambda$  dsDNA, 48.5 kb  $\lambda$  ssDNA and 48.5 kb  $\lambda$  ssDNA coated by RPA. (C) Force measured between the traps as a function of time in the presence of 500 nM RAD-51; shaded area represents SEM. ( $n = 3-8$  molecules).

### 3.2 RAD51 nucleation and growth regulation

To characterize the role of mediator proteins in the system, I performed RPA-eGFP displacement experiments with RAD-51 in the presence or absence of his<sub>6</sub>-MBP-BRC-2 (further referred to as BRC-2) or RFS-1/RIP-1 complex (Figure 3.4A). While RAD-51 alone slowly assembles on RPA-eGFP coated ssDNA (half-time of  $10.16 \pm 0.8$  min, 95% CI), addition of sub-stoichiometric concentrations of BRC-2 stimulates the overall assembly rate (Figure 3.4B), reducing assembly half-time to  $5.3 \pm 0.3$  min (95% CI). Next, I performed RPA-eGFP displacement assays with RAD-51 in the presence of the RFS-1/RIP-1 complex. Addition of sub-stoichiometric concentrations of RFS-1/RIP-1 greatly stimulates the RAD-51 filament assembly rate (Figure 3.4C), reducing assembly half-time from  $\sim 10$  min to  $\sim 1$  min. In addition to estimating overall RAD51 filament assembly rate, I was also able to resolve individual growing RAD-51 filaments and measure their growth rates (Figure 3.4D). RAD-51 grows slowly (mean  $17.9 \pm 1.8$  nm/min, 95% CI; which corresponds roughly to  $38.6 \pm 3.9$  nt/min; at 500 nM RAD-51) compared to bacterial RecA ( $\sim 40$  nm/min under similar conditions (Bell et al., 2012)). Strikingly, I found that RFS-1/RIP-1 strongly stimulates growth rates of individual RAD-51 filaments (mean of  $38.1 \pm 4.0$  nm/min, 95% CI; which corresponds to  $82.1 \pm 8.6$  nt/min; at 10 nM RFS-1/RIP-1). BRC-2 had a significant, but only modest effect on RAD-51 growth (mean of  $26.4 \pm 3.2$  nm/min, 95% CI; which corresponds to  $56.9 \pm 6.9$  nt/min; at 10 nM BRC-2) (Figure 3.4E). My data suggests that BRC-2 acts primarily as a RAD-51 nucleation factor, which is in line with previous negative stain EM (Shahid et al., 2014), where inclusion of human BRCA2 increased overall number of RAD51 filaments observed, but not their length. Further, my data suggests that RFS-1/RIP-1 acts primarily as a growth factor for RAD-51 filaments assembling on RPA-coated ssDNA.



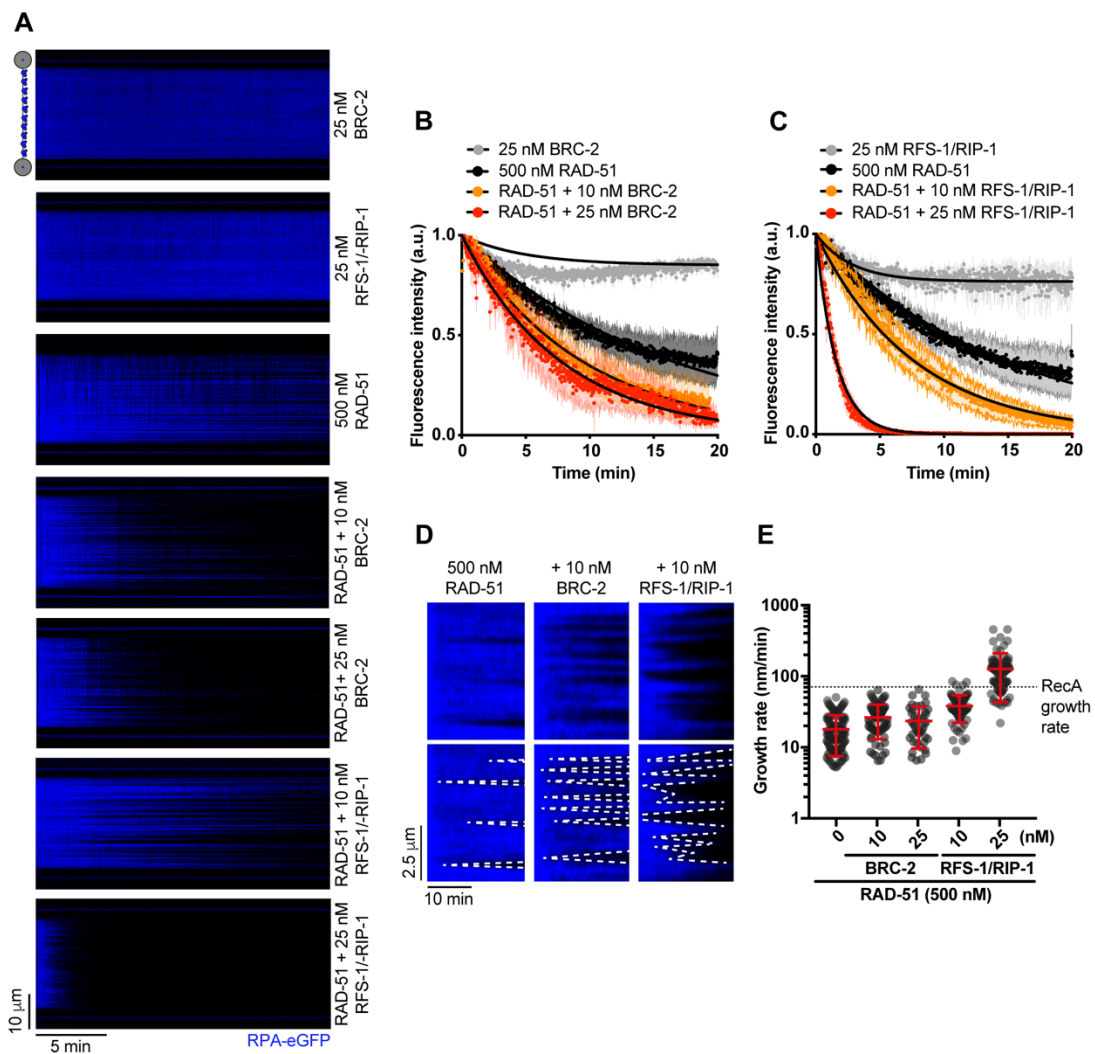


**Figure 3.4: Single-molecule imaging of RAD-51 filament assembly in the presence of mediator proteins. (A)** Kymograph showing the displacement of RPA-eGFP by 500 nM RAD-51 in the presence or absence of BRC-2 or RFS-1/RIP-1. **(B)** Normalized fluorescence intensity for RPA-eGFP signal over time in the presence of RAD-51 and indicated amounts of BRC-2; shaded area represents SEM. ( $n = 3-8$  molecules). Black lines represent exponential fits. **(C)** Normalized fluorescence intensity for RPA-eGFP signal over time in the presence of RAD-51 and indicated amounts of RFS-1/RIP-1; shaded area represents SEM. ( $n = 3-6$  molecules). Black lines represent exponential fits. **(D)** Examples of individual growing RAD-51 filaments (dark). Growth rate was measured as a slope of the border of RPA-eGFP displaced signal. **(E)** Quantification of growth rates in indicated conditions.

These observations raised the possibility that the BRC-2 and RFS-1/RIP-1 may cooperate to enhance RAD-51 filament assembly by their sequential action. Inclusion of both proteins in a single reaction results in increased growth rates of individual

RAD-51 filaments (mean of  $43.8 \pm 7.0$  nm/min, 95% CI; which corresponds to  $94.4 \pm 15.1$  nt/min; at 10 nM BRC-2 and 10 nM RFS-1/RIP-1). These rates, however, were not significantly different from the RAD-51 filament growth rates measured in the presence of 10 nM RFS-1/RIP-1 alone (Figure 3.5A, B). These results indicate that RFS-1/RIP-1 may be the major filament growth factor in the combined assembly reaction. However, when combined, BRC-2 and RFS-1/RIP-1 display a synergistic effect on overall RAD-51 assembly rates on RPA-coated ssDNA (Figure 3.5A, C), which results in a strong reduction in the overall assembly half-time to 2.4 min (95% CI) and increase the overall assembly rate to  $0.29 \text{ min}^{-1}$ . In the absence of mediator proteins, the RAD-51 assembly rate was  $0.07 \text{ min}^{-1}$ . In the presence of BRC-2 or RFS-1/RIP-1, 0.1 and  $0.13 \text{ min}^{-1}$  overall assembly rates were observed (Figure 3.5D). Force measurements confirmed assembly kinetics obtained from fluorescence intensity quantification, indicating formation of stiff nucleofilament structure (Figure 3.5E). Taken together, these results further strengthen the notion that BRC-2 primarily nucleates RAD-51 on RPA-coated ssDNA. The RAD-51 nucleus is then extended into nascent filament by the help of RFS-1/RIP-1.

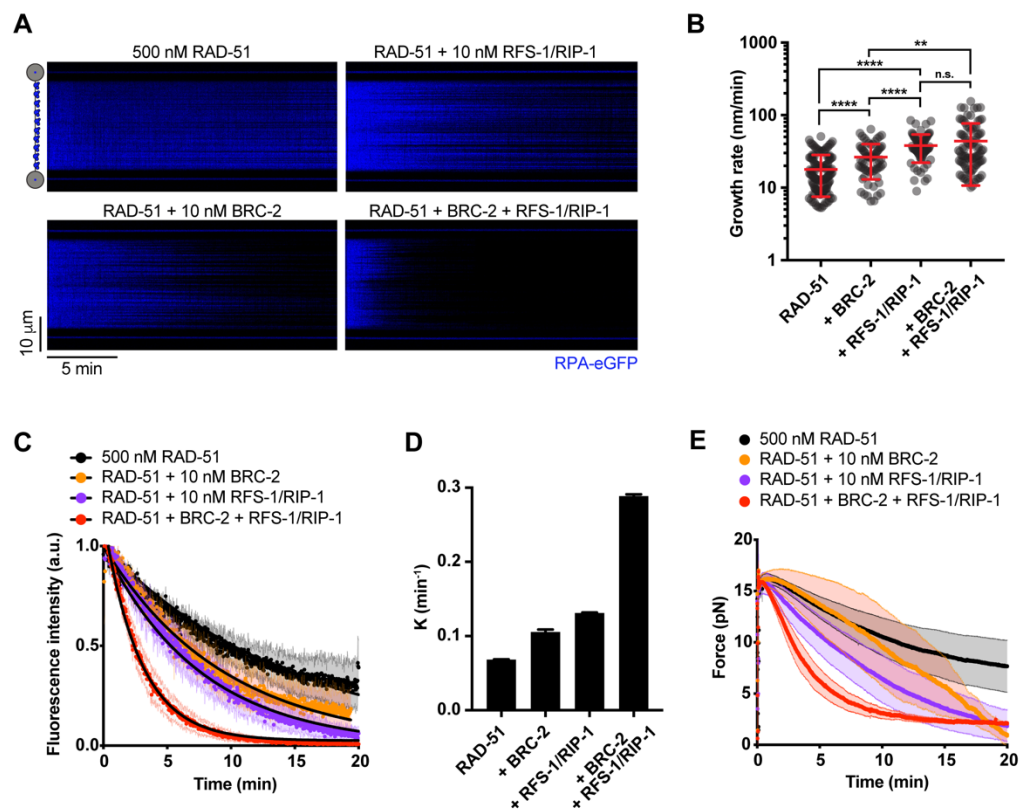


**Figure 3.5: BRC-2 and RFS-1/RIP-1 synergize to promote RAD-51 filament assembly. (A)** Kymograph showing the displacement of RPA-eGFP by 500 nM RAD-51 in the presence or absence of BRC-2 and/or RFS-1/RIP-1. **(B)** Quantification of growth rates in indicated conditions. Error bars represent SD.  $P > 0.05$  (n.s.),  $P \leq 0.05$  (\*),  $P \leq 0.01$  (\*\*),  $P \leq 0.001$  (\*\*\*),  $P \leq 0.0001$  (\*\*\*\*). Mann-Whitney test. **(C)** Normalized fluorescence intensity for RPA-eGFP signal in the presence or absence of BRC-2 and/or RFS-1/RIP-1; shaded area represents SEM. ( $n = 4-8$  molecules). Black lines represent exponential fits. **(D)**  $k_{\text{off}}$  values for RPA-eGFP displacement traces calculated from exponential fits to the data in 2C; error bars represent upper and lower  $k$  value limit. **(E)** Force measured between the traps as a function of time in the indicated conditions; shaded area represents SEM. ( $n = 3-8$  molecules).

### 3.3 RAD-51 filament growth polarity

During image analysis, I observed that, in the presence of RFS-1/RIP-1, RPA-eGFP displacement slopes appear steeper in one direction in kymographs compared to the 'RAD-51 only' condition (Figure 3.4D). Given RFS-1/RIP-1 was previously proposed to bind and stabilize the 5' end of pre-assembled RAD-51 filaments (Taylor et al., 2016), I reasoned that growth stimulation promoted by RFS-1/RIP-1 might lead to preferential protomer addition at only one end of the presynaptic filament. However, which end it might be is not possible to test in the aforementioned setup, as the polarity of tethered ssDNA is not known.

To examine the polarity of filament growth, I developed a rapid method to generate an asymmetrically positioned ssDNA gap of defined length within  $\lambda$  DNA using Cas9 D10A variants and subsequent DNA melting using the optical trap (Figure 3.6A). This protocol yields  $\lambda$  gapped DNA (gDNA) precursors in good quantity (~50  $\mu$ L of 1.35 nM precursor) and good quality (low frequency of additional nicks observed – roughly 1 in 10 molecules melted). The length and position of the gap are customizable and can be controlled by the combination of RNA guides used to make the two nicks. I was able to generate gaps of various lengths – from 0.2 to 18 knt. To calculate the apparent contour length of these molecules, I applied eWLC model fitting (Equation 6) to FD curves of individual constructs (Figure 3.6B). From relative contour length increases, I calculated the length of ssDNA ( $l_{gap}$  in nt) within individual constructs as follows:

$$l_{gap} = \frac{L_c(\lambda \text{ gDNA}) - L_c(\lambda \text{ dsDNA})}{r_{ssDNA} - r_{dsDNA}} \quad (12)$$

where  $L_c$  is contour length of a  $\lambda$  gDNA construct or  $\lambda$  dsDNA,  $r$  is rise in nm per bp (or nt) of dsDNA ( $r_{dsDNA} = 0.33$  nm/bp) or ssDNA ( $r_{ssDNA} = 0.61$  nm/nt).

The calculated ssDNA gap length corresponded well to the predicted gap size (Figure 3.6C). I confirmed the position of the ssDNA gap using eGFP-RPA fluorescence to mark the ssDNA portion of the gapped molecule (Figure 3.6D, E).

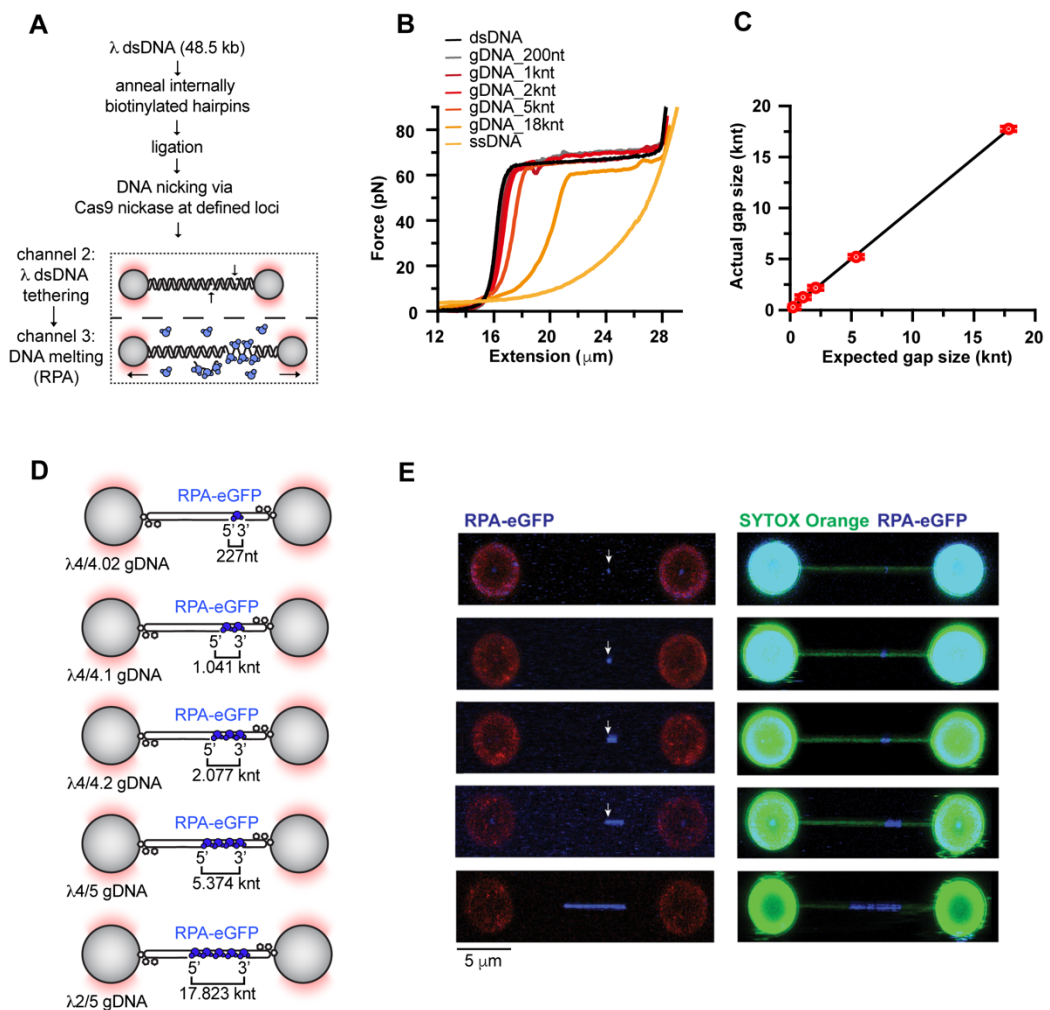


**Figure 3.6: A method to generate gapped  $\lambda$  DNA substrates.** (A) Schematic of protocol designed to generate gapped  $\lambda$  DNA (gDNA) substrates. (B) Force-extension curves of  $\lambda$  dsDNA,  $\lambda$  ssDNA and different  $\lambda$  gDNA constructs. Gap sizes are indicated. (C) Contour length of  $\lambda$  dsDNA and different  $\lambda$  gDNA constructs calculated from worm-like chain (WLC) fits to individual force-extension curves from 2B compared with the expected gap length. (D) Schematics of the  $\lambda$  gDNA substrates generated in this study. (E) Representative images of individual asymmetrically positioned RPA-eGFP coated ssDNA gaps within  $\lambda$  DNA held at 5 pN force. Arrow indicates position of  $\lambda 4$  crRNA cut site indicating 5' end of 0.2, 1, 2 and 5 knt long gaps for reference. dsDNA was stained by 50 nM SYTOX Orange.

Inclusion of free RPA during human RAD51 assembly has previously shown to suppress nucleation and help better resolve growing RAD51 filaments in experiments using ssDNA curtains (Ma et al., 2017). Therefore, to accurately assess growth directionality of individual RAD-51 filaments, I included 15 nM free RPA-eGFP in the

imaging channel. Unlike RecA, which grows preferentially in a 5'→3' direction (Bell et al., 2012), nematode RAD-51 displays mostly symmetric growth (Figure 3.7A). Addition of 10 nM RFS-1/RIP-1 resulted in a two-fold stimulation of 3'→5' growth rates, indicating that RFS-1/RIP-1 mediated growth stimulation of RAD-51 filaments is asymmetric and occurs at 5' filament ends (Figure 3.7B).

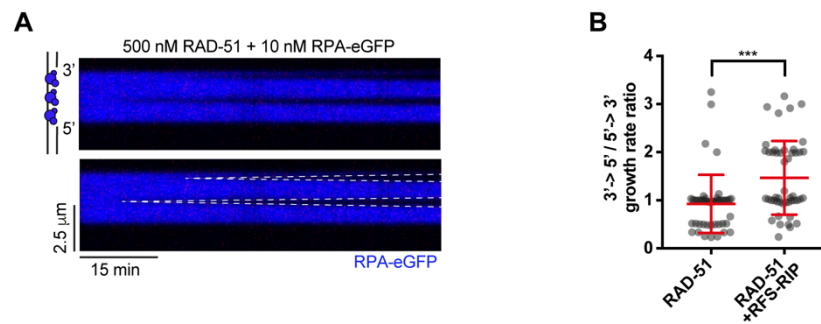


**Figure 3.7: RFS-1/RIP-1 promotes filament growth in 3' to 5' direction. (A)** Examples of individual growing RAD-51 filaments (dark) on gapped DNA construct. Growth rate was measured as a slope of the border of RPA-eGFP displaced signal. **(B)** Quantification of growth rate polarity of 500 nM RAD-51 in the presence or absence of 10 nM RFS-1/RIP-1.

### 3.4 RFS-1/RIP-1 chaperones RAD-51 filaments

Previous work has shown that recombinase-ssDNA filaments are in a state of dynamic equilibrium, where they grow and shrink from filament ends (Joo et al., 2006; van Mameren et al., 2009). Human RAD51-dsDNA (van Mameren et al., 2009) and RAD51-ssDNA (Candelli, 2013) filaments dissociate from the ends in bursts of multiple protomers interspersed by pauses. On the other hand, growth of RecA (Bell et al., 2012) and RAD51 (Candelli et al., 2014) filaments occurs predominantly by rate-limiting addition of monomers. Given the resolution of the setup, I was not able to accurately monitor association and dissociation events at RAD-51 filament ends at the level of a single RAD-51 monomer. To bypass this problem, I employed a previously described ‘dipping protocol’ (Candelli et al., 2014), where low concentrations of labelled recombinase are used to obtain sparse nucleation events containing only a small number of RAD-51 monomers (Figure 3.8A). Then single-step photobleaching calibration can be used to quantify the number of fluorophores present in each RAD-51 cluster. Since RAD-51 filaments can grow and dissociate only from filament ends (Joo et al., 2006; van Mameren et al., 2009), this system allowed me to assess growth and dissociation dynamics of small RAD-51 clusters and use it as a proxy for events occurring at the ends of long RAD-51 filaments.

For the analysis,  $\lambda$  ssDNA trapped between two beads was incubated for a defined period of time in the protein channel. Beads with tethered ssDNA are subsequently moved to a protein-free observation channel and an image is acquired using confocal fluorescence microscopy. To analyse kinetics of RAD-51<sup>f</sup> nucleation and growth, incubation-detection cycles are iteratively repeated (Figure 3.8A). ssDNA must be held at higher forces (~15 pN) to be present in a single plane for optimal confocal imaging. Previous work (Brouwer et al., 2018; Candelli et al., 2014) implicated that RAD-51 binding to ssDNA is not affected by the force at which ssDNA is held. To confirm this in my system, I performed nucleation experiments on bare ssDNA held at different forces (Figure 3.8B). This analysis confirmed that force has no effect on RAD-51 cluster assembly on ssDNA and justified the usage of 15 pN imaging force regime. Nucleation frequency of RAD-51<sup>f</sup> clusters ( $k_{\text{obs}}$ ) assessed after a single round of dipping in the presence of ATP displays power dependence with respect to RAD-

51<sup>f</sup> concentration, according to Equation 9 described in Section 2.2.4. From this fit,  $n$ , number of RAD51 monomers in a minimal nucleus can be determined. In agreement with studies of RecA ( $n = 1.5$  in ATP and  $n = 2.2$  in ATP- $\gamma$ -S; (Bell et al., 2012) and human RAD51 ( $n = 1.5$ ; (Candelli et al., 2014)),  $n = 1.6 \pm 0.2$  for *C. elegans* RAD-51 (Figure 3.8C, D) indicating that RAD-51<sup>f</sup> nucleates as a dimer or a monomer on ssDNA both in the presence or absence of RPA. Consistent with my previous result, inclusion of BRC-2 increased nucleation frequencies in the presence of RPA in this assay. Interestingly, when stoichiometric amounts of BRC-2 were added, I obtained  $n = 1.1 \pm 0.4$ , which indicates that BRC-2 bypasses the need for RAD-51 dimerization to form a stable nuclei. Addition of unlabelled RFS-1/RIP-1 also increased RAD-51 nucleation rates, albeit to a much lesser extent than in the presence of BRC-2. Interestingly, the presence of RFS-1/RIP-1 and RPA, result in  $n = 1.5 \pm 0.1$ . This indicates that, in contrast to BRC-2, RFS-1/RIP-1 does not alter the size of the minimal RAD-51 nucleation unit.

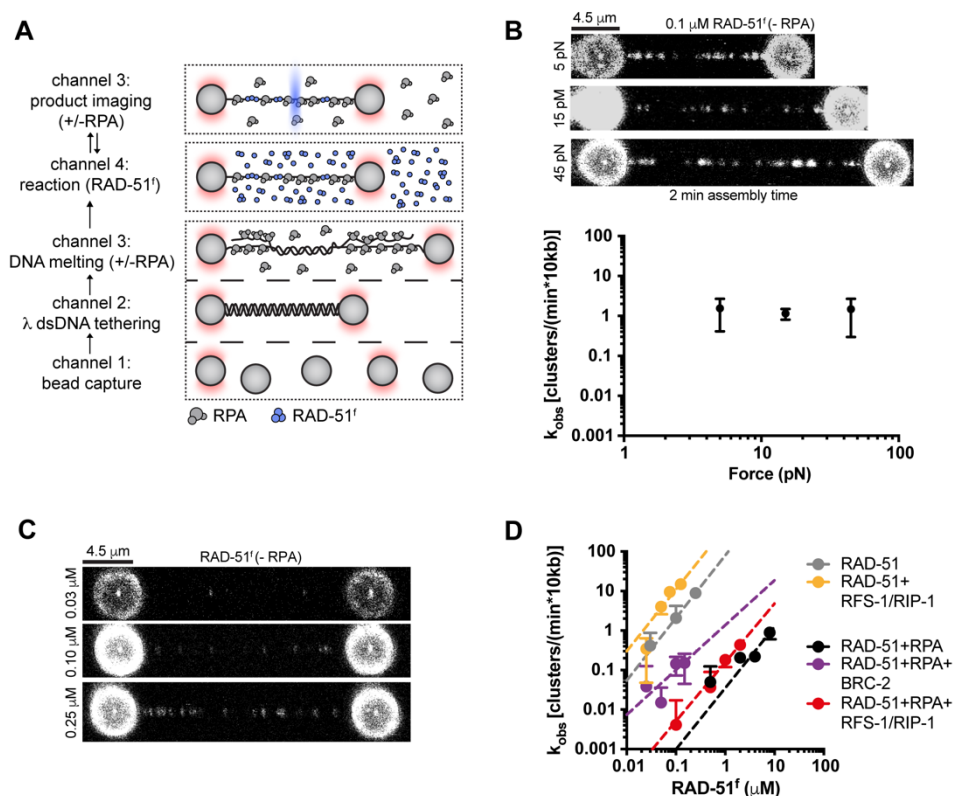


**Figure 3.8: 'Dipping' protocol to determine RAD-51 nucleation rates. (A)** A four-channel microfluidics device was used for the assembly of the 5-step single-molecule binding experiments. **(B)** Representative fluorescence images of RAD-51<sup>f</sup> clusters formed on ssDNA molecules held at 5, 15 and 45 pN force. 4.5  $\mu$ m scale bar. RAD-51<sup>f</sup> nucleation rates at 5, 15 and 45 pN forces



are plotted. **(C)** Representative fluorescence images taken after 30s of RAD-51<sup>f</sup> incubation–detection cycle with different RAD-51<sup>f</sup> concentrations present in the solution. 4.5  $\mu\text{m}$  scale bar. **(D)** RAD-51<sup>f</sup> concentration dependence of nucleation rate. Dotted line represents power-law fit yielding an exponent  $n = 1.6 \pm 0.2$  for RAD-51<sup>f</sup> in the absence of RPA ( $R^2 = 0.72$ ),  $n = 1.6 \pm 0.2$  for RAD-51<sup>f</sup> in the absence of RPA and the presence of stoichiometric amounts of RFS-1/RIP-1 ( $R^2 = 0.90$ ),  $n = 1.6 \pm 0.4$  for RAD-51<sup>f</sup> in the presence of RPA ( $R^2 = 0.83$ ),  $n = 1.1 \pm 0.4$  for RAD-51<sup>f</sup> in the presence of RPA and stoichiometric amounts of BRC-2 ( $R^2 = 0.21$ ) and  $n = 1.5 \pm 0.1$  for RAD-51<sup>f</sup> in the presence of RPA and stoichiometric amounts of RFS-1/RIP-1 ( $R^2 = 0.88$ ). Error bars indicate SD.

Next, I proceeded to visualize both RAD51<sup>f</sup> and RFS-1/RIP-1(A647) in the ‘dipping’ assay. Time-resolved experiments revealed a strong accumulation of RAD-51<sup>f</sup> clusters over time in the presence of RFS-1/RIP-1(A647) and ATP (**Figure 3.9A, B**). Without RFS-1/RIP-1(A647), RAD-51<sup>f</sup> clusters are highly dynamic, binding and dissociating rapidly from ssDNA (**Figure 3.9C**). To estimate off-rates of RAD-51<sup>f</sup>, I measured dwell-times of RAD-51<sup>f</sup> clusters - calculated from the number of consecutive frames (33 kHz frame acquisition frequency) in which detectable FAM signal was present at the same genomic position. I observed that RAD-51<sup>f</sup> clusters bind to ssDNA with short dwell-times, catastrophically disassembling seconds after their initial arrival (**Figure 3.9D**). These observations are reminiscent of burst-like dissociation events reported previously at human Rad51 filament ends (van Mameren et al., 2009). Inclusion of RFS-1/RIP-1(A647) in the reaction resulted in a significant increase in the dwell-times of RAD-51<sup>f</sup> clusters indicating a stabilizing effect of the Rad51 paralogs. Unexpectedly, when observing RFS-1/RIP-1(A647) fluorescent signal, I observed that RFS-1/RIP-1(A647) binds to RAD-51<sup>f</sup> clusters with extremely short dwell-times. RFS-1/RIP-1(A647) signal colocalizes with RAD-51<sup>f</sup> clusters (**Figure 3.9E**) - consistent with recognition of nascent RAD-51 filaments. These data indicate that RFS-1/RIP-1 promotes assembly of RAD-51 filaments by shutting down disassembly events at filament ends. In addition, RFS-1/RIP-1 is not a stable component of ssDNA-bound RAD-51<sup>f</sup> clusters. Collectively, these data indicate RFS-1/RIP-1 acts in a transient manner as a dynamic RAD-51 filament ‘chaperone’.

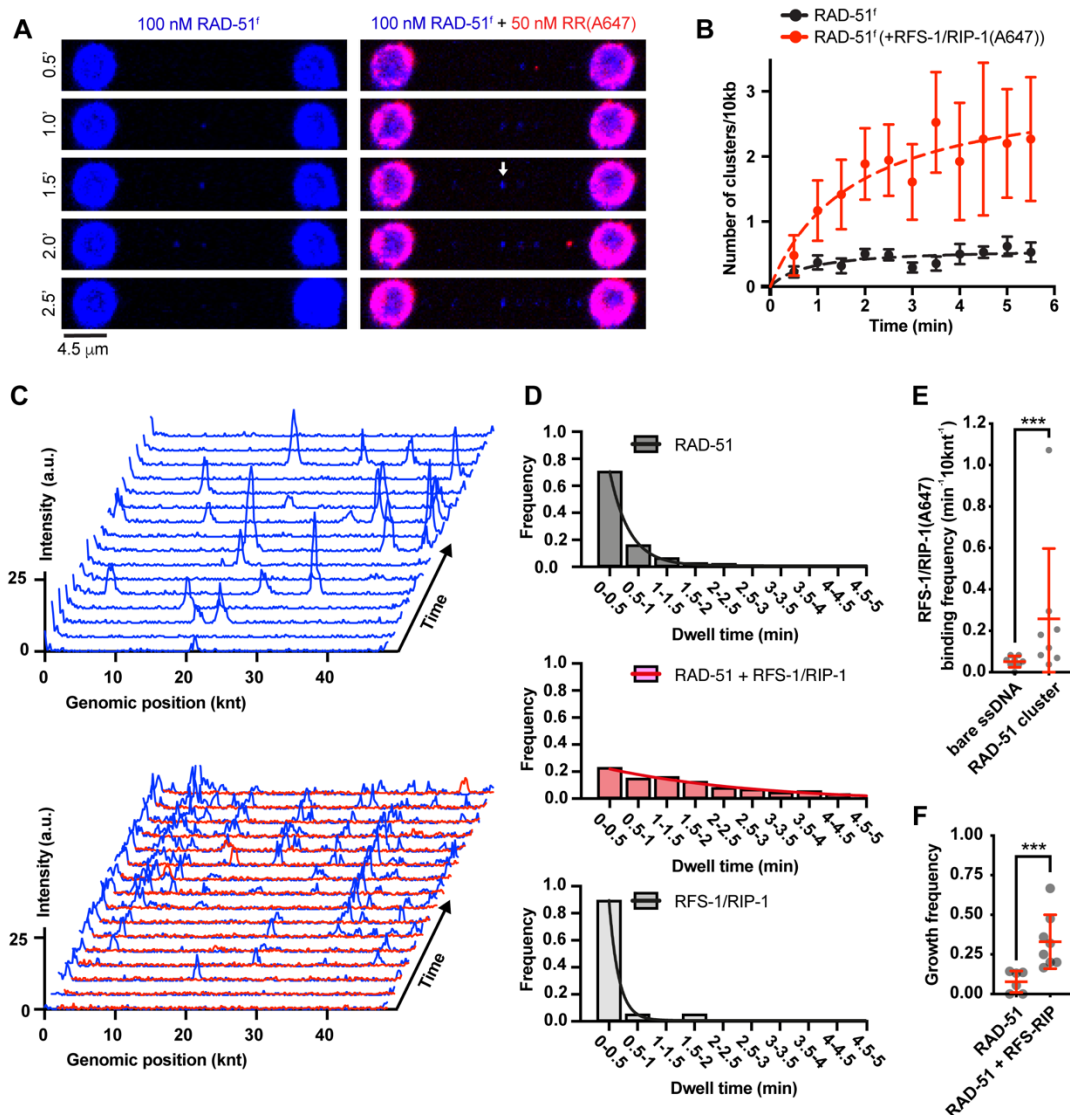


**Figure 3.9: RFS-1/RIP-1 ‘chaperones’ DNA-bound RAD-51 clusters by preventing RAD-51 dissociation.** (A) Fluorescence images taken after subsequent RAD-51<sup>f</sup> or RAD-51<sup>f</sup>+RFS-1/RIP-1(A647) incubation-detection cycles with the same ssDNA (no RPA) construct; cumulative incubation time (min) is indicated. 4.5 μm scale bar. Arrow indicates a growth event. RAD-51<sup>f</sup> signal shown in blue. RFS-1/RIP-1(A647) signal shown in red. (B) Quantification of RAD-51<sup>f</sup> nucleation frequency over time in the presence (n = 9 molecules) or absence (n = 11 molecules) of RFS-1/RIP-1(A647). Exponential fits are displayed. Error bars represent SEM. (C) Representative histogram of time-binned intensity versus genomic position on lambda DNA for RAD-51<sup>f</sup> signal (blue) in the absence (upper panel) or presence (lower panel) of RFS-1/RIP-1(A647). Each line represents 30 s timepoint. RFS-1/RIP-1(A647) signal is in red. (D) Histograms of dwell times of RAD-51<sup>f</sup> in the absence (top panel) or presence of RFS-1/RIP-1(A647) (middle panel) or dwell times of RFS-1/RIP-1(A647) in the presence of RAD-51<sup>f</sup> (bottom panel). Lines represent exponential fits. (top panel: RAD-51<sup>f</sup>,  $\tau \sim 21.12$  s,  $R^2 = 0.99$ , n = 167 clusters; middle

panel: RAD-51<sup>f</sup>+ RFS-1/RIP-1(A647),  $\tau \sim 150.6$  s,  $R^2 = 0.95$ ,  $n = 87$  clusters; bottom panel: RFS-1/RIP-1(A647),  $\tau \sim 10.28$ ,  $R^2 = 0.99$ ,  $n = 19$  clusters). **(E)** Quantification of the frequency of RFS-1/RIP-1(A647) binding to ssDNA and RAD-51 clusters. Individual DNA molecules were analyzed and the fraction of RFS-1/RIP-1(A647) bound to ssDNA or RAD-51<sup>f</sup> cluster was calculated. Each data point represents one ssDNA molecule analyzed.  $p = 0.005$ . Wilcoxon test. **(F)** Growth frequencies of RAD-51<sup>f</sup> clusters (fraction of clusters on a given ssDNA molecule displaying at least one growth event – defined by an increase of protomer number by a minimum of 1) in the presence or absence of RFS-1/RIP-1.  $p = 0.0003$ . Mann-Whitney test.

Rapid photobleaching and step-finding analysis (Autour et al., 2018; Watkins and Yang, 2005) allowed for imaging system calibration and direct assessment of the number of fluorophores in individual nucleating clusters and RAD-51 cluster growth frequency analysis (Figure 3.10A, B). In accordance with a power-law fit, most RAD-51<sup>f</sup> clusters are dimeric. Addition of RFS-1/RIP-1(A647) shifts the cluster population towards smaller species with the monomer fraction corresponding to approximately half of the population (Figure 3.10C). These data also remain consistent with the power-law fit,  $k_{obs} = J[\text{RAD-51}]^n$ , where  $n = 1.6$ , indicating monomers, in addition to dimers, represent a significant fraction of minimal nucleating units. Consistent with RFS-1/RIP-1(A647) stabilising RAD-51<sup>f</sup> on ssDNA, I observed more frequent RAD-51<sup>f</sup> cluster growth (Figure 3.9F). The increased frequency of RAD-51<sup>f</sup> cluster growth provides an explanation for the stimulation of filament growth rates observed with RFS-1/RIP-1, indicating transient engagement of RFS-1/RIP-1 with RAD-51 filaments shuts down RAD-51 dissociation events at filament ends and shifts protomer addition-dissociation equilibrium towards higher net filament growth rates.

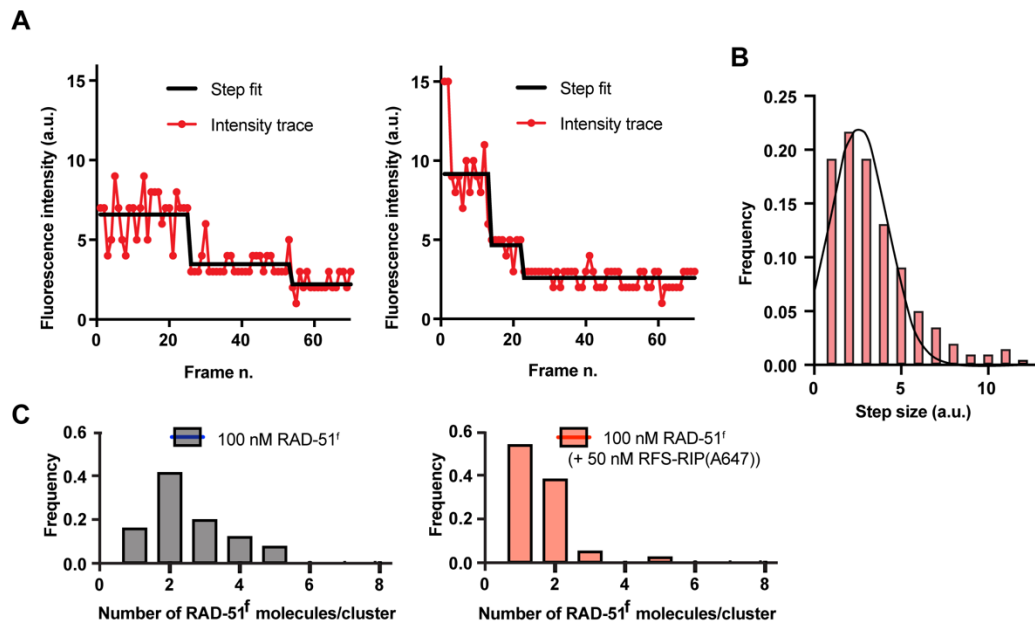


**Figure 3.10: Single-step photobleaching analysis.** (A) Examples of a fluorescence intensity trace of the RAD-51<sup>f</sup> cluster during continuous photobleaching. Black line represents stepping fit of the trace. (B) Fluorescence intensity single-molecule calibration histogram for RAD-51<sup>f</sup>. The histogram shows the values of the fluorescence intensity trace of the single steps of multiple photobleaching traces ( $n = 198$  steps). Black line represents gaussian fit. Second two-step gaussian was excluded from the analysis. Mean = 2.55. S.D. = 1.67.  $R^2 = 0.90$ . (C) Histogram of RAD-51<sup>f</sup> cluster size in the presence ( $n = 76$  clusters) or absence ( $n = 181$  clusters) of RFS-1/RIP-1(A647).

### 3.5 ATPase controls RFS-1/RIP-1 dynamics

To more precisely measure dwell times of RFS-1/RIP-1(A647), I performed real-time imaging of RFS-1/RIP-1(A647) association with RPA-eGFP coated ssDNA in the presence of RAD-51 and ATP (Figure 3.11A). When RAD-51 was absent from the reaction, minimal binding of RFS-1/RIP-1(A647) to RPA-eGFP coated ssDNA was observed (Figure 3.11B). Individual RFS-1/RIP-1(A647) molecules display very short dwell-times on RPA-eGFP coated ssDNA with RAD-51 and ATP (median of 11.3 s, 9.5 - 15.8 s, 96% CI; Figure 3.11A), similar to the dwell-times observed using the 'dipping' protocol described in Figure 3.9D. Given ATP hydrolysis releases Rad51 from DNA (Chi et al., 2006; Gataulin et al., 2018; Robertson et al., 2009), I hypothesized that short dwell-times of RFS-1/RIP-1 might result from ATP hydrolysis by RFS-1 or RAD-51. Indeed, upon inclusion of ATP- $\gamma$ -S, the dwell-time of RFS-1/RIP-1(A647) significantly increased (median of 28.3 s; 22 s - 56.2 s, 97.6% CI; Figure 3.11A). Notably, dwelling RFS-1/RIP-1(A647) molecules are frequently (71% of events scored, n = 26) located at the border of RPA-eGFP (blue) and RAD-51 filaments (dark; Figure 3.11C, D). This corroborates previous negative stain EM data (Taylor et al., 2015) where RFS-1/RIP-1 was observed to be bound to RAD-51 filament ends, but not interstitially. I have shown that RAD-51 filaments grow preferentially in 3' to 5' direction in the presence of RFS-1/RIP-1 and that RFS-1/RIP-1 shuts down dissociation of RAD-51 clusters on ssDNA leading to increased dwell-times and growth frequencies. Therefore, I proceeded to investigate whether labelled RFS-1/RIP-1 directly binds to 5' filament ends using gapped DNA substrates with defined polarity. To this end, I incubated RAD-51 filaments with 100 nM RFS-1/RIP-1(A647) in the presence of ATP- $\gamma$ -S (Figure 3.11E), which revealed proximity to 5', but not 3', filament ends (Figure 3.11F, G). Taken together, these data confirm RFS-1/RIP-1 transiently binds 5' filament ends to allow for efficient filament growth in a 3' to 5' direction.

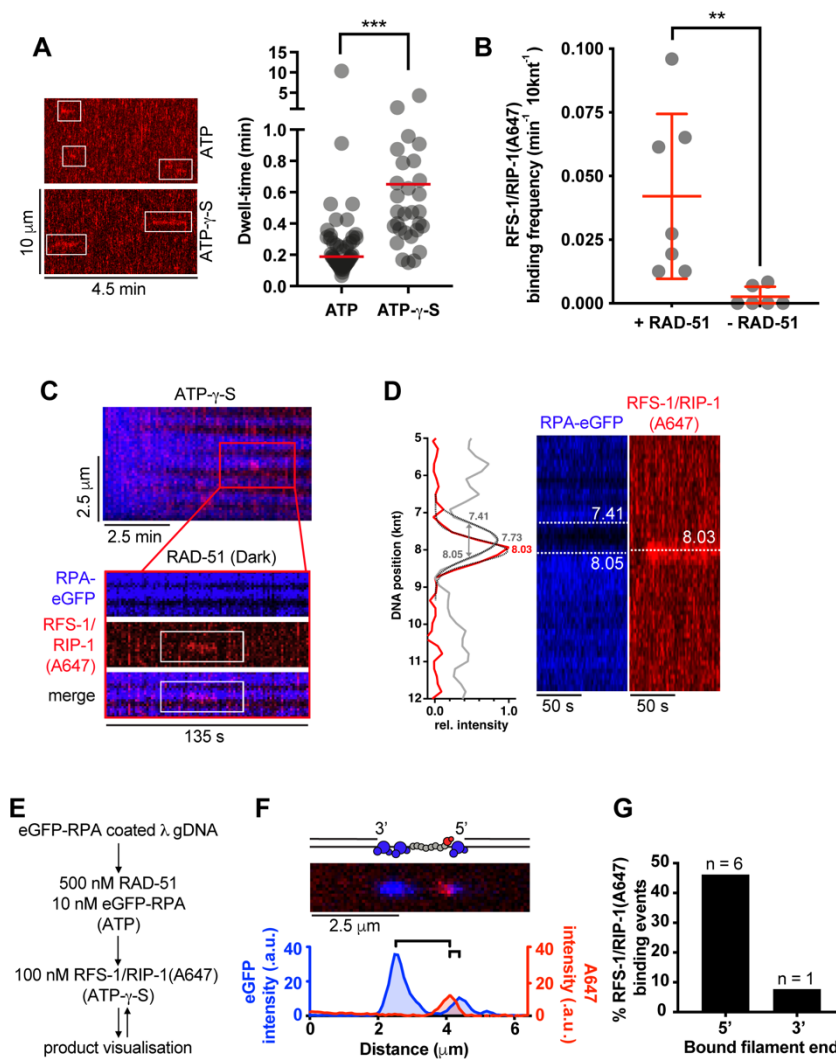


**Figure 3.11: Transient engagement of RFS-1/RIP-1 with 5' filament ends mediated by ATP hydrolysis.** (A) Representative kymographs of dwelling single RFS-1/RIP-1(A647) (2.5 nM) complexes on RPA-eGFP coated ssDNA in the presence of 500 nM RAD-51 and ATP or ATP- $\gamma$ -S (left panel). Quantification of experiment shown in left panel, for ATP ( $n = 47$  binding events) and ATP- $\gamma$ -S ( $n = 29$  binding events). Black line represents median.  $p < 0.0001$ . Mann-Whitney test. (right panel). (B) Quantification of RFS-1/RIP-1(A647) binding frequencies on individual RPA-eGFP coated ssDNA molecules in the presence or absence of RAD-51.  $p = 0.0012$ . Mann-Whitney test. (C) Representative traces of single RFS-1/RIP-1(A647) complexes binding to RAD-51 filaments in ATP- $\gamma$ -S. RPA-eGFP shown in blue, RAD-51 dark, RFS-1/RIP-1(A647) red. (D) Quantification of the RFS-1/RIP-1(A647) end binding using custom position analysis algorithm (written by Dr. A. Kaczmarczyk). To obtain the exact location of the RAD-51 paralog with respect to the RAD-51 filament, the centre of the filament is resolved first by fitting the reversed eGFP intensity (grey peak). Grey arrow, representing the peak's width, marks the filament's edges.

Gaussian fit of the RFS-1/RIP-1(A647) intensity (red peak, red channel) indicates that the paralog binds to the periphery of the RAD-51 filament. **(E)** Protocol designed to visualise RFS-1/RIP-1(A647) binding to RAD-51 filaments grown on gapped  $\lambda$  DNA. **(F)** 2D scan of representative RAD-51-DNA complex obtained using protocol described in E. Proximity of A647 signal maximum to eGFP signal maximum on either 3' or 5' RAD-51 filament border was used to estimate 3' or 5' filament end binding polarity. **(G)** Quantification of filament 5' or 3' end binding frequencies by RFS-1/RIP-1(A647) ( $n = 13$  binding events).

To further verify whether the ATPase activity of RFS-1/RIP-1 is critical for the dissociation from RAD-51 filament ends, I prepared Alexa 647-labelled RFS-1 K56A/RIP-1 complex, where the putative catalytic lysine residue of the Walker A box of RFS-1 is mutated to alanine. Then, I performed 'dipping' experiments (**Figure 3.12A**) and observed that RFS-1 K56A/RIP-1(A647) displays dramatically increased dwell-times on RAD-51 ssDNA clusters when compared to RFS-1/RIP-1(A647) (**Figure 3.12B**). RFS-1 K56A/RIP-1(A647) also retained the ability to stabilise RAD-51<sup>f</sup> clusters on ssDNA (**Figure 3.12C**). Inclusion of RFS-1 K56A/RIP-1 also resulted in less efficient stimulation of RAD-51 assembly on RPA-eGFP-coated ssDNA (**Figure 3.13A, B**). When compared to wt RFS-1/RIP-1, RAD-51 filaments grow more slowly in the presence of RFS-1 K56A/RIP-1 (**Figure 3.13C**).

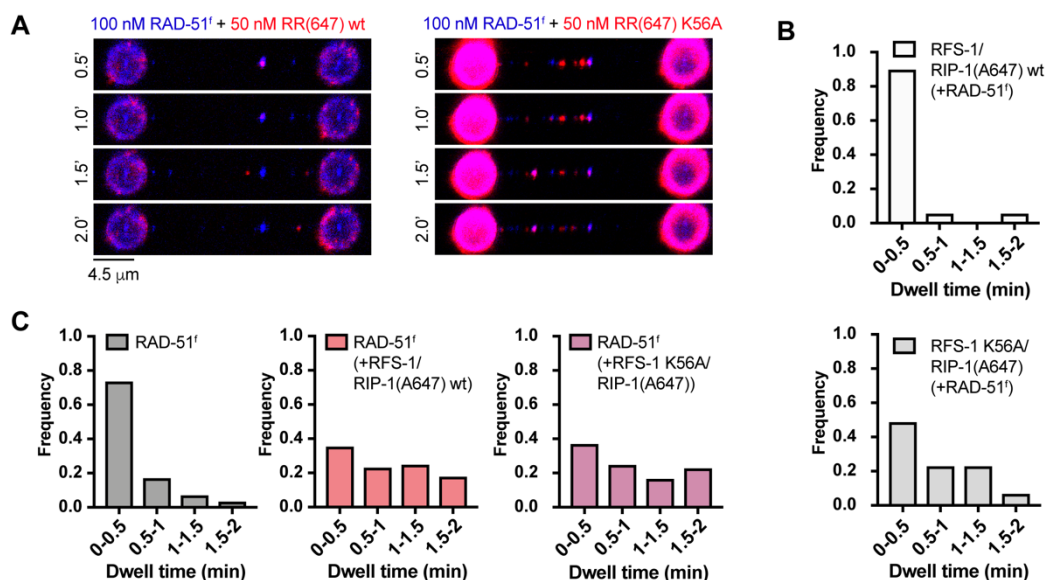


**Figure 3.12: RFS-1/RIP-1 K56A fails to disengage from RAD-51 clusters.** **(A)** Representative fluorescence images taken after RAD-51<sup>f</sup>+RFS-1/RIP-1(A647) or RAD-51<sup>f</sup>+RFS-1 K56A/RIP-1(A647) incubation–detection cycles with the same ssDNA construct; cumulative incubation time

is indicated. RAD-51<sup>f</sup> signal shown in blue. RFS-1/RIP-1(A647) signal shown in red. **(B)** Histograms of dwell times of wt RFS-1/RIP-1(A647) (n = 19 clusters; top) or RFS-1 K56A/RIP-1(A647) (n = 31 clusters; bottom) in the presence of RAD-51<sup>f</sup>. Number of dwell-time categories was adjusted to accommodate lower stability of bare ssDNA in the presence of RFS-1 K56A/RIP-1(A647). **(C)** Histograms of dwell times of RAD-51<sup>f</sup> alone (n = 160 clusters; left) or in the presence of RFS-1/RIP-1(A647) wt (n = 57 clusters; middle), or dwell times of RAD-51<sup>f</sup> in the presence of RFS-1 K56A/RIP-1(A647) (n = 49 clusters; right).

These data indicate that the RFS-1 K56A/RIP-1 mutant is effective at filament end-binding and stabilization of nucleating RAD-51 clusters but is compromised for the ability to stimulate RAD-51 filament growth. Interestingly, when wt RFS-1/RIP-1 concentrations were increased to near stoichiometric levels with RAD-51, this compromised RAD51 filament assembly and hindered filament growth, compared to the growth stimulation with sub-stoichiometric levels of wt RFS-1/RIP-1) (Figure 3.13A, B, C). This indicates that excessive filament end binding at high of RFS-1/RIP-1 concentrations or Walker A box mutation in RFS-1 blocks further recruitment of RAD-51 protomers hindering filament elongation.

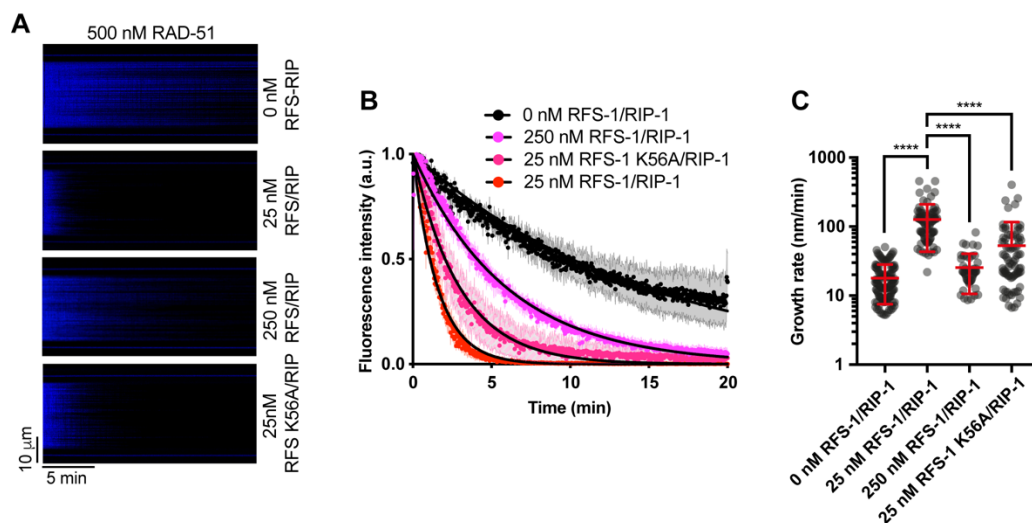


**Figure 3.13: RFS-1/RIP-1 K56A hinders RAD-51 filament assembly and growth.** **(A)** Kymograph showing the displacement of RPA-eGFP by RAD-51 in indicated conditions. **(B)** Normalized fluorescence intensity for RPA-eGFP signal in indicated conditions; shaded area represents SEM. (n = 3-7 molecules). Black lines represent exponential fits. **(C)** Quantification of growth rates in indicated conditions. P < 0.0001. Mann-Whitney test.

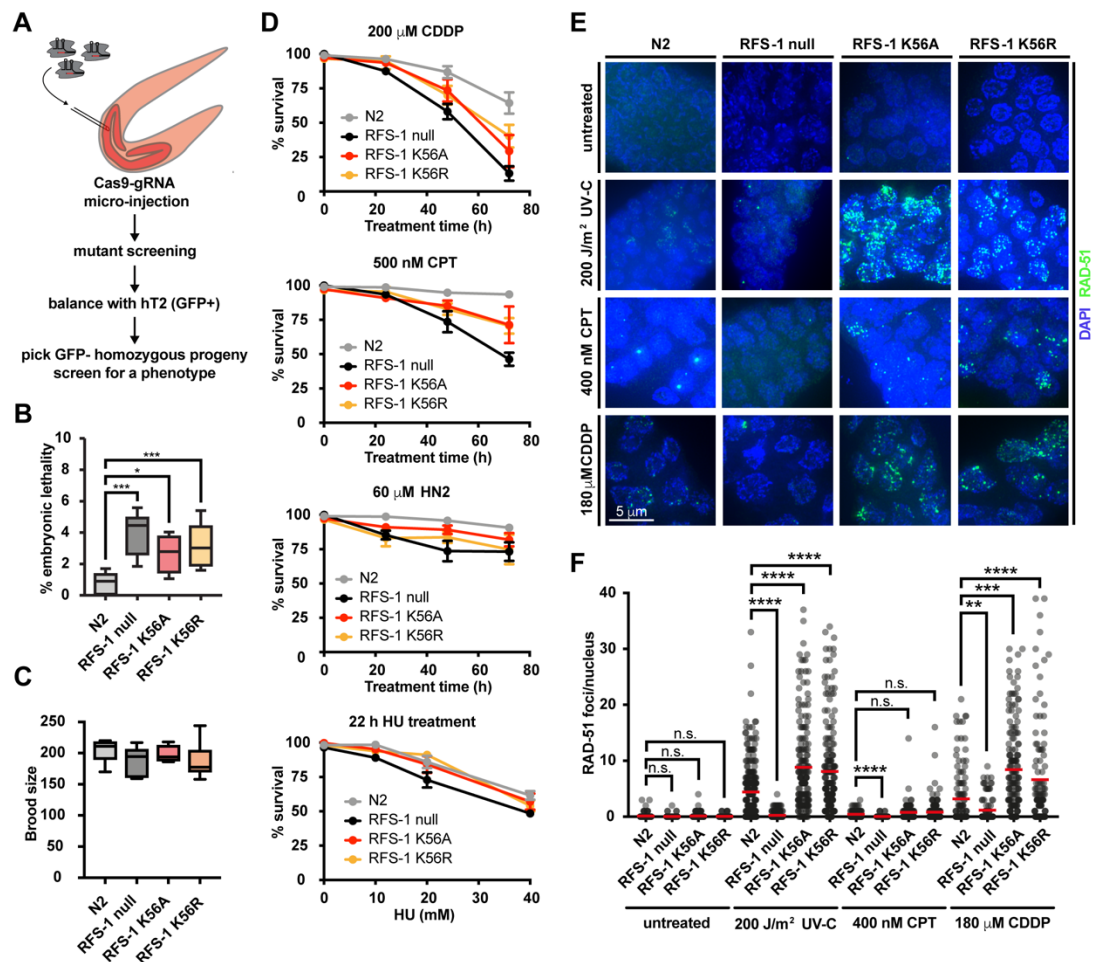


### 3.6 Nematode phenotype of RFS-1 Walker A mutants

To assess whether the dynamic engagement of RFS-1/RIP-1 during RAD-51 filament assembly plays an important role in HR *in vivo*, I generated nematode knock-in mutant strains for both RFS-1 K56A and RFS-1 K56R using the CRISPR-Cas9 system with help from Dr. Consuelo Barroso (Figure 3.14A). In a manner similar to the *rfs-1* (null) strain, *rfs-1* K56A and *rfs-1* K56R mutant strains display a modest increase in the levels of embryonic lethality when compared to the N2 (wt) strain (Figure 3.14B). No significant brood size reduction was observed (Figure 3.14C). In agreement with previous work (Taylor et al., 2015; Ward et al., 2007), the *rfs-1* null strain are hyper-sensitive to agents that induce replication fork breakage (Ward et al., 2007), such as cisplatin (CDDP), camptothecin (CPT) and nitrogen mustard (HN2). Notably, *rfs-1* K56A and K56R Walker A mutants are also sensitive to these compounds, although to a lesser extent than *rfs-1* null animals (Figure 3.14D). However, I did not observe strong sensitivity to hydroxyurea (HU) in the *rfs-1* K56A and *rfs-1* K56R mutant strains. Mitotic zones of extruded germlines were then examined for RAD-51 focus formation before and after CDDP, UV-C and CPT treatment (Figure 3.14E). In agreement with previous results (Ward et al., 2007), RAD-51 forms DNA damage-induced foci in N2 strain, but not in the *rfs-1* null mutant. Strikingly, *rfs-1* K56A and K56R Walker A mutants displayed extensive accumulation of RAD-51 foci in response to DNA damage (Figure 3.14F). These data, together with DNA damage sensitivity, indicate that RAD-51 is stabilized on ssDNA in the *rfs-1* K56A and *rfs-1* K56R mutant strains, but the resulting RAD-51 species are non-functional for repair of DNA damage via HR, presumably due to their short length or persistent filament end binding by RFS-1/RIP-1 Walker A mutants, or both.

To summarize, my single-molecule and genetic data support a model where BRC-2 facilitates RAD-51 nucleation on RPA-coated ssDNA. In steady state, RAD-51 monomer recruitment is in equilibrium with disassembly bursts from nascent RAD-51 filament ends. To shift the equilibrium in favour of filament growth, RFS-1/RIP-1 acts as a molecular 'chaperone' by transiently binding RAD-51 filaments and preventing RAD-51 dissociation from 5' filament ends, leading to stabilisation of nascent RAD-51 filaments. Subsequent ATPase dependent release of RFS-1/RIP-1

allows for further addition of RAD-51 monomers at 5' filament end. Iterative cycles of RFS-1/RIP-1 binding, filament stabilization, RFS-1/RIP-1 release and RAD-51 recruitment leads to the formation of long RAD-51 filaments proficient for strand exchange.

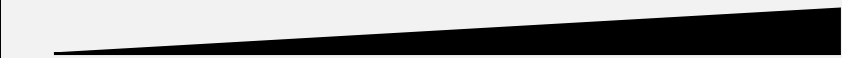


**Figure 3.14: RFS-1 Walker A mutants cause DNA damage sensitivity and abnormal RAD-51 focus formation *in vivo*.** (A) A schematic for CRISPR-Cas9 knock-in strategy for generation of RFS-1 mutants. (B) Embryonic lethality analysis of *rfs-1* mutants *in vivo*. Percentage of unhatched eggs was scored after 24 hours for the progeny of 6-8 worms. (C) Brood size of strains of the indicated genotype. Progeny 5-8 worms were evaluated. (D) Nematode strains were treated with the indicated dose of genotoxin. Percentage of unhatched eggs was scored after the indicated exposure time. Error bars represent SEM. (E) Representative images of the mitotic compartment of *C. elegans* germline after genotoxin exposure. (F) Quantification of RAD-51 focus formation in the mitotic zone of the worm germline under different treatments in strains of the indicated genotype. Between 99 and 261 cells were quantified for each condition in 2-3 representative germlines for each genotype. Mann-Whitney test.

## Chapter 4. Results 2: Exploring the genetic consequences of recombination mediator bypass

### 4.1 Engineering a self-loading human RAD51 variant

In the previous chapter, I presented results that indicate Rad51 paralogs act as transient ‘chaperones’ or switches, that turn on filament growth and to a lesser extent nucleation in order to assemble Rad51 in response to DSB formation. Interestingly however, bacterial RecA can rapidly grow into filaments on its own (Bell et al., 2012). Not only that, RecA is a much more proficient enzyme in terms of ATPase activity compared to human RAD51 (Wright et al., 2018). RecA also displays significantly higher efficiency in DNA strand exchange reactions when compared to nematode or human RAD51. In fact, when looking at core recombinases from different domains of life, a clear pattern of downscaling core recombinase enzyme activity emerges (Table 3), with a more pronounced need for auxiliary factors, such as Rad51 paralogs, which ‘switch on’ Rad51 when needed.

Recombinase	UvsX	RecA	RadA	Rad51
Domain	Bacteriophage	Bacteria	Archea	Eukaryota
ATPase ( $k_{cat}$ ; $\text{min}^{-1}$ ) on ssDNA	~ 200	~ 20	~ 2	~ 0.2
Strand exchange activity	N/A	Strong	Medium. Fluctuates with temperature. Weaker than RecA.	Weak
Auxiliary factor dependence				

**Table 3: Recombinase enzymatic activity decreases with organism complexity.** Adapted from (Wright et al., 2018).

Why evolution has selected for the attenuation of activity of the most critical DNA pairing enzyme is unclear? And what are the consequences of a self-sufficient recombinase operating in eukaryotes? A possible means to investigate this outstanding question came from the laboratory of Prof. Lorraine S. Symington, where a genetic screen in *S. cerevisiae* was conducted to isolate Rad51 alleles suppressing DNA damage sensitivity of Rad51 paralog deficient yeast strain ( $\Delta rad55$ ;  $\Delta rad57$ ) (Fortin and Symington, 2002). Multiple Rad51 alleles were isolated with Rad51 I345T suppressing the phenotype most consistently. Biochemical work has shown that

Rad51 I345T binds both ssDNA and dsDNA with higher affinity than wt Rad51 (Malik and Symington, 2008). Rad51 I345T also forms more stable filaments than wt Rad51 and displays higher DNA strand exchange activity. However, no strong phenotype is observed in *rad51-I345T* yeast strains, which are sensitive to DNA damage only in the absence of main yeast anti-recombinase Srs2 ( $\Delta$ *srs2* background) (Fung et al., 2009; Malik and Symington, 2008). This raised the possibility that the permanently 'switched on' Rad51 variant is generally well tolerated. However, no follow up work in yeast assessing possible long-term mutagenic consequences of Rad51 I345T expression, similar to those taking place during mammalian development in mouse DNA repair deficient models, has been conducted. In addition, complex genomes of higher organisms, such as mammals, contain many repetitive sequences, which may be particularly vulnerable to illegitimate recombination.

To address these possibilities and ultimately understand the reason why the intrinsic activity of the core recombinase has been reduced during evolution, I engineered the corresponding mutation into recombinant human RAD51 (Figure 4.1A). In a manner similar to yeast homolog, purified human RAD51 I287T displays higher affinity for both ssDNA (for wt RAD51:  $K_d = 0.51 \pm 0.04 \mu\text{M}$ , 95% CI; for RAD51 I287T:  $K_d = 0.23 \pm 0.02 \mu\text{M}$ , 95% CI) and dsDNA (for wt RAD51:  $K_d = 0.42 \pm 0.03 \mu\text{M}$ , 95% CI; for RAD51 I287T:  $K_d = 0.21 \pm 0.03 \mu\text{M}$ , 95% CI) (Figure 4.1B, C). To assess DNA pairing activity of RAD51 I287T, I performed D-loop formation assays.  $\text{CaCl}_2$  was present in the buffer to stabilize RAD51 and obtain detectable product yields. RAD51 I287T displays much higher D-loop formation when compared to wt RAD51 (Figure 4.1D, E). Given ATPase dead RAD51 variant RAD51 K133R forms abnormally stable filaments, which also results in high D-loop formation *in vitro*, but completely stalls recombination *in vivo*, I tested for ATPase activity of RAD51 I287T (Figure 4.1F). Unlike RAD51 K133R, which is dead for ATPase ( $k_{\text{cat}} \sim 0.02 \text{ min}^{-1}$ ), RAD51 I287T displays ssDNA-dependent ATPase activity ( $k_{\text{cat}} = 0.28 \pm 0.01 \text{ min}^{-1}$ ) similar to that of wt RAD51 ( $k_{\text{cat}} = 0.35 \pm 0.01 \text{ min}^{-1}$ ), indicating it is a functional enzyme. Finally, to test whether RAD51 I287T can assemble better than wt RAD51 on a physiologically relevant substrate, proteins were sent to the laboratory of Dr. Eric C. Greene, where single-molecule RPA-eGFP displacement experiments using ssDNA curtains were performed (Figure 4.1G), similarly to those described in the previous chapter with

nematode proteins. RAD51 I287T displaces RPA-eGFP with  $\sim 1.6$ -fold faster rate ( $k_{on} = 0.84 \pm 0.03 \text{ min}^{-1}$ ; 95% CI) than wt RAD51 ( $k_{on} = 0.54 \pm 0.03 \text{ min}^{-1}$ ; 95% CI) or RAD51 K133R ( $k_{on} = 0.53 \pm 0.02 \text{ min}^{-1}$ ; 95% CI) (Figure 4.1H). Conversely, RAD51 I287T dissociates from ssDNA slower (half-time  $\sim 10.35 \text{ min}$ ) than RAD51 wt (half-time  $\sim 8.18 \text{ min}$ ), but faster than RAD51 K133R (half-time  $\sim 13.40 \text{ min}$ ) (Figure 4.1I) – the most stable variant described in the literature (Chi et al., 2006). The faster assembly rate and slower disassembly rate are in line with estimated bulk  $K_d$  values and reminiscent of phenomena observed when Rad51 paralogs are present in the reaction with Rad51 (Belan et al., 2021a; Taylor et al., 2016).

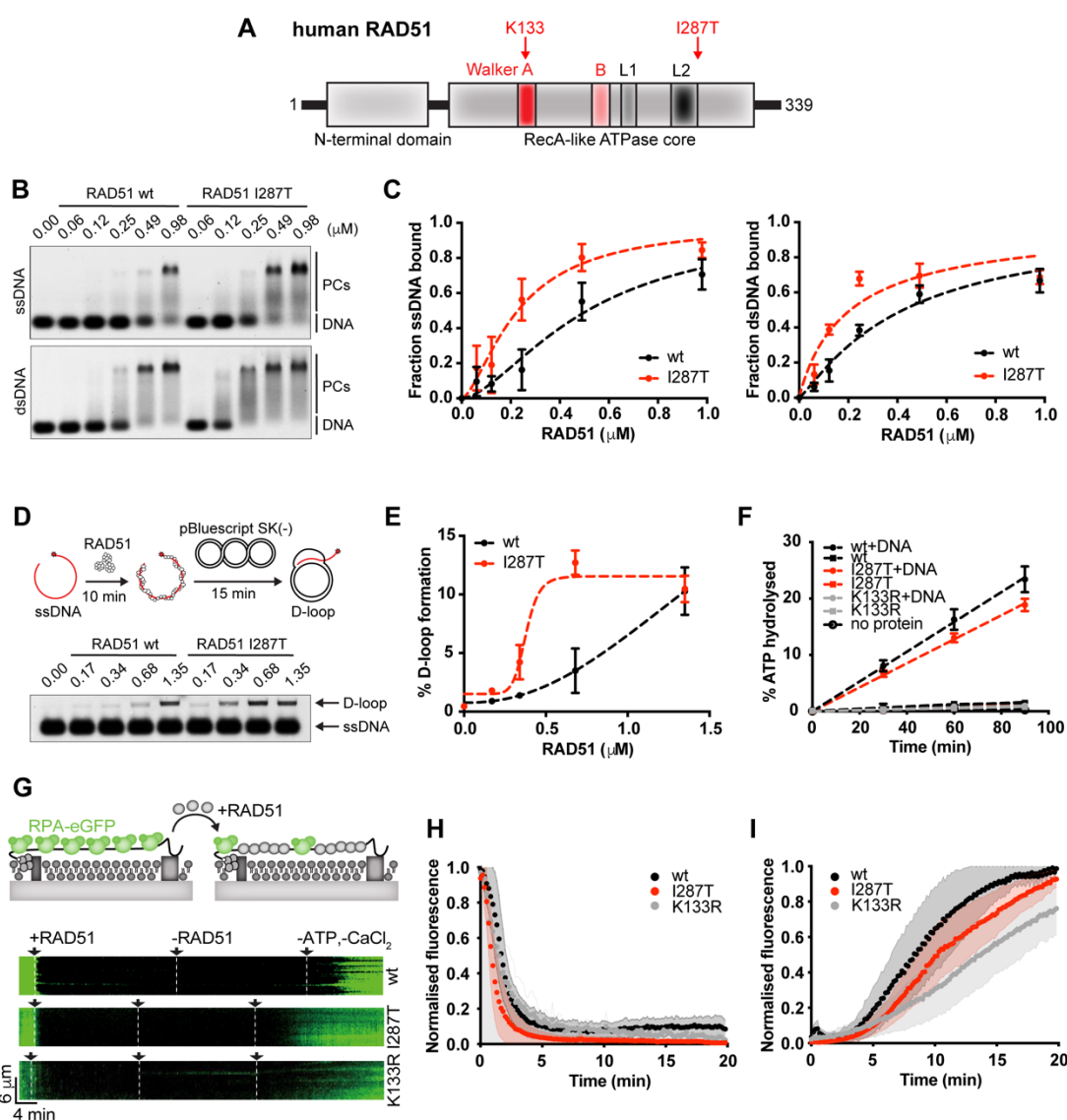


**Figure 4.1: Biochemical characterization of RAD51 I287T.** (A) A schematic of human RAD51. Position of I287T mutation and catalytic lysine are indicated. (B) EMSA comparing ssDNA and

dsDNA binding affinity of wt RAD51 and RAD51 I287T. **(C)** Quantification of B. Error bars indicate S.D. N = 3. Lines represent sigmoid fit. **(D)** D-loop formation assay comparing wt RAD51 and RAD51 I287T. **(E)** Quantification of E. Error bars indicate S.D. N = 3. Lines represent sigmoid fit. **(F)** ATPase assay for wt RAD51, RAD51 I287T and RAD51 K133R. 0.75  $\mu$ M protein was used with 100  $\mu$ M ATP. **(G)** A schematic of ssDNA curtain assay for RPA-eGFP displacement. Kymographs showing the assembly and disassembly of RAD51 filaments on single ssDNA molecules in the presence of 0.5 nM RPA-eGFP (green). Assembly reactions were initiated by injecting 2  $\mu$ M RAD51 together with 2 mM ATP and 5 mM  $\text{Ca}^{2+}$  into sample chambers containing ssDNA molecules coated with RPA-eGFP, while monitoring the loss of RPA-eGFP signal. Disassembly reactions were initiated by flushing ATP and  $\text{Ca}^{2+}$  from the sample chambers while monitoring the increase in ssDNA-bound RPA-GFP signal. **(H)** Graphs showing the normalized RPA-eGFP signal intensity integrated over entire ssDNA molecules during the assembly of the RAD51 filaments. Shaded error bars represent 68% confidence intervals. N = 60. **(I)** Graphs showing the normalized RPA-eGFP signal intensity integrated over entire ssDNA molecules during the disassembly of the RAD51 filaments. Shaded error bars represent 68% confidence intervals. N = 60.

## 4.2 RAD51 I287T causes replication stress *in vivo*

With biochemical data confirming RAD51 I287T mimics the general characteristics of yeast Rad51 I345T mutant, I proceeded to test the impact of RAD51 I287T mutation *in vivo*. To do this, RAD51 I287T knock-in mice were generated in the Genetic Modification Service (GeMS) at the Francis Crick Institute by knocking in the allele via CRISPR-Cas9 into the inbred C57BL/6 genetic background. Rad51 gene deletion is embryonically lethal and results in developmental arrest at embryonic day 5 (Lim and Hasty, 1996). Surprisingly, homozygous RAD51 I287T mutant mice are viable. Currently, this makes the RAD51 I287T mice the only reported viable RAD51 mutant in mammalian cells. Parental mice, heterozygous RAD51 +/-I287T mice and homozygous RAD51 I287T/I287T mice were maintained in a colony phenotypically analysed by Dr. Valerie Borel. RAD51 I287T/I287T are smaller than RAD51 +/+ mice and display a complex phenotype which includes white belly patches, kinks in the tail, facial abnormalities, smaller testes and reduced litter sizes over 21 days of gestation. These phenotypes are highly reminiscent of a recently reported Pol Epsilon hypomorph mouse model, *Pole4*-deficient mouse strain (Bellelli et al., 2018), which exhibits stochastic cell death during embryonic development due to heightened replication stress. Interestingly, RAD51 I287T/I287T mice also displayed eye abnormalities, which is similar to *fancd2* deficient mouse models, where microphthalmia is observed (Parmar et al., 2009). Given that FA pathway is important for replication-coupled repair of DNA ICLs, this is also suggestive of elevated replication stress levels in these animals. Given RAD51 Walker A mutations (K133R and K133A) have a strong dominant-negative effect in cells (Kim et al., 2012), it was expected that heterozygous RAD51 +/-I287T mice might display a phenotype similar to that of RAD51 I287T/I287T mice. However, this was not the case as heterozygous animals seem phenotypically indistinguishable from RAD51 +/+ mice. This observation further supports my biochemical data showing that ATPase activity is intact in RAD51 I287T and thus incorporation of RAD51 I287T into the filaments does not poison wt RAD51 *in vivo*.

To examine cellular consequences of RAD51 I287T mutations, Dr. Valerie Borel isolated and immortalized fibroblasts from RAD51 +/+, RAD51 +/-I287T and RAD51

I287T/I287T mouse embryos (mouse embryonic fibroblasts, MEFs). I then proceeded with detailed phenotypic analysis of these cells. For the purpose of this study, I focused mainly on RAD51 +/+ and RAD51 I287T/I287T (referred to as RAD51 IT/IT further in the text) MEFs as heterozygous mice do not display any phenotype. For the purpose of the study, two clones of RAD51 IT/IT from two RAD51 +/+ parents were examined as independent biological replicates:

- I) clone C5 (RAD51 +/+) and corresponding knock-in clone C6 (RAD51 IT/IT)
- II) clone C10 (RAD51 +/+) and corresponding knock-in clone C9 (RAD51 IT/IT)

First, I performed T3T protocol to calculate cumulative population doublings (Equation 10) of isolated cell lines. In accordance with the smaller size of the mice, RAD51 IT/IT MEFs proliferated more slowly than RAD51 +/+ MEFs (Figure 4.2A). To investigate whether genome duplication defects underline this phenotype, I performed the SMARD assay (Figure 4.2B) to estimate replication rates of individual replisomes (Equation 11) and assess replication fork dynamics in RAD51 IT/IT MEFs. While in RAD51 +/+ MEFs, physiological replication fork rates were observed (C5:  $1.02 \pm 0.02$  kb/min; 95% CI), RAD51 IT/IT MEFs displayed ~30 % slower overall fork speed (C6:  $0.70 \pm 0.05$  kb/min; 95% CI) in both clones (Figure 4.2C, D, E). Next, I reasoned that the slower fork rates in RAD51 IT/IT mutant cells may be the result of stochastic replication fork stalling upon encountering an obstacle. To address this, the progression of two replication forks firing from the same origin was compared (Figure 4.2F). If no obstacle is present in front of the replication fork, CldU replication tracts will be mostly symmetric with respect to their length. If one of the ongoing forks encounters an obstacle, a shortening of the tract will be observed, resulting in decrease in apparent fork speed and an increase in asymmetry between the length of CldU tracts. Indeed, while RAD51 +/+ MEFs display low levels of fork asymmetry (C5:  $16.0 \pm 1.7$  %), RAD51 IT/IT MEFs display a ~2-fold increase in replication fork asymmetry (C6:  $36.7 \pm 2.7$  %). The phenomenon is observed in both biological clones (Figure 4.2G, H, I).



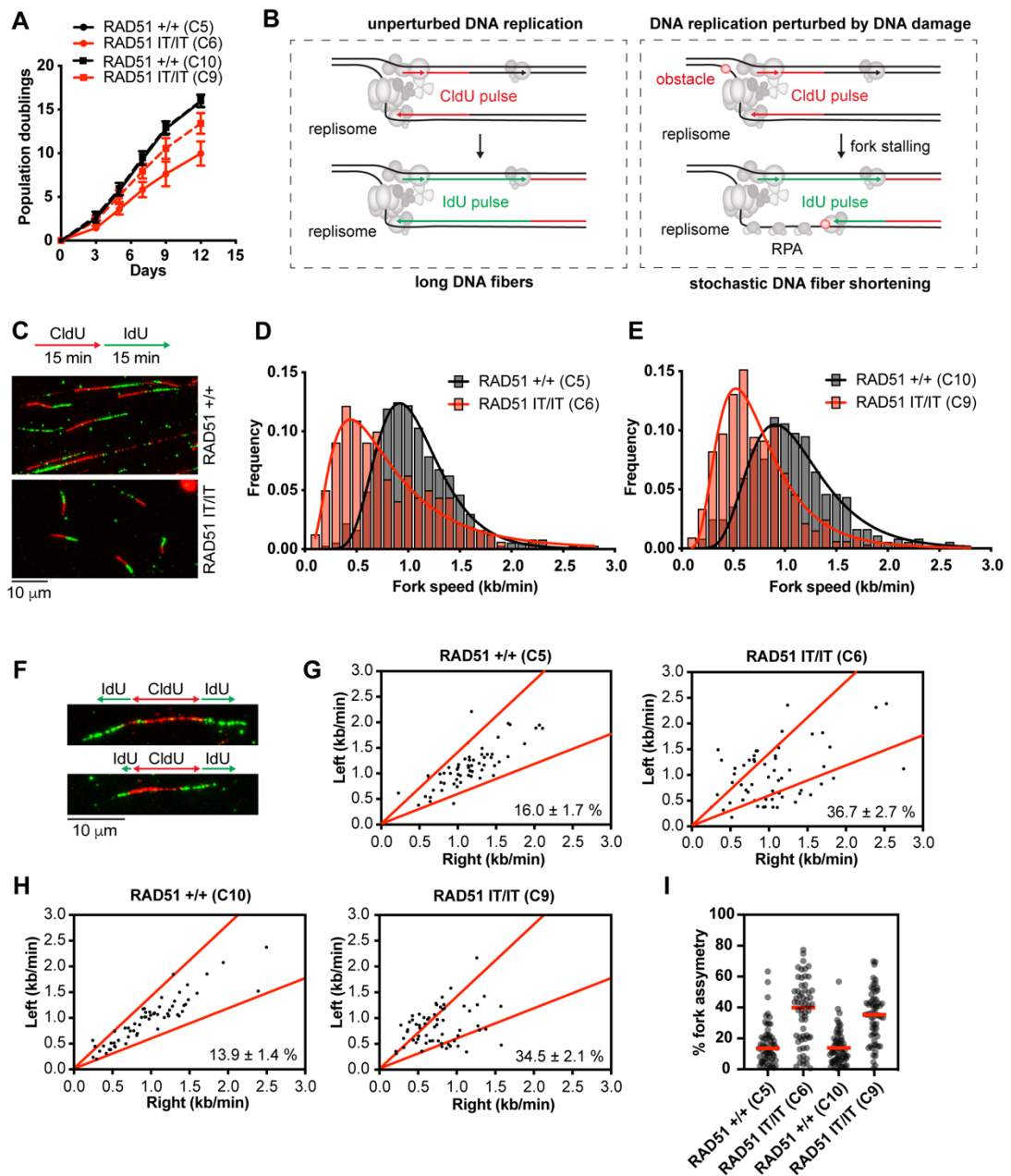


**Figure 4.2: Replication stress in RAD51 IT/IT MEFs. (A)** Analysis of proliferation of RAD51 +/+ and RAD51 IT/IT MEFs, measured as accumulation of population doublings. Cells were cultured according to 3T3 protocol; Error bars indicate SEM. N= 3. **(B)** Schematic of SMARD to analyse replication fork progression. **(C)** Replicating cells were pulse-labelled for 15 min with IdU and for 15 min with CldU. Representative images of spread DNA fibres in RAD51 +/+ and RAD51 IT/IT MEFs. **(D)** Histogram of replication fork speed in RAD51 +/+ (clone 5, C5) and RAD51 IT/IT (clone 6, C6) MEFs. N = 300-360 fiber tract/condition. Lines represent lognormal fit. **(E)** Histogram of replication fork speed in RAD51 +/+ (clone 10, C10) and RAD51 IT/IT (clone 9, C9) MEFs. N = 300-360 fiber tract/condition. Lines represent lognormal fit. **(F)** Representative images of

symmetric or asymmetric forks firing from a single origin. **(G)** Analysis of fork symmetry in RAD51 +/+ (clone 5, C5) and RAD51 IT/IT (clone 6, C6) MEFs reported as left/right moving fork ratio. N = 60. **(H)** Analysis of fork symmetry in RAD51 +/+ (clone 10, C10) and RAD51 IT/IT (clone 9, C9) MEFs reported as left/right moving fork ratio. N = 62. **(I)** Summary of fork asymmetry in RAD51 +/+ and RAD51 IT/IT MEFs reported as percentage of fibre length difference. N = 60-62.

### 4.3 RAD51 I287T accumulation at replicating chromatin

To investigate the source of the stochastic replisome stalling and global replication fork slowing in RAD51 IT/IT MEFs, I performed subcellular fractionation to analyse chromatin-bound fraction of critical HR factors in RAD51 +/+ and RAD51 IT/IT MEFs under non-damaging conditions (Figure 4.3A). The analysis revealed that in asynchronous Wt cell populations, a low level of RAD51 is present on chromatin, however, in both isolated clones of RAD51 IT/IT MEFs, I observed a significant enrichment of RAD51 on chromatin. This is accompanied by a corresponding decrease in RPA70, as expected, given recombination mediators help RAD51 to displace RPA and RAD51 I287T is representative of a mediator bypassing RAD51 mutant. The overall levels of RAD51 I287T trapped on chromatin seems relatively low, compared to the cytoplasmic fraction of RAD51. I reasoned that this might be the case in bulk asynchronous population of cells, while the population of replicating cells may accumulate much high levels of chromatin bound RAD51 I287T. To examine RAD51 binding specifically at active replication forks, I performed iPOND analysis in RAD51 +/+ and RAD51 IT/IT MEFs (Figure 4.3B). Strikingly, the levels of RAD51 bound to replicating chromatin were strongly increased in RAD51 IT/IT MEFs, when compared to RAD51 +/+ MEFs. This is not simply a by-product of replication stress, due to increased dormant origin firing (and in turn higher number of active replication forks) as levels of fork-bound PCNA are similar between RAD51 IT/IT and RAD51 +/+ MEFs. Finally, to further validate these results, indirect immunofluorescence was performed to visualize spontaneous accumulation of RAD51 foci (Figure 4.3C). Consistent with previous results, I observed an increase in spontaneous RAD51 focus formation in RAD51 IT/IT compared to RAD51 +/+ MEFs in both clones (Figure 4.3D). Collectively, these observations suggest that in RAD51 IT/IT MEFs, RAD51 extensively accumulates on chromatin at sites of active replication, which may cause the replisome to stall or inhibit restart, resulting in replication fork slowing and asymmetry.

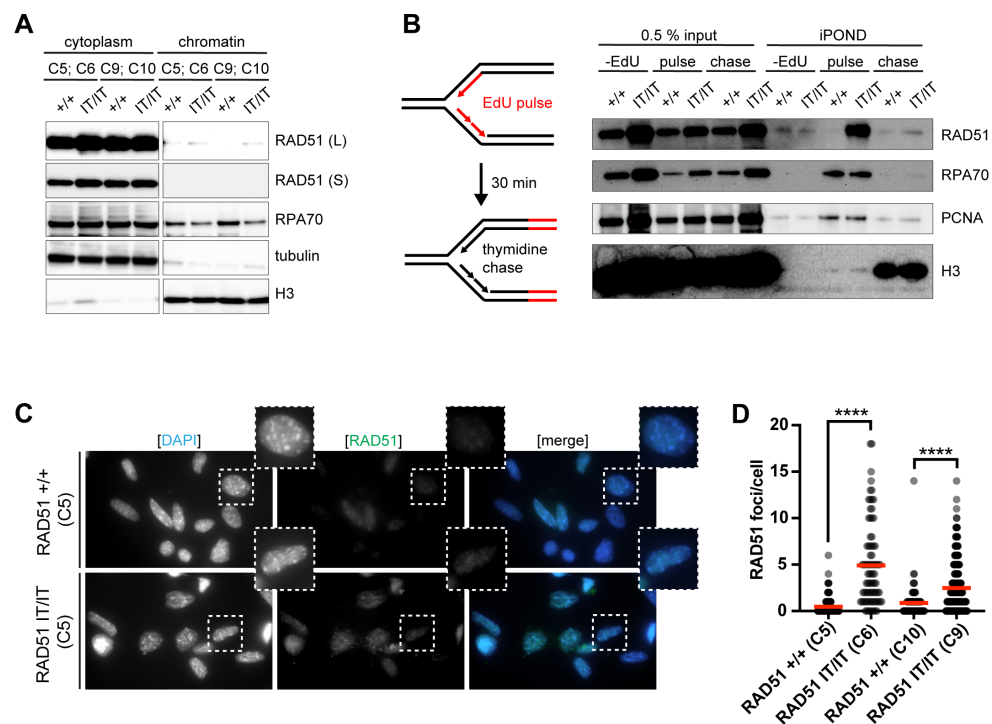


**Figure 4.3: RAD51 I287T accumulates on replicating chromatin. (A)** Immunoblot of cytoplasmic versus chromatin extract in RAD51 +/+ and RAD51 IT/IT MEFs probed for RAD51 and RPA70.  $\alpha$ -tubulin was used as a loading control for cytoplasmic fraction. Histone H3 was used as a loading control for chromatin fraction (data are representative of 2 independent technical and 2 independent biological replicates). L indicates long exposure. S indicates short exposure. **(B)** RAD51 +/+ (C5) and RAD51 IT/IT (C6) MEFs were labelled with EdU for 10 min and subjected (or not) to 30 min chase in media containing thymidine before being processed for iPOND. Captured proteins were analysed by SDS-PAGE and probed by indicated antibodies. **(C)** Representative images of RAD51 +/+ (C5) and RAD51 IT/IT (C6) MEFs stained with anti-RAD51 antibody and DAPI. **(D)** Quantification of RAD51 focus formation under non-damaging conditions in RAD51 +/+ and RAD51 IT/IT MEFs. Between 83 and 283 cells were quantified for each condition. Mann-Whitney test.

#### 4.4 RAD51 I287T and sensitivity to fork-blocking lesions

Given the RAD51 IT/IT phenotype outlined above, I reasoned that increased replication stress levels in RAD51 IT/IT MEFs may also lead to increased sensitivity to certain forms of DNA damage. To explore this, I treated RAD51 +/+ and RAD51 IT/IT MEFs with the indicated doses of DNA damaging agent for a period of 5 days and then assessed the surviving fraction of cells (Figure 4.4A, B). I observed profound sensitivity to PARP inhibitor/trapping agent, olaparib in RAD51 IT/IT MEFs (IC<sub>50</sub> of  $1.8 \pm 0.2 \mu\text{M}$  for C5 (wt) and  $1.7 \pm 0.2 \mu\text{M}$  for C6 (IT/IT)), together with sensitivity to replication-fork progression blocking agents, such as cisplatin (causing ICLs; IC<sub>50</sub> of  $0.64 \pm 0.01 \mu\text{M}$  for C5 (wt) and  $0.42 \pm 0.02 \mu\text{M}$  for C6 (IT/IT)), MMS (causing bulky alkylating lesions; IC<sub>50</sub> of  $0.078 \pm 0.003 \%$  for C5 (wt) and  $0.045 \pm 0.003 \%$  for C6 (IT/IT)) and pyridostatin (PDS, stabilizing secondary DNA structures – mainly G-quadruplexes, G4s; IC<sub>50</sub> of  $15.9 \pm 0.8 \mu\text{M}$  for C5 (wt) and  $7.6 \pm 0.7 \mu\text{M}$  for C6 (IT/IT)). Interestingly, no sensitivity was observed with regards to treatment with replication poisons, such as hydroxyurea (HU, which depletes dNTP pool; IC<sub>50</sub> of  $52.8 \pm 2.0 \mu\text{M}$  for C5 (wt) and  $52.8 \pm 1.7 \mu\text{M}$  for C6 (IT/IT)) and aphidicolin (APH, which inhibits main replicative DNA polymerases; IC<sub>50</sub> of  $0.15 \pm 0.2 \mu\text{M}$  for C5 (wt) and  $0.20 \pm 0.2 \mu\text{M}$  for C6 (IT/IT)). Finally, no sensitivity to lesions causing non-replication associated DSBs, such as bleomycin (IR mimicking agent; IC<sub>50</sub> of  $0.23 \pm 0.02 \text{ mM}$  for C5 (wt) and  $2.42 \pm 0.27 \text{ mM}$  for C6 (IT/IT)) and etoposide (TOPII poison; IC<sub>50</sub> of  $64.9 \pm 1.1 \text{ nM}$  for C5 (wt) and  $88.9 \pm 6.3 \text{ nM}$  for C6 (IT/IT)) was observed for RAD51 IT/IT cells. On the contrary, RAD51 IT/IT cells were found to be consistently resistant to bleomycin treatment (see IC<sub>50</sub> values above). From these experiments, I conclude that RAD51 IT/IT MEFs are selectively sensitive to genotoxins causing blockages that are toxic upon encountering moving replication fork. These data are in line with the observed replication stress phenotype observed in the IT mutant mice and are reminiscent of data presented in Section 3.6 for nematode RFS-1 null and Walker A mutants, where negligible sensitivity to HU, but strong sensitivity to replication fork blocking treatments such as CDDP, NH<sub>2</sub> or CPT is observed. This is also consistent with previous reports (Taylor et al., 2015; Ward et al., 2007) where only mild effect of *rfs-1* deletion on nematode survival and RAD51 foci formation in response to IR, but strong effects survival and RAD51 focus formation in response

to CDDP, HN2 and CTP. This is particularly interesting, as RAD51 I287T is expected to be a mediator 'bypass' mutant, rather than an hypomorph and indicates that perhaps both RAD51 paralog loss and 'bypass' ultimately manifest into similar cellular phenotypes. Importantly, the sensitivity profile of RAD51 IT/IT MEFs is reminiscent of models of FA, where strong sensitivity to CDDP and MMS, but not HU, or IR is observed (Adelman et al., 2013).

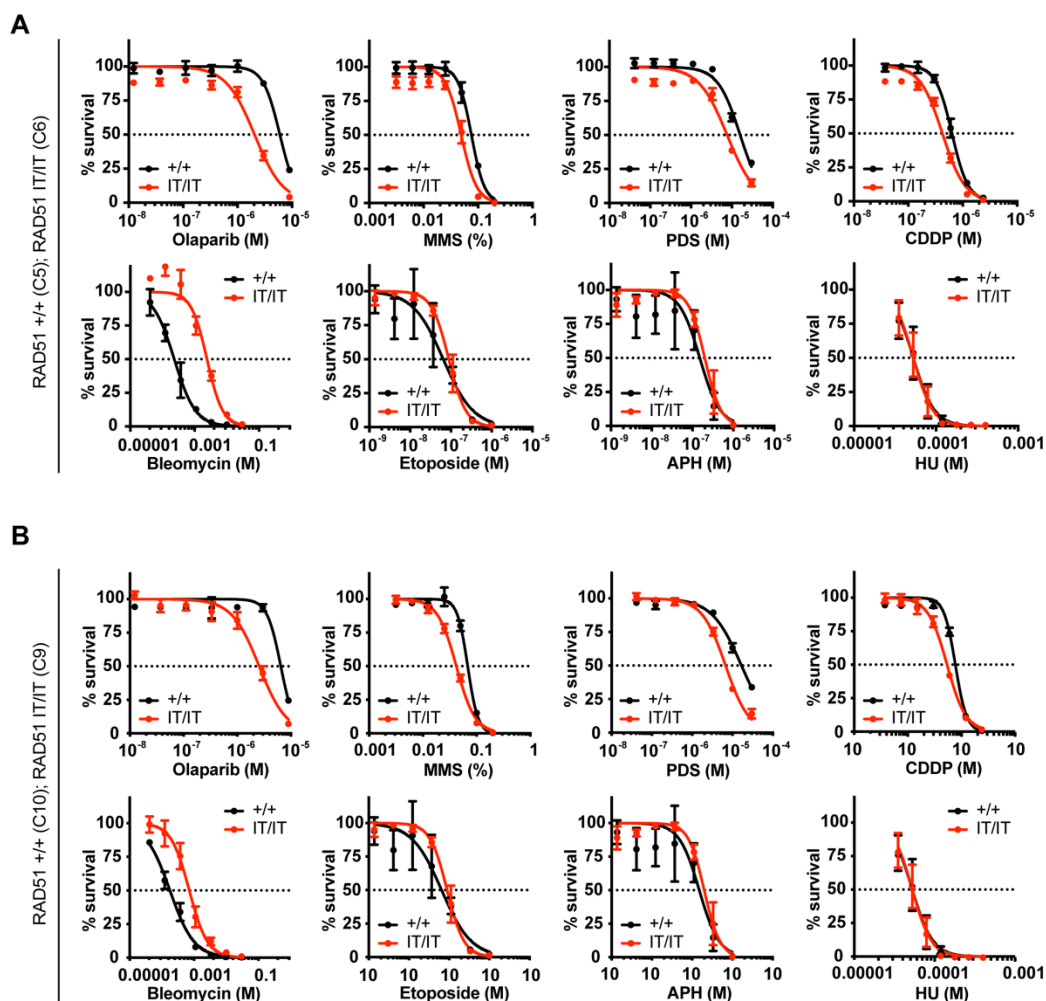


**Figure 4.4: Genotoxin sensitivity of RAD51 IT/IT MEFs. (A)** Cellular survival in RAD51 +/- (C5) and RAD51 IT/IT (C6) MEFs after 5 days of indicated drug treatment. Data are mean  $\pm$  SEM normalized to untreated cells ( $n = 3-4$ ). Lines represent sigmoid fit to calculate IC50 values. **(B)** Cellular survival in RAD51 +/- (C10) and RAD51 IT/IT (C9) MEFs after 5 days of indicated drug treatment. Data are mean  $\pm$  SEM normalized to untreated cells ( $n = 3-4$ ). Lines represent sigmoid fit to calculate IC50 values.

Olaparib, CDDP, MMS, PDS and CDDP may also cause DSB formation due to fork breakage. To more confidently rule out that the observed sensitivity to the aforementioned agents might be simply a result of impaired efficiency of overall DSB repair by HR, I monitored RAD51 foci formation kinetics following DSB formation induced by IR. RAD51 foci are a good marker for recombination, as in BRCA2 or RAD51 paralog deficient cells RAD51 foci formation in response to IR is severely attenuated (Garcin et al., 2019; Martin et al., 2005; Ward et al., 2007; Yuan et al., 1999). Similarly, when HR is stalled downstream of RAD51 filament assembly (due to defective strand exchange or D-loop processing), RAD51 foci accumulate and fail to resolve even 24 hours after DNA damage induction (Adelman et al., 2013; Ward et al., 2010). To assess this, I irradiated RAD51 +/+ and RAD51 IT/IT MEFs and monitored RAD51 foci formation by indirect immunofluorescence 1, 2, 4, 8 and 24 hours post-irradiation (Figure 4.5A). Overall, RAD51 +/+ and RAD51 IT/IT MEFs display similar kinetics of RAD51 foci formation and resolution, indicating no strong defect in DSB repair. To further assess recombination efficiency, I used plasmid based pre-digested substrates containing two copies of incomplete nanoluciferase gene, one with a I-SceI induced cut, the other one intact, serving as a substrate for HR-mediated reconstitution of functional nanoluciferase gene (Figure 4.5B). The assay is based on previously described eGFP HR reporter system (Seluanov et al., 2010). Luminescence signal detection can be then used as a readout for HR efficiency. I transfected both clones of RAD51 IT/IT MEFs and compared their HR efficiencies to corresponding RAD51 +/+ MEF parent. No significant difference in HR efficiency was observed. This indicates that even though RAD51 I287T has better strand exchange yields *in vitro*, this does not cause hyperrecombination phenotype *in vivo*. This can be explained by extensive loading of RAD51 I287T at replication forks, but not conventional DSBs. Similar findings were previously observed for yeast Rad51 I345T, where only a subtle increase in gene-conversion frequencies, monitored by physical recombination assays, was observed (Fortin and Symington, 2002).

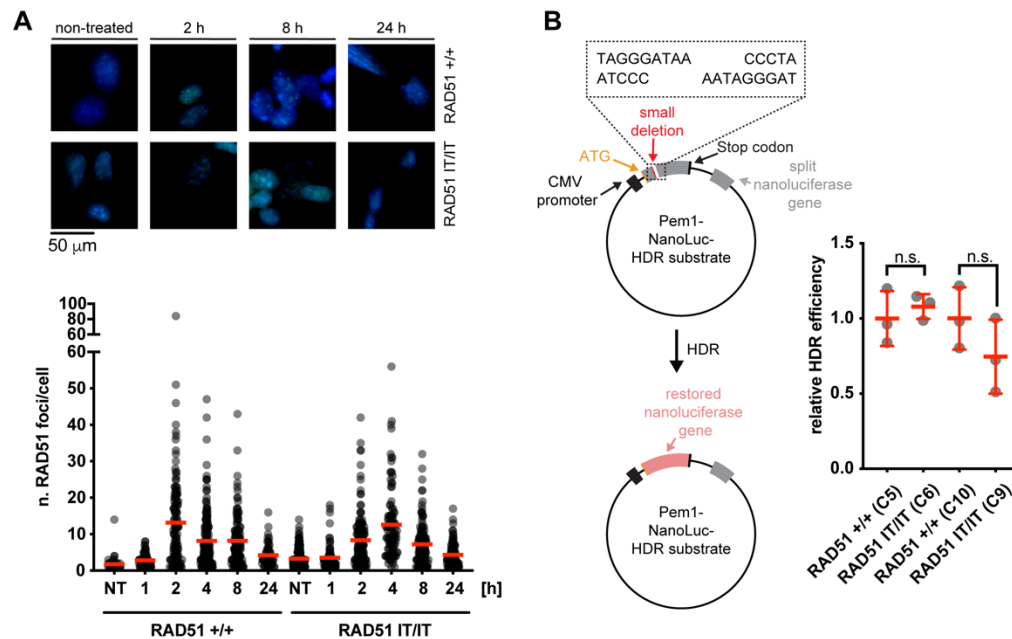


**Figure 4.5: RAD51 IT/IT MEFs displays HDR efficiency similar to that of RAD51 +/+ MEFs.**

**(A)** Representative images of RAD51 +/+ (C10) and RAD51 IT/IT (C9) MEFs stained with anti-RAD51 antibody and DAPI. Quantification of RAD51 focus formation under non-damaging conditions and in indicated timepoints after exposure to 1 Gy of IR in RAD51 +/+ (C10) and RAD51 IT/IT (C9) MEFs. Between 41 and 211 cells were quantified for each condition. **(B)** A schematic of I-SceI digested extrachromosomal plasmid used for HDR efficiency assessment. HDR of the plasmid by gene conversion results in restoration of nanoluciferase gene and can be monitored by detecting luminescent signal in 96 well plate format. Quantification of HDR efficiencies in RAD51 +/+ and RAD51 IT/IT MEFs. Mann-Whitney test.

Taken together, these results indicate that RAD51 I287T does not cause hyper-recombination *in vivo*, nor does it strongly impair DSB repair by HR via formation of persistent, dead-end filaments and/or strand invasion products, as it was reported previously for RAD51 K133R (Stark et al., 2002). Yet, interference with replication fork progression results in heightened replication stress and reduced cellular survival of RAD51 IT/IT MEFs.



## 4.5 RAD51 I287T and fork slowing after DNA damage

To test whether there is a link between sensitivity to replication-blocking genotoxins, RAD51 I287T accumulation at replication chromatin and overall replication stress phenotype of RAD51 IT/IT MEFs and mice, I performed chromatin fractionation experiments after exposure of RAD51 IT/IT MEFs (C6) to 10  $\mu$ M olaparib for 24 hours (Figure 4.6A). Upon olaparib treatment, a slight enrichment of PARP1 on chromatin due to trapping was observed together with increased RPA levels and ub- $\gamma$ H2AX species appearance, which indicates that drug treatment was successful and caused DNA damage (Hewitt et al., 2020; Luczak and Zhitkovich, 2018). Interestingly, treatment with olaparib resulted in even greater RAD51 accumulation on chromatin in RAD51 IT/IT MEFs when compared to non-treated cells. To investigate whether these results correlate with a change in replication dynamics, I performed the SMARD assay using a modified protocol where cells were grown and treated 24h prior to the experiment with either 10  $\mu$ M olaparib or 5  $\mu$ M cisplatin (Figure 4.6B, C). Under conditions where cells were grown without exogenous DNA damage, RAD51 +/+ MEFs replicated their DNA with physiological rates (geometric mean of  $0.97 \pm 0.01$  kb/min; C5). RAD51 IT/IT MEFs displayed slower replisome progression rate (geometric mean of  $0.84 \pm 0.02$  kb/min; C6). Upon 24 h treatment with 10  $\mu$ M olaparib, replisome rate very slightly increased in RAD51 +/+ MEFs (geometric mean of  $1.07 \pm 0.03$  kb/min; C5). This is reminiscent of increased fork rates in human cells treated with olaparib reported previously (Maya-Mendoza et al., 2018). However, in RAD51 IT/IT MEFs, the same olaparib treatment resulted in further fork slowing (geometric mean of  $0.79 \pm 0.01$  kb/min; C6). The treatment with 10  $\mu$ M cisplatin resulted in strong fork slowing in RAD51 +/+ MEFs ( $0.63 \pm 0.01$  kb/min; C5), which was further exacerbated in RAD51 IT/IT MEFs ( $0.51 \pm 0.01$  kb/min; C6). I also observed a similar phenomenon of increased fork slowing in RAD51 IT/IT MEFs with two different replication-blocking agents (Figure 4.6D). I also investigated fork asymmetry after these treatments (Figure 4.6E), but did not observe exacerbation in fork asymmetry in RAD51 IT/IT MEFs after treatment with either olaparib or cisplatin when compared to RAD51 +/+ MEFs (Figure 4.6F). Compared to overall fork speed, perhaps fork asymmetry measurement result in effect size underestimation when probability of fork stalling is high enough to cause both forks to stall.

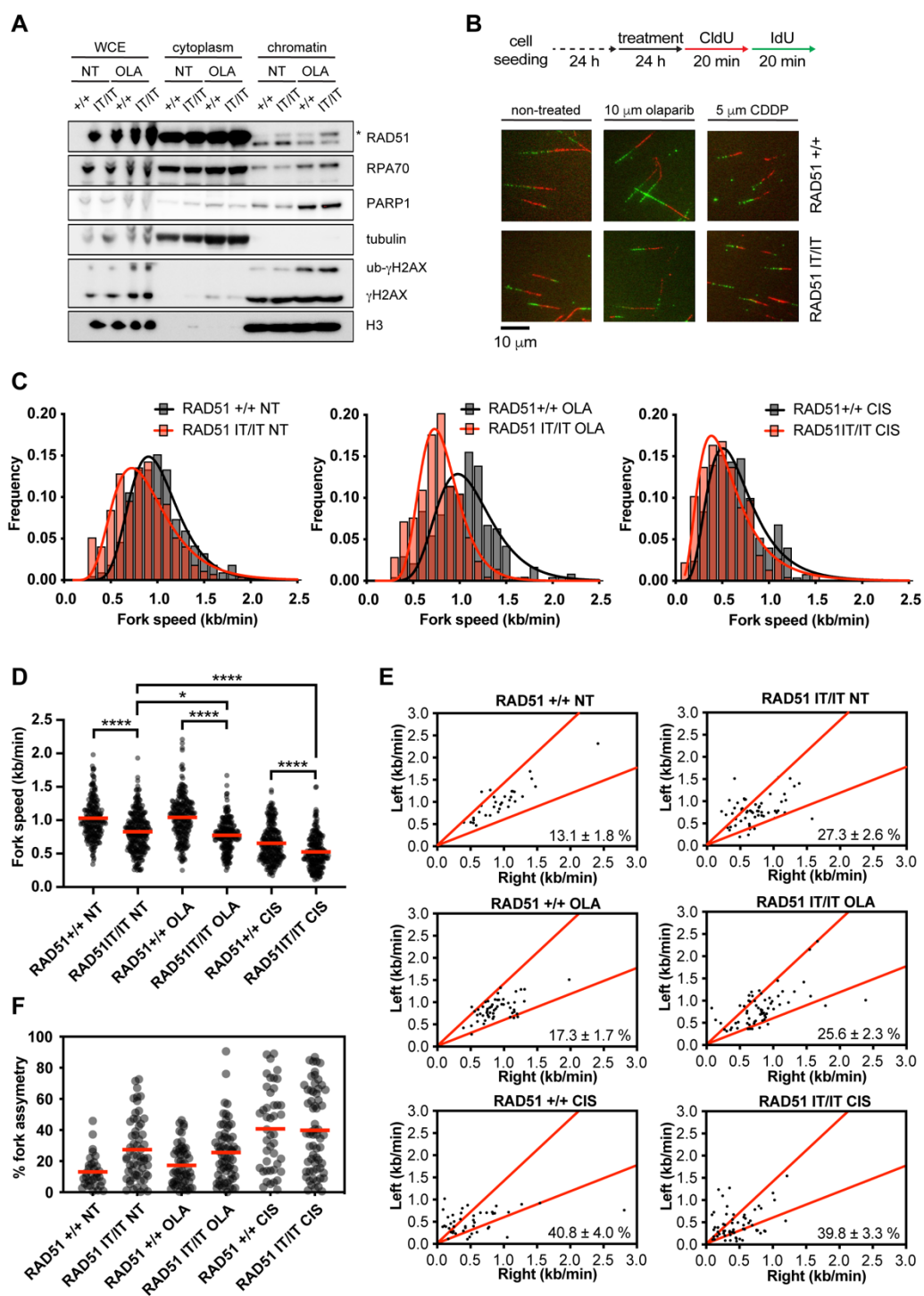


**Figure 4.6: Further analysis of DNA damage sensitivity in RAD51 IT/IT MEFs. (A)** Immunoblot of whole cell extract (WCE), cytoplasmic and chromatin extract in RAD51 +/+ (C5) and RAD51 IT/IT (C6) MEFs untreated or treated with 10  $\mu$ M olaparib (OLA) for 24 h probed for RAD51, PARP1,  $\gamma$ H2AX and RPA70.  $\alpha$ -tubulin was used as a loading control for cytoplasmic fraction. Histone H3 was used as a loading control for chromatin fraction. **(B)** Replicating cells

were untreated or treated with 10  $\mu$ M olaparib (OLA) or 10  $\mu$ M cisplatin (CIS) for 24 h following a day after seeding, pulse-labelled for 20 min with IdU and for 20 min with CldU. Representative images of spread DNA fibres in RAD51 +/+ (C5) and RAD51 IT/IT (C6) MEFs are shown. **(D)** Histogram of replication fork speed in RAD51 +/+ (C5) and RAD51 IT/IT (C6) MEFs following treatment with 10  $\mu$ M olaparib (OLA) or 10  $\mu$ M cisplatin (CIS) for 24 h. N = 209-272 fiber tract/condition. Lines represent lognormal fit. **(D)** Summary of fork rate data with indicated means (red line) for individual conditions. Mann-Whitney test. **(E)** Analysis of fork symmetry in RAD51 +/+ (C5) and RAD51 IT/IT (C6) MEFs following treatment with 10  $\mu$ M olaparib (OLA) or 10  $\mu$ M cisplatin (CIS) for 24 h reported as left/right moving fork ratio. N = 33-64. **(F)** Summary of fork asymmetry in RAD51 +/+ and RAD51 IT/IT MEFs reported as percentage of fibre length difference. N = 33-64.

In summary, I have successfully engineered human RAD51 (I287T) variant that recapitulates biochemical characteristics of yeast Rad51 paralog bypass variant (I345T). I validated that this variant assembles faster on ssDNA, and disassembles slower than wt RAD51, and has intact ATPase activity, making it a functional enzyme *in vivo*. RAD51 IT/IT homozygous knock-in mice are viable and exhibit features of exacerbated replication stress with some features reminiscent of FA deficient mice. Further investigation revealed that this is due to global replication fork slowing caused by stochastic replisome stalling or defective restart, likely caused by promiscuous RAD51 I287T loading on replicating chromatin. The underlying replication defect renders RAD51 IT/IT cells sensitive to replication fork blocking agents and constitutes FA-like features in these cells and partially in mice. These findings highlight the need for a 'Goldilocks regulation' of RAD51 assembly on DNA *in vivo*, where optimal RAD51 assembly kinetics is sufficient to accurately repair DSBs, while preventing spontaneous assembly of RAD51 at ssDNA segments generated during genome duplication, which leads to fork slowing and replication stress. An alternative explanation to unscheduled spontaneous RAD51 assembly causing stochastic fork slowing is a fork restart/remodelling defect due to reduction of intrinsic filament disassembly rates of RAD51 IT mutant. This would cause the blocked forks to remain stalled and would present with elevated levels of RAD51 IT. Which of these two alternatives better describes the replication dynamics deregulation in RAD51 IT/IT MEFs remains to be determined.

## Chapter 5. Results 3: The influence of mismatch tolerance during meiotic DNA pairing

### 5.1 *C. elegans* RAD-51 tolerates mismatches

Most eukaryotes possess two main recombinases: Rad51, which is ubiquitously expressed, and Dmc1, which is meiosis specific. The evolutionary origin of the two-recombinase system remains poorly understood. Interestingly, Dmc1 is capable of stabilizing a mismatch within three-nucleotides during heteroduplex DNA formation, whereas Rad51 cannot (Lee et al., 2015). It has been suggested that the intrinsic ability of Dmc1 to tolerate mismatches during DNA strand exchange is a critical feature enabling interhomolog recombination during meiosis, thus explaining the evolutionary need for two-recombinase system. Yet the evidence for this *in vivo* is lacking.

To address the evolutionary origin of two-recombinase system, I and Dr. Justin Steinfeld (Columbia University, Dr. Eric Greene group) have inspected the sequence of RecA-like ATPase core of the two main recombinases from various organisms including bacteria, yeast, human, *Drosophila* and nematode in order to find residues responsible for mismatch tolerance of Dmc1. Furthermore, we presumed that amino acids responsible for this effect should fulfil three criteria outlined below:

- I) The residues should be conserved within the Dmc1 recombinase family.
- II) They should not be present in the Rad51 recombinase family.
- III) They would be found within one of the two known DNA-binding motifs, DNA-binding loop 1 (L1) or DNA-binding loop 2 (L2), which are conserved in all recombinases (Chen et al., 2008; Story et al., 1993).

Given these criteria, we examined L1 and L2 sequences of Rad51-like and Dmc1-like proteins from various species and concluded that for *Saccharomyces cerevisiae* Rad51 (ScRad51), these lineage-specific residues correspond to L1 amino acids T288, A298, and H302. The *Saccharomyces cerevisiae* Dmc1 (ScDmc1) lineage-specific residues include L1 amino acids V224, E234 and K238 (Figure 5.1A).

Interestingly, some organisms, such as *Caenorhabditis sp.*, have lost the Dmc1 gene, even though the reasons for this loss remain unclear (Brown and Bishop, 2014). Surprisingly, sequence inspection of RAD-51 protein from *Caenorhabditis sp.* revealed that the lineage-specific amino acids present in L1 loop - N246, E256 and K260, do not correspond to “canonical” Rad51 (we use the term “canonical” to identify Rad51-like proteins from species that contain both recombinases) but instead more closely resemble Dmc1 (Figure 5.1A). To validate our bioinformatic analysis, purified *C. elegans* RAD-51 (CeRAD-51) was assembled into filament on ssDNA curtains by Dr. Justin Steinfeld and single-molecule DNA strand exchange reaction using dsDNA fragments with varying length of homology were conducted (Figure 5.1B). Like yeast and human recombinases, CeRAD-51 performs DNA strand exchange resulting in heteroduplex DNA formation. The lifetime of the heteroduplex scales in 3-nt increments (Figure 5.1C) consistent with a base triple stepping mechanism (Lee et al., 2015; Qi et al., 2015). Free energy change ( $\Delta\Delta G^\ddagger$ ) used to quantitatively describe stability of individual 3-nt stepping states was calculated as described previously (Lee et al., 2015; Qi et al., 2015):

$$\Delta\Delta G^\ddagger = \Delta G_2^\ddagger - \Delta G_1^\ddagger = k_b T \ln \frac{k_d^1}{k_d^2} \quad (13)$$

where  $k_b$  is the Boltzmann constant,

T is absolute temperature,

$\Delta\Delta G^\ddagger$  is the free energy difference between two escape processes described by the dissociation rates  $k_d^1$  and  $k_d^2$ . Dissociation rates are measured experimentally from captured dsDNA lifetimes.

When a single nucleotide mismatch is introduced into the middle repeat of a substrate containing three triplets, CeRAD-51 and ScDmc1 are capable of ‘overstepping’ it. This results in captured dsDNA fragment lifetimes comparable to lifetimes of fully homologous dsDNA fragment. However, this is not the case for ScRad51, which fails to overstep and tolerate the mismatch (Figure 5.1D, E). If the mismatch is present in terminal triplet of a two-triplet dsDNA substrate, none of the

recombinases (ScRad51, ScDmc1 or CeRad51) are capable of increasing stability of the formed heteroduplex (Figure 5.1D, F).

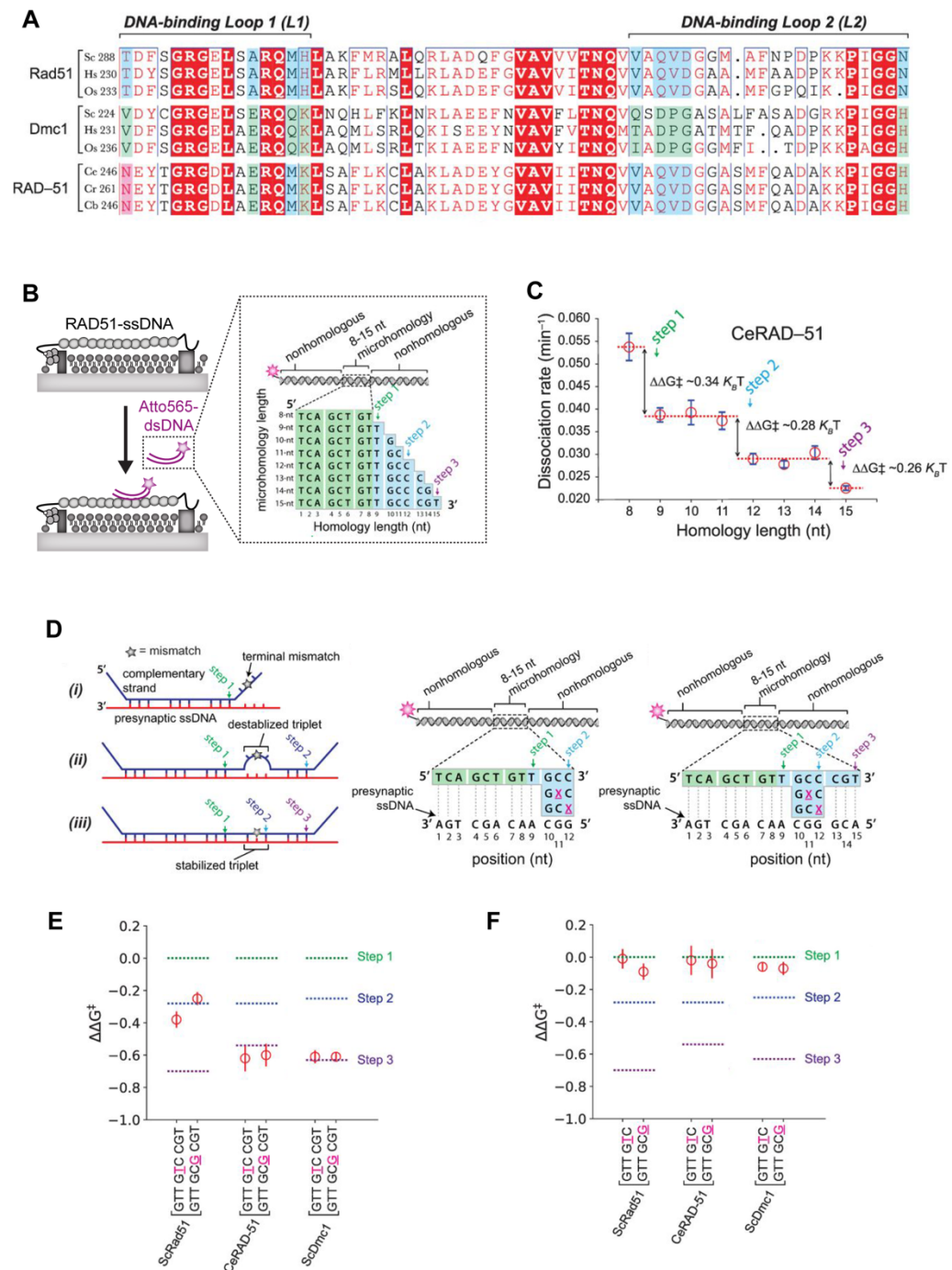


**Figure 5.1: Nematode RAD-51 tolerates mismatches during DNA strand exchange. (A)** Comparison of *Caenorhabditis* sp. RAD-51 sequences (*C. elegans*, *C. remanei*, and *C. brenneri*) with Rad51 and Dmc1 sequences from organisms with both recombinases (*S. cerevisiae*, *H. sapiens*, and *O. sativa*). Amino acids conserved in all three lineages are highlighted in red, Rad51

lineage-specific amino acids are highlighted in blue, and Dmc1 lineage-specific amino acids are highlighted in green. **(B)** A schematic of single-molecule DNA strand exchange DNA curtains assay. Illustration of dsDNA substrates used for base triplet stepping assays. The 8-nt tract of microhomology highlighted in green is required for efficient binding, and the nucleotides highlighted in blue represent incremental increases in the microhomology length. Color-coded designations here and in all subsequent figure panels indicate the length of homology at which steps 1–3 are detected. **(C)** Dissociation rate data obtained from the single-exponential fitting of lifetimes of captured dsDNA by CeRAD-51. **(D)** Left - schematic illustration of a dsDNA substrate (shown in blue; the noncomplementary strand is omitted for clarity) bound to a presynaptic ssDNA (in red). A single mismatch is indicated with a star (★) and is positioned in either the terminal base triplet (panel i), an internal base triplet that is not stabilized (as with Rad51; panel ii), or an internal triplet that is stabilized (as with Dmc1; panel iii). The binding steps relative to triplet length are highlighted, where step 1 corresponds to the initial binding interaction, whereas steps 2 and 3 reflect the changes in dissociation rates that occur for each 3-nt increase in length. Right - schematic of dsDNA substrates with mismatches positioned within the terminal base triplet. The locations and identities of the mismatches are highlighted as an underlined magenta “X.”. **(E)** Internal mismatch triplet assays for CeRAD-51. Data for ScRad51 and ScDmc1 are shown for comparison. The free energy changes associated with each step (for fully homologous substrates) are indicated with color-coded dashed lines. **(F)** Terminal mismatch triplet assays for CeRAD-51. Data for ScRad51 and ScDmc1 are shown for comparison. The free energy changes associated with each step (for fully homologous substrates) are indicated with color-coded dashed lines.

## 5.2 Engineering mismatch-intolerant RAD-51 mutant

If the hypothesis regarding mismatch stabilization by specific L1 amino acids is correct, then *C. elegans* RAD-51 (CeRAD-51) mutant in which the “Dmc1-like” amino acids were changed to the “Rad51-like” residues might lose the ability to overstep DNA mismatches. To test for this, I made a CeRAD-51 N246S, E256A, K260H triple mutant (corresponding to ScRad51 amino acids T288, A298, and H302), which I refer to as CeRAD-51-TM.

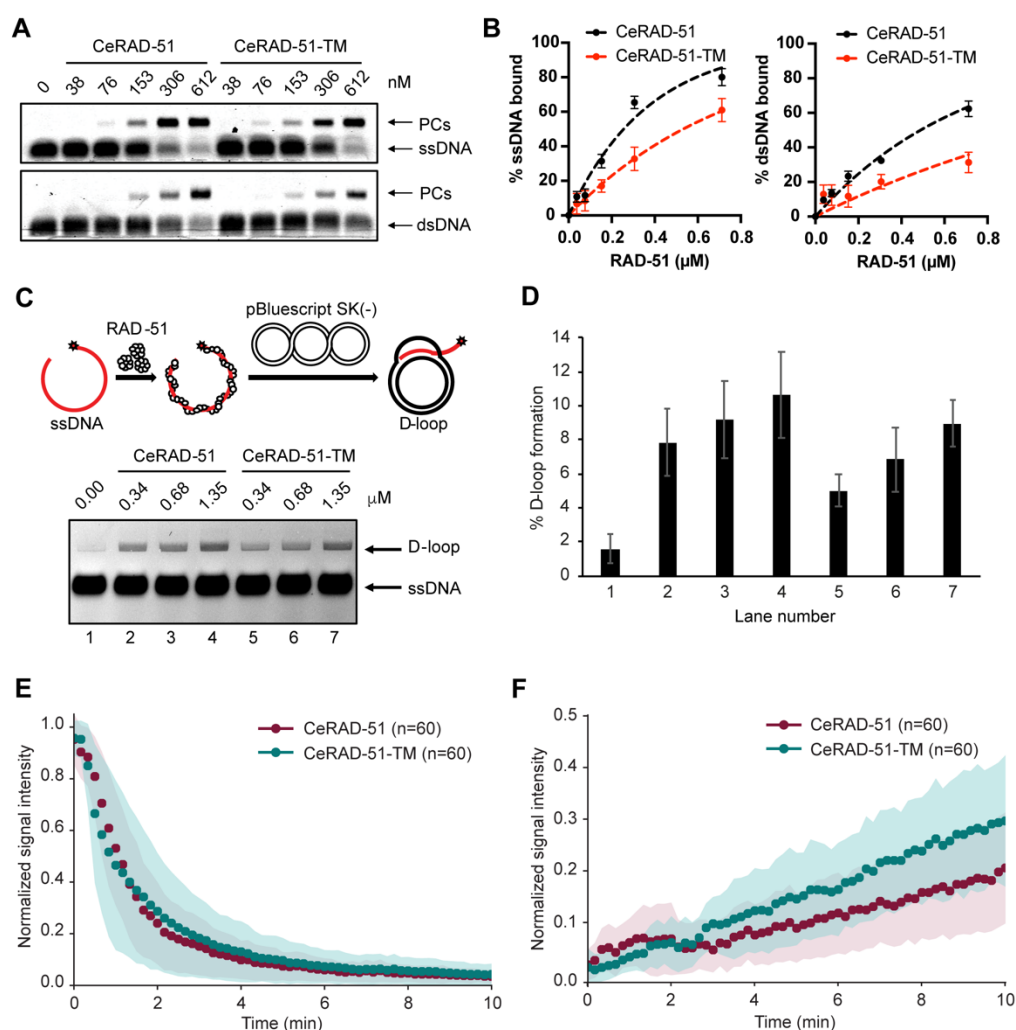


**Figure 5.2: Characterization of RAD-51 triple mutant.** (A) ssDNA and dsDNA binding assays and (B) quantitation for wt CeRAD-51 and CeRAD-51-TM; error bars represent S.D. from three separate measurements. (C) D-loop formation assays and (D) quantitation for wt CeRAD-51 and CeRAD-51-TM; error bars represent S.D. from three separate measurements. (E) Assembly and (F) disassembly kinetics for CeRAD-51 and CeRAD-51-TM filaments obtained from ssDNA



curtain assays; error bars represent S. D. calculated from the indicated number of single ssDNA molecules.

CeRAD-51-TM retain similar, albeit attenuated ssDNA (for CeRAD-51:  $K_d = 0.256 \pm 0.038 \mu\text{M}$ ; for CeRAD-51-TM:  $K_d = 0.532 \pm 0.091 \mu\text{M}$ ) and dsDNA (for CeRAD-51:  $K_d = 0.489 \pm 0.053 \mu\text{M}$ ; for CeRAD-51-TM:  $K_d = 1.113 \pm 0.303 \mu\text{M}$ ) binding activity (Figure 5.2A, B). CeRAD-51 and CeRAD-51-TM also display a similar ability to form strand invasion products in D-loop formation assay (Figure 5.2C, D). CeRAD-51 and CeRAD-51-TM can displace RPA-eGFP in the single-molecule ssDNA curtain assay with similar assembly and disassembly rates, although CeRAD-51-TM binds ~21% less fast (for CeRAD-51: halftime of  $1.24 \pm 0.02 \text{ min}$ ; for CeRAD-51-TM: halftime of  $1.50 \pm 0.04 \text{ min}$ ) (Figure 5.2E) and disassembles ~26% more quickly than CeRAD-51 (for CeRAD-51: halftime of  $30.4 \pm 0.5 \text{ min}$ ; for CeRAD-51-TM: halftime of  $22.5 \pm 0.2 \text{ min}$ ) (Figure 5.2F). To interrogate whether CeRAD-51-TM has lost the ability to stabilize DNA mismatched during strand exchange, I first performed a modified D-loop formation assay, where a fluorescently labelled 90mer ssDNA substrate containing 29 A to T mismatches was used (Figure 5.3A). Strikingly, even though this substrate contained multiple mismatches, CeRAD-51 was capable of limited invasion of the mismatched 90mer into negatively supercoiled pBluescript plasmid. However, this ability was completely abolished in the case of CeRAD-51-TM (Figure 5.3B), confirming a loss of mismatch tolerance in bulk strand exchange assay. To confirm these ensemble findings, Dr. Justin Steinfeld performed single-molecule ssDNA curtain DNA strand exchange assays with Atto565-dsDNA fragments, which confirmed that CeRAD-51 and CeRAD-51-TM, both displayed base triplet stepping (Figure 5.3C, D). Similar to ScRad51 and ScDmc1, both CeRAD-51 and CeRAD-51-TM were unable to stabilize DNA mismatches present at the end of a microhomology region within the short dsDNA substrates (Figure 5.3E). However, in contrast to ScRad51, CeRAD-51 could stabilize mismatches located at an internal position within the microhomology region, while CeRAD-51 TM could not (Figure 5.3F). When combined, these results demonstrate the ability to stabilize mismatched base triplets was abolished for the CeRAD-51-TM. These findings confirm the premise that lineage specific L1 residues in Dmc1 constitute the ability to stabilize mismatched triplets within the context of DNA strand exchange intermediates.

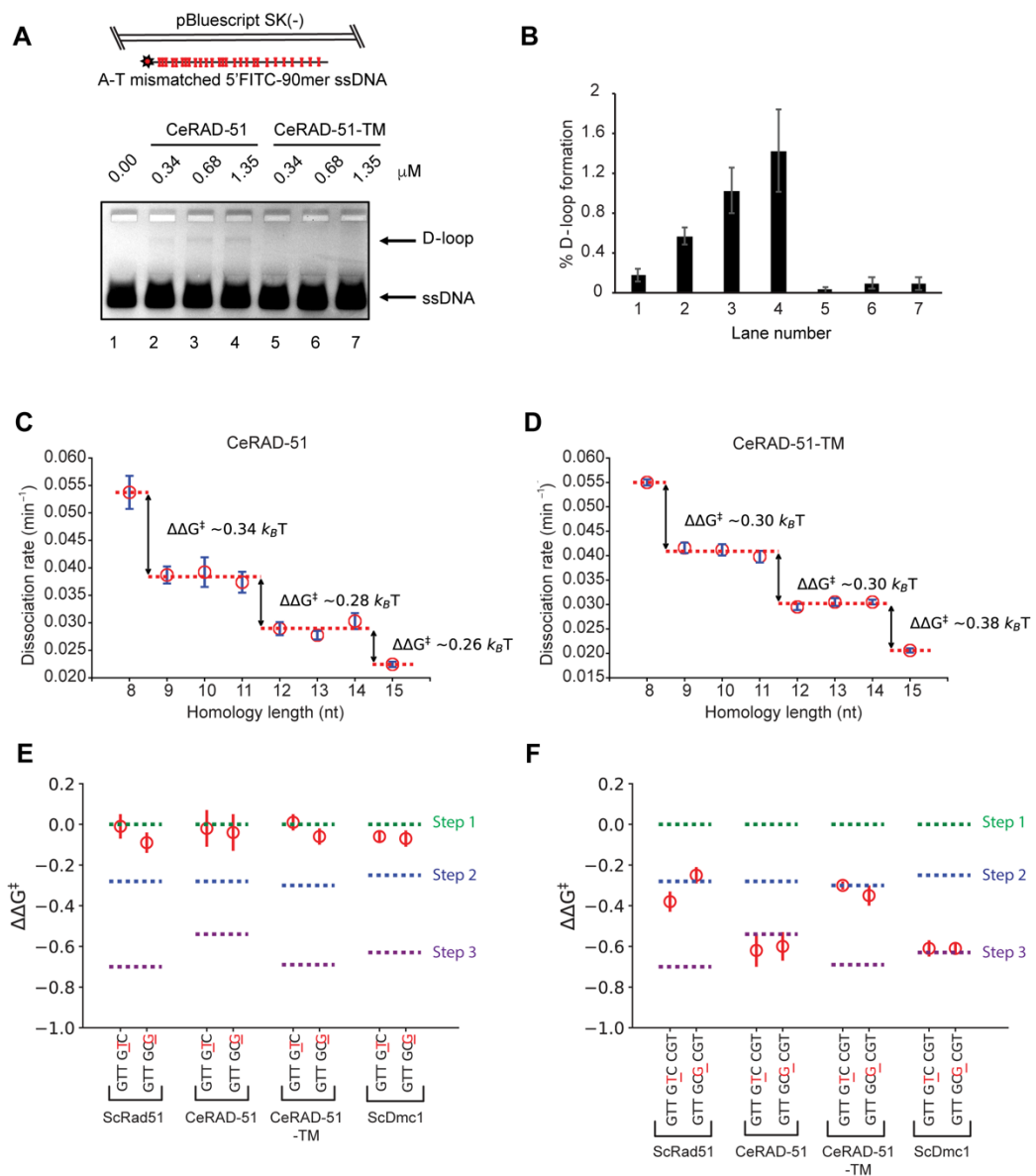


**Figure 5.3: RAD-51 triple mutant fails to tolerate mismatches during strand exchange.** (A) D-loop formation assay and (B) corresponding quantitation for a 90-nt D-loop substrate harbouring 29 mutations, corresponding to 32% sequence divergence with the dsDNA plasmid substrate. Error bars in (B) represent S.D. from three separate measurements. (C-D) Dissociation rate data obtained from the single-exponential fitting of lifetimes of captured dsDNA by CeRAD-51 or CeRAD-51-TM. (E) Terminal mismatch triplet assays for CeRAD-51 and CeRAD-51-TM. Data for ScRad51 and ScDmc1 are shown for comparison. The free energy changes associated with each step (for fully homologous substrates) are indicated with color-coded dashed lines. (F) Internal mismatch triplet assays for CeRAD-51. Data for ScRad51 and ScDmc1 are shown for comparison. The free energy changes associated with each step (for fully homologous substrates) are indicated with color-coded dashed lines.

### 5.3 Mismatch (in)tolerance of CeRAD-51-TM *in vivo*

To investigate the role of the L1 lineage-specific residues *in vivo*, genome editing by CRISPR–Cas9 was performed to insert three mutations (N246S, E256A, and K260H) by Knudra transgenics into the *C. elegans rad-51* gene (Figure 5.4A, B). The *rad-51(knu529)* strain was viable. Scoring the recombination between visible markers *dpy-17* and *unc-36* at a fully homologous genetic interval on chromosome III (Section 2.3.4), did not demonstrate a significant difference in crossover formation frequencies between N2 (wt) and *rad-51(knu529)* strains (Figure 5.4C, D). These data indicate that CeRAD-51-TM is competent in meiotic HR progression *in vivo*. *C. elegans* is a highly inbred organism with low DNA sequence divergence in parental N2 strain, which may provide a partial explanation for the lack of an apparent meiotic phenotype in *rad-51(knu529)* knock-in strain. To circumvent this issue, I utilized the previously described heterozygous *mln-1* inversion system (Leon-Ortiz et al., 2018) on chromosome II (Section 2.3.4). The *mln-1* inversion is flanked by *gfp* and *rol-1* visible markers, while the noninverted chromosome contains the *dpy-25* allele (Figure 5.4C). Very rare meiotic heterologous recombination (het-rec) events between synapsed 8 Mbp *mln-1* inverted sequence can be monitored by scoring recombination between the visible markers. In N2 (wt) and *rad-51(knu529)* strains, het-rec events are extremely rare (Section 2.3.4). Depletion of RTEL-1 or BRC-1 in the N2 strain leads to a strong increase in the het-rec frequency, which is mismatch-dependent (Leon-Ortiz et al., 2018). Given the increase of het-rec well above very rare basal frequencies in RTEL-1 and BRC-1 deficient background, this system can be used to investigate the mismatch tolerance of CeRAD-51 and CeRAD-51-TM *in vivo*. Compared to the N2(Wt) strain, depletion of RTEL-1 or BRC-1 yields a significantly reduced frequency of het-rec events in the *rad-51(knu529)* strain (Figure 5.4D). Given the lack of mismatch tolerance of CeRAD-51-TM *in vitro*, these results suggest that the reduction in het-rec frequency observed in the *rad-51(knu529)* background likely stems from an inability to promote efficient DNA pairing between mismatch-containing sequences in the inverted *mln-1* region.

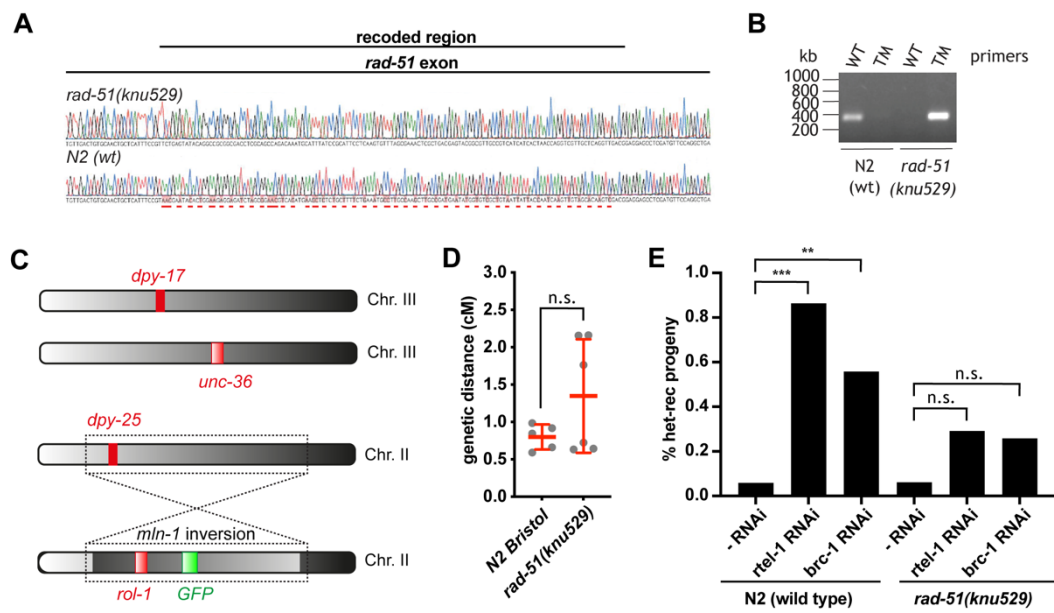


**Figure 5.4: RAD-51 triple mutant is intolerant to heterology in vivo.** (A) CRISPR-generated base-pair substitutions within the L1 domain of *C. elegans* RAD-51. Substituted nucleotides are underlined by a red line. (B) PCR validation of the substitution in *rad-51* gene by using primers provided by Knudra transgenics. (C) A schematic of meiotic recombination assay between visible markers for homologous genetic interval and het-rec assay. (D) Recombination frequency as measured by genetic map distance between pair of marker genes *dpy-17/unc-36* on chromosome III. Error bars represent S.D. (E) Increased recombination between heterologous sequences induced by RTEL-1 or BRC-1 depletion is suppressed in the *rad-51(knu529)* background - indicating loss of tolerance for DNA sequence heterology during CeRAD-51-TM mediated recombination *in vivo*. The “-RNAi” label corresponds to conditions in which the *C. elegans* strain was treated with control bacteria lacking an expression plasmid for RNAi. P-values by  $\chi^2$ .

## 5.4 Genetic interactions of CeRAD-51-TM

Given the *rad-51(knu529)* allele suppresses the *rtel-1* het-rec phenotype, I asked if other *rtel-1*-associated phenotypes could also be suppressed in *rad-51(knu529)* background. Among these are decreased brood size, decreased embryonic survival, and sensitivity to DNA damaging compounds (Barber et al., 2008). Contrary to my expectations, I observed a synthetic sickness in *rtel-1; rad-51(knu529)* double mutant worms, manifested as a further decrease in brood size (Figure 5.5A), increased levels of embryonic lethality (Figure 5.5B), and higher sensitivity to certain DNA damaging agents (Figure 5.5C). RECQL5 helicase was previously shown to suppress recombination by dismantling RAD51 filaments (Hu et al., 2007), while RTEL1 was implicated in disrupting D-loop intermediates formed during HR to alter the outcome of meiotic DSB repair. *C. elegans* RCQ-5 helicase does not seem to suppress additional meiotic crossovers or het-rec events (Barber et al., 2008; Youds et al., 2010). Consistently, no strong genetic interaction was observed for *rad-51(knu529)* in *rcq-5* background (Figure 5.5A, B).

Next, I investigated *rtel-1; rad-51(knu529)* strain for changes in RAD-51 focus formation and resolution in the *C. elegans* germline. Premeiotic S phase at the distal tip of the germline is followed by progressive stages of meiosis I, which are defined by specific features associated with homologous chromosome alignment, pairing, synapsis, and formation of chiasmata. DNA strand exchange intermediates formed during meiosis by RAD-51 are repaired to produce crossovers or non-crossovers and can be visualized by the formation and timely resolution of RAD-51 foci starting in pachytene and disappearing in early diplotene (Figure 5.5D, E). Quantification of RAD-51 foci in each of meiotic germline zones revealed that the timing and levels of RAD-51 accumulation at meiotic DSBs were similar between N2 and *rad-51(knu529)* strain, supporting the conclusion that CeRAD-51-TM is a competent recombinase *in vivo*. However, unlike the N2 and *rad-51(knu529)* nematode strains, RAD-51 foci persisted into late stages of meiosis I in the *rtel-1; rad-51(knu529)* strain (Figure 5.5D, E). The observed phenotype is similar to that reported for *helq-1; rtel1-1* double mutants, which also display smaller brood sizes, low embryonic viability levels, and RAD-51 foci foci (Ward et al., 2010). Prompted by this similarity, I made a *rad-*

*51(knu529); helq-1* double-mutant. Intriguingly, the *helq-1; rad-51(knu529)* strain also showed persistence of RAD-51 foci in late phases of meiotic prophase (Figure 5.5D, E). The *helq-1; rad-51(knu529)* strain also displayed a significant reduction in brood size and increased numbers of unhatched eggs (Figure 5.5A, B).

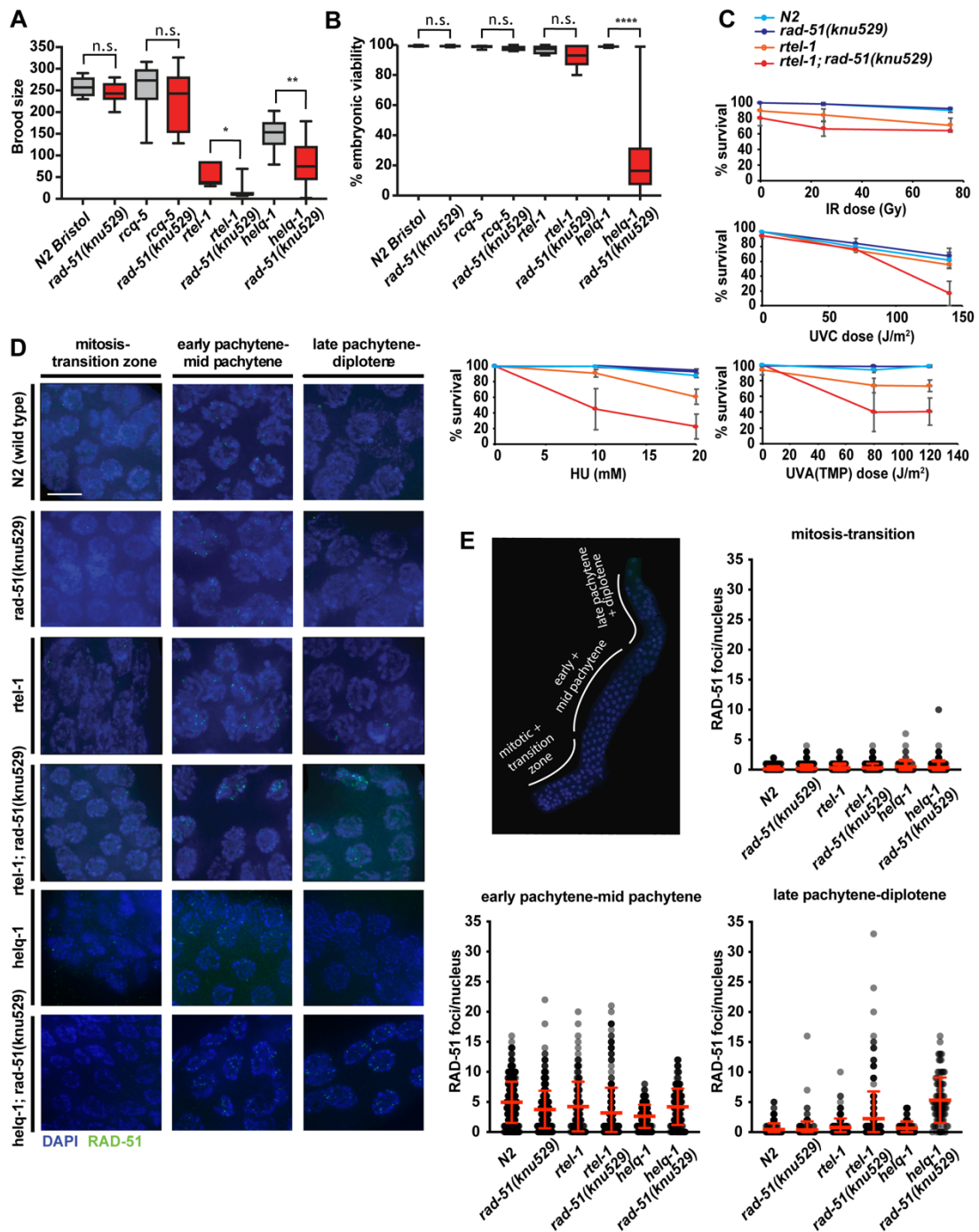


**Figure 5.5: RAD-51 triple mutant causes toxicity in the absence of RTEL-1 or HELQ-1 *in vivo*.** (A) Brood size in strains of the indicated genotype. Progeny of five to 12 worms were evaluated. P-values by Mann-Whitney test. (B) Percentage of hatched eggs after 24 h in strains

of the indicated genotype. Progeny of five to 12 worms were evaluated. P-values by Mann-Whitney test. **(C)** DNA damage sensitivity assays. The indicated strains were treated with increasing doses of genotoxins, *rtel-1*; *rad-51(knu529)* display increased sensitivity to replication-associated lesions caused by HU, TMP-UVA and UVA, but not to IR. **(D)** Representative images of different compartments of the *C. elegans* germline. (Blue) DAPI staining; (green) RAD-51 staining. Scale bar, 5  $\mu$ m. **(E)** *C. elegans* germline with marked zones used to score meiotic RAD-51 focus formation. Quantification of meiotic RAD-51 focus formation in the different zones of the worm germline in strains of the indicated genotype. *helq-1*; *rad-51(knu529)* and *rtel-1*; *rad-51(knu529)* display persistent RAD-51 foci in late stages of meiosis. Between 67 and 548 cells were quantified for each zone in two independent experiments for each genotype. P-values by Mann-Whitney test.

Taken together, our data reveal that CeRAD-51-TM is a functional enzyme proficient in meiotic recombination *in vivo* but is impaired for strand invasion in the context of divergent DNA sequences. Given, RTEL-1 and HELQ-1 act to process postsynaptic recombination intermediates, the synthetic sick interactions of *rad-51(knu529)* with *rtel-1* and *helq-1* points to a dependence on postsynaptic recombination regulators for effective repair meiotic DSBs and promote embryonic survival. This implies the presence of a fraction of toxic recombination intermediates that arise in the *rad-51(knu529)* strain that must be removed by RTEL-1 or HELQ-1 to allow meiotic progression. The nature of these intermediates is not clear. Perhaps destabilized three nucleotides generated by CeRAD-51-TM cause perturbations in DNA heteroduplex structure, which may interfere with downstream processing of a subset of meiotic DSBs, and to avoid stalled meiotic break repair resulting in cell death, RTEL-1 or HELQ-1 are required to disassemble the toxic joint molecules and channel the repair through different recombination sub-pathways. Another explanation is that lower stability of CeRAD-51-TM on ssDNA observed *in vitro* may partially phenocopy RFS-1 loss and result in synthetic sickness, similar to that observed between *helq-1* and *rfs-1* (Ward et al., 2010).

## Chapter 6. Discussion

### 6.1 Mechanism of Rad51 presynaptic filament assembly

In [Chapter 3](#), I proposed that, similarly to RecA, Rad51 filament assembly occurs by a two-step process, which requires the sequential action of BRC-2 and RFS-1/RIP-1. BRC-2 acts primarily at the RAD-51 nucleation step to promote RAD-51 accumulation on RPA-coated ssDNA. Unlike RecA, Rad51 nuclei grow very slowly. However, inclusion of RFS-1/RIP-1 promotes faster growth of RAD-51 filaments in a 3'→5' direction. RFS-1/RIP-1 engages in a highly dynamic manner with the 5' ends of RAD-51 filaments. RFS-1/RIP-1 dissociation is regulated by its intrinsic ATPase activity and is critical to allow filament growth. Hence, RFS-1/RIP-1 functions as a classical 'chaperone', mediating the formation of functional RAD-51 filaments *in vitro* and *in vivo* ([Figure 6.1](#)).

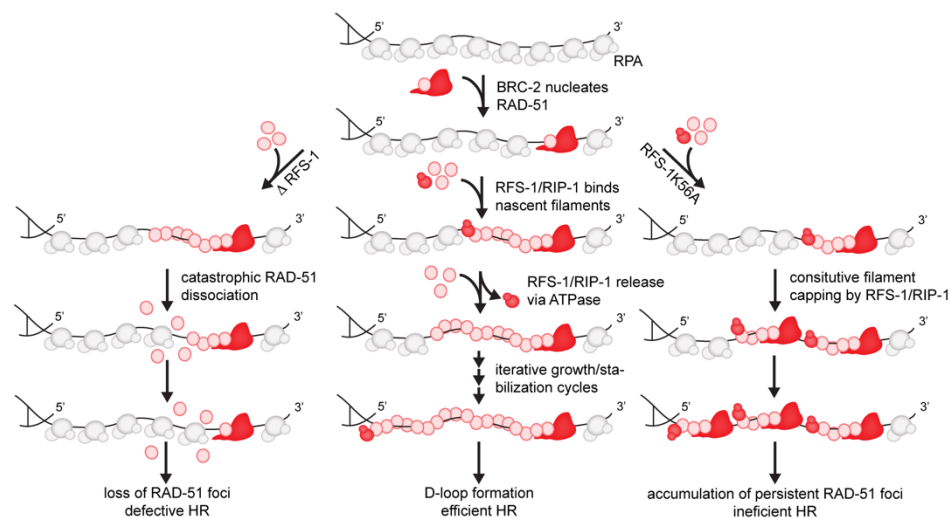


**Figure 6.1: Model of metazoan RAD-51 presynaptic filament assembly.** BRC-2 nucleates RAD-51 on RPA-coated ssDNA. Nascent RAD-51 filaments are bound at 5' filament end by RFS-1/RIP-1. RFS-1/RIP-1 stabilizes growing RAD-51 filaments by preventing disassembly bursts from filament ends. Dissociation of RFS-1/RIP-1 mediated by ATP hydrolysis allows for further recruitment of RAD-51 protomers promoting filament growth in 5' direction. Inability of RFS-1 K56A/RIP-1 to dissociate from RAD-51 filaments results in prolonged end-capping and formation of stable, but shorter less active filaments.



**Division of labour between mediator proteins.** My single-molecule data reveal the contribution of recombination mediators to RAD51 nucleation and growth. The division of labour between BRC-2 and Rad51 paralogs likely comes from their intrinsic biochemical properties: BRC-2 possesses high affinity for ssDNA and RAD-51 in solution (Martin et al., 2005; Petalcorin et al., 2006); while RFS-1/RIP-1 binds ssDNA very poorly and does not interact with RAD-51 in solution (Taylor et al., 2015). Therefore, RFS-1/RIP-1 is most likely acting on RAD-51 filaments, which is in line with studies performed in cells showing Rad51 paralogs act downstream of BRCA2 (Chun et al., 2013; Jensen et al., 2013). Consistently, recruitment of yeast (Lisby et al., 2004) and vertebrate (Raschle et al., 2015) Rad51 paralogs (Rad55-Rad57) to DNA damage sites is dependent on Rad51, while nematode BRC-2 foci accumulate independently of RAD-51 (Martin et al., 2005) in response to DSBs. In line with *in vivo* data, *in vitro* studies have shown that addition of full-length hBRCA2 increases the overall amount of RAD51 filaments, but not their mean length in negative stain EM (Shahid et al., 2014). On the other hand, yeast Rad51 paralogs, Rad55-Rad57, were shown to increase the length of Rad51 filaments when added together with Rad51 in negative stain EM (Liu et al., 2011). Taken together, my findings, consistent with previous data, support the notion that BRCA2 acts first to promote Rad51 nucleation, followed by Rad51 paralogs acting on nascent Rad51 filaments to promote their growth. The division of labour between BRC-2 and RAD-51 paralogs, however, is not absolute, as BRC-2 can also stimulate RAD-51 filament growth, albeit to a lower extent than RFS-1/RIP-1. It remains to be assessed whether different BRCA2 binding partners factors (e.g. PALB2 or DSS1) may influence to its ability to further stimulate filament growth. Given both PALB2 and DSS1 enhance BRCA2's mediator activity in bulk DNA strand exchange assays (Buisson et al., 2010; Zhao et al., 2015), this seems like a plausible hypothesis. In my system, Rad51 paralogs also modestly increase RAD-51 nucleation rates. This is likely due to stabilization of smaller RAD-51 clusters on DNA, rather than through direct loading.

**Directionality of RAD-51 filament growth.** RecA was previously shown to grow into filaments bi-directionally with a two-fold faster rate in the 5'→3' direction than 3'→5' direction (Bell et al., 2012). Using asymmetrically positioned ssDNA gaps within long dsDNA substrates, I have shown that, unlike RecA, nematode RAD-51 filaments grow in both directions, albeit very slowly. Addition of RFS-1/RIP-1

stimulated filament growth rates in a 3'→5' direction - opposite to that of RecA. This is consistent with previous bulk assays showing that the polarity of DNA strand exchange catalysed by Rad51 is opposite to that of RecA (Baumann and West, 1997; Cox and Lehman, 1981; Sung and Robberson, 1995). Furthermore, as it has been previously proposed (Shahid et al., 2014), the structural architecture of Rad51 (where a smaller N-terminal domain is connected to C-terminal RecA-like core), which is inverted to that of RecA (where a smaller C-terminal domain is connected to N-terminal RecA core) may play a role in this evolutionary growth polarity switch. Given that the crystal structure of a single human BRC repair fused to RAD51 monomer human shown that BRC recognizes the 3' monomer interface (Pellegrini et al., 2002) and full-length hBRCA2 was present at the 3' filament ends in negative stain EM (Shahid et al., 2014), a hypothesis can be proposed: RAD-51 nucleation starts with the 3' end of the nucleus bound and stabilized by BRC repeat of BRC-2; this leaves the free 5'-end to engage with and be stabilized by RFS-1/RIP-1, promoting nascent RAD-51 filaments extension in a 3'→5' direction. Engagement of opposing filament ends by recombination mediators may allow for highly efficient cooperation during filament assembly and may explain the synergistic interaction between BRC-2 and RFS-1/RIP-1 observed in the RPA-eGFP displacement assay.

**Rad51 paralogs act as Rad51 filament “chaperones”.** A previous study postulated Rad51 paralogs stabilize Rad51 filaments via stable intercalation (Liu et al., 2011). Single molecule imaging presented in [Chapter 3](#) demonstrated that RFS-1/RIP-1 does not intercalate into the RAD-51 filaments, but rather engages with their 5' ends in a dynamic fashion. This is in line with predictions from bulk fluorescence experiments performed previously (Taylor et al., 2016). Regulating RAD-51 filaments at their ends can also explain the binding stimulation at sub-stoichiometric RFS-1/RIP-1 concentrations (Taylor et al., 2015). Disassembly from Rad51 filament ends takes place by catastrophic dissociation bursts with multiple Rad51 monomers disengaging at once (van Mameren et al., 2009), while filaments grow slowly by rate-limiting addition of Rad51 monomers (Bell et al., 2012; Joo et al., 2006). Suppressing these dissociation bursts, as observed in my 'dipping' experiments, could make for an effective mechanism to promote net filament growth or stabilize small metastable RAD-51 nuclei. Fast RFS-1/RIP-1 turnover is dependent on its intrinsic ATPase activity. RFS-1/RIP-1 Walker A mutants stabilize RAD-51 on ssDNA, but fail to

disengage from filament ends, which hinders further filament growth. These results suggest that nematode RAD-51 paralogs act as filament 'chaperones': RFS-1/RIP-1 recognizes nascent 5' RAD-51 filament ends, binds them preventing dissociation bursts, and later disengages to allow for further Rad51 addition. Iterative cycles of this process enable efficient filament growth. The process is similar to how classical molecular chaperones suppress proteotoxic stress by polypeptide binding, folding, and release cycles. The model is consistent with genetic analysis of *rfs-1* null and Walker A box K56A/R nematode strains, with deletion of *rfs-1* conferring strong DNA damage sensitivity with the loss of RAD-51 foci. *rfs-1* Walker A box K56A/R strains are also found to be sensitive to DNA damage, but RAD-51 foci accumulate extensively in these strains. This is indicative of formation of stable, but HR-incompetent RAD-51 complexes. Collectively, my work contrasts the previous model that suggested Rad51 paralogs intercalate into and/or stably associate with Rad51 filaments (Liu et al., 2011). The intercalation model also suggests Rad51 paralogs may act as roadblocks for the anti-recombinase Srs2 helicase and directly prevent filament disruption by motor proteins, which would not be possible when considering our end-binding model. A study complementary to my work was recently published (Roy et al., 2021) and directly showed that fluorescently labelled yeast Rad55-Rad57 also exhibits highly dynamic engagement with Rad51-ssDNA. Importantly, inhibition of ATP hydrolysis traps Rad55-Rad57 on Rad51-ssDNA complexes. Direct imaging of labelled Srs2 performed by Roy et al, demonstrated eviction of individual Rad55-Rad57 by bypassing Srs2 molecules without any reduction in translocation velocity – further arguing against the roadblock model. Rad55-Rad57 promoted Rad51 assembly behind moving Srs2 molecules when free Rad51 was present in solution. In support of these observations, in Chinese hamster ovary cells, different Rad51 paralogs were shown to turnover rapidly from the stressed replication forks, whereas Rad51 halftimes at damaged forks are significantly longer (Somyajit et al., 2015). In the same study, Walker A box mutants of different hamster Rad51 paralogs decreased their turnover. Interestingly, dissociation following human RAD51 nucleation was also proposed for full-length human BRCA2 *in vitro* (Shahid et al., 2014). In conclusion, the observations presented here, together with data from other published work, imply that Rad51 filament assembly is catalysed by a conserved mechanism involving Rad51 'chaperones'.

**Possible mechanisms of mammalian mitotic and meiotic presynaptic filament assembly.** The nematode system employed in this work is easily amenable to biochemical characterization, however, several key players present in mammalian cells are not found in *C. elegans*. Among these are the meiotic recombinase Dmc1 (Bishop et al., 1992), BRCA2 binding partner PALB2 (Xia et al., 2006), more Rad51 paralog complexes, such as CX3 and BCDX2 (Masson et al., 2001) or meiotic recombination mediator proteins (Swi5-Sfr1) (Haruta et al., 2006). In light of my findings presented in [Chapter 3](#), I will discuss the possibilities of how mammalian presynaptic filament mechanism assembly can be catalysed by recombination mediators. First, the best studied recombination mediator, BRCA2, binds 4-6 RAD51 monomers in solution (Jensen et al., 2010), implying it may nucleate RAD51 as a tetra-hexamer. Given BRCA2 was shown to multimerize (Shahid et al., 2014; Thorslund et al., 2010), RAD51 species nucleated on DNA could also be larger. However, recent *in vitro* and *in vivo* work indicates that a large fraction of BRCA2 can exist also in monomeric state (Le et al., 2020; Mateos-Gomez et al., 2015). Which species is the most efficient for RAD51 nucleation and how BRCA2 binding partners influence BRCA2 oligomeric state or RAD51 nucleus size are not known. Whether BRCA2 remains stably bound to RAD51 nucleus or dissociates once nucleation has occurred is not clear yet, although evidence from visualizing RAD51 assembly reactions by negative stain EM suggested most BRCA2 dissociated from RAD51 filaments after ~10 min (Shahid et al., 2014), an idea supported by very low minimal amounts of BRCA2 (1:100 in respect to RAD51 monomers) required to promote RAD51-ssDNA complex formation *in vitro* (Thorslund et al., 2010). Following RAD51 recruitment and nucleation by BRCA2, filament stabilization/growth must inevitably take place. An interesting question is why there are (at least) two RAD51 paralog complexes present in mammalian cells, when nematode and yeast require a single complex to perform this action. With respect to my work, it is tempting to speculate that two Rad51 paralog complexes have evolved to stabilize the two filament ends ([Figure 6.2](#)). If this is the case, only two out of five paralogs would contact the Rad51 filament directly and hydrolyse ATP, while the others might serve a similar role to nematode RIP-1 or yeast Rad57, which are not required for ATPase activity, but play rather a structural role in Rad51 paralog heterodimer stability. In theory, two paralogs present in the heterodimer should be sufficient for active and stable complex formation. This is easily applicable to CX3,

but not BCDX2, which contains 4 different paralogs. Why are there 4 different paralogs present in BCDX2? One possibility is better anchoring to ssDNA and RAD51 when engaging with nascent filaments. Alternatively, BCDX2 might perform other roles distinct from RAD51 filament assembly. Indeed, BCDX2 also interacts with mammalian HELQ (Adelman et al., 2013) and perhaps different components are engaged in different steps in HR. Yet, recent work has revealed that RAD51B is not required for cellular survival, nor it is absolutely required for RAD51 focus formation and efficient HDR (Garcin et al., 2019). This raises the possibility that only DX2 and CX3 dimers, but not BC dimer are strictly required for efficient RAD51 filament assembly in mammalian cells. Hence, what is the cellular role of RAD51B? Furthermore, if the two paralog complexes: CX3 and (BC)DX2, stabilize opposing filament ends, which complex engages with 5' filament end and which with 3' filament end? And which paralog is the one in contact with RAD51? Only future biochemical and structural investigation of Rad51 paralog complexes can shine light on these questions.

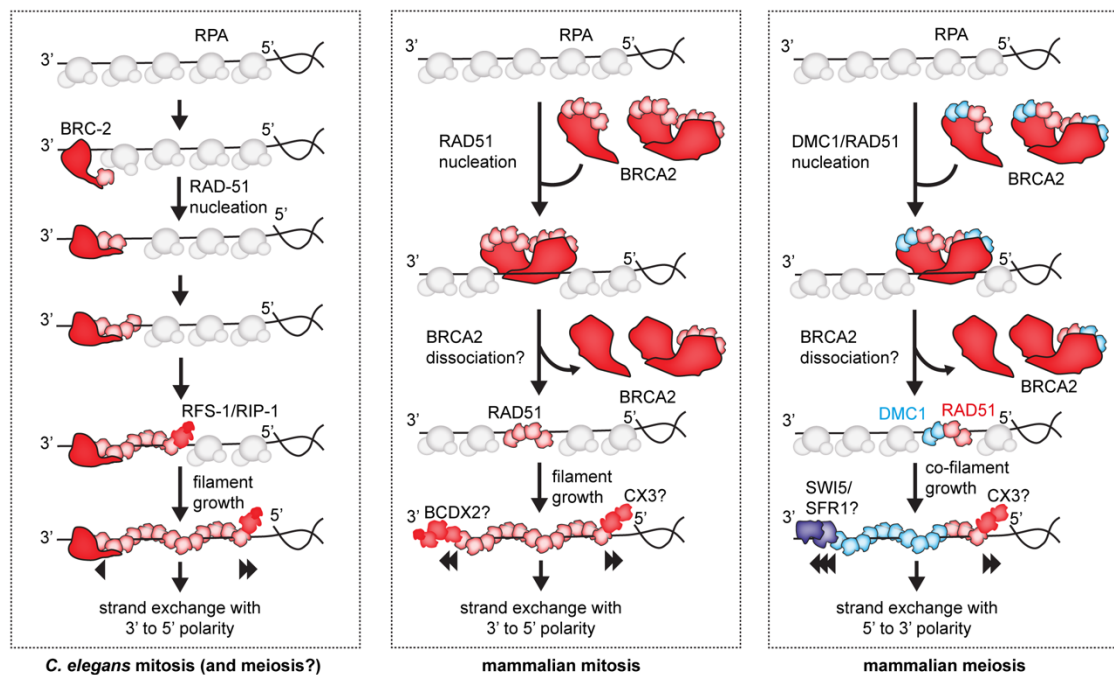


**Figure 6.2: Proposed models for recombinase presynaptic filament assembly in nematode and mammalian cells.** See text for details.

The situation is even more complex during meiosis (Figure 6.2), where the meiotic recombinase, Dmc1 and Dmc1-specific mediator complex Swi5-Sfr1 play a critical

role. Genetic studies have shown that Rad51 is required for Dmc1 focus formation (Bishop et al., 1992) but does not play a catalytic role in meiotic recombination itself, rather serving as an accessory factor for Dmc1-mediated DNA strand exchange (Cloud et al., 2012). *In vitro* studies with purified Dmc1 and purified BRCA2 fragments have demonstrated that DMC1 binds at a unique site downstream of BRC repeats (Thorslund et al., 2007) but is also capable of interacting with several of the 8 BRC repeats themselves (Martinez et al., 2016). Given BRCA2 is required for both RAD51 and DMC1 assembly on ssDNA during meiosis, it seems plausible that BRCA2 nucleates both RAD51 and DMC1, possibly a mixed RAD51-DMC1 nucleus. High-resolution ChIP-seq (Hinch et al., 2020) and super-resolution microscopy imaging (Brown et al., 2015) in cells concluded that RAD51 and DMC1 form co-filaments with well separated Dmc1 and Rad51 segments, rather than mixed co-filaments. RAD51 segment is shorter and present at 5' end, while DMC1 segment is longer and extending towards the 3' end of the presynaptic co-filament (Hinch et al., 2020). In a minimal *in vitro* system consisting only of Rad51, Dmc1 and RPA, segmented co-filaments do not form, instead mixed filament formation is observed (Crickard et al., 2018). This discrepancy between *in vivo* analysis and *in vitro* reconstitution can be explained by lack of factors orchestrating physiological assembly and/or lack of high enough resolution to spatially separate very short co-filament segments in single-molecule systems *in vitro*. Given my bi-directional growth stimulation hypothesis, it can be envisioned that either:

- I) DMC1 grows intrinsically faster, extending rapidly towards 3' end, making DMC1 segment longer, or
- II) the action of meiotic mediator complex, Swi5-Str1 helps DMC1 segment to grow fast towards 3' direction, while in the case of RAD51, only 5' filament end is available for extension from mixed nucleus, which may make it grow overall more slowly than during mitosis and make up the short 5' segment of the co-filament.
- III) Alternatively, RAD51 growth from the 5' end is actively inhibited by permanent capping in meiosis, which allows only for extension of mixed nucleus by addition of DMC1 monomers at 3' end of the co-filament.

Interestingly, in *Arabidopsis thaliana* where impact of essential protein deletion on meiosis can be studied, it was shown that AtCX3, but not AtBCDX2 is required for meiotic HR to take place, while both paralog complexes are important for mitotic HR (Bleuyard et al., 2005). If this phenotype holds up in mammalian systems, it would support the 2<sup>nd</sup> hypothesis outlined above. Dmc1 also promotes strand exchange with a polarity of 5'→3' with respect to ssDNA on which the nucleoprotein filament had formed (Murayama et al., 2011), which is the same as RecA strand exchange polarity (Cox and Lehman, 1981) and opposite to that of Rad51 (Baumann and West, 1997; Sung and Robberson, 1995). Given exchange polarity correlates with nucleofilament polarity for both RecA (Bell et al., 2012) and Rad51 (this work), it can be assumed that Dmc1 would grow preferentially in a 5'→3' direction. This biochemical observation is in line with the discussion in [Section 6.3](#) where I speculate about the possibility that evolution of meiotic mismatch tolerant/'low-fidelity' Dmc1-like protein from bacterial RecA-like ancestor may have predated mitotic 'high fidelity' Rad51-like recombinase. In conclusion, my work and the work of others suggests that growth regulation at 5' and 3' ends of both mitotic and meiotic presynaptic filaments might serve as an elegant control to ensure efficient strand exchange and HDR in mammalian cells.

## 6.2 DNA metabolism and optimal Rad51 filament assembly

**The Goldilocks principle of optimal RAD51 filament assembly.** Homologous recombination repairs DSBs in various different scenarios, in addition to canonical IR-induced double sided DSBs. Different forms of DNA damage, which require HR for the repair (such as ICLs, broken forks or post-replicative gaps) display differential requirements for individual mediator proteins and by proxy different rate of RAD51 filament assembly (Ward et al., 2007). This phenomenon is likely related to the levels of RPA-coated ssDNA substrate generated in the process. RAD51 filaments are more likely to form on longer ssDNA stretches than shorter ones, given constant nucleation and growth rate. Furthermore, stability of RAD51 filament assembled on short oligonucleotides increases dramatically with oligonucleotide length (Carreira et al., 2009). Thus, both higher assembly rates and stronger stabilization of RAD51 are required when shorter ssDNA is available. During classical DSB repair, resection length varies between 1 to 3 knt (Symington, 2016), while resection track lengths at broken replication forks is <500 nt (Jakobsen et al., 2019). The length of ssDNA gaps formed at and behind the replisome upon replication perturbation by low dose of genotoxins (such as HU), that does not cause significant levels of DNA breakage, is ~100 nt (Zellweger et al., 2015). Finally, during unperturbed DNA replication, occasional 30 – 40 nt long ssDNA gaps, at and behind the replication fork, can be observed (Hashimoto et al., 2010; Zellweger et al., 2015). Therefore, an optimal RAD51 assembly rate must be maintained within the nucleus – a rate fast enough to allow assembly on canonical DSBs and broken/perturbed RFs, but slow enough to prevent spontaneous assembly at ssDNA regions generated during unperturbed DNA replication. I refer to this phenomenon as “Goldilocks principle” of RAD51 assembly (Figure 6.3). A robust body of the literature already demonstrated that slight impairment of RAD51 loading or stability can be sufficient for HDR at canonical DSBs as monitored by physical recombination assay, such as those described in Section 2.4.7. For instance, a point mutation in C-terminus of BRCA2, S3291A, seems functional for canonical DSB repair, but causes global replication stress following HU exposure due to MRE11-dependent degradation of stalled RFs (Schlacher et al., 2011). Similarly, FA-associated dominant-negative RAD51 T131P variant, poisons RAD51 filaments by making them less stable. This results in reduced



ability to repair DNA ICLs, and replication stress following ICL-inducing agent exposure. However, analogous to BRCA2 S3291A, canonical HDR seems functional in RAD51 T131P-expressing cells (Wang et al., 2015). In nematode, BRC-2 is required for repair of IR-induced DSBs, meiotic DSBs, blocked replication forks (RFs) and ICLs. RAD-51 paralogs are, however, largely dispensable for IR-induced DSB repair and meiotic DSB repair, but necessary for the repair of perturbed replication forks and DNA ICLs (Ward et al., 2007). DSBs are extremely toxic lesions with a single DSB being capable of causing cell death (Chapman et al., 2012). This raises the possibility that mediator protein mutations, which slow RAD51 assembly rate just enough to perturb DNA replication but keep canonical DSB repair intact are those contributing to early cancer development, allowing cancer to accumulate mutations without significantly compromising cancer cell viability.

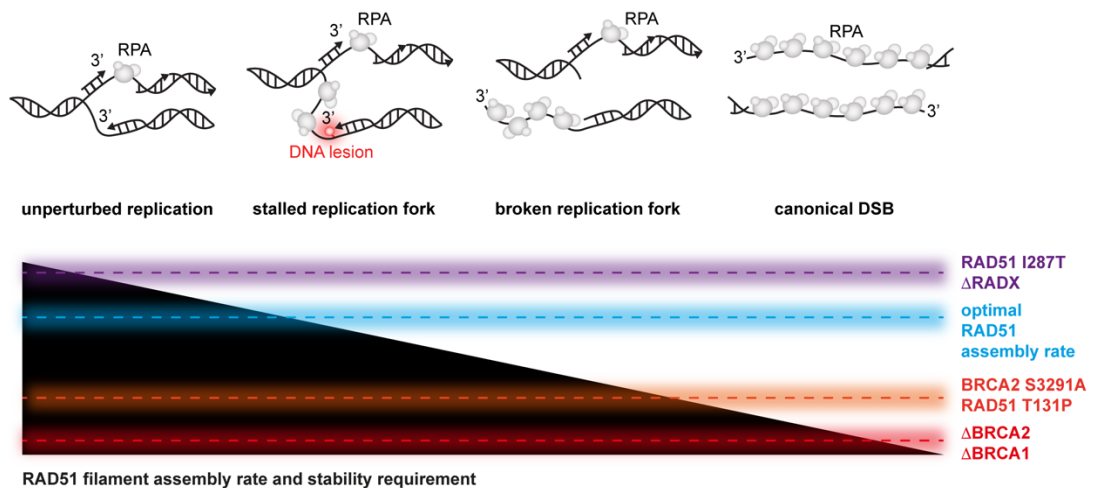


**Figure 6.3: The Goldilocks principle of optimal RAD51 assembly rates.** See text for details.

I outlined above several mechanisms that slow down RAD51 assembly rate in cells to perturb DNA replication, but not canonical DSB repair. However, little is known about mechanisms that shift the balance the other way around and increase RAD51 assembly rates. In [Chapter 4](#), I utilized a combination of *in vitro* and cellular approaches to engineer and characterize a RAD51 variant, RAD51 I287T, which assembles on RPA-coated ssDNA with rates faster than wt RAD51. Surprisingly, mouse expressing RAD51 I287T variant suffer from developmental abnormalities caused by replication stress and display a subset of FA-like features, such as sensitivity to ICLs and smaller eyes (Adelman et al., 2013; Collis et al., 2006; Parmar

et al., 2009; Smogorzewska et al., 2007; Wang et al., 2015). Yet, even though RAD51 IT/IT MEFs show hallmarks of replication stress and are sensitive to replication fork blocking agents (cisplatin, MMS and PDS), there is no evidence for impairment of canonical DSB repair in these cells. This phenotype is reminiscent of BRCA2 S3291A, RAD51 T131P and even RFS-1 K56A/R mutants (Section 3.6). Therefore, paradoxically, more stable mediator bypassing RAD51 variant causes similar phenotype in cells as mutations destabilizing RAD51 filaments. This can be explained by the importance of Rad51 is protection damage forks, but also by the need to remodel the fork and disassemble Rad51 to allow forks to restart. Hence, tipping the balance of RAD51 assembly rates towards binding to short ssDNA stretches generated during replication under unperturbed conditions, results in hampered fork progression or restart. The basal replication stress is then exacerbated when exogenous fork-blocking agents are applied resulting in defects in cellular proliferation.

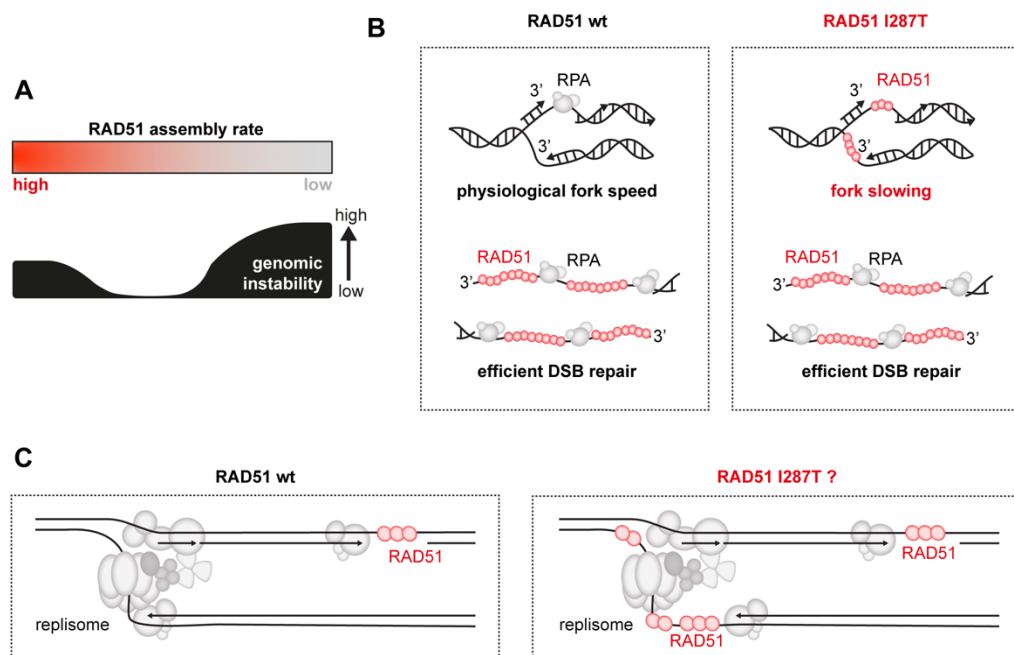


**Figure 6.4: Mechanisms of genome instability in RAD51 IT/IT MEFs. (A)** A disbalance in RAD51 assembly rate on either side can cause genome instability. **(B)** Model of genome instability mechanism in RAD51 IT/IT MEFs. **(C)** A possible explanation of fork slowing in RAD51 I287T expressing cells. In wt cells, small amount of RAD51 binds predominantly at post-replicative gaps, in RAD51 IT/IT MEFs, RAD51 I287T at ssDNA generated in the proximity of replisome interfering with fork progression.

**RAD51 levels at replication forks regulate fork speed.** Anti-recombinase motor proteins are capable of disrupting RAD51 filaments and preventing unscheduled recombination. In mammalian cells, the best described anti-recombinase is RECQL5. Deletion of RECQL5 results in increased RAD51 focus formation following IR, increased sister chromatid exchange and increased levels of HDR measured in physical recombination assays (Hu et al., 2007). This is not the case however, for RAD51 I287T mutation, which does not lead to increased RAD51 foci following IR treatment, nor increased levels of HDR (Section 4.4). More interestingly, deletion of recently identified replication fork binding factors, RADX, was shown to increase spontaneous RAD51 foci at replicating cells, slow down fork speed specifically under non-damaging conditions, cause fork asymmetry and rescues DNA damage sensitivity caused by BRCA2 or RAD51 depletion (Dungrawala et al., 2017). This is likely due to the ability of RADX to destabilize RAD51 filaments (Adolph et al., 2021). RADX depletion phenotype is very reminiscent of RAD51 IT/IT MEFs and consistent with replication stress caused by excessive RAD51 binding to ongoing replication forks. The opposite phenomenon can also be previously observed as depletion of RAD51 or RAD51 paralogs leading to increased fork speed following exposure to DNA damage (Berti et al., 2020; Zellweger et al., 2015). Overall, my observations together with previously published findings establish that RAD51 levels at replicating chromatin are tightly linked to fork speed. Finally, it seems tempting to speculate where exactly at the fork does RAD51 I287T binds. Recent work using SIM imaging suggested that under non-perturbed conditions, RAD51 mostly binds to post-replicative gaps, behind the replisome (Somyajit et al., 2021). This notion is supported by observed defects in post-replicative ssDNA gaps sealing following BRCA2 depletion as well as defects in lagging strand processing in HDR-deficient models (Cong et al., 2021). It is tempting to speculate that perhaps RAD51 I287T assembles primarily at the replication fork itself, rather than at the gaps behind it, forming a direct obstacle to leading DNA polymerase. This possibility should be addressed in future work.

**Fork reversal as a possible mechanism behind fork slowing in RAD51 IT/IT MEFs.** Replication fork backtracking and formation of four-strand chicken foot structure was initially suggested as a potential mechanism of fork repair in bacteria (Atkinson and McGlynn, 2009; Hotchkiss, 1974). The first direct evidence of fork

reversal in eukaryotes comes from negative stain EM imaging of crosslinked replication intermediates in *S. cerevisiae* (Sogo et al., 2002). Yet, in this work, reversed forks were observed only in Rad53 checkpoint deficient yeast strains upon treatment with HU, suggesting that formation of chicken foot structure at replication forks is a pathological phenomenon. Further work in human cells demonstrated that fork reversal can be observed even in non-damaging conditions and increases upon exposure to different genotoxins (Zellweger et al., 2015). The fork reversal increase is dependent on multiple factors including RAD51 itself and DNA translocases SMARCAL1, ZRANB3 and HLTF (Quinet et al., 2017). This raises the possibility that fork reversal might be a physiological phenomenon. However, SMARCAL1 (Ciccia et al., 2009), ZRANB3 (Ciccia et al., 2012), nor HLTF (Bai et al., 2020) display strong DNA damage sensitivity to replication-fork blocking agents. There is also no mouse phenotype reported for deletion of these proteins. One explanation is redundancy in fork reversal between different pathways, however, another possibility is that fork reversal is indeed a pathological phenomenon occurring when fork stalls and fails to restart. Interestingly, increased chicken foot structures were recently observed in RADX knockout cell lines (Krishnamoorthy et al., 2021). The latter hypothesis aligns with these data and my work presented in this thesis. Perhaps the mechanism behind fork slowing is formation of dead-end intermediate, the reversed fork, following fork stalling due to unscheduled RAD51 filament assembly at sites of ongoing replication. This is supported by increased spontaneous formation of 4-way junctions during DNA replication in living *E. coli* overexpressing RecA (Xia et al., 2016). For future work, it would be interesting to test whether increased reversed fork formation is observable by negative stain EM following crosslinking in RAD51 IT/IT MEFs.

**Why did evolution decide to downscale core recombinase activity?** RAD51 I287T causes primarily replication fork slowing/stalling and replication stress-related phenotypes *in vivo*. This implies that a recombinase that assembles on DNA on its own can interfere with the process of DNA replication. This raises the possibility that recombinase activity has been downscaled in evolution to match the changes in the replication programme. Indeed, when looking at features of replication between bacteria, archaea and eukaryotes, several trends are observable. First and foremost, the overall replication fork speed slows down dramatically, from 60 kb/min in *E. coli*, roughly 20 kb/min at archaea, to 1-2 kb/min in eukaryotes. Bacteria have also

considerably smaller genomes - 4.4 Mb genome in *E. coli*, when compared to 250 Mb-sized chromosome I in humans (O'Donnell et al., 2013). Finally, while replication in bacteria occurs by firing a single origin, in eukaryotes multiple origins fire on the same chromosome, which leads to many replication forks active at the same time. In archaea, some species contain a single origin of replication, while other species have multiple origins present on the same chromosome. All of this considered, given the large size of the chromosome, slower forks and more replication bubbles present, the ssDNA content present at a given window of time during genome duplication is significantly higher in eukaryotes than in bacteria. Given all the ssDNA generated during genome duplication is a potential substrate for recombinase filament assembly, bacteria can afford to express highly efficient recombinase as its chance to assemble on the relatively low levels of ssDNA generated during rapid genome duplication are small, while eukaryotes had to likely downscale recombinase activity and filament growth rates given the high levels of ssDNA accessible at a given time during DNA replication. This hypothesis is supported by work in bacteria where directed evolution was used to evolve 'super-RecA' variants, which display better SSB displacement as well as faster filament growth in bulk EM assays (Kim et al., 2015). Yet *in vivo*, these variants interfere with DNA metabolism, reduce bacterial proliferation and cause sensitivity to genotoxins – a phenomenon similar to the phenotype of RAD51 IT/IT MEFs.

### 6.3 Role of mismatch tolerance during meiotic recombination

In [Chapter 5](#) I have explored the amino acid sequence features that contribute to the differential response of Rad51 and Dmc1 to mismatch-containing base triplets. I propose that reported functional differences represent a fundamental distinction between Rad51 and Dmc1 lineages of eukaryotic DNA recombinases. In the following paragraphs, I discuss possible implications of these findings with respect to meiotic recombination mechanisms and the evolution of Rad51/RecA family members.

#### **Impact of mismatch tolerance during DNA strand exchange on recombination.**

At least two general ways of how DNA mismatches could affect strand invasion and recombination can be envisioned:

- I) lowering of the intrinsic stability of the strand exchange DNA intermediates
- II) alteration of the structure of the resulting recombinase-heteroduplex DNA complex. Perhaps, mismatches may make these intermediates less suited for downstream processing and/or more susceptible to disruption by anti-recombination enzymes.

The hypothesis that a small number of mismatches greatly alters the inherent stability of DNA heteroduplex is not highly plausible. Although a single mismatch influences the binding stability of dsDNA fragments in Dr. Steinfeld's biophysical assays, overall, these intermediates are all still relatively long-lived. For instance, in the case of ScRad51, a dsDNA substrate with 12 nt microhomology, has a lifetime of approximately 33 min; when increased to 15 nt the lifetime increases to ~47 min, and addition of a single DNA mismatch in the middle of 15-nt microhomology tract decreases the lifetime to ~35 min. This conclusion is supported by studies showing that bacterial RecA is surprisingly tolerant to DNA mismatches *in vitro* (Danilowicz et al., 2015). However, it cannot be accurately predicted how our *in vitro* measurement of DNA heteroduplex stability will scale for the longer substrates forming in the cell as precise measurements of the equivalent biophysical parameters *in vitro* with longer substrates are not feasible. Nevertheless, the available biophysical data imply

that mismatched heteroduplex strand exchange intermediates are not inherently unstable. Thus, the favoured hypothesis is that mismatches may somehow alter the structure of the nucleoprotein complexes - rendering them more prone to disruption by enzymatic regulators. Multiple proteins are known to disrupt HR intermediates. These include *S. cerevisiae* Srs2 and Sgs1 helicases. Mismatch repair machinery also has a role in minimizing recombination between divergent sequences following DNA replication (Branzei and Szakal, 2017; Lorenz, 2017; Spell and Jinks-Robertson, 2004; Spies and Fishel, 2015; Sugawara et al., 2004). One possibility is that these proteins may recognize some distinct structural feature of the mismatched heteroduplex that allows them to more act on Rad51-bound intermediates, while Dmc1 could shield mismatched strand intermediates from these enzymes (Figure 6.5A). This hypothesis is also in line with observed synthetic sickness between the CeRAD-51-TM and RTEL-1/HELQ-1.

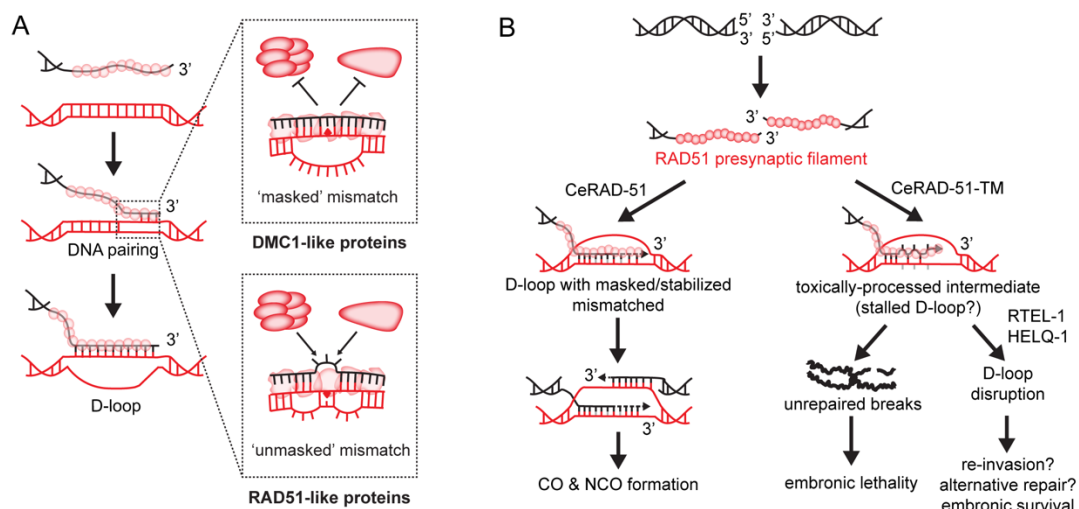


**Figure 6.5: Model depicting mismatch processing during meiotic recombination: (A)** DNA strand exchange mismatch masking by DMC1-like recombinases. **(B)** Model of CeRAD-51-TM mediated aberrant recombination intermediate formation and processing in nematodes.

The evidence presented in Chapter 5 suggests lineage-specific residues found within the L1 DNA-binding loop constitute the ability of Dmc1 to tolerate DNA mismatches during duplex capture. Dr. Steinfeld proposed (Steinfeld et al., 2019) that these amino acids could allow Dmc1 to make compensatory contacts with the phosphate backbone of the DNA - consistent with the previous findings that Dmc1 can stabilize base triplets containing an abasic site (Lee et al., 2017). Previous structural work

lacked sufficient data to fully describe the relevant protein–DNA interfaces as DNA was not present in the structures (Kinebuchi et al., 2004), or the resolution was too low to accurately define the L1 loop–DNA contacts (Short et al., 2016; Xu et al., 2017). Although a crystal structure of ScRad51 I287T-DNA filament exists, the L1-DNA contacts are not visible (Conway et al., 2004). More recently however, structures of human DMC1 presynaptic and postsynaptic complexes were resolved using cryoEM (Luo et al., 2021). Consistently with my results and Dr. Steinfeld’s prediction, DMC1 lineage-specific L1 residue Q244 and conserved R242 make contact with phosphate backbone of DNA duplex bound within DMC1 to stabilize mismatched heteroduplex. This notion is also supported by published MD simulations (Steinfeld et al., 2019), together with the data showing Dmc1 can stabilize dsDNA fragments that contain abasic sites (Lee et al., 2017). Furthermore, Luo et al also observed DMC1 lineage-specific L2 residues P274 and G275 provide flexibility of mismatched DNA base pairing by making a ‘triplet-gate’ next to the mismatched triplet. Corresponding RAD51 L2 residues (V273 and D274) decrease the solvent-accessible volume of this cavity by steric occlusion and salt-bridging between D274 and R235.

**Nematode RAD-51 requires Dmc1-like amino acids in specific context.**

*Caenorhabditis sp.* and *Drosophila sp.*, possess Rad51 but have lost Dmc1 with the genes encoding core meiotic Dmc1-stimulating proteins (Hop2/Mnd1 and Swi5–Sfr1) (Chintapalli et al., 2013; Hunter, 2015; Lin et al., 2006; Ramesh et al., 2005; Villeneuve and Hillers, 2001). It remains uncertain why these species have lost Dmc1. However, *Caenorhabditis sp.* and *Drosophila sp.* display very high rates of Rad51 gene evolution (Lin et al., 2006) compared to other organisms. Interestingly, I have shown that the lineage-specific amino acids of the L1 loop of *C. elegans* RAD-51 have evolved to more closely resemble Dmc1 and that CeRAD-51 can stabilize mismatched DNA strand exchange intermediates *in vitro*. Thus, the loss of Dmc1 may be responsible for adaptation of CeRAD-51 to become “Dmc1-like” with respect to the L1 loop of the protein. In line with the importance of “Dmc1-like” residues within the L1 DNA binding loop, I found that the chimeric CeRad51-TM variant, which bears ‘Rad51-like’ amino acids in the L1 loop, is a functional recombinase *in vivo*, but displays an impairment in the ability to promote recombination between highly divergent (heterologous) sequences *in vivo* and a synthetic lethal/sick genetic interaction with anti-recombinase RTEL1 and HELQ-1. These data imply that “Dmc1-



like” amino acids within the L1 loop of CeRAD-51 cannot be converted to amino acids present in the canonical Rad51-like protein without affecting the fidelity of meiotic HR in the absence of regulatory proteins RTEL-1 or HELQ-1. It is tempting to speculate that mismatches that would normally be masked by CeRAD-51 are not properly hidden within the context of CeRAD-51-TM filaments, resulting in a dead-end D-loop intermediate that must be disrupted by RTEL-1 or HELQ-1. Thus, the most important effect of the canonical Dmc1-like amino acids may be with respect to differences in their ability to mask mismatched strand exchange intermediates from toxic processing (Figure 6.5B). Identity of enzymes that may toxically process these intermediates remains unknown, but interestingly, previous work has shown that MSH-2 is responsible for increased frequency of het-rec in the absence of RTEL-1 (Leon-Ortiz et al., 2018), making it an interesting candidate. *Drosophila* Rad51 L1 amino acids are reminiscent of those found in Rad51-like proteins. However, N301 (corresponding to ScRad51 residue labelling) in *Drosophila* Rad51 does not match the methionine in canonical Rad51 but is similar to the glutamine from Dmc1 (Steinfeld et al., 2019). Thus, *Drosophila* Rad51 seems like Rad51-Dmc1 hybrid and may also display “Dmc1-like” behaviour with regards to stabilizing DNA mismatches as CeRAD-51.

Organisms that possess Dmc1 require recombination-dependent chromosome pairing to complete meiosis (Brown and Bishop, 2014; Hunter, 2015; Neale and Keeney, 2006). In contrast, both *C. elegans* and *D. melanogaster* have recombination-independent chromosome pairing initiation (Gerton and Hawley, 2005; Villeneuve and Hillers, 2001). However, the use of alternative chromosome pairing is not necessarily the defining feature of species lacking Dmc1. For example, *Ustilago maydis* or *Neurospora crassa* have lost Dmc1, but require HR to initiate meiotic chromosome pairing (Storlazzi et al., 2003). Interestingly, both *U. maydis* and *N. crassa* possess Rad51-like amino acids in the L1 DNA binding site (Steinfeld et al., 2019). It should be noted that the L1 residues from bacterial RecA are highly divergent when compared to eukaryotic Rad51 and Dmc1 (Steinfeld et al., 2019). Therefore, the mechanisms by which bacterial recombinase interacts with the DNA may be distinct from those of the eukaryotic recombinases.

**Origins of the dual-recombinase system.** Rad51 and Dmc1 evolved early by a gene duplication event from archaeal RadA recombinase. This gene duplication event may have been responsible for the emergence of meiosis and sexual reproduction (Chintapalli et al., 2013; Lin et al., 2006; Ramesh et al., 2005). Some archaea, including *Haloferax volcanii*, undergo a conjugation process entailing the exchange of divergent genetic information by HR. The conjugation mechanism bears some resemblance to the meiotic programme in eukaryotes (Cohan and Aracena, 2012; Mevarech and Werczberger, 1985; Naor and Gophna, 2013; Naor et al., 2012; Papke et al., 2004; Rosenshine et al., 1989). Very interestingly, the RadA L1 amino acids located at the positions important for in mismatch stabilization are similar to those in the Dmc1-like proteins of eukaryotic recombinase family (Steinfeld et al., 2019). One possibility is that a “lower-fidelity” Dmc1-like protein may have predated the “high-fidelity” Rad51-like protein present in eukaryotic cells. This way, the emergence of Rad51 in evolution may have enabled eukaryotic cells to better utilize HR as an error-free mitotic DSB repair pathway.

## Chapter 7. Conclusion

### 7.1 Thesis conclusion

In this thesis, I utilized ensemble biochemistry, single-molecule imaging, force spectroscopy and genetics to investigate mechanisms of the early steps in homologous recombination. To understand how eukaryotic RAD51 assembles into filaments when it does not grow nearly as fast as its bacterial counterpart, RecA, I reconstituted nematode RAD-51 presynaptic filament assembly in the presence of mediator proteins ([Chapter 3](#)). I have established that two recombination mediators have contribution to different subsets of the RAD51 assembly reaction: nucleation and growth. More specifically, this work reveals ATPase-dependent dynamics of a mediator complex, RFS-1/RIP-1 by direct real-time fluorescent imaging for the first time. I established that RFS-1/RIP-1 functions as RAD-51 chaperone to stabilize nascent growing RAD-51 filaments. This work establishes RFS-1/RIP-1 as the elusive RAD-51 filament growth factor.

This raises an interesting conundrum, why does eukaryotic RAD51 filaments not grow efficiently on its own? And why there seems to be a trend of downscaling recombinase activity in evolution? In [Chapter 4](#) I set out to answer these questions by engineering a human RAD51 variant, RAD51 I287T that binds DNA tighter, has better strand exchange and assembles faster on RPA-coated ssDNA. Phenotypic analysis of this mutant in mouse embryonic fibroblasts showed slower proliferation and sensitivity to replication-fork blocking genotoxins, but not impairment of canonical HR at DSBs. To investigate this phenotype in greater detail, I performed single-molecule replication dynamics analysis and demonstrated global fork slowing and stochastic fork stalling in these cells, which is associated with accumulation of RAD51 I287T on replicating chromatin. I proposed that intrinsic recombinase activity of a cellular recombinase must be limited by the amount of ssDNA content generated during DNA replication to prevent unscheduled RAD51 assembly on unperturbed replication forks, resulting in their replication slowing.

Finally, in [Chapter 5](#), I explored mechanisms of mismatch tolerance during meiotic DNA strand exchange. I demonstrated that nematode RAD-51 displays Dmc1-like properties in respect to tolerance of mismatches during strand invasion reaction. Furthermore, by introducing three mutations in L1 DNA binding loop of nematode

RAD-51, I managed to abolish mismatch tolerance of nematode RAD-51, while still retaining most of its strand exchange activity with non-mismatches sequences. The resulting mutant, termed RAD51 triple mutant (RAD-51-TM) was knocked-in into nematode Bristol strain and analysed phenotypically. I subsequently showed that RAD-51-TM can support recombination between homologous sequences but does not suppress heterologous recombination events unleashed by depletion of RTEL-1 or BRC-1. Finally, RAD-51-TM allele confers synthetic sickness with loss of RTEL-1 and HELQ-1. I proposed that this is due to formation of a toxic intermediate, which is processed by motor proteins and further hypothesize that this intermediate may be a structurally unmasked DNA mismatch formed during strand invasion by mismatch intolerant RAD-51-TM. Taken together, these findings demonstrate the importance of mismatch tolerance during meiosis and imply that perhaps Dmc1-like proteins play more additional role in mismatched heteroduplex masking from other factors, in addition to simple stabilization of mismatched heteroduplex DNA.

In conclusion, in this thesis, I utilized different single-molecule approaches to dissect the heterogeneity of mechanism maintaining genomic integrity in higher organisms. The findings presented here demonstrate how single-molecule approach can provide unprecedented insights into complex biological processes such as DNA double strand break repair. Dissecting heterogeneity and understanding how stochastic behaviour of individual components of a biological system leads to highly ordered deterministic responses to stress is becoming increasingly important. In the future, this type of knowledge will be instrumental in our race against highly heterogeneous, fast evolving and adaptable diseases, such as cancer.

## 7.2 Future perspectives

In this thesis, I have demonstrated the possibility of nematode RAD-51 presynaptic filament assembly reconstitution at single molecule level. Adaptation of this system to investigate assembly and dynamics of human core recombination machinery would be of interest. Several improvements must be made in production and labelling of recombinant human recombination mediator proteins including BRCA2 and RAD51 paralog complexes. Furthermore, recombination mediators in human cells are capable of possibly forming mediator supra-complexes such as the BRCA1-PALB2-BRCA2 complex. Deeper understanding of the human recombination machinery would require reconstituting human recombination 'mediasome' in bulk first, which is a monumental task even before performing the single-molecule imaging experiments, but given the recent advances in the field, certainly not impossible. One more step further is single molecule analysis of human meiotic recombination machinery, which entails several more factors, most importantly, one more core recombinase, DMC1.

With regards to my genetic work on characterizing RAD51 I287T allele, unbiased mapping of genetic interactions by whole-genome CRISPR screen would shed light on DNA repair pathways that are compensating for increased assembly rate of RAD51 *in vivo*, and possibly new mediator proteins loss of which is suppressed by fast-assembling RAD51 I287T. Fundamentally, a direct proof of mediator bypass in RAD51 IT/IT MEFs is required to fully validate the mutation phenocopies yeast Rad51 I345T. Further descriptive work on DNA damage markers in RAD51 IT/IT MEFs would be beneficial, as well as more detailed *in vitro* analysis of nucleation and growth rates using optical tweezers. Finally, to better understand the phenotype on whole organism level, exacerbation of replication stress in IT/IT mice coupled with post-mortem examination is required.

## Reference List

- Abreu, C.M., Prakash, R., Romanienko, P.J., Roig, I., Keeney, S., and Jasin, M. (2018). Shu complex SWS1-SWSAP1 promotes early steps in mouse meiotic recombination. *Nat Commun* 9, 3961.
- Adelman, C.A., Lolo, R.L., Birkbak, N.J., Murina, O., Matsuzaki, K., Horejsi, Z., Parmar, K., Borel, V., Skehel, J.M., Stamp, G., *et al.* (2013). HELQ promotes RAD51 paralogue-dependent repair to avert germ cell loss and tumorigenesis. *Nature* 502, 381-384.
- Adolph, M.B., Mohamed, T.M., Balakrishnan, S., Xue, C., Morati, F., Modesti, M., Greene, E.C., Chazin, W.J., and Cortez, D. (2021). RADX controls RAD51 filament dynamics to regulate replication fork stability. *Mol Cell* 81, 1074-1083 e1075.
- Amitani, I., Liu, B., Dombrowski, C.C., Baskin, R.J., and Kowalczykowski, S.C. (2010). Watching individual proteins acting on single molecules of DNA. *Methods Enzymol* 472, 261-291.
- Anand, R., Ranjha, L., Cannavo, E., and Cejka, P. (2016). Phosphorylated CtIP Functions as a Co-factor of the MRE11-RAD50-NBS1 Endonuclease in DNA End Resection. *Mol Cell* 64, 940-950.
- Arunkumar, A.I., Stauffer, M.E., Bochkareva, E., Bochkarev, A., and Chazin, W.J. (2003). Independent and coordinated functions of replication protein A tandem high affinity single-stranded DNA binding domains. *J Biol Chem* 278, 41077-41082.
- Ashkin, A. (1970). Acceleration and trapping of particles by radiation pressure. *Phys. Rev. Lett.* 24.
- Ashkin, A., Dziedzic, M., Bjorkholm, J.E., and Chu, S. (1986). Observation of a single-beam gradient force optical trap for dielectric particles. *Opt. Lett.* 11, 288-290.
- Atkinson, J., and McGlynn, P. (2009). Replication fork reversal and the maintenance of genome stability. *Nucleic Acids Res* 37, 3475-3492.
- Autour, A., S, C.Y.J., A, D.C., Abdolazadeh, A., Galli, A., Panchapakesan, S.S.S., Rueda, D., Ryckelynck, M., and Unrau, P.J. (2018). Fluorogenic RNA Mango aptamers for imaging small non-coding RNAs in mammalian cells. *Nat Commun* 9, 656.
- Axelrod, D., Thompson, N.L., and Burghardt, T.P. (1983). Total internal inflection fluorescent microscopy. *J Microsc* 129, 19-28.
- Bai, G., Kermi, C., Stoy, H., Schiltz, C.J., Bacal, J., Zaino, A.M., Hadden, M.K., Eichman, B.F., Lopes, M., and Cimprich, K.A. (2020). HLTf Promotes Fork Reversal, Limiting Replication Stress Resistance and Preventing Multiple Mechanisms of Unrestrained DNA Synthesis. *Mol Cell* 78, 1237-1251 e1237.
- Bar-Ziv, R., and Libchaber, A. (2001). Effects of DNA sequence and structure on binding of RecA to single-stranded DNA. *Proc Natl Acad Sci U S A* 98, 9068-9073.

- Barber, L.J., Youds, J.L., Ward, J.D., Mcllwraith, M.J., O'Neil, N.J., Petalcorin, M.I., Martin, J.S., Collis, S.J., Cantor, S.B., Auclair, M., *et al.* (2008). RTEL1 maintains genomic stability by suppressing homologous recombination. *Cell* *135*, 261-271.
- Baumann, P., and West, S.C. (1997). The human Rad51 protein: polarity of strand transfer and stimulation by hHR23A. *EMBO J* *16*, 5198-5206.
- Belan, O., Barroso, C., Kaczmarczyk, A., Anand, R., Federico, S., O'Reilly, N., Newton, M.D., Maeots, E., Enchev, R.I., Martinez-Perez, E., *et al.* (2021a). Single-molecule analysis reveals cooperative stimulation of Rad51 filament nucleation and growth by mediator proteins. *Mol Cell* *81*, 1058-1073 e1057.
- Belan, O., Moore, G., Kaczmarczyk, A., Newton, M.D., Anand, R., Boulton, S.J., and Rueda, D.S. (2021b). Generation of versatile ss-dsDNA hybrid substrates for single-molecule analysis. *STAR Protoc* *2*, 100588.
- Bell, J.C., Plank, J.L., Dombrowski, C.C., and Kowalczykowski, S.C. (2012). Direct imaging of RecA nucleation and growth on single molecules of SSB-coated ssDNA. *Nature* *491*, 274-278.
- Bellelli, R., Borel, V., Logan, C., Svendsen, J., Cox, D.E., Nye, E., Metcalfe, K., O'Connell, S.M., Stamp, G., Flynn, H.R., *et al.* (2018). Polepsilon Instability Drives Replication Stress, Abnormal Development, and Tumorigenesis. *Mol Cell* *70*, 707-721 e707.
- Berg, O.G., and von Hippel, P.H. (1985). Diffusion-controlled macromolecular interactions. *Annu Rev Biophys Chem* *14*, 131-160.
- Berg, O.G., Winter, R.B., and von Hippel, P.H. (1981). Diffusion-driven mechanisms of protein translocation on nucleic acids. 1. Models and theory. *Biochemistry* *20*, 6929-6948.
- Berti, M., Teloni, F., Mijic, S., Ursich, S., Fuchs, J., Palumbieri, M.D., Krietsch, J., Schmid, J.A., Garcin, E.B., Gon, S., *et al.* (2020). Sequential role of RAD51 paralog complexes in replication fork remodeling and restart. *Nat Commun* *11*, 3531.
- Bianco, P.R., Brewer, L.R., Corzett, M., Balhorn, R., Yeh, Y., Kowalczykowski, S.C., and Baskin, R.J. (2001). Processive translocation and DNA unwinding by individual RecBCD enzyme molecules. *Nature* *409*, 374-378.
- Bishop, D.K., Park, D., Xu, L., and Kleckner, N. (1992). DMC1: a meiosis-specific yeast homolog of *E. coli* recA required for recombination, synaptonemal complex formation, and cell cycle progression. *Cell* *69*, 439-456.
- Bleuyard, J.Y., Gallego, M.E., Savigny, F., and White, C.I. (2005). Differing requirements for the Arabidopsis Rad51 paralogs in meiosis and DNA repair. *Plant J* *41*, 533-545.
- Branzei, D., and Szakal, B. (2017). Building up and breaking down: mechanisms controlling recombination during replication. *Crit Rev Biochem Mol Biol* *52*, 381-394.
- Brenner, S. (1974). The genetics of *Caenorhabditis elegans*. *Genetics* *77*, 71-94.

- Brouwer, I., Moschetti, T., Candelli, A., Garcin, E.B., Modesti, M., Pellegrini, L., Wuite, G.J., and Peterman, E.J. (2018). Two distinct conformational states define the interaction of human RAD51-ATP with single-stranded DNA. *EMBO J* 37.
- Brown, M.S., and Bishop, D.K. (2014). DNA strand exchange and RecA homologs in meiosis. *Cold Spring Harb Perspect Biol* 7, a016659.
- Brown, M.S., Grubb, J., Zhang, A., Rust, M.J., and Bishop, D.K. (2015). Small Rad51 and Dmc1 Complexes Often Co-occupy Both Ends of a Meiotic DNA Double Strand Break. *PLoS Genet* 11, e1005653.
- Buisson, R., Dion-Cote, A.M., Coulombe, Y., Launay, H., Cai, H., Stasiak, A.Z., Stasiak, A., Xia, B., and Masson, J.Y. (2010). Cooperation of breast cancer proteins PALB2 and piccolo BRCA2 in stimulating homologous recombination. *Nat Struct Mol Biol* 17, 1247-1254.
- Bunting, S.F., Callen, E., Wong, N., Chen, H.T., Polato, F., Gunn, A., Bothmer, A., Feldhahn, N., Fernandez-Capetillo, O., Cao, L., *et al.* (2010). 53BP1 inhibits homologous recombination in Brca1-deficient cells by blocking resection of DNA breaks. *Cell* 141, 243-254.
- Burma, S., Chen, B.P., Murphy, M., Kurimasa, A., and Chen, D.J. (2001). ATM phosphorylates histone H2AX in response to DNA double-strand breaks. *J Biol Chem* 276, 42462-42467.
- Bustamante, C., Marko, J.F., Siggia, E.D., and Smith, S. (1994). Entropic elasticity of lambda-phage DNA. *Science* 265, 1599-1600.
- Candelli, A. (2013). Physical Mechanisms of DNA repair: A single molecule perspective. In Department of Physics and Astronomy (Vrije Universiteit Amsterdam, Vrije Universiteit Amsterdam), p. 188.
- Candelli, A., Holthausen, J.T., Depken, M., Brouwer, I., Franker, M.A., Marchetti, M., Heller, I., Bernard, S., Garcin, E.B., Modesti, M., *et al.* (2014). Visualization and quantification of nascent RAD51 filament formation at single-monomer resolution. *Proc Natl Acad Sci U S A* 111, 15090-15095.
- Cannavo, E., Reginato, G., and Cejka, P. (2019). Stepwise 5' DNA end-specific resection of DNA breaks by the Mre11-Rad50-Xrs2 and Sae2 nuclease ensemble. *Proc Natl Acad Sci U S A* 116, 5505-5513.
- Carreira, A., Hilario, J., Amitani, I., Baskin, R.J., Shivji, M.K., Venkitaraman, A.R., and Kowalczykowski, S.C. (2009). The BRC repeats of BRCA2 modulate the DNA-binding selectivity of RAD51. *Cell* 136, 1032-1043.
- Carreira, A., and Kowalczykowski, S.C. (2011). Two classes of BRC repeats in BRCA2 promote RAD51 nucleoprotein filament function by distinct mechanisms. *Proc Natl Acad Sci U S A* 108, 10448-10453.
- Ceccaldi, R., Liu, J.C., Amunugama, R., Hajdu, I., Primack, B., Petalcorin, M.I., O'Connor, K.W., Konstantinopoulos, P.A., Elledge, S.J., Boulton, S.J., *et al.* (2015).



Homologous-recombination-deficient tumours are dependent on Poltheta-mediated repair. *Nature* 518, 258-262.

Ceppi, I., Howard, S.M., Kasaciunaite, K., Pinto, C., Anand, R., Seidel, R., and Cejka, P. (2020). CtIP promotes the motor activity of DNA2 to accelerate long-range DNA end resection. *Proc Natl Acad Sci U S A* 117, 8859-8869.

Chapman, J.R., Barral, P., Vannier, J.B., Borel, V., Steger, M., Tomas-Loba, A., Sartori, A.A., Adams, I.R., Batista, F.D., and Boulton, S.J. (2013). RIF1 is essential for 53BP1-dependent nonhomologous end joining and suppression of DNA double-strand break resection. *Mol Cell* 49, 858-871.

Chapman, J.R., Taylor, M.R., and Boulton, S.J. (2012). Playing the end game: DNA double-strand break repair pathway choice. *Mol Cell* 47, 497-510.

Chen, Z., Yang, H., and Pavletich, N.P. (2008). Mechanism of homologous recombination from the RecA-ssDNA/dsDNA structures. *Nature* 453, 489-484.

Chi, P., Van Komen, S., Sehorn, M.G., Sigurdsson, S., and Sung, P. (2006). Roles of ATP binding and ATP hydrolysis in human Rad51 recombinase function. *DNA Repair (Amst)* 5, 381-391.

Chintapalli, S.V., Bhardwaj, G., Babu, J., Hadjiyianni, L., Hong, Y., Todd, G.K., Boosalis, C.A., Zhang, Z., Zhou, X., Ma, H., *et al.* (2013). Reevaluation of the evolutionary events within recA/RAD51 phylogeny. *BMC Genomics* 14, 240.

Cho, S.W., Lee, J., Carroll, D., Kim, J.S., and Lee, J. (2013). Heritable gene knockout in *Caenorhabditis elegans* by direct injection of Cas9-sgRNA ribonucleoproteins. *Genetics* 195, 1177-1180.

Chun, J., Buechelmaier, E.S., and Powell, S.N. (2013). Rad51 paralog complexes BCDX2 and CX3 act at different stages in the BRCA1-BRCA2-dependent homologous recombination pathway. *Mol Cell Biol* 33, 387-395.

Ciccia, A., Bredemeyer, A.L., Sowa, M.E., Terret, M.E., Jallepalli, P.V., Harper, J.W., and Elledge, S.J. (2009). The SIOD disorder protein SMARCAL1 is an RPA-interacting protein involved in replication fork restart. *Genes Dev* 23, 2415-2425.

Ciccia, A., Nimonkar, A.V., Hu, Y., Hajdu, I., Achar, Y.J., Izhar, L., Petit, S.A., Adamson, B., Yoon, J.C., Kowalczykowski, S.C., *et al.* (2012). Polyubiquitinated PCNA recruits the ZRANB3 translocase to maintain genomic integrity after replication stress. *Mol Cell* 47, 396-409.

Cloud, V., Chan, Y.L., Grubb, J., Budke, B., and Bishop, D.K. (2012). Rad51 is an accessory factor for Dmc1-mediated joint molecule formation during meiosis. *Science* 337, 1222-1225.

Cohan, F.M., and Aracena, S. (2012). Prokaryotic sex: eukaryote-like qualities of recombination in an Archaeal lineage. *Curr Biol* 22, R601-602.

- Collis, S.J., Barber, L.J., Ward, J.D., Martin, J.S., and Boulton, S.J. (2006). *C. elegans* FANCD2 responds to replication stress and functions in interstrand cross-link repair. *DNA Repair (Amst)* 5, 1398-1406.
- Cong, K., Peng, M., Kousholt, A.N., Lee, W.T.C., Lee, S., Nayak, S., Kraiss, J., VanderVere-Carozza, P.S., Pawelczak, K.S., Calvo, J., *et al.* (2021). Replication gaps are a key determinant of PARP inhibitor synthetic lethality with BRCA deficiency. *Mol Cell*.
- Conway, A.B., Lynch, T.W., Zhang, Y., Fortin, G.S., Fung, C.W., Symington, L.S., and Rice, P.A. (2004). Crystal structure of a Rad51 filament. *Nat Struct Mol Biol* 11, 791-796.
- Cox, M.M., and Lehman, I.R. (1981). Directionality and polarity in recA protein-promoted branch migration. *Proc Natl Acad Sci U S A* 78, 6018-6022.
- Crickard, J.B., Kaniecki, K., Kwon, Y., Sung, P., and Greene, E.C. (2018). Spontaneous self-segregation of Rad51 and Dmc1 DNA recombinases within mixed recombinase filaments. *J Biol Chem* 293, 4191-4200.
- Crickard, J.B., Moevus, C.J., Kwon, Y., Sung, P., and Greene, E.C. (2020). Rad54 Drives ATP Hydrolysis-Dependent DNA Sequence Alignment during Homologous Recombination. *Cell* 181, 1380-1394 e1318.
- Danilowicz, C., Yang, D., Kelley, C., Prevost, C., and Prentiss, M. (2015). The poor homology stringency in the heteroduplex allows strand exchange to incorporate desirable mismatches without sacrificing recognition in vivo. *Nucleic Acids Res* 43, 6473-6485.
- Davies, O.R., and Pellegrini, L. (2007). Interaction with the BRCA2 C terminus protects RAD51-DNA filaments from disassembly by BRC repeats. *Nat Struct Mol Biol* 14, 475-483.
- Daza-Martin, M., Starowicz, K., Jamshad, M., Tye, S., Ronson, G.E., MacKay, H.L., Chauhan, A.S., Walker, A.K., Stone, H.R., Beesley, J.F.J., *et al.* (2019). Isomerization of BRCA1-BARD1 promotes replication fork protection. *Nature* 571, 521-527.
- Dev, H., Chiang, T.W., Lescale, C., de Krijger, I., Martin, A.G., Pilger, D., Coates, J., Sczaniecka-Clift, M., Wei, W., Ostermaier, M., *et al.* (2018). Shieldin complex promotes DNA end-joining and counters homologous recombination in BRCA1-null cells. *Nat Cell Biol* 20, 954-965.
- Di Capua, E., Engel, A., Stasiak, A., and Koller, T. (1982). Characterization of complexes between recA protein and duplex DNA by electron microscopy. *J Mol Biol* 157, 87-103.
- Di Virgilio, M., Callen, E., Yamane, A., Zhang, W., Jankovic, M., Gitlin, A.D., Feldhahn, N., Resch, W., Oliveira, T.Y., Chait, B.T., *et al.* (2013). Rif1 prevents

- resection of DNA breaks and promotes immunoglobulin class switching. *Science* 339, 711-715.
- Doil, C., Mailand, N., Bekker-Jensen, S., Menard, P., Larsen, D.H., Pepperkok, R., Ellenberg, J., Panier, S., Durocher, D., Bartek, J., *et al.* (2009). RNF168 binds and amplifies ubiquitin conjugates on damaged chromosomes to allow accumulation of repair proteins. *Cell* 136, 435-446.
- Dungrawala, H., Bhat, K.P., Le Meur, R., Chazin, W.J., Ding, X., Sharan, S.K., Wessel, S.R., Sathe, A.A., Zhao, R., and Cortez, D. (2017). RADX Promotes Genome Stability and Modulates Chemosensitivity by Regulating RAD51 at Replication Forks. *Mol Cell* 67, 374-386 e375.
- Esashi, F., Galkin, V.E., Yu, X., Egelman, E.H., and West, S.C. (2007). Stabilization of RAD51 nucleoprotein filaments by the C-terminal region of BRCA2. *Nat Struct Mol Biol* 14, 468-474.
- Essmann, C.L., Martinez-Martinez, D., Pryor, R., Leung, K.Y., Krishnan, K.B., Lui, P.P., Greene, N.D.E., Brown, A.E.X., Pawar, V.M., Srinivasan, M.A., *et al.* (2020). Mechanical properties measured by atomic force microscopy define health biomarkers in ageing *C. elegans*. *Nat Commun* 11, 1043.
- Fan, J., and Pavletich, N.P. (2012). Structure and conformational change of a replication protein A heterotrimer bound to ssDNA. *Genes Dev* 26, 2337-2347.
- Fanconi, G. (1927). Familiäre infantile perniziösaartige Anämie (perniziöses Blutbild und Konstitution). *Jahrbuch für Kinderheilkunde und physische Erziehung (Wien)* 117, 257-280.
- Feng, W., Simpson, D.A., Carvajal-Garcia, J., Price, B.A., Kumar, R.J., Mose, L.E., Wood, R.D., Rashid, N., Purvis, J.E., Parker, J.S., *et al.* (2019). Genetic determinants of cellular addiction to DNA polymerase theta. *Nat Commun* 10, 4286.
- Forget, A.L., and Kowalczykowski, S.C. (2012). Single-molecule imaging of DNA pairing by RecA reveals a three-dimensional homology search. *Nature* 482, 423-427.
- Fortin, G.S., and Symington, L.S. (2002). Mutations in yeast Rad51 that partially bypass the requirement for Rad55 and Rad57 in DNA repair by increasing the stability of Rad51-DNA complexes. *EMBO J* 21, 3160-3170.
- Frank, K.M., Sekiguchi, J.M., Seidl, K.J., Swat, W., Rathbun, G.A., Cheng, H.L., Davidson, L., Kangaloo, L., and Alt, F.W. (1998). Late embryonic lethality and impaired V(D)J recombination in mice lacking DNA ligase IV. *Nature* 396, 173-177.
- Friedland, A.E., Tzur, Y.B., Esvelt, K.M., Colaiacovo, M.P., Church, G.M., and Calarco, J.A. (2013). Heritable genome editing in *C. elegans* via a CRISPR-Cas9 system. *Nat Methods* 10, 741-743.
- Fung, C.W., Mozlin, A.M., and Symington, L.S. (2009). Suppression of the double-strand-break-repair defect of the *Saccharomyces cerevisiae* rad57 mutant. *Genetics* 181, 1195-1206.

- Galletto, R., Amitani, I., Baskin, R.J., and Kowalczykowski, S.C. (2006). Direct observation of individual RecA filaments assembling on single DNA molecules. *Nature* 443, 875-878.
- Garcin, E.B., Gon, S., Sullivan, M.R., Brunette, G.J., Cian, A., Concordet, J.P., Giovannangeli, C., Dirks, W.G., Eberth, S., Bernstein, K.A., *et al.* (2019). Differential Requirements for the RAD51 Paralogs in Genome Repair and Maintenance in Human Cells. *PLoS Genet* 15, e1008355.
- Gataulin, D.V., Carey, J.N., Li, J., Shah, P., Grubb, J.T., and Bishop, D.K. (2018). The ATPase activity of *E. coli* RecA prevents accumulation of toxic complexes formed by erroneous binding to undamaged double stranded DNA. *Nucleic Acids Res* 46, 9510-9523.
- Gerton, J.L., and Hawley, R.S. (2005). Homologous chromosome interactions in meiosis: diversity amidst conservation. *Nat Rev Genet* 6, 477-487.
- Ghezraoui, H., Oliveira, C., Becker, J.R., Bilham, K., Moralli, D., Anzilotti, C., Fischer, R., Deobagkar-Lele, M., Sanchiz-Calvo, M., Fueyo-Marcos, E., *et al.* (2018). 53BP1 cooperation with the REV7-shieldin complex underpins DNA structure-specific NHEJ. *Nature* 560, 122-127.
- Godin, S., Wier, A., Kabbinar, F., Bratton-Palmer, D.S., Ghodke, H., Van Houten, B., VanDemark, A.P., and Bernstein, K.A. (2013). The Shu complex interacts with Rad51 through the Rad51 paralogues Rad55-Rad57 to mediate error-free recombination. *Nucleic Acids Res* 41, 4525-4534.
- Gottlieb, T.M., and Jackson, S.P. (1993). The DNA-dependent protein kinase: requirement for DNA ends and association with Ku antigen. *Cell* 72, 131-142.
- Grawunder, U., Wilm, M., Wu, X., Kulesza, P., Wilson, T.E., Mann, M., and Lieber, M.R. (1997). Activity of DNA ligase IV stimulated by complex formation with XRCC4 protein in mammalian cells. *Nature* 388, 492-495.
- Gross, P., Laurens, N., B., O.L., Bockelmann, U., Peterman, E.J.G., and Wuite, G.J. (2011). Quantifying how DNA stretches, melts and changes twist under tension. *Nature Physics* 7, 731-736.
- Gupta, R., Somyajit, K., Narita, T., Maskey, E., Stanlie, A., Kremer, M., Typas, D., Lammers, M., Mailand, N., Nussenzweig, A., *et al.* (2018). DNA Repair Network Analysis Reveals Shieldin as a Key Regulator of NHEJ and PARP Inhibitor Sensitivity. *Cell* 173, 972-988 e923.
- Gutierrez-Escribano, P., Newton, M.D., Llauro, A., Huber, J., Tanasie, L., Davy, J., Aly, I., Aramayo, R., Montoya, A., Kramer, H., *et al.* (2019). A conserved ATP- and Scc2/4-dependent activity for cohesin in tethering DNA molecules. *Sci Adv* 5, eaay6804.

- Haruta, N., Kurokawa, Y., Murayama, Y., Akamatsu, Y., Unzai, S., Tsutsui, Y., and Iwasaki, H. (2006). The Swi5-Sfr1 complex stimulates Rhp51/Rad51- and Dmc1-mediated DNA strand exchange in vitro. *Nat Struct Mol Biol* 13, 823-830.
- Hashimoto, Y., Ray Chaudhuri, A., Lopes, M., and Costanzo, V. (2010). Rad51 protects nascent DNA from Mre11-dependent degradation and promotes continuous DNA synthesis. *Nat Struct Mol Biol* 17, 1305-1311.
- Hegner, M., Smith, S.B., and Bustamante, C. (1999). Polymerization and mechanical properties of single RecA-DNA filaments. *Proc Natl Acad Sci U S A* 96, 10109-10114.
- Hell, S.W., Sahl, S.J., Bates, M., Zhuang, X., Heintzmann, R., Booth, M.J., Bewersdorf, J., Shtengel, G., Hess, H., and Tinnefeld, P. (2015). The 2015 super-resolution microscopy roadmap. *Journal of Physics D: Applied Physics* 48.
- Heller, I., Sitters, G., Broekmans, O.D., Farge, G., Menges, C., Wende, W., Hell, S.W., Peterman, E.J., and Wuite, G.J. (2013). STED nanoscopy combined with optical tweezers reveals protein dynamics on densely covered DNA. *Nat Methods* 10, 910-916.
- Hewitt, G., Borel, V., Segura-Bayona, S., Takaki, T., Ruis, P., Bellelli, R., Lehmann, L.C., Sommerova, L., Vancevska, A., Tomas-Loba, A., *et al.* (2020). Defective ALC1 nucleosome remodeling confers PARPi sensitization and synthetic lethality with HRD. *Mol Cell*.
- Hilario, J., Amitani, I., Baskin, R.J., and Kowalczykowski, S.C. (2009). Direct imaging of human Rad51 nucleoprotein dynamics on individual DNA molecules. *Proc Natl Acad Sci U S A* 106, 361-368.
- Hinch, A.G., Becker, P.W., Li, T., Moralli, D., Zhang, G., Bycroft, C., Green, C., Keeney, S., Shi, Q., Davies, B., *et al.* (2020). The Configuration of RPA, RAD51, and DMC1 Binding in Meiosis Reveals the Nature of Critical Recombination Intermediates. *Mol Cell* 79, 689-701 e610.
- Hong, Y., Sonnevile, R., Wang, B., Scheidt, V., Meier, B., Woglar, A., Demetriou, S., Labib, K., Jantsch, V., and Gartner, A. (2018). LEM-3 is a midbody-tethered DNA nuclease that resolves chromatin bridges during late mitosis. *Nat Commun* 9, 728.
- Hotchkiss, R.D. (1974). Models of genetic recombination. *Annu Rev Microbiol* 28, 445-468.
- Howlett, N.G., Taniguchi, T., Olson, S., Cox, B., Waisfisz, Q., De Die-Smulders, C., Persky, N., Grompe, M., Joenje, H., Pals, G., *et al.* (2002). Biallelic inactivation of BRCA2 in Fanconi anemia. *Science* 297, 606-609.
- Hu, Y., Raynard, S., Sehorn, M.G., Lu, X., Bussen, W., Zheng, L., Stark, J.M., Barnes, E.L., Chi, P., Janscak, P., *et al.* (2007). RECQL5/Recql5 helicase regulates homologous recombination and suppresses tumor formation via disruption of Rad51 presynaptic filaments. *Genes Dev* 21, 3073-3084.

- Huen, M.S., Grant, R., Manke, I., Minn, K., Yu, X., Yaffe, M.B., and Chen, J. (2007). RNF8 transduces the DNA-damage signal via histone ubiquitylation and checkpoint protein assembly. *Cell* 131, 901-914.
- Hunter, N. (2015). *Meiotic Recombination: The Essence of Heredity*. Cold Spring Harb Perspect Biol 7.
- Ip, S.C., Rass, U., Blanco, M.G., Flynn, H.R., Skehel, J.M., and West, S.C. (2008). Identification of Holliday junction resolvases from humans and yeast. *Nature* 456, 357-361.
- Jackson, D.A., and Pombo, A. (1998). Replicon clusters are stable units of chromosome structure: evidence that nuclear organization contributes to the efficient activation and propagation of S phase in human cells. *J Cell Biol* 140, 1285-1295.
- Jakobsen, K.P., Nielsen, K.O., Lovschal, K.V., Rodgaard, M., Andersen, A.H., and Bjergbaek, L. (2019). Minimal Resection Takes Place during Break-Induced Replication Repair of Collapsed Replication Forks and Is Controlled by Strand Invasion. *Cell Rep* 26, 836-844 e833.
- Janisiw, E., Dello Stritto, M.R., Jantsch, V., and Silva, N. (2018). BRCA1-BARD1 associate with the synaptonemal complex and pro-crossover factors and influence RAD-51 dynamics during *Caenorhabditis elegans* meiosis. *PLoS Genet* 14, e1007653.
- Jensen, R.B., Carreira, A., and Kowalczykowski, S.C. (2010). Purified human BRCA2 stimulates RAD51-mediated recombination. *Nature* 467, 678-683.
- Jensen, R.B., Ozes, A., Kim, T., Estep, A., and Kowalczykowski, S.C. (2013). BRCA2 is epistatic to the RAD51 paralogs in response to DNA damage. *DNA Repair (Amst)* 12, 306-311.
- Johansen, P.L., Fenaroli, F., Evensen, L., Griffiths, G., and Koster, G. (2016). Optical micromanipulation of nanoparticles and cells inside living zebrafish. *Nat Commun* 7, 10974.
- Joo, C., McKinney, S.A., Nakamura, M., Rasnik, I., Myong, S., and Ha, T. (2006). Real-time observation of RecA filament dynamics with single monomer resolution. *Cell* 126, 515-527.
- Kamath, R.S., and Ahringer, J. (2003). Genome-wide RNAi screening in *Caenorhabditis elegans*. *Methods* 30, 313-321.
- Karow, J.K., Constantinou, A., Li, J.L., West, S.C., and Hickson, I.D. (2000). The Bloom's syndrome gene product promotes branch migration of holliday junctions. *Proc Natl Acad Sci U S A* 97, 6504-6508.
- Kelley, J.A., and Knight, K.L. (1997). Allosteric regulation of RecA protein function is mediated by Gln194. *J Biol Chem* 272, 25778-25782.

- Kent, T., Chandramouly, G., McDevitt, S.M., Ozdemir, A.Y., and Pomerantz, R.T. (2015). Mechanism of microhomology-mediated end-joining promoted by human DNA polymerase theta. *Nat Struct Mol Biol* 22, 230-237.
- Kim, D.H., Lee, K.H., Kim, J.H., Ryu, G.H., Bae, S.H., Lee, B.C., Moon, K.Y., Byun, S.M., Koo, H.S., and Seo, Y.S. (2005). Enzymatic properties of the *Caenorhabditis elegans* Dna2 endonuclease/helicase and a species-specific interaction between RPA and Dna2. *Nucleic Acids Res* 33, 1372-1383.
- Kim, H., Chen, J., and Yu, X. (2007). Ubiquitin-binding protein RAP80 mediates BRCA1-dependent DNA damage response. *Science* 316, 1202-1205.
- Kim, T., Chitteni-Pattu, S., Cox, B.L., Wood, E.A., Sandler, S.J., and Cox, M.M. (2015). Directed Evolution of RecA Variants with Enhanced Capacity for Conjugal Recombination. *PLoS Genet* 11, e1005278.
- Kim, T.M., Ko, J.H., Hu, L., Kim, S.A., Bishop, A.J., Vijg, J., Montagna, C., and Hasty, P. (2012). RAD51 mutants cause replication defects and chromosomal instability. *Mol Cell Biol* 32, 3663-3680.
- Kinebuchi, T., Kagawa, W., Enomoto, R., Tanaka, K., Miyagawa, K., Shibata, T., Kurumizaka, H., and Yokoyama, S. (2004). Structural basis for octameric ring formation and DNA interaction of the human homologous-pairing protein Dmc1. *Mol Cell* 14, 363-374.
- King, G.A., Burla, F., Peterman, E.J.G., and Wuite, G.J.L. (2019). Supercoiling DNA optically. *Proc Natl Acad Sci U S A* 116, 26534-26539.
- King, M.C., Marks, J.H., Mandell, J.B., and New York Breast Cancer Study, G. (2003). Breast and ovarian cancer risks due to inherited mutations in BRCA1 and BRCA2. *Science* 302, 643-646.
- Krishnamoorthy, A., Jackson, J., Mohamed, T., Adolph, M., Vindigni, A., and Cortez, D. (2021). RADX prevents genome instability by confining replication fork reversal to stalled forks. *Mol Cell* 81, 3007-3017 e3005.
- Le, H.P., Ma, X., Vaquero, J., Brinkmeyer, M., Guo, F., Heyer, W.D., and Liu, J. (2020). DSS1 and ssDNA regulate oligomerization of BRCA2. *Nucleic Acids Res* 48, 7818-7833.
- Lee, J.Y., Steinfeld, J.B., Qi, Z., Kwon, Y., Sung, P., and Greene, E.C. (2017). Sequence imperfections and base triplet recognition by the Rad51/RecA family of recombinases. *J Biol Chem* 292, 11125-11135.
- Lee, J.Y., Terakawa, T., Qi, Z., Steinfeld, J.B., Redding, S., Kwon, Y., Gaines, W.A., Zhao, W., Sung, P., and Greene, E.C. (2015). DNA RECOMBINATION. Base triplet stepping by the Rad51/RecA family of recombinases. *Science* 349, 977-981.
- Leon-Ortiz, A.M., Panier, S., Sarek, G., Vannier, J.B., Patel, H., Campbell, P.J., and Boulton, S.J. (2018). A Distinct Class of Genome Rearrangements Driven by Heterologous Recombination. *Mol Cell* 69, 292-305 e296.

- Li, Q., Saito, T.T., Martinez-Garcia, M., Deshong, A.J., Nadarajan, S., Lawrence, K.S., Checchi, P.M., Colaiacovo, M.P., and Engebrecht, J. (2018). The tumor suppressor BRCA1-BARD1 complex localizes to the synaptonemal complex and regulates recombination under meiotic dysfunction in *Caenorhabditis elegans*. *PLoS Genet* *14*, e1007701.
- Lieber, M.R., Ma, Y., Pannicke, U., and Schwarz, K. (2003). Mechanism and regulation of human non-homologous DNA end-joining. *Nat Rev Mol Cell Biol* *4*, 712-720.
- Lim, C.J., Zaug, A.J., Kim, H.J., and Cech, T.R. (2017). Reconstitution of human shelterin complexes reveals unexpected stoichiometry and dual pathways to enhance telomerase processivity. *Nat Commun* *8*, 1075.
- Lim, D.S., and Hasty, P. (1996). A mutation in mouse *rad51* results in an early embryonic lethal that is suppressed by a mutation in *p53*. *Mol Cell Biol* *16*, 7133-7143.
- Lin, Z., Kong, H., Nei, M., and Ma, H. (2006). Origins and evolution of the *recA/RAD51* gene family: evidence for ancient gene duplication and endosymbiotic gene transfer. *Proc Natl Acad Sci U S A* *103*, 10328-10333.
- Lisby, M., Barlow, J.H., Burgess, R.C., and Rothstein, R. (2004). Choreography of the DNA damage response: spatiotemporal relationships among checkpoint and repair proteins. *Cell* *118*, 699-713.
- Liu, J., Renault, L., Veaute, X., Fabre, F., Stahlberg, H., and Heyer, W.D. (2011). Rad51 paralogues Rad55-Rad57 balance the antirecombinase Srs2 in Rad51 filament formation. *Nature* *479*, 245-248.
- Lorenz, A. (2017). Modulation of meiotic homologous recombination by DNA helicases. *Yeast* *34*, 195-203.
- Luczak, M.W., and Zhitkovich, A. (2018). Monoubiquitinated gamma-H2AX: Abundant product and specific biomarker for non-apoptotic DNA double-strand breaks. *Toxicol Appl Pharmacol* *355*, 238-246.
- LUMICKS (2019). Manipulating and Studying Cellular Mechanics and Functions in Real-Time: Cellular Mechanics and Functions Application Note. (Amsterdam, The Netherlands., LUMICKS), p. 8.
- Luo, S.C., Yeh, H.Y., Lan, W.H., Wu, Y.M., Yang, C.H., Chang, H.Y., Su, G.C., Lee, C.Y., Wu, W.J., Li, H.W., *et al.* (2021). Identification of fidelity-governing factors in human recombinases DMC1 and RAD51 from cryo-EM structures. *Nat Commun* *12*, 115.
- Ma, C.J., Gibb, B., Kwon, Y., Sung, P., and Greene, E.C. (2017). Protein dynamics of human RPA and RAD51 on ssDNA during assembly and disassembly of the RAD51 filament. *Nucleic Acids Res* *45*, 749-761.



- Mailand, N., Bekker-Jensen, S., Faustrup, H., Melander, F., Bartek, J., Lukas, C., and Lukas, J. (2007). RNF8 ubiquitylates histones at DNA double-strand breaks and promotes assembly of repair proteins. *Cell* *131*, 887-900.
- Malik, P.S., and Symington, L.S. (2008). Rad51 gain-of-function mutants that exhibit high affinity DNA binding cause DNA damage sensitivity in the absence of Srs2. *Nucleic Acids Res* *36*, 6504-6510.
- Marko, J.F., and Siggia, E.D. (1995). Stretching DNA. *Macromolecules* *28*, 8759-8770.
- Martin, J.S., Winkelmann, N., Petalcorin, M.I., McIlwraith, M.J., and Boulton, S.J. (2005). RAD-51-dependent and -independent roles of a *Caenorhabditis elegans* BRCA2-related protein during DNA double-strand break repair. *Mol Cell Biol* *25*, 3127-3139.
- Martinez, J.S., von Nicolai, C., Kim, T., Ehlen, A., Mazin, A.V., Kowalczykowski, S.C., and Carreira, A. (2016). BRCA2 regulates DMC1-mediated recombination through the BRC repeats. *Proc Natl Acad Sci U S A* *113*, 3515-3520.
- Masson, J.Y., Tarsounas, M.C., Stasiak, A.Z., Stasiak, A., Shah, R., McIlwraith, M.J., Benson, F.E., and West, S.C. (2001). Identification and purification of two distinct complexes containing the five RAD51 paralogs. *Genes Dev* *15*, 3296-3307.
- Mateos-Gomez, P.A., Gong, F., Nair, N., Miller, K.M., Lazzerini-Denchi, E., and Sfeir, A. (2015). Mammalian polymerase theta promotes alternative NHEJ and suppresses recombination. *Nature* *518*, 254-257.
- Mateos-Gomez, P.A., Kent, T., Deng, S.K., McDevitt, S., Kashkina, E., Hoang, T.M., Pomerantz, R.T., and Sfeir, A. (2017). The helicase domain of Poltheta counteracts RPA to promote alt-NHEJ. *Nat Struct Mol Biol* *24*, 1116-1123.
- Mattiroli, F., Vissers, J.H., van Dijk, W.J., Ikpa, P., Citterio, E., Vermeulen, W., Marteijs, J.A., and Sixma, T.K. (2012). RNF168 ubiquitinates K13-15 on H2A/H2AX to drive DNA damage signaling. *Cell* *150*, 1182-1195.
- Maya-Mendoza, A., Moudry, P., Merchut-Maya, J.M., Lee, M., Strauss, R., and Bartek, J. (2018). High speed of fork progression induces DNA replication stress and genomic instability. *Nature* *559*, 279-284.
- McClendon, T.B., Sullivan, M.R., Bernstein, K.A., and Yanowitz, J.L. (2016). Promotion of Homologous Recombination by SWS-1 in Complex with RAD-51 Paralogs in *Caenorhabditis elegans*. *Genetics* *203*, 133-145.
- McIlwraith, M.J., Vaisman, A., Liu, Y., Fanning, E., Woodgate, R., and West, S.C. (2005). Human DNA polymerase eta promotes DNA synthesis from strand invasion intermediates of homologous recombination. *Mol Cell* *20*, 783-792.
- Meindl, A., Hellebrand, H., Wiek, C., Erven, V., Wappenschmidt, B., Niederacher, D., Freund, M., Lichtner, P., Hartmann, L., Schaal, H., *et al.* (2010). Germline mutations

- in breast and ovarian cancer pedigrees establish RAD51C as a human cancer susceptibility gene. *Nat Genet* 42, 410-414.
- Mevarech, M., and Werczberger, R. (1985). Genetic transfer in *Halobacterium volcanii*. *J Bacteriol* 162, 461-462.
- Mimitou, E.P., and Symington, L.S. (2008). Sae2, Exo1 and Sgs1 collaborate in DNA double-strand break processing. *Nature* 455, 770-774.
- Mirman, Z., Lottersberger, F., Takai, H., Kibe, T., Gong, Y., Takai, K., Bianchi, A., Zimmermann, M., Durocher, D., and de Lange, T. (2018). 53BP1-RIF1-shieldin counteracts DSB resection through CST- and Polalpha-dependent fill-in. *Nature* 560, 112-116.
- Modesti, M. (2018). Fluorescent Labeling of Proteins. *Methods Mol Biol* 1665, 115-134.
- Mortensen, U.H., Bendixen, C., Sunjevaric, I., and Rothstein, R. (1996). DNA strand annealing is promoted by the yeast Rad52 protein. *Proc Natl Acad Sci U S A* 93, 10729-10734.
- Muller, B., Koller, T., and Stasiak, A. (1990). Characterization of the DNA binding activity of stable RecA-DNA complexes. Interaction between the two DNA binding sites within RecA helical filaments. *J Mol Biol* 212, 97-112.
- Murayama, Y., Tsutsui, Y., and Iwasaki, H. (2011). The fission yeast meiosis-specific Dmc1 recombinase mediates formation and branch migration of Holliday junctions by preferentially promoting strand exchange in a direction opposite to that of Rad51. *Genes Dev* 25, 516-527.
- Myler, L.R., Gallardo, I.F., Soniat, M.M., Deshpande, R.A., Gonzalez, X.B., Kim, Y., Paull, T.T., and Finkelstein, I.J. (2017). Single-Molecule Imaging Reveals How Mre11-Rad50-Nbs1 Initiates DNA Break Repair. *Mol Cell* 67, 891-898 e894.
- Nakamura, K., Saredi, G., Becker, J.R., Foster, B.M., Nguyen, N.V., Beyer, T.E., Cesa, L.C., Faull, P.A., Lukauskas, S., Frimurer, T., *et al.* (2019). H4K20me0 recognition by BRCA1-BARD1 directs homologous recombination to sister chromatids. *Nat Cell Biol* 21, 311-318.
- Naor, A., and Gophna, U. (2013). Cell fusion and hybrids in Archaea: prospects for genome shuffling and accelerated strain development for biotechnology. *Bioengineered* 4, 126-129.
- Naor, A., Lapierre, P., Mevarech, M., Papke, R.T., and Gophna, U. (2012). Low species barriers in halophilic archaea and the formation of recombinant hybrids. *Curr Biol* 22, 1444-1448.
- Neale, M.J., and Keeney, S. (2006). Clarifying the mechanics of DNA strand exchange in meiotic recombination. *Nature* 442, 153-158.
- Neuman, K.C., and Block, S.M. (2004). Optical trapping. *Rev Sci Instrum* 75, 2787-2809.

- Neuman, K.C., and Nagy, A. (2008). Single-molecule force spectroscopy: optical tweezers, magnetic tweezers and atomic force microscopy. *Nat Methods* 5, 491-505.
- Newton, M.D., Taylor, B.J., Driessen, R.P.C., Roos, L., Cvetesic, N., Allyjaun, S., Lenhard, B., Cuomo, M.E., and Rueda, D.S. (2019). DNA stretching induces Cas9 off-target activity. *Nat Struct Mol Biol* 26, 185-192.
- Nimonkar, A.V., Genschel, J., Kinoshita, E., Polaczek, P., Campbell, J.L., Wyman, C., Modrich, P., and Kowalczykowski, S.C. (2011). BLM-DNA2-RPA-MRN and EXO1-BLM-RPA-MRN constitute two DNA end resection machineries for human DNA break repair. *Genes Dev* 25, 350-362.
- Noordermeer, S.M., Adam, S., Setiaputra, D., Barazas, M., Pettitt, S.J., Ling, A.K., Olivieri, M., Alvarez-Quilon, A., Moatti, N., Zimmermann, M., *et al.* (2018). The shieldin complex mediates 53BP1-dependent DNA repair. *Nature* 560, 117-121.
- O'Donnell, M., Langston, L., and Stillman, B. (2013). Principles and concepts of DNA replication in bacteria, archaea, and eukarya. *Cold Spring Harb Perspect Biol* 5.
- Odijk, T. (1995). Stiff chains and filaments under tension. *Macromolecules* 28, 7016-7018.
- Ono, S. (2010). Dynamic regulation of sarcomeric actin filaments in striated muscle. *Cytoskeleton (Hoboken)* 67, 677-692.
- Paix, A., Schmidt, H., and Seydoux, G. (2016). Cas9-assisted recombineering in *C. elegans*: genome editing using in vivo assembly of linear DNAs. *Nucleic Acids Res* 44, e128.
- Papke, R.T., Koenig, J.E., Rodriguez-Valera, F., and Doolittle, W.F. (2004). Frequent recombination in a saltern population of *Halorubrum*. *Science* 306, 1928-1929.
- Parmar, K., D'Andrea, A., and Niedernhofer, L.J. (2009). Mouse models of Fanconi anemia. *Mutat Res* 668, 133-140.
- Pasero, P., Bensimon, A., and Schwob, E. (2002). Single-molecule analysis reveals clustering and epigenetic regulation of replication origins at the yeast rDNA locus. *Genes Dev* 16, 2479-2484.
- Paull, T.T., and Gellert, M. (1998). The 3' to 5' exonuclease activity of Mre 11 facilitates repair of DNA double-strand breaks. *Mol Cell* 1, 969-979.
- Pellegrini, L., Yu, D.S., Lo, T., Anand, S., Lee, M., Blundell, T.L., and Venkitaraman, A.R. (2002). Insights into DNA recombination from the structure of a RAD51-BRCA2 complex. *Nature* 420, 287-293.
- Perkins, T.T., Quake, S.R., Smith, D.E., and Chu, S. (1994a). Relaxation of a single DNA molecule observed by optical microscopy. *Science* 264, 822-826.
- Perkins, T.T., Smith, D.E., and Chu, S. (1994b). Direct observation of tube-like motion of a single polymer chain. *Science* 264, 819-822.

- Petalcorin, M.I., Galkin, V.E., Yu, X., Egelman, E.H., and Boulton, S.J. (2007). Stabilization of RAD-51-DNA filaments via an interaction domain in *Caenorhabditis elegans* BRCA2. *Proc Natl Acad Sci U S A* *104*, 8299-8304.
- Petalcorin, M.I., Sandall, J., Wigley, D.B., and Boulton, S.J. (2006). CeBRC-2 stimulates D-loop formation by RAD-51 and promotes DNA single-strand annealing. *J Mol Biol* *361*, 231-242.
- Petukhova, G., Stratton, S., and Sung, P. (1998). Catalysis of homologous DNA pairing by yeast Rad51 and Rad54 proteins. *Nature* *393*, 91-94.
- Prakash, R., Sandoval, T., Morati, F., Zigelbaum, J.A., Lim, P.X., White, T., Taylor, B., Wang, R., Desclos, E.C.B., Sullivan, M.R., *et al.* (2021). Distinct pathways of homologous recombination controlled by the SWS1-SWSAP1-SPIDR complex. *Nat Commun* *12*, 4255.
- Qi, Z., Redding, S., Lee, J.Y., Gibb, B., Kwon, Y., Niu, H., Gaines, W.A., Sung, P., and Greene, E.C. (2015). DNA sequence alignment by microhomology sampling during homologous recombination. *Cell* *160*, 856-869.
- Quinet, A., Lemacon, D., and Vindigni, A. (2017). Replication Fork Reversal: Players and Guardians. *Mol Cell* *68*, 830-833.
- Ragunathan, K., Liu, C., and Ha, T. (2012). RecA filament sliding on DNA facilitates homology search. *Elife* *1*, e00067.
- Ramesh, M.A., Malik, S.B., and Logsdon, J.M., Jr. (2005). A phylogenomic inventory of meiotic genes; evidence for sex in *Giardia* and an early eukaryotic origin of meiosis. *Curr Biol* *15*, 185-191.
- Raschle, M., Smeenk, G., Hansen, R.K., Temu, T., Oka, Y., Hein, M.Y., Nagaraj, N., Long, D.T., Walter, J.C., Hofmann, K., *et al.* (2015). DNA repair. Proteomics reveals dynamic assembly of repair complexes during bypass of DNA cross-links. *Science* *348*, 1253671.
- Reginato, G., Cannavo, E., and Cejka, P. (2017). Physiological protein blocks direct the Mre11-Rad50-Xrs2 and Sae2 nuclease complex to initiate DNA end resection. *Genes Dev* *31*, 2325-2330.
- Robertson, R.B., Moses, D.N., Kwon, Y., Chan, P., Zhao, W., Chi, P., Klein, H., Sung, P., and Greene, E.C. (2009). Visualizing the disassembly of *S. cerevisiae* Rad51 nucleoprotein filaments. *J Mol Biol* *388*, 703-720.
- Rogakou, E.P., Pilch, D.R., Orr, A.H., Ivanova, V.S., and Bonner, W.M. (1998). DNA double-stranded breaks induce histone H2AX phosphorylation on serine 139. *J Biol Chem* *273*, 5858-5868.
- Rosenshine, I., Tchelet, R., and Mevarech, M. (1989). The mechanism of DNA transfer in the mating system of an archaebacterium. *Science* *245*, 1387-1389.

- Roy, U., Kwon, Y., Marie, L., Symington, L., Sung, P., Lisby, M., and Greene, E.C. (2021). The Rad51 paralog complex Rad55-Rad57 acts as a molecular chaperone during homologous recombination. *Mol Cell* *81*, 1043-1057 e1048.
- Saini, N., Ramakrishnan, S., Elango, R., Ayyar, S., Zhang, Y., Deem, A., Ira, G., Haber, J.E., Lobachev, K.S., and Malkova, A. (2013). Migrating bubble during break-induced replication drives conservative DNA synthesis. *Nature* *502*, 389-392.
- Sartori, A.A., Lukas, C., Coates, J., Mistrik, M., Fu, S., Bartek, J., Baer, R., Lukas, J., and Jackson, S.P. (2007). Human CtIP promotes DNA end resection. *Nature* *450*, 509-514.
- Schlacher, K., Christ, N., Siaud, N., Egashira, A., Wu, H., and Jasin, M. (2011). Double-strand break repair-independent role for BRCA2 in blocking stalled replication fork degradation by MRE11. *Cell* *145*, 529-542.
- Schmidt, J.C., Zaug, A.J., and Cech, T.R. (2016). Live Cell Imaging Reveals the Dynamics of Telomerase Recruitment to Telomeres. *Cell* *166*, 1188-1197 e1189.
- Seluanov, A., Mao, Z., and Gorbunova, V. (2010). Analysis of DNA double-strand break (DSB) repair in mammalian cells. *J Vis Exp*.
- Semlow, D.R., and Walter, J.C. (2021). Mechanisms of Vertebrate DNA Interstrand Cross-Link Repair. *Annu Rev Biochem* *90*, 107-135.
- Sfeir, A., and Symington, L.S. (2015). Microhomology-Mediated End Joining: A Backup Survival Mechanism or Dedicated Pathway? *Trends Biochem Sci* *40*, 701-714.
- Shahid, T., Soroka, J., Kong, E., Malivert, L., McIlwraith, M.J., Pape, T., West, S.C., and Zhang, X. (2014). Structure and mechanism of action of the BRCA2 breast cancer tumor suppressor. *Nat Struct Mol Biol* *21*, 962-968.
- Short, J.M., Liu, Y., Chen, S., Soni, N., Madhusudhan, M.S., Shivji, M.K., and Venkitaraman, A.R. (2016). High-resolution structure of the presynaptic RAD51 filament on single-stranded DNA by electron cryo-microscopy. *Nucleic Acids Res* *44*, 9017-9030.
- Siaud, N., Barbera, M.A., Egashira, A., Lam, I., Christ, N., Schlacher, K., Xia, B., and Jasin, M. (2011). Plasticity of BRCA2 function in homologous recombination: genetic interactions of the PALB2 and DNA binding domains. *PLoS Genet* *7*, e1002409.
- Sigurdsson, S., Van Komen, S., Bussen, W., Schild, D., Albala, J.S., and Sung, P. (2001). Mediator function of the human Rad51B-Rad51C complex in Rad51/RPA-catalyzed DNA strand exchange. *Genes Dev* *15*, 3308-3318.
- Sirbu, B.M., Couch, F.B., Feigerle, J.T., Bhaskara, S., Hiebert, S.W., and Cortez, D. (2011). Analysis of protein dynamics at active, stalled, and collapsed replication forks. *Genes Dev* *25*, 1320-1327.
- Smith, S.B., Cui, Y., and Bustamante, C. (1996). Overstretching B-DNA: the elastic response of individual double-stranded and single-stranded DNA molecules. *Science* *271*, 795-799.

- Smith, S.B., Finzi, L., and Bustamante, C. (1992). Direct mechanical measurements of the elasticity of single DNA molecules by using magnetic beads. *Science* 258, 1122-1126.
- Smogorzewska, A., Matsuoka, S., Vinciguerra, P., McDonald, E.R., 3rd, Hurov, K.E., Luo, J., Ballif, B.A., Gygi, S.P., Hofmann, K., D'Andrea, A.D., *et al.* (2007). Identification of the FANCI protein, a monoubiquitinated FANCD2 paralog required for DNA repair. *Cell* 129, 289-301.
- Sobhian, B., Shao, G., Lilli, D.R., Culhane, A.C., Moreau, L.A., Xia, B., Livingston, D.M., and Greenberg, R.A. (2007). RAP80 targets BRCA1 to specific ubiquitin structures at DNA damage sites. *Science* 316, 1198-1202.
- Sogo, J.M., Lopes, M., and Foiani, M. (2002). Fork reversal and ssDNA accumulation at stalled replication forks owing to checkpoint defects. *Science* 297, 599-602.
- Solinger, J.A., Lutz, G., Sugiyama, T., Kowalczykowski, S.C., and Heyer, W.D. (2001). Rad54 protein stimulates heteroduplex DNA formation in the synaptic phase of DNA strand exchange via specific interactions with the presynaptic Rad51 nucleoprotein filament. *J Mol Biol* 307, 1207-1221.
- Somyajit, K., Saxena, S., Babu, S., Mishra, A., and Nagaraju, G. (2015). Mammalian RAD51 paralogs protect nascent DNA at stalled forks and mediate replication restart. *Nucleic Acids Res* 43, 9835-9855.
- Somyajit, K., Spies, J., Coscia, F., Kirik, U., Rask, M.B., Lee, J.H., Neelsen, K.J., Mund, A., Jensen, L.J., Paull, T.T., *et al.* (2021). Homology-directed repair protects the replicating genome from metabolic assaults. *Dev Cell* 56, 461-477 e467.
- Spell, R.M., and Jinks-Robertson, S. (2004). Examination of the roles of Sgs1 and Srs2 helicases in the enforcement of recombination fidelity in *Saccharomyces cerevisiae*. *Genetics* 168, 1855-1865.
- Spies, M., and Fishel, R. (2015). Mismatch repair during homologous and homeologous recombination. *Cold Spring Harb Perspect Biol* 7, a022657.
- Spirek, M., Mlcouskova, J., Belan, O., Gyimesi, M., Harami, G.M., Molnar, E., Novacek, J., Kovacs, M., and Krejci, L. (2018). Human RAD51 rapidly forms intrinsically dynamic nucleoprotein filaments modulated by nucleotide binding state. *Nucleic Acids Res* 46, 3967-3980.
- Stark, J.M., Hu, P., Pierce, A.J., Moynahan, M.E., Ellis, N., and Jasin, M. (2002). ATP hydrolysis by mammalian RAD51 has a key role during homology-directed DNA repair. *J Biol Chem* 277, 20185-20194.
- Steinfeld, J.B., Belan, O., Kwon, Y., Terakawa, T., Al-Zain, A., Smith, M.J., Crickard, J.B., Qi, Z., Zhao, W., Rothstein, R., *et al.* (2019). Defining the influence of Rad51 and Dmc1 lineage-specific amino acids on genetic recombination. *Genes Dev* 33, 1191-1207.

- Sternberg, S.H., Redding, S., Jinek, M., Greene, E.C., and Doudna, J.A. (2014). DNA interrogation by the CRISPR RNA-guided endonuclease Cas9. *Nature* 507, 62-67.
- Stewart, G.S., Panier, S., Townsend, K., Al-Hakim, A.K., Kolas, N.K., Miller, E.S., Nakada, S., Ylanko, J., Olivarius, S., Mendez, M., *et al.* (2009). The RIDDLE syndrome protein mediates a ubiquitin-dependent signaling cascade at sites of DNA damage. *Cell* 136, 420-434.
- Stewart, G.S., Wang, B., Bignell, C.R., Taylor, A.M., and Elledge, S.J. (2003). MDC1 is a mediator of the mammalian DNA damage checkpoint. *Nature* 421, 961-966.
- Storlazzi, A., Tesse, S., Gargano, S., James, F., Kleckner, N., and Zickler, D. (2003). Meiotic double-strand breaks at the interface of chromosome movement, chromosome remodeling, and reductional division. *Genes Dev* 17, 2675-2687.
- Story, R.M., Bishop, D.K., Kleckner, N., and Steitz, T.A. (1993). Structural relationship of bacterial RecA proteins to recombination proteins from bacteriophage T4 and yeast. *Science* 259, 1892-1896.
- Stucki, M., Clapperton, J.A., Mohammad, D., Yaffe, M.B., Smerdon, S.J., and Jackson, S.P. (2005). MDC1 directly binds phosphorylated histone H2AX to regulate cellular responses to DNA double-strand breaks. *Cell* 123, 1213-1226.
- Sugawara, N., Goldfarb, T., Studamire, B., Alani, E., and Haber, J.E. (2004). Heteroduplex rejection during single-strand annealing requires Sgs1 helicase and mismatch repair proteins Msh2 and Msh6 but not Pms1. *Proc Natl Acad Sci U S A* 101, 9315-9320.
- Sung, P., and Roberson, D.L. (1995). DNA strand exchange mediated by a RAD51-ssDNA nucleoprotein filament with polarity opposite to that of RecA. *Cell* 82, 453-461.
- Symington, L.S. (2016). Mechanism and regulation of DNA end resection in eukaryotes. *Crit Rev Biochem Mol Biol* 51, 195-212.
- Taylor, M.R.G., Spirek, M., Chaurasiya, K.R., Ward, J.D., Carzaniga, R., Yu, X., Egelman, E.H., Collinson, L.M., Rueda, D., Krejci, L., *et al.* (2015). Rad51 Paralogs Remodel Pre-synaptic Rad51 Filaments to Stimulate Homologous Recombination. *Cell* 162, 271-286.
- Taylor, M.R.G., Spirek, M., Jian Ma, C., Carzaniga, R., Takaki, T., Collinson, L.M., Greene, E.C., Krejci, L., and Boulton, S.J. (2016). A Polar and Nucleotide-Dependent Mechanism of Action for RAD51 Paralogs in RAD51 Filament Remodeling. *Mol Cell* 64, 926-939.
- Taylor, M.R.G., and Yeeles, J.T.P. (2018). The Initial Response of a Eukaryotic Replisome to DNA Damage. *Mol Cell* 70, 1067-1080 e1012.
- Thorslund, T., Esashi, F., and West, S.C. (2007). Interactions between human BRCA2 protein and the meiosis-specific recombinase DMC1. *EMBO J* 26, 2915-2922.

- Thorslund, T., McIlwraith, M.J., Compton, S.A., Lekomtsev, S., Petronczki, M., Griffith, J.D., and West, S.C. (2010). The breast cancer tumor suppressor BRCA2 promotes the specific targeting of RAD51 to single-stranded DNA. *Nat Struct Mol Biol* 17, 1263-1265.
- van Mameren, J., Modesti, M., Kanaar, R., Wyman, C., Peterman, E.J., and Wuite, G.J. (2009). Counting RAD51 proteins disassembling from nucleoprotein filaments under tension. *Nature* 457, 745-748.
- Villeneuve, A.M., and Hillers, K.J. (2001). Whence meiosis? *Cell* 106, 647-650.
- von Hippel, P.H., and Berg, O.G. (1989). Facilitated target location in biological systems. *J Biol Chem* 264, 675-678.
- Wang, A.T., Kim, T., Wagner, J.E., Conti, B.A., Lach, F.P., Huang, A.L., Molina, H., Sanborn, E.M., Zierhut, H., Cornes, B.K., *et al.* (2015). A Dominant Mutation in Human RAD51 Reveals Its Function in DNA Interstrand Crosslink Repair Independent of Homologous Recombination. *Mol Cell* 59, 478-490.
- Wang, B., Matsuoka, S., Ballif, B.A., Zhang, D., Smogorzewska, A., Gygi, S.P., and Elledge, S.J. (2007). Abraxas and RAP80 form a BRCA1 protein complex required for the DNA damage response. *Science* 316, 1194-1198.
- Wang, M.D., Yin, H., Landick, R., Gelles, J., and Block, S.M. (1997). Stretching DNA with optical tweezers. *Biophys J* 72, 1335-1346.
- Ward, J.D., Barber, L.J., Petalcorin, M.I., Yanowitz, J., and Boulton, S.J. (2007). Replication blocking lesions present a unique substrate for homologous recombination. *EMBO J* 26, 3384-3396.
- Ward, J.D., Muzzini, D.M., Petalcorin, M.I., Martinez-Perez, E., Martin, J.S., Plevani, P., Cassata, G., Marini, F., and Boulton, S.J. (2010). Overlapping mechanisms promote postsynaptic RAD-51 filament disassembly during meiotic double-strand break repair. *Mol Cell* 37, 259-272.
- Watkins, L.P., and Yang, H. (2005). Detection of intensity change points in time-resolved single-molecule measurements. *J Phys Chem B* 109, 617-628.
- Williams, R.C., and Spengler, S.J. (1986). Fibers of RecA protein and complexes of RecA protein and single-stranded phi X174 DNA as visualized by negative-stain electron microscopy. *J Mol Biol* 187, 109-118.
- Williams, R.S., Moncalian, G., Williams, J.S., Yamada, Y., Limbo, O., Shin, D.S., Grocock, L.M., Cahill, D., Hitomi, C., Guenther, G., *et al.* (2008). Mre11 dimers coordinate DNA end bridging and nuclease processing in double-strand-break repair. *Cell* 135, 97-109.
- Wilson, M.A., Kwon, Y., Xu, Y., Chung, W.H., Chi, P., Niu, H., Mayle, R., Chen, X., Malkova, A., Sung, P., *et al.* (2013). Pif1 helicase and Poldelta promote recombination-coupled DNA synthesis via bubble migration. *Nature* 502, 393-396.



- Woglar, A., and Villeneuve, A.M. (2018). Dynamic Architecture of DNA Repair Complexes and the Synaptonemal Complex at Sites of Meiotic Recombination. *Cell* 173, 1678-1691 e1616.
- Wright, W.D., and Heyer, W.D. (2014). Rad54 functions as a heteroduplex DNA pump modulated by its DNA substrates and Rad51 during D loop formation. *Mol Cell* 53, 420-432.
- Wright, W.D., Shah, S.S., and Heyer, W.D. (2018). Homologous recombination and the repair of DNA Double-Strand Breaks. *J Biol Chem*.
- Wyatt, H.D., Laister, R.C., Martin, S.R., Arrowsmith, C.H., and West, S.C. (2017). The SMX DNA Repair Tri-nuclease. *Mol Cell* 65, 848-860 e811.
- Xia, B., Sheng, Q., Nakanishi, K., Ohashi, A., Wu, J., Christ, N., Liu, X., Jasin, M., Couch, F.J., and Livingston, D.M. (2006). Control of BRCA2 cellular and clinical functions by a nuclear partner, PALB2. *Mol Cell* 22, 719-729.
- Xia, J., Chen, L.T., Mei, Q., Ma, C.H., Halliday, J.A., Lin, H.Y., Magnan, D., Pribis, J.P., Fitzgerald, D.M., Hamilton, H.M., *et al.* (2016). Holliday junction trap shows how cells use recombination and a junction-guardian role of RecQ helicase. *Sci Adv* 2, e1601605.
- Xu, G., Chapman, J.R., Brandsma, I., Yuan, J., Mistrik, M., Bouwman, P., Bartkova, J., Gogola, E., Warmerdam, D., Barazas, M., *et al.* (2015). REV7 counteracts DNA double-strand break resection and affects PARP inhibition. *Nature* 521, 541-544.
- Xu, J., Zhao, L., Xu, Y., Zhao, W., Sung, P., and Wang, H.W. (2017). Cryo-EM structures of human RAD51 recombinase filaments during catalysis of DNA-strand exchange. *Nat Struct Mol Biol* 24, 40-46.
- Yang, H., Li, Q., Fan, J., Holloman, W.K., and Pavletich, N.P. (2005). The BRCA2 homologue Brh2 nucleates RAD51 filament formation at a dsDNA-ssDNA junction. *Nature* 433, 653-657.
- Yang, H., Zhou, C., Dhar, A., and Pavletich, N.P. (2020). Mechanism of strand exchange from RecA-DNA synaptic and D-loop structures. *Nature* 586, 801-806.
- Yates, L.A., Aramayo, R.J., Pokhrel, N., Caldwell, C.C., Kaplan, J.A., Perera, R.L., Spies, M., Antony, E., and Zhang, X. (2018). A structural and dynamic model for the assembly of Replication Protein A on single-stranded DNA. *Nat Commun* 9, 5447.
- Yin, J., Lin, A.J., Golan, D.E., and Walsh, C.T. (2006). Site-specific protein labeling by Sfp phosphopantetheinyl transferase. *Nat Protoc* 1, 280-285.
- Youds, J.L., Mets, D.G., McIlwraith, M.J., Martin, J.S., Ward, J.D., NJ, O.N., Rose, A.M., West, S.C., Meyer, B.J., and Boulton, S.J. (2010). RTEL-1 enforces meiotic crossover interference and homeostasis. *Science* 327, 1254-1258.
- Yuan, S.S., Lee, S.Y., Chen, G., Song, M., Tomlinson, G.E., and Lee, E.Y. (1999). BRCA2 is required for ionizing radiation-induced assembly of Rad51 complex in vivo. *Cancer Res* 59, 3547-3551.

- Zahn, K.E., Jensen, R.B., Wood, R.D., and Doublet, S. (2021). Human DNA polymerase theta harbors DNA end-trimming activity critical for DNA repair. *Mol Cell* 81, 1534-1547 e1534.
- Zellweger, R., Dalcher, D., Mutreja, K., Berti, M., Schmid, J.A., Herrador, R., Vindigni, A., and Lopes, M. (2015). Rad51-mediated replication fork reversal is a global response to genotoxic treatments in human cells. *J Cell Biol* 208, 563-579.
- Zhang, F., Ma, J., Wu, J., Ye, L., Cai, H., Xia, B., and Yu, X. (2009). PALB2 links BRCA1 and BRCA2 in the DNA-damage response. *Curr Biol* 19, 524-529.
- Zhang, J., Dewar, J.M., Budzowska, M., Motnenko, A., Cohn, M.A., and Walter, J.C. (2015). DNA interstrand cross-link repair requires replication-fork convergence. *Nat Struct Mol Biol* 22, 242-247.
- Zhao, W., Steinfeld, J.B., Liang, F., Chen, X., Maranon, D.G., Jian Ma, C., Kwon, Y., Rao, T., Wang, W., Sheng, C., *et al.* (2017). BRCA1-BARD1 promotes RAD51-mediated homologous DNA pairing. *Nature* 550, 360-365.
- Zhao, W., Vaithiyalingam, S., San Filippo, J., Maranon, D.G., Jimenez-Sainz, J., Fontenay, G.V., Kwon, Y., Leung, S.G., Lu, L., Jensen, R.B., *et al.* (2015). Promotion of BRCA2-Dependent Homologous Recombination by DSS1 via RPA Targeting and DNA Mimicry. *Mol Cell* 59, 176-187.
- Zimmermann, M., Lottersberger, F., Buonomo, S.B., Sfeir, A., and de Lange, T. (2013). 53BP1 regulates DSB repair using Rif1 to control 5' end resection. *Science* 339, 700-704.